Design of a Water-Propelled Modular Vaporizing Liquid Micro-Resistojet (VLM) Propulsion System for CubeSat Integration

Niek Zandvliet

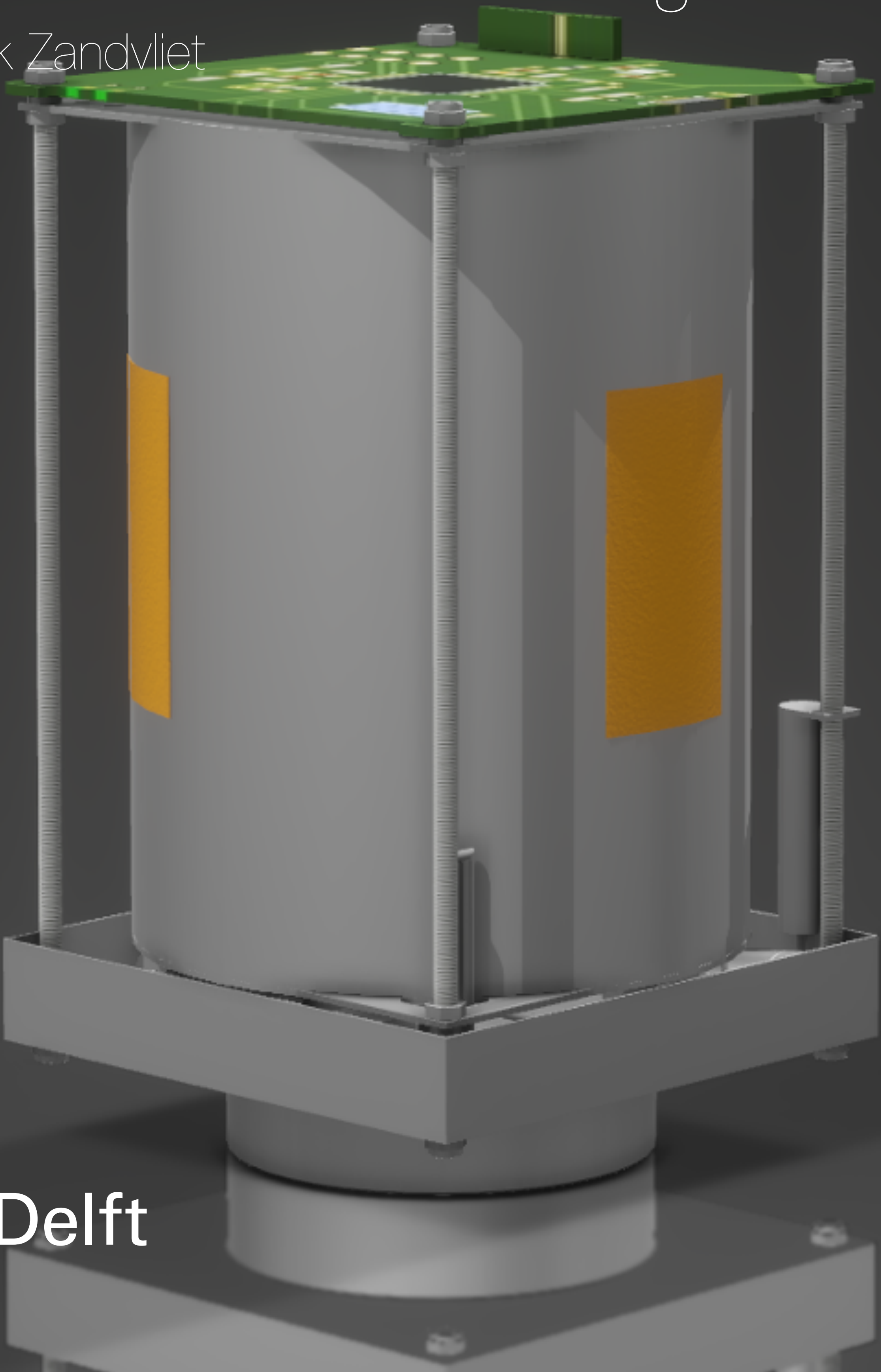

TU Delft

Design of a Water-Propelled Modular Vaporizing Liquid Micro-Resistojet (VLM) Propulsion System for CubeSat Integration

by

Niek Zandvliet

to obtain the degree of Master of Science
at the Delft University of Technology
to be defended publicly on January 22, 2025 at 10:00

Thesis committee:

Chair:	Alessandra Menicucci
Supervisor:	Angelo Cervone
External examiner:	Ines Uriol Balbin
Place:	Faculty of Aerospace Engineering, Delft
Project Duration:	February, 2024 - December, 2024
Student number:	4796403

Faculty of Aerospace Engineering · Delft University of Technology

Preface

This thesis marks the end of my 6-year study period at Delft University of Technology. I vividly remember the day I was accepted to start my bachelor's in Aerospace Engineering. I could have never imagined how this journey would shape me as a person. The many challenges throughout these six years made me grow both personally and professionally and showed me that determination and hard work pays off. I am grateful for the opportunities that the TU Delft provided me, all the projects that I have been involved in, and the people that I have met along the way.

I would like to thank several people, without whom this thesis would not have been possible. First, I would like to thank my supervisor, Angelo Cervone. He guided me through this project, was always willing to meet, and answered any questions I had. I would like to thank Barry Zandbergen for the several meetings we had where we discussed the design considerations regarding the propellant management devices. I would like to thank Ines Uriol Balbin and Niels van der Pas for their insights on thermal analysis, Daniël Peeters for his expertise in structural analysis, and Daniel Atherstone for his assistance with the 3DExperience modelling software.

Finally, I would like to thank my parents for their unwavering support throughout my academic career. I could always rely on them, no matter what day or time. Their encouragements gave me confidence in my abilities. A special thanks to my partner, whom I met around the start of my master's program. He supported me throughout these final years, and his reminders to take breaks and step away from studying at times had a positive impact on my work and results.

Niek Zandvliet
Delft, December 2024

Abstract

The high costs associated with launching satellites into orbit drives the market towards more compact satellites. These compact satellites require the development of miniaturized components, including a propulsion system. The Space Engineering (SpE) department of the Faculty of Aerospace engineering at the TU Delft is actively working on developing these miniaturized propulsion systems, including the Vaporizing Liquid Micro-resistojet (VLM). This thesis aims to "design a modular micro-resistojet propulsion system that is capable of delivering three distinct total impulse levels, based on a pre-existing VLM thruster developed by the TU Delft, with a focus on integration into a CubeSat configuration. The three systems developed in this thesis comprise a printed circuit board (PCB), a propellant tank with integrated propellant management devices (PMDs), piping, tank heaters, and a TunaCan add-on, utilizing water as the propellant and gaseous nitrogen as the pressurant. The PMD is a combination of a radial sponge, consisting of 70 sponge panels, and a 6-vane configuration. This vane configuration consists of 3 short and 3 long vanes to increase the expulsion efficiency without altering the ability to move propellant from the top of the tank towards the sponge and tank outlet. A preliminary thermal analysis on simplified versions of propulsion systems showed that a combination of tank heaters, each capable of providing 0.5 W, and a Zerlauts Z-93 white coating applied to the thruster side of the propulsion system are required to maintain a propellant temperature between 10 °C and 50 °C, whilst ensuring that the propellant within the piping does neither freeze nor boil. The final system designs achieve a thrust level of 1 mN and specific impulse of 130 s for a maximum input power of 7.9 W. A detailed thruster design is outside the scope of this thesis hence these performance values are calculated using ideal rocket theory. The three systems are capable of delivering a total impulse of 226 Ns, 465 Ns, and 700 Ns at a wet mass of 777 grams, 998 grams, and 1217 grams respectively. Several recommendations are proposed for further research, including the redesign of the thruster, enhancements to the tankage and PMD design, and improvements to the thermal and structural analyses.

Contents

List of Symbols

Latin Letters	**Quantity**	**Symbol Unit**
A	Cross-sectional area of propellant fillet	[m^2]
A_c	Cross-sectional area of beam	[m^2]
A_e	Nozzle exit area	[m^2]
A_i	Area of node i	[m^2]
A_{in}	Inner cross-sectional area	[m^2]
A_o	Orifice area	[m^2]
A_t	Nozzle throat area	[m^2]
a	Lateral acceleration	[m/s^2]
a_{limit}	Limit acceleration	[m/s^2]
a_r	Relative acceleration	[m/s^2]
a_s	Surface area to volume ratio	[1/m]
a_x	Lateral acceleration	[m/s^2]
a_y	Axial acceleration	[m/s^2]
B_{ij}	Gebhart factor from node i to j	[-]
Bo	Bond number	[-]
C	Attachment design factor	[-]
C_D	Chord length based on vane height	[m]
C_d	Discharge coefficient	[-]
C_p	Specific heat capacity	[J/(kg·K)]
C_S	Chord length based on sponge height	[m]
C_v	Specific heat at constant volume	[J/(kg·K)]
c	Area wave propagation speed	[m/s]
c_{pG}	Constant pressure specific heat of gas	[J/(kg·K]
c_{p_i}	Specific heat capacity of node i	[J/(kg·K)]
c_{pL}	Constant pressure specific heat of liquid	[J/(kg·K]
D	Diameter	[m]
D_h	Hole diameter	[m]
D_i	Inner diameter	[m]
D_m	Mean diameter	[m]
D_o	Outer diameter	[m]
D_p	Pore diameter	[m]
D_V	Distance between two vanes	[m]
d_p	Distance between propellant and tank wall	[m]
E	Young's modulus	[Pa]
E_j	Joint efficiency factor	[-]
F_A	Reaction force at point A	[N]
F_C	Maximum compressive force	[N]
F_i	Fill ratio	[-]
F_{ij}	View factor from node i to j	[-]
F_R	Reaction force	[N]
F_t	Thrust force	[N]
F_T	Maximum tensile force	[N]
f	Friction factor	[-]
f_n	Natural frequency	[Hz]
g_0	Gravitational acceleration at sea level	[m/s^2]
g_{avg}	Average slot width	[m]
g_{inner}	Inner panel gap	[m]
g_{outer}	Outer panel gap	[m]
H	Enthalpy	[J/kg]
H_{dyn}	Dynamic head	[m^2/s^2]
H_i	Inner tank height	[m]
H_{loss}	Flow loss head	[m^2/s^2]
H_o	Outer tank height	[m]
H_{prop}	Propellant height in tank	[m]
H_S	Sponge height	[m]
Hst	Surface tension head	[m^2/s^2]
H_t	Inner tank height	[m]
H_V	Vane height	[m]
h_{orbit}	Orbital altitude	[km]
h_p	Height of cylindrical propellant surface	[m]
h_s	Sponge height	[m]
h_{tank}	Tank height	[m]
$h_{thruster}$	Thruster height	[m]
I	Moment of inertia	[m^4]

I_{bit}	Impulse bit per orbit	[Ns]
I_{sc}	Achievable impulse	[Ns]
I_{sp}	Specific impulse	[s]
I_{tot}	Total impulse	[Ns]
k	Thermal conductivity	[W/(m·K)]
L	Lohm rate	[Lohms]
L_{avg}	Average beam length	[m]
L_c	Characteristic length	[m]
L_{eq}	Equivalent length	[m]
L_h	Latent heat of vaporization	[kJ/kg]
L_i	Inner length of propellant tank	[m]
L_o	Outer length of propellant tank	[m]
L_p	Sponge panel length	[m]
L_{pipe}	Length of pipe	[m]
L_V	Vane length	[m]
M_A	Reaction moment at point A	[Nm]
M_b	Bending moment	[Nm]
M_{dry}	Dry mass	[kg]
M_{fluid}	Combined pressurant and propellant mass	[kg]
M_i	Internal bending moment	[Nm]
M_{N_2}	Nitrogen mass	[kg]
M_P	Reaction moment at point P	[Nm]
M_p	Propellant mass	[kg]
M_R	Reaction moment at point R	[Nm]
M_s	Sponge mass	[kg]
M_{sc}	Spacecraft mass	[kg]
M_{sl}	Slosh mass	[kg]
M_{st}	Stationary mass	[kg]
M_{tank}	Tank shell mass	[kg]
M_W	Molar mass	[kg/mol]
M_{wet}	Wet mass	[kg]
M_{pres}	Pressurant mass	[kg]
M_{prop}	Propellant mass	[kg]
m	Mass	[kg]
$\dot{m}$	Mass flow rate	[kg/s]
m_i	Mass of node i	[kg]
N_i	Internal normal force	[N]
N_p	Number of radial sponge panels	[-]
N_V	Number of vanes	[-]
P	Pressure	[N/m^2]
P_{BP}	Bubble point pressure	[Pa]
P_{drive}	Driving pressure	[Pa]
P_{FTS}	Flow-through-screen pressure	[Pa]
P_{gas}	Gas pressure	[N/m^2]
P_h	Heating power	[W]
P_{liquid}	Liquid pressure	[N/m^2]
P_{st}	Surface tension pressure	[Pa]
P_v	Vapor pressure	[Pa]
p_a	Ambient pressure	[Pa]
p_c	Chamber pressure	[Pa]
p_e	Nozzle exit pressure	[Pa]
p_{pres_f}	Final pressurant tank pressure	[Pa]
p_{pres_i}	Initial pressurant tank pressure	[Pa]
p_{tank}	Tank pressure	[Pa]
p_{tank_f}	Final tank pressure	[Pa]
p_{tank_i}	Initial tank pressure	[Pa]
Q	Volumetric flow rate	[m^3/s]
$\dot{Q}$	Volumetric flow rate along vane	[m^3/s]
Q_{albedo}	Albedo load	[W]
Q_{IR}	Planetary infrared load	[W]
Q_i	Power entering node i	[W]
Q_{max}	Maximum volumetric flow rate	[m^3/s]
Q_{req}	Required volumetric flow rate	[m^3/s]
Q_{sun}	Direct solar load	[W]
R	Reliability	[-]
R	Radius of curvature	[m]
R_A	Universal gas constant	[J/(mol·K)]
R_D	Downstream radius of curvature	[m]
Re	Reynolds number	[-]
R_e	Earth radius	[km]
R_i	Radiative link between node i and space	[m^2]
R_{ij}	Radiative link between node i and j	[m^2]
R_{low}	Lower principal radius of curvature	[m]
R_{pres}	Pressurant specfic gas constant	[J/(kg·K)]
R_S	Sponge outer radius	[m]
R_t	Tank inner radius	[m]

R_{tank_i}	Tank inner radius	[m]
R_U	Upstream radius of curvature	[m]
R_{up}	Upper principal radius of curvature	[m]
r	Radial distance between sponge center and propellant surface	[m]
r_{low}	Lower radial distance to sponge center	[m]
r_p	Radius of cylindrical propellant surface	[m]
r_s	Sponge radius	[m]
$r_{s_{inner}}$	Sponge inner radius	[m]
$r_{s_{max}}$	Maximum allowed sponge outer radius	[m]
$r_{s_{outer}}$	Sponge outer radius	[m]
r_{tank}	Tank radius	[m]
$r_{thruster}$	Thruster radius	[m]
r_{up}	Upper radial distance to sponge center	[m]
S	Solubility	[g/kg]
S_b	Bending stress	[Pa]
S_c	Solar flux constant	[W/m^2]
S_m	Membrane stress	[Pa]
S_T	Total stress in tank skin	[Pa]
s	Wetted circumference	[m]
T_{avg}	Average temperature	[K]
T_{boil}	Boiling temperature	[K]
T_c	Chamber temperature	[K]
T_{earth}	Effective Earth temperature	[K]
T_{fin}	Final temperature	[K]
T_i	Temperature of node i	[K]
T_{ini}	Initial temperature	[K]
T_P	Reaction force at point P	[N]
T_R	Reaction force at point R	[N]
T_{sc}	Spacecraft bus temperature	[K]
T_{tank}	Tank temperature	[K]
t	Time step	[s]
t_b	Burn duration	[s]
t_c	Thickness of tank mechanical interface	[m]
t_h	Head thickness	[m]
t_m	Mission duration	[years]
t_p	Panel thickness	[m]
t_s	Skin thickness	[m]
t_{sc}	Screen thickness	[m]
U	Internal energy	[J]
U_{st}	Total elastic strain energy	[J]
u	Flow velocity	[m/s]
u_{max}	Maximum flow velocity	[m/s]
u_p	Propellant flow velocity	[m/s]
V	Velocity	[m/s]
V_g	Pressurant volume	[m^3]
V_{head}	Required flat endcap material volume	[m^3]
V_i	Internal shear force	[N]
V_{man}	Required propellant volume per manoeuvre	[m^3]
V_p	Propellant volume	[m^3]
V_{prop}	Propellant volume in tank at BOL	[m^3]
V_{pres_f}	Final pressurant volume	[m^3]
V_{pres_i}	Initial pressurant volume	[m^3]
V_R	Residual propellant volume	[m^3]
V_{shell}	Required seamless tube volume	[m^3]
V_{tank}	Tank volume	[m^3]
v	Flow velocity	[m/s]
v_e	Jet velocity	[m/s]
w_c	Width of tank mechanical interface	[m]
W_i	Inner width of propellant tank	[m]
W_o	Outer width of propellant tank	[m]
z_{low}	Lower height relative to acceleration vector	[m]
z_{up}	Upper height relative to acceleration vector	[m]

Greek Letters	**Quantity**	**Symbol Unit**
α	Absorptivity	[-]
α_i	Absorptivity of node i	[-]
α_f	Fitting parameter	[-]
α_{th}	Thermal diffusivity	[m^2/s]
β_f	Fitting parameter	[-]
β_p	Coefficient of volumetric expansion of propellant	[1/K]
Γ	Vandenkerckhove function	[-]
γ	Specific heat ratio	[-]
γ_d	Damping ratio	[-]
Δ	Change	[-]

ϵ	Emissivity	[-]
ϵ_i	Emissivity of node i	[-]
ϵ_v	Dimensionless void fraction	[-]
θ	Angle between propulsion system and launch vehicle	[rad]
θ_c	Contact angle	[rad]
λ_i	Component failure rate	[-]
μ	Dynamic viscosity	[Ns/m^2]
ν	Kinematic viscosity	[m^2/s]
ρ	Density	[kg/m^3]
ρ_{mat}	Density of propellant tank material	[kg/m^3]
ρ_p	Propellant density	[kg/m^3]
ρ_{prop}	Propellant density	[kg/m^3]
ρ_{pres}	Pressurant density	[kg/m^3]
ρ_{pres_i}	Initial pressurant density	[kg/m^3]
ρ_t	Density of titanium	[kg/m^3]
σ	Stefan-Boltzmann constant	[W/(m^{2}K^4)]
σ_a	Absolute surface tension	[N/m]
σ_C	Maximum compressive load	[Pa]
σ_c	Circumferential stress	[Pa]
σ_m	Maximum allowable stress	[Pa]
σ_s	Surface tension	[N/m]
σ_{st}	Standard deviation	[-]
σ_T	Maximum tensile load	[Pa]
σ_u	Ultimate tensile strength	[Pa]
σ_{VM}	Von Mises Stress	[Pa]
σ_y	Tensile yield strength	[Pa]
τ	Shear load	[Pa]
ϕ	Angle relative to acceleration vector	[rad]
ψ	Slosh angle	[rad]
ω_n	Angular natural frequency	[rad/s]

List of Abbreviations

ACS	*Attitude Control System*
BOL	*Beginning Of Life*
CAD	*Computer Aided Design*
COTS	*Commercial Off The Shelf*
DOT	*Design Option Tree*
DW	*Diffusion Welding*
EBW	*Electron-Beam Welding*
EE	*Expulsion Efficiency*
EOL	*End Of Life*
EP	*Extended Performance*
EW	*Explosive Welding*
FBD	*Free Body Diagram*
FoS	*Factor of Safety*
FSW	*Friction Stir Welding*
FTS	*Flow Through Screen*
CHIPS	*CubeSat High Impulse Propulsion System*
CFH	*Cubic Feet per Hour*
FEA	*Finite Element Analysis*
FMMR	*Free Molecular Micro-Resistojet*
FRW	*FRiction Welding*
GTAW	*Gas-Tungsten Arc Welding*
HAZ	*Heat Affected Zone*
ID	*Inner Diameter*
ISS	*International Space Station*
JAXA	*Japan Aerospace Exploration Agency*
KD	*Kinetic Diagram*
LBW	*Laser-Beam Welding*
LEO	*Low Earth Orbit*
LPBF	*Laser Powder Bed Fusion*
LPM	*Low Pressure Micro-resistojet*
LSV	*Linear Structural Validation*
LW	*Laser Welding*
MEMS	*Micro Electronic Mechanical Systems*
MIB	*Minimum Impulse Bit*
MIG	*Metal Inert Gas*
MMA	*Manual Metal Arc*
MRJ	*Micro-ResistoJet*
NFPA	*National Fire Protection Association*
OD	*Outer Diameter*
PAW	*Plasma Arc Welding*
PCB	*Printed Circuit Board*
PED	*Positive Expulsion Device*
PMD	*Propellant Management Device*
PWM	*Pulse Width Monitoring*
RAMPART	*RApid prototyped Mems Propulsion And Radiation Test*
RAMS	*Reliability, Availability, Maintainability, and Safety*
RPS	*RAMPART Propulsion System*
RW	*Resistance Welding*
SCFH	*Standard Cubic Feet per Hour*
SHC	*Super Heater Cartridge*
SpE	*Space Engineering*
STD	*Surface Tension Device*
TC	*Thermal Couple*
THC	*THruster Chip*
TIG	*Tungsten Inert Gas*
VLM	*Vaporizing Liquid Micro-resistojet*
WEDM	*Wire Electrical Discharge Machining*

List of Figures

List of Tables

Introduction 1

The space market is experiencing continuous growth, with an increasing number of companies developing and launching spacecraft. Among these, nanosatellites have emerged as a particularly attractive option due to their small size, lightweight design, and low cost. To enhance the capabilities of such satellites, propulsion systems play a crucial role in extending mission duration and expanding operational possibilities. As a result, significant research is being conducted to develop compact and efficient propulsion systems tailored for this group of satellites. The space engineering department (SpE) of the Faculty of Aerospace Engineering of the TU Delft is one of the institutions actively contributing to this field, including ongoing research into the Vaporizing Liquid Micro-resistojet (VLM) and the Low-Pressure Micro-Resistojet (LPM). This thesis aims to make a small contribution to this ongoing research.

The aim of this thesis is expressed by the research objective: "Designing a modular micro-resistojet propulsion system that is capable of delivering three distinct total impulse levels, based on a pre-existing VLM thruster developed by the TU Delft, with a focus on integration into a CubeSat configuration".

This thesis has the following structure. A literature review on the current state-of-the-art micro-resistojet propulsion systems is presented in Chapter 2, and is followed by the research plan in Chapter 3. The thruster and system requirements are outlined in Chapter 4, after which the propellant trade-off is performed in Chapter 5. A trade-off between different types of feed systems is then performed Chapter 6. The outcomes of both the propellant and feed system trade-offs are used to establish design budgets, as outlined in Chapter 7. Subsequently, the propellant tank and piping are designed in Chapter 8 and Chapter 9 respectively. A structural analysis then conducted in Chapter 10, followed by a thermal analysis in Chapter 11. The three propulsion system assemblies, along with their respective performance metrics, are presented in Chapter 12. The thesis is concluded by answering the research questions, and their associated sub-questions in Chapter 13, followed by several recommendations for further research provided in Chapter 14.

Literature Study 2

2.1 Introduction

The launch of the Sputnik satellite in 1957 marked the beginning of the space industry. This 85 kg satellite orbited the Earth for three months, and travelled over 70 million kilometres around our planet [1]. As of March 7th 2024, there are over 9450 active satellites that orbit the Earth [2]. Many of these satellites contain some form of propulsion that is required to fulfil their mission. An overview of possible propulsion systems is shown in Figure 2.1.

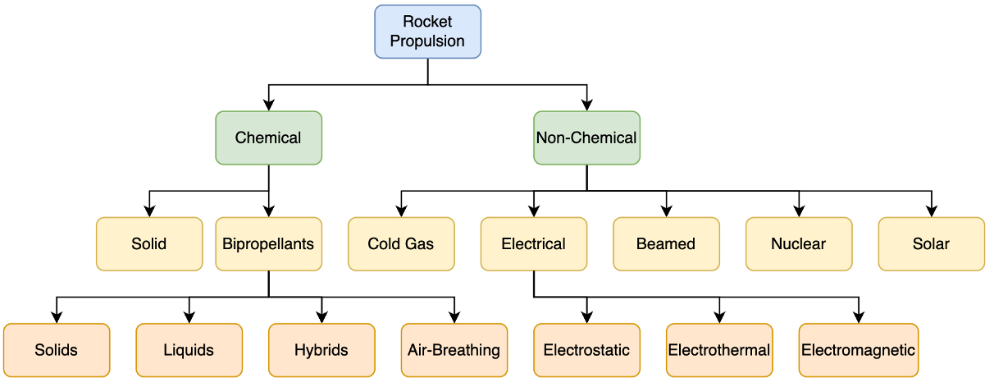

Figure 2.1: Propulsion options for satellites [3] [4].

This literature study focusses on a specific type of propulsion, namely micro-resistojet propulsion: an electrothermal propulsion type. The objective is "to investigate the current state-of-the-art micro-resistojet propulsion system composition of small satellites." This investigation into the current state-of-the-art marks the starting point of my thesis that aims to design a micro-resistojet propulsion system around an existing thruster. Investigating these systems allows for a better understanding of not only the types and configurations of micro-resistojet propulsion systems that are out there, but also helps in gaining an understanding of why systems look the way they do.

The objective is achieved by finding answers to the three following research questions:

1. What is the current state-of-the-art regarding micro-resistojet propulsion systems in small satellites, and why are these current configurations chosen?
2. What design parameters have the most significant impact on the propulsion system performance, and how can they be adjusted to balance efficiency, mass, and complexity?
3. What are the existing configurations and rationale behind the mechanical, electrical, and thermal interfaces between micro-resistojet propulsion systems and the rest of the spacecraft, and what factors influence the selection of these specific interface configurations in current state-of-the-art designs?

To find answers to these questions, and to achieve the objective of this literature study, the following structure is proposed. First, an introduction on electrothermal propulsion is given in Section 2.2. This is followed by a detailed description of several micro-resistojet propulsion systems in Section 2.3. Section 2.4 outlines linear trends that have been found between several thruster performance characteristics of current micro-resistojet propulsion systems. Finally, answers to the research questions, are documented in Section 2.5.

2.2 Electrothermal Propulsion

Electrothermal propulsion, also known as warm gas propulsion, uses electrical power to heat a propellant [5]. This type of propulsion is very similar to cold gas propulsion with the addition of a heater in the sense that the propellant is stored in a tank, and pressurized by a pressurant when stored in its liquid phase, and is injected into the heating chamber by opening a thrust valve. The heating of the propellant results in a higher, but limited, specific impulse (Isp) than that of cold gas systems. The limited increase in Isp is a direct result of the available heating power in satellites [6]. A schematic of a typical electrothermal propulsion system is shown in Figure 2.2.

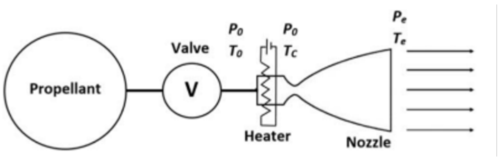

Figure 2.2: Schematic of a typical electrothermal propulsion system [6].

There are four heating mechanisms used in electrothermal propulsion systems: radio frequency (RF) heating, micro cavity discharge (MCD) heating, microwave heating, and resistive heating. The latter is the most common heating method, and propulsion systems that use this method of heating are called resistojets [5]. Resistojets have been used since the 1960s on board of the Vela satellites. The TRW single-nozzle resistojet, flown on the Vela III satellite in 1965, produced a thrust of approximately 187 mN at an Isp of 123 s and an input power of 42 W by using gaseous nitrogen. Other resistojet propulsion systems were designed, but it never became a popular option for use in spacecraft and satellites [6].

However, research on miniaturized electrothermal thrusters is thriving due to the simplicity of the concept, and the high thrust-to-power ratio compared to other electric propulsion concepts, especially in the 1-100 mN thrust level range. There are two groups of micro-resistojet propulsion systems: the conventional micro-resistojet thrusters, and the less conventional micro-resistojet thrusters. An overview of all micro-resistojet concepts can be found in Figure 2.3. The conventional thrusters refer to either the warm gas micro-resistojets or the vaporizing liquid micro-resistojets (VLM). In the warm gas micro-resistojet thruster gaseous propellant is (moderately) heated and expelled through the nozzle, whereas a liquid propellant is vaporized (by heating) and expelled through the nozzle in the VLM. Most VLM systems vaporizes the propellant by heating it just before the nozzle during a manoeuvre, resulting in a highly dynamic two-phase flow in the thrust chamber. The two-phase flow, a consequence of the "real time" heating process, results in fluid dynamic complications such as microbubbles and instabilities. A novel VLM water micro-resistojet system concept, named AQUARIUS, separates the thrust chamber and the heating chamber by using a separate vaporization chamber. This feature allows for the vaporization of propellant before the actual manoeuvre is started, and removes most of the fluid dynamic complications that result from two-phase flow. An added benefit to this concept is the ability to use waste heat from other subsystems to prevaporize the propellant [6]. The AQUARIUS propulsion system, and conventional VLMs are discussed in detail in Section 2.3.

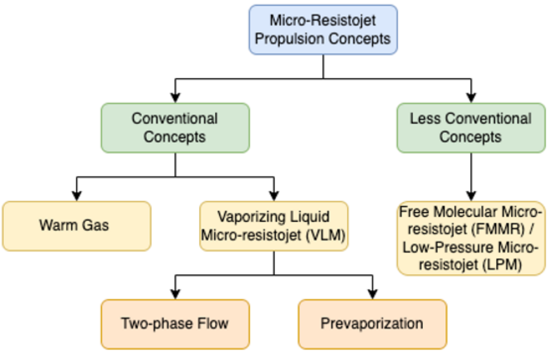

Figure 2.3: Micro-resistojet concepts.

The less conventional thrusters refer to the free molecular micro-resistojets (FMMR), also known as the low-pressure micro-resistojets (LPM). This concept mitigates the issues of micronozzles in vaporizing micro-resistojets by working in the rarefield or transitional flow regime. The traditional convergent-divergent nozzle is replaced with a low-pressure plenum and expansion slots. Propellant particles are accelerated through collisions with the heated expansion slot walls. This system also allows for so-called "dual use": it can act as a micro-resistojet and a cold gas thruster by simply turning the expansion slot wall heater on or off. The FMMR concept was first researched by the Air Force Research Laboratory and the University of Southern California in the early 2000s [6]. The concept is visualized in Figure 2.4.

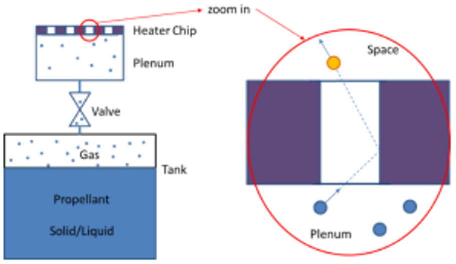

Figure 2.4: LPM concept scheme [7].

2.3 Micro-Resistojet Propulsion Systems

2.3.1 CubeSat High Impulse Propulsion System

The CubeSat High Impulse Propulsion System, also known as CHIPS, combines both the primary propulsion, and the attitude control system (ACS) into a single, bolt-on module that can be used in 2-6U CubeSats. It is designed and tested by CU Aerospace and VACCO industries in 2015. This propulsion system is not only able to perform orbital maintenance, but can also achieve significant altitude changes, perform rendezvous and docking manoeuvres, and can be used for formation flying missions.

Nine propellants have been investigated during the design of this system, including liquid water, isobutane, and two refrigerants: R134a and R236fa. Seven criteria are used in the trade-off, and are summarized in Table 2.1. A big part of the design is based on the self-pressurization ability of the propellant, as this simplifies the feed system significantly; there is no need for a separate pressurization system. R134a was chosen, as it complied with all the criteria that can be found in Table 2.1.

Table 2.1: Propellant trade-off criteria [8].

Criterion	**Justification**
High liquid density	Maximize propellant mass and ΔV.
High density x sound speed	Maximize ΔV.
Low heat of vaporization	Low propellant heater power required.
Self-pressurizing	Simplifies the feed system.
Critical temperature > 60 °C	Liquid between 0 °C and 60 °C.
Low freezing point	Liquid between 0 °C and 60 °C.
Compatible with materials and electronics	Enables location of electronics inside storage tank.

CHIPS primary propulsion system can achieve a thrust of 30 mN and an Isp of 82s at an input power of 30W. The total achievable impulse of the system is 564 Ns. These values are for the warm-firing of the thruster. The system can also perform cold fires for smaller manoeuvres and has a separate set of thrusters built in for ACS purposes. These figures are not considered in this literature study, as the goal is to create an overview of the current resistojet configurations only. The CHIPS system occupies a total volume of 1020 cm^3 and has a cross-section of 95 mm x 95 mm to allow room for the mounting of other subsystems, such as a solar array. The length of the system can be system can be altered as per mission requirement. Examples of this are the use of larger (or smaller) propellant tank, and the use of an optional energy reservoir of 8.7 Wh to power the propulsion system [8].

System Configuration

The thruster used in CHIPS is the high-efficiency micro-resistojet, also known as the superheater cartridge (SHC). This cartridge makes use of a resistive heating, thin-walled superheat tube that feeds propellant to the supersonic nozzle. It has been optimized in such a way that thermal conduction and radiation losses are minimized. Furthermore, a coaxial shroud is used to further reduce thermal losses, and to protect the thruster during transportation and handling. A prototype of the SHC can be seen in Figure 2.5.

Figure 2.5: SHC prototype [8].

The self-pressurizing propellant R134a is stored in an integral tank and includes a heater. This heater ensures that the propellant stays at saturation conditions within the tank. This is required, as the propellant temperature (and pressure) drops when the propellant in the tank evaporates. The propellant passes through a micro-heat exchanger feed dryer as soon as the shutoff valve is opened. This dryer ensures that no liquids enter the vapor planum. The pressure inside the vapor chamber is controlled through a closed-loop control system between the pressure control valve and the CHIPS controller board. Finally, the feed valves in the planum control the flow of gaseous propellant to the required thrusters. An overview of the CHIPS propulsion system can be found in Figure 2.6.

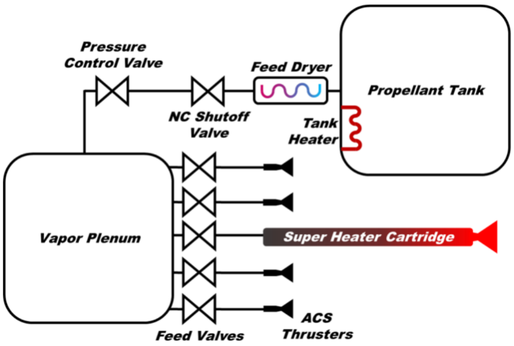

Figure 2.6: CHIPS system configuration [8].

The seven valves in the propulsion system are the so-called normally closed, frictionless soft-seat solenoid micro-valves from VACCO Industries and have been tested for more than 200,000 cold gas firings. Furthermore, the propellant tank and vapor plenum are welded to prevent leakage, and the feed system topology is designed to be dual-fault tolerant against leakage, as to comply with Air Force Space Command range safety user requirements AFSPCMAN 91-710 [8].

Current CHIPS Thrusters

The performance characteristics of thrusters tend to be improved upon in time, as is also the case for CHIPS. Currently, as of June 2023, CU Aerospace offers three variants of the thruster, namely the CHIPS-180, CHIPS-500, and CHIPS-1000 [9]. None of these thrusters match the performance figures of the system described in this section. The performance of these three thrusters (for hot firing) is summarized in Table 2.2.

Table 2.2: Current CHIPS resistojet propulsion systems [9].

Thruster	**CHIPS-180**	**CHIPS-500**	**CHIPS-1000**
Thrust [mN]	15	25	31
Isp [s]	67	69	70
Total Impulse [Ns]	176	505	1030
Wet Mass [kg]	1.027	1.835	3.13
Envelope [U]	0.54	1.3	2.5
Power [W]	20	25	30

The CHIPS-1000 is the closest to the CHIPS thruster discussed above in terms of thrust and power draw. It must be noted that the total impulse of the CHIPS-1000 is significantly larger than original thruster, as is the volume that the system occupies. These two observations are most likely a result of the use of a larger propellant tank. An interesting observation that can be made is the overall decrease in Isp of all systems (approximately 70 s vs the initially stated 82 s whilst using the same R134a propellant). This can be a result of an increase in the chamber temperature and/or an updated nozzle design.

CHIPS Interfaces

Figure 2.7 shows the CHIPS-180 propulsion module's technical drawing. This system is used to outline the interfaces of the propulsion system with the rest of the spacecraft, and it is assumed that the larger systems follow a similar interface approach. A first observation that can be made is that this system is fully enclosed on all sides, and results in a smooth, continuous box design. The CHIPS-180 contains 12 bus mounting holes of the type 4-40-UNC-2B, with a depth of 4 mm each hole, that functions as the mechanical interface between the propulsion system and the bus. These mounting points are also visible in Figure 2.8, where the electrical interfaces are highlighted.

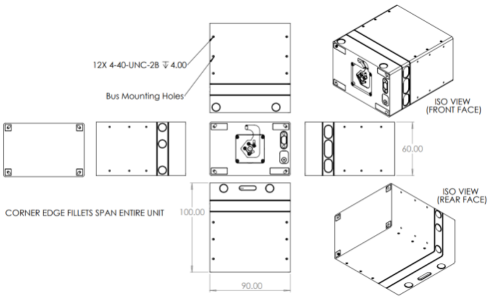

Figure 2.7: Technical drawing of the CHIPS-180 propulsion module [9].

These electrical interfaces consist of the firmware reprogramming port, and the command and data port. The latter allows for controlling the burn duration, and for receiving telemetry and system status packets for heath monitoring. No information regarding thermal interfaces is provided. This could be explained by the enclosed nature of the system, that results in a thermally isolated module, but this cannot be verified [9].

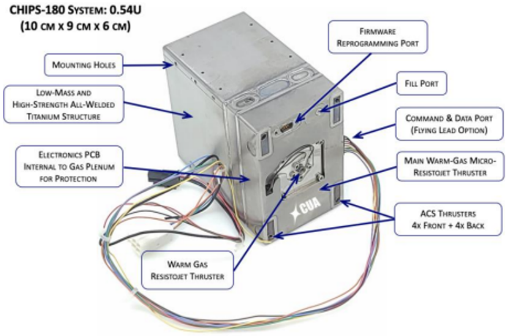

Figure 2.8: CHIPS-180 propulsion module [9].

2.3.2 AQUARIUS

The development of the AQUARIUS micro-resistojet propulsion system started in April 2016 at the University of Tokyo in Japan. The system was on-boarded on the EQUULEUS spacecraft, developed by The University of Tokyo in collaboration with the Japan Aerospace Exploration Agency (JAXA), and launched from the International Space Station (ISS) in November 2019 [10].

Water is used as a propellant, as this allows for low pressures within the feed system, a reduction of the dry mass ratio when comparing to a high pressure gas system, and for simplification of the feedlines, as soft tubes can be used. Another consideration is the non-toxic nature of water, as it is difficult to meet launch safety requirements when using toxic propellants in a secondary payload. However, the high latent heat of vaporization of water is an issue. This is mitigated by using the waste heat from communication components to vaporize the water [11]. The use of waste heat is possible, as the AQUARIUS propulsion system makes use of a separate vaporization chamber, rather than using a more conventional real time heating process when thrusting as explained in Section 2.2.

The AQUARIUS micro-resistojet propulsion system can achieve thrust levels of 2 mN for the reaction control system (RCS) thruster,a and 4 mN for the DeltaV thruster. An Isp of 70 s is reached at the pre-heater temperature of 100 K, and a total power consumption of less than 20W. A total impulse of $<$ 250 Ns is achieved. The total volume of the AQUARIUS system is $<$ 1.0 U, with a dry mass of $<$ 0.8 kg, and a wet mass of $<$ 1.2 kg [10].

System Configuration

The AQUARIUS propulsion system contains 5 thrusters: 1 DeltaV thruster, and 4 RCS thrusters [10]. These thrusters consist of a pre-heater, a thermal insulator, and a nozzle. The flow path diameter of the pre-heater is 4 mm, and the total flow path length is approximately 130 mm. The throat diameter of the RCS and DeltaV thruster are 1.2 mm and 1.6 mm respectively. The AQUARIUS propulsion system can be seen in Figure 2.9.

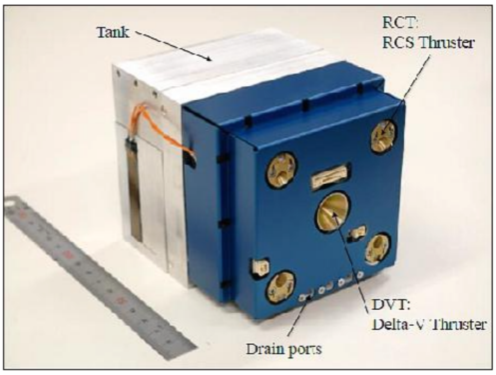

Figure 2.9: AQUARIUS propulsion system unit [10].

The propellant (water) is stored in a propellant tank. This tank also contains a bladder that separates the propellant from the pressurant, as a blow down system is used. Water droplets are injected and vaporized in the vaporizer at room-temperature (290-310 K) when opening the regulating valves. The water vapor inside the vaporizer is at saturation pressure (< 5 kPa) and flows to the thrusters under its own pressure. The vapor is heated to approximately 343 K in the pre-heater and accelerated through the nozzle. A schematic overview of the system can be found in Figure 2.10. The system contains 4 regulating valves, 2 fill-drain valves, 5 thruster valves, and 4 pressure sensors [10].

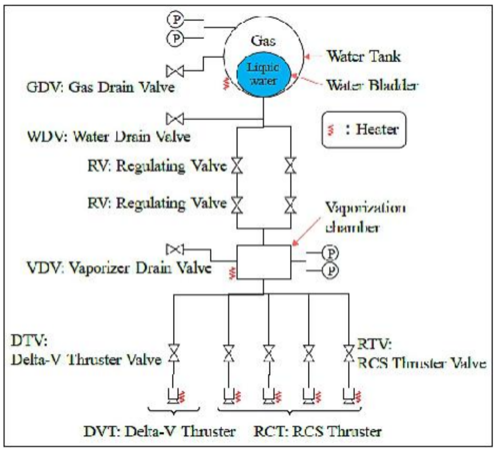

Figure 2.10: AQUARIUS system configuration [10].

AQUARIUS Interfaces

Figure 2.9 shows the AQUARIUS propulsion system unit, which again is a smooth box. No detailed information on any of the interfaces is provided, but some can be deduced from Figure 2.9 and Figure 2.11 where the AQUARIUS-1U module is integrated in the AQT-D spacecraft.

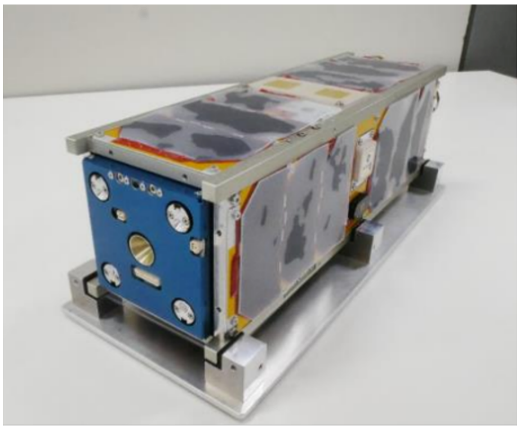

Figure 2.11: AQUARIUS integrated in the AQT-D spacecraft [10].

First, three mounting holes can be seen in Figure 2.9. It is safe to assume that this configuration is similar on the other side of the thruster, thus a total of 6 mounting holes are used to mechanically fasten the propulsion unit to the bus. Furthermore, three ports can be seen on the thruster nozzle side of the propulsion unit in both figures. These are most likely programming ports, as no wires are visible in Figure 2.11 where the system is fully integrated. Finally, orange wires from the front of the thruster to the side could be a thermal interface with the communication device from which heat flows to vaporize propellant, or an electrical interface that powers the system, but no information on this specific feature is provided.

2.3.3 Pale Blue Resistojet Thruster

A resistojet thruster, designed by Pale Blue, is based on the AQUARIUS design that is outlined in Subsection 2.3.2. The system is designed for orbit raising and keeping, and was launched at the beginning of 2023 onboard the SPHERE-1 EYE: a 6U CubeSat developed by Sony Group Corporation. Like AQUARIUS, water is used as a propellant.

The thruster was ground qualified in a vacuum chamber at Pale Blue Inc (with a back pressure of < 1 Pa), and achieved an average thrust of 2.7 mN, an Isp of > 60 s, and a total impulse of > 170 Ns at in input power < 30 W. The estimated thrust on orbit is 6.1-7.2 mN due to higher vapor pressure [12]. The system fits within 1.25 U, and the wet and dry mass are 1.4kg, and 1.114kg respectively. The propulsion system is shown in Figure 2.12.

Figure 2.12: Pale Blue resistojet thruster [12].

2.3.4 System Configuration

The propulsion system consists of a control board, a power processing unit, a propellant tank, a vaporizer, and four nozzles. No detailed information on the nozzles is provided, other than that they are heating to avoid condensation and to increase Isp [13]. A schematic of the system can be seen in Figure 2.13.

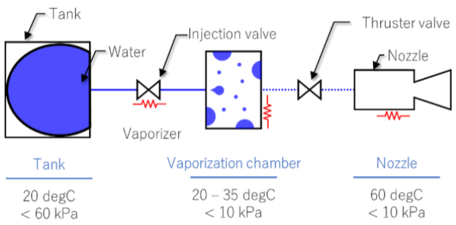

Figure 2.13: Pale Blue resistojet thruster system configuration [13].

The propellant (liquid water) is stored in the propellant tank at a temperature and pressure of 293K and < 60 kPa respectively. The propellant is injected into the vaporization chamber when the injection valve is opened. Water vapor is separated from the liquid water, and heated to 303-313 K in this chamber at a pressure below 10 kPa. The thruster valve(s) open when the pressure in the vaporization chamber stabilizes, and the propellant enters the nozzle where it is heated (to 333 K), accelerated, and expelled. As mentioned already, this final heating of the propellant is done to avoid condensation and to increase the specific impulse. The system contains a total of one injection valve, and four thruster valves [12].

2.3.5 Current Pale Blue Resistojet Thrusters

Pale Blue currently offers three resistojet propulsion systems, of which two can be integrated in a 3U CubeSat format. These are the PBR-10, and PBR-20 [14]. The specifications of these thrusters can be found in Table 2.3.

Table 2.3: Current Pale Blue micro-resistojet propulsion systems [14].

Thruster	**PBR-10**	**PBR-20**
Thrust [mN]	1	1
Isp [s]	55	70
Total Impulse [Ns]	50	200
Wet Mass [kg]	0.6	1.5
Envelope [U]	0.5	1
Power [W]	6.5	20

2.3.6 Pale Blue Resistojet Interfaces

No detailed information regarding the interfaces of Pale Blue resistojet propulsion systems. However, as with the AQUARIUS system, some interfaces can be deduced from images. Figure 2.12 shows the propulsion system that flew onboard the SPHERE-1 EYE CubeSat. Furthermore, Figure 2.14 shows the current PBR-10 and PBR-20 resistojet systems.

(a) PBR-10

(b) PBR-20

Figure 2.14: Current Pale Blue resistojet propulsion systems [14].

These three systems are all enclosed in a smooth box that allows for easy integration with a spacecraft. The locations of the mounting holes differ between the systems, where the PBR-10 mounting holes are located at the nozzle side, and the mounting holes of the SPHERE-1 EYE, and the PBR-20 are located on the side. The number of mounting points for the latter two systems is unknown; the PBR-10 system contains four mounting holes. Furthermore, programming ports are shown on the nozzle side in both Figure 2.12, and Figure 2.14a. The system makes use of a 5V, and an unregulated supply voltage, and uses the RS-422 UART communication protocol [13].

2.3.7 RAMPART

The RAMPART (stands for Rapid prototyped Mems Propulsion And Radiation Test) is a 2U CubeSat, designed by Dr Adam Huang and his graduate students at the University of Arkansas. The RAMPART propulsion system (RPS), a micro-resistojet, is designed and manufactured by using rapid prototyping and microelectromechanical system (MEMS) technologies. The system was supposed to be piggy-back launched on the Minotaur-1 in June 2013 to a 450 km by 1200 kg elliptical orbit but was delayed and later cancelled [15].

The RPS uses R134a as a propellant, due to its self-pressurizing capability at the RAMPART satellite design temperature range, and its non-toxic and non-flammable nature. The use of a self-pressurizing propellant simplifies the feed system by eliminating the need for pumps or other pressurization systems.

The RPS can, as some other micro-resistojet propulsion systems, both cold and hot fire. This results in a vacuum Isp range of 67 s for cold firing, and 90 s for hot firing. A thrust level of 500 mN can be achieved, and the whole system first within a 1U enclosure. The power usage of the propulsion system is not specified. The only information that is available on the power system of the RAMPART CubeSat is that there are 8 NMH batteries on board and four double-sided solar panels that consist of 32 SpectroLab triple-junction solar cells [16].

System Configuration

The heater section is integrated in the nozzle, resulting in one heater/nozzle assembly that is fabricated using MEMS technology, and shown in Figure 2.15. This assembly is made from bonded silicon layers, and the convergent-divergent nozzle has an expansion ratio of 50:1 with adiabatic nozzle walls to minimize heat loss that is typical in resistojets.

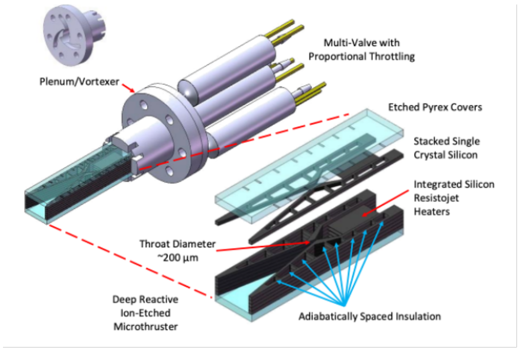

Figure 2.15: RAMPART Propulsion System (RPS) heater/nozzle assembly [16].

The heater/nozzle assembly is supplied with propellant through the feed system that of which a schematic overview is depicted in Figure 2.16. The propellant tank is filled through a LEE Extended Performance (EP) Schrader Valve A MEMS porous etched membrane inside the propellant tank acts as both a propellant phase separator that prevents liquid propellant from entering the feed lines, and a coarse propellant filter. Propellant starts flowing towards the fluid mixer when the 2-way LEE EP solenoid valve assembly is opened. These LEE EP valves are rated at 12V, 0.5W and 500 Hz, and allow for throttling of the RPS by using the Pulse Width Monitoring (PWM) technique. The propellant flows through the swirl flow mixer and enters the heater/nozzle assembly where it is heated, accelerated, and expelled.

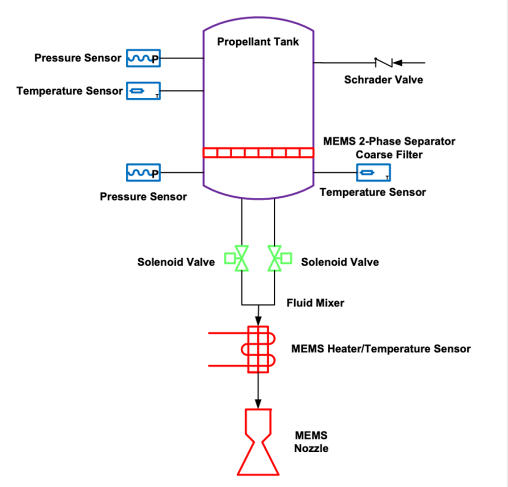

Figure 2.16: RAMPART Propulsion System (RPS) configuration [16].

The propulsion system has a total of 2 pressure sensors, 3 temperature sensors (one is embedded in the MEMS heater), and 3 LEE EP valves (2 solenoid valves, and 1 Schrader valve) [16].

RAMPART Interfaces

No detailed description on any of the interfaces of the RAMPART Propulsion System with the spacecraft bus can be found. Two CAD drawings of the system are available, one that shows the propulsion module (Figure 2.17), and one that shows the integrated propulsion module in the 2U CubeSat (Figure 2.18).

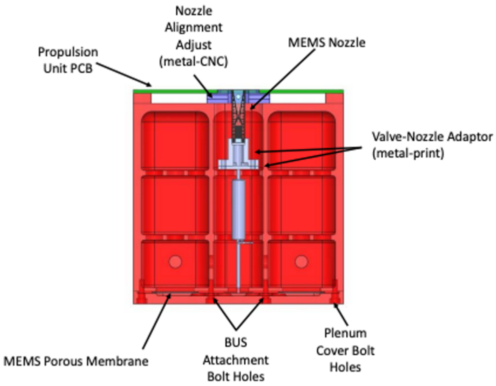

Figure 2.17: RAMPART Propulsion System [16].

Figure 2.17 is the most useful when considering the interfaces, as it indicates the presence of bus attachment bolt holes. Only two bolt holes are shown here, but it can be assumed that there are two other attachment points on the other side of the module, resulting in a total of 4 bus attachment points. The electrical, and thermal interfaces cannot be deduced from these images.

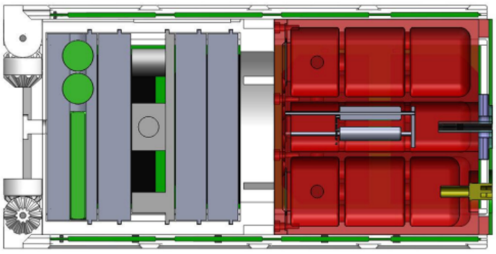

Figure 2.18: Integrated RAMPART Propulsion System [16].

2.3.8 3U CubeSat Propulsion Module

The 3U CubeSat Propulsion Module (3UCPM) is designed by NanoSpace/GOMSpace and is integrated in CubeSats since September 2015. MEMS technologies are used to produce parts of the system, and the module can both hot and cold fire.

Butane is used as a propellant and results in a total impulse of 40 Ns, and a specific impulse of 81 s. There are 4 nozzles that can each produce a maximum thrust of 1 mN with a thrust resolution < 10 microN by using a closed loop thrust control method. These thrust levels are achieved by consuming an average operating power of 2W per nozzle at an operating pressure between 2 and 5 bar. The wet and dry mass of the system are 0.35 kg and 0.3 kg respectively and fits within an 0.5U enclosure (10 x 10 x 5 cm).

System Configuration

A schematic overview of the 3UCPM can be found in Figure 2.19. Butane is stored in the heated propellant tank and flows, through a filter, to the thrusters when the barrier (ON/OFF) valves are opened. A pressure/mass flow sensors and a MEMS Proportional Flow Control Valve manage the mass flow rate (hence the thrust level) through each Thruster Chip (THC) by using a closed loop thrust control method. The propellant that enters the thruster is first heated in the chamber, after which it is accelerated in the nozzle. No details on the nozzle and heater chips are found.

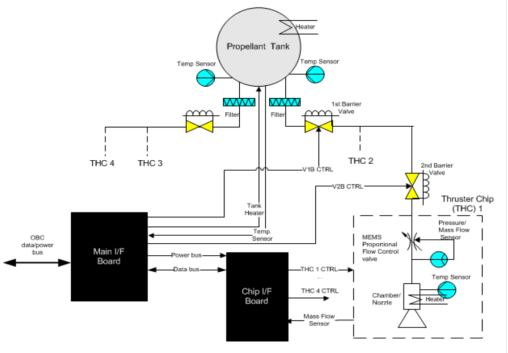

Figure 2.19: 3U CubeSat Propulsion System Configuration [17].

The propulsion system has a total of 2 propellant filters, 4 barrier (ON/OFF) valves, 6 temperature sensors, and 4 pressure/mass flow sensors [17].

3U CubeSat Propulsion Module Interfaces

Figure 2.20: Assembled 3U CubeSat propulsion module [17].

Figure 2.20 shows the assembled 3U CubeSat propulsion module. The system has 4 M3 attachment points, in accordance to the PC/104 specification, that allows for fastening to the bus. Furthermore, both 12 V and 3.3 V electrical interfaces are present, and the CAN/I2C protocols are used as a communication interface with the rest of the spacecraft [17]. No information on thermal interfaces is provided in literature.

2.3.9 Ammonia Micro-Resistojet

The ammonia micro-resistojet (MRJ) is designed by Busek. As the name suggests, ammonia is used as a propellant. Ammonia is chosen due to its low meting point of -78 °C and its impressive thrust/power potential. The latter is due to fact that the propellant doesn't require any cracking energy. Propellant freezing will not be a problem due to the low melting point [18].

The MRJ consists of both a primary thruster and ACS thrusters. The primary thruster delivers a total impulse of 404 Ns, a thrust level of 2-10 mN, and a specific impulse of 150 s. The ACS thrusters deliver a total impulse of 23 Ns, a thrust level of 0.5 mN, and a specific impulse of 80 s. The propulsion system uses 3-15 W of power, has a dry mass of 1.25 kg and occupies a volume < 1U (9 x 9 x 10 cm3) [19].

System Configuration

The system configuration of the MRJ propulsion system with the performance figures is unavailable. However, a paper by Busek [18] describes the design of another ammonia micro resistojet that achieves similar performance figures as described above. This MRJ achieves a thrust level of 5-12 mN, and Isp between 150-210 s whilst using a nominal power of 25 W. The design of this system is presented below due to the similar performance figures.

A co-axial heater, made of tantalum, is inserted in the inner platinum tube of the annulus through which the propellant flows. The outer platinum tube of this annulus is insulated by a 10-layer radiation shield. This heater heats the propellant to approximately 1100 °C through convection. The heated propellant is accelerated in the titanium nozzle that has an expansion ratio of 23:1. The assembled MRJ can be seen in Figure 2.21.

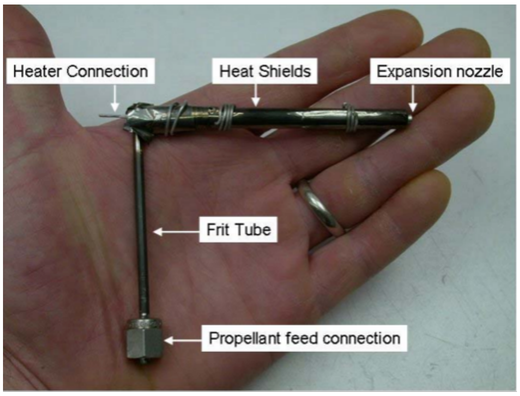

Figure 2.21: Assembled MRJ thruster [18].

The ammonia is stored at its vapor pressure (8.5 bar at ambient temperature) in the propellant tank. Propellant vapor starts flowing towards the MRJ when the shutoff valve is opened. The mass flow rate is measured and controlled by a MKS flow controller, and the propellant passes through a filter before entering the MRJ. Several thermal couples (TCs) monitor the temperature throughout the system. A TC located at the nozzle exit is there to shut the system down when the temperature at the exit exceeds the limit temperature. This can happen when the flow rate decreases, the nozzle is blocked, or due to another upset. A schematic overview of the system can be found in Figure 2.22.

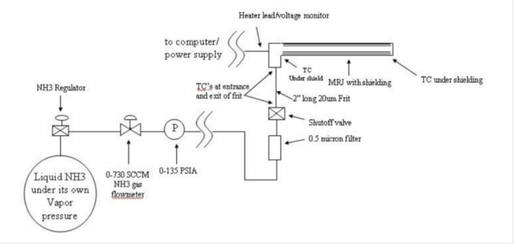

Figure 2.22: MRJ system configuration [18].

MRJ Interfaces

Figure 2.23 shows the enclosed micro-resistojet system. As with many of the other systems discussed in this chapter, there is no detailed information on any of the interfaces found in literature, other than the 5V DC electrical interface.

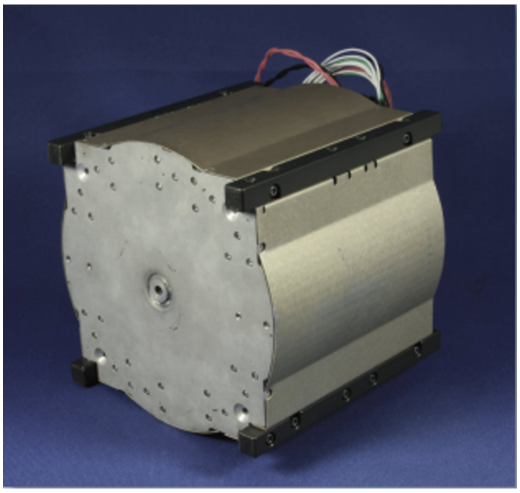

Figure 2.23: Assembled MRJ propulsion module [19].

The mechanical interface with the reset of the bus can be deduced from Figure 2.23, as 4 attachment points are visible at the nozzle side of the propulsion unit. The location of the electrical interface can also be seen in this figure, as cables are found at the back side of the unit.

2.3.10 Delfi-PQ Dual Thruster System

The Delfi-PQ Dual Thruster System is designed by the University of Technology in Delft for the use on their pico-satellite platform named Delfi-PQ. This propulsion system was designed to demonstrate two different micro-resistojet concepts, namely the Vaporizing Liquid Micro-resistojet (VLM), and the Low Pressure Micro-resistojet (LPM). This demonstrator system is part of this literature study, as it encompasses all the components present in a fully realized propulsion system. Both the VLM and the LPM use water as a propellant that is stored in a common propellant tank.

The Dual Thruster System can achieve a maximum thrust of 0.6 mN with a ΔV capability in the range of 0.5 – 1.5 m/s. This thrust level requires a maximum heating power of 2 W. The power budget for this thruster is set to a maximum of 4 W, which result in a necessary heating efficiency of > 50 %. The dry and wet mass of the system are < 74.5 g and < 75 g respectively. The VLM thruster uses approximately 0.3 g of propellant, and the LPM thruster uses the remaining 0.2 g. The propulsion system maximum volume envelope is set to be 42 x 42 x 30 mm^3 [20].

System Configuration

The VLM thruster contains both the heating chamber and the nozzle. The propellant (water) enters the heating chamber in its liquid state at 1-5 bar. The MEMS chip is made of silicon, and the electrical resistance wires are made of molybdenum. The heater section vaporizes the propellant after which it is accelerated in a convergent-divergent nozzle The nozzle has a throat area of 45 x 100 μm. The VLM thruster chip is shown in Figure 2.24.

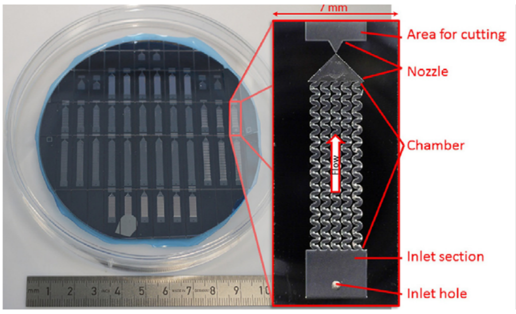

Figure 2.24: MEMS wafer with 36 different VLM devices and close-up view of one thruster [21].

The LPM thruster accelerates the propellant in a different way. Low pressure (1-5 mbar) water vapor enters the thruster planum. The propellant is in its transitional or free molecular regime, which allows for the use of heated expansion slots rather than a more traditional nozzle. The water vapor is heated and accelerated by collisions with these heated slot walls. The MEMS chip, on which the thruster is located, is made of the same materials as the VLM thruster, and shown in Figure 2.25.

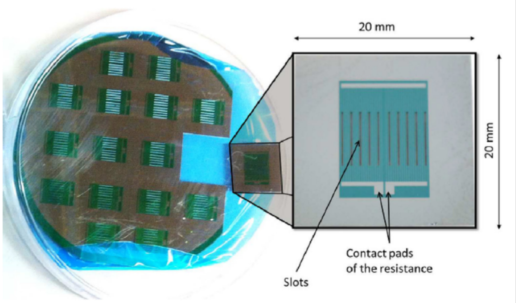

Figure 2.25: MEMS wafer with 16 different LPM thruster chips and close-up view of one chip [22].

A schematic overview of the Dual Thruster System can be seen in Figure 2.26. The propellant is stored in its liquid state in the propellant tank and is pressurized by gaseous nitrogen. Flexible tubing allows the propellant to flow to both the VLM and LPM when the gate valves are opened. The propellant enters the thruster, where it is heated, accelerated, and expelled [20].

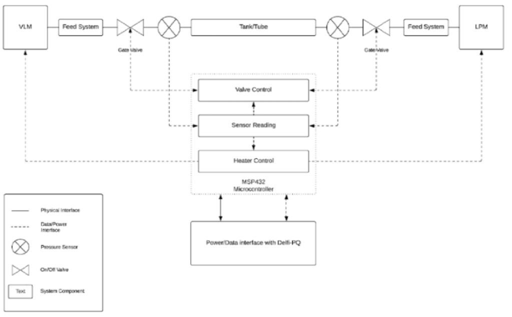

Figure 2.26: Delfi-PQ dual thruster system configuration [20].

Delfi-PQ Dual Thruster System Interfaces

The interfaces of the Delfi-PQ Dual Thruster System result from the interface requirements. It must be noted that the requirements are not describing the actual interface layouts. The first requirement is the mechanical interface requirement PROP-INT-100: “The mechanical interface between the propulsion system and the satellite shall be compliant with the option 7 from the PQ9 standard connection stacking and shall respect the PQ9 standard in PCB selection and sizing”. The second requirement is the thermal interface requirement PROP-INT-200: “The thermal interface between the propulsion system and the satellite shall allow for the propulsion system components to stay in a temperature range between +5 °C and +85 °C during all mission phases.” And finally, the electrical interface requirement PROP-INT-300: “The propulsion system shall be electrically connected to the satellite power subsystem through the standard RS-485 interface and shall respect the mechanical and electrical interface of connector stacking option 7 from the PQ9 standard. [20]”

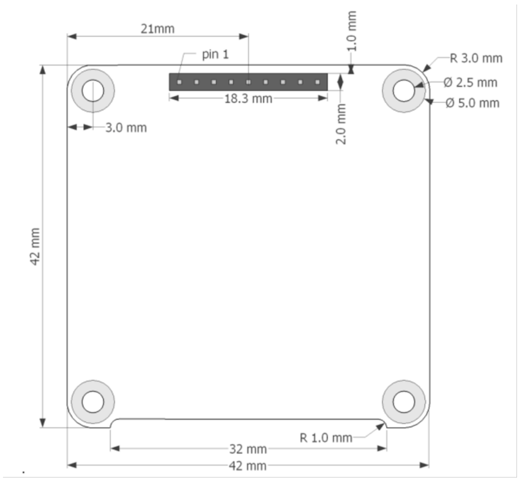

Figure 2.27: PQ9 Printed Circuit Board outline [23].

Figure 2.27 shows the PCB layout that is compliant with the PQ9 guidelines that are mentioned in the requirements. Furthermore, Figure 2.28 shows a CAD drawing of the demonstrator propulsion module, and this PCB layout can clearly be seen in this figure (in green).

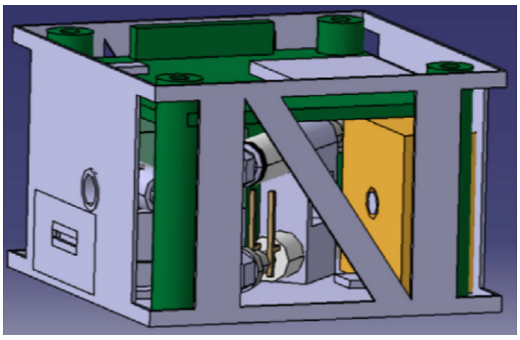

Figure 2.28: CAD drawing of the micro-propulsion demonstrator [20].

2.4 Linear Trends in Micro-Resistojet Propulsion Systems

The aim of this section is to find relationship between several variables of resistojet thrusters. An overview of all thrusters can be found in Table 2.4. It must be noted that these are the thrusters of which sufficient information could be found (as of March 2024) on the internet and, as a result of this, might not include all existing resistojet thrusters. Finding relationships between characteristics of thrusters allow for the generation of requirements and budgets (e.g. mass, power, and volume budgets) of a new, yet to be designed, propulsion system.

2.4.1 Reconstruction of Wet, Dry and Propellant Mass Data

Table 2.4 shows values for dry mass of the ThrustMe RCS, and wet mass of the MRJ in *italics*. These values, including the value of propellant mass for the CHIPS Initial Design, are derived from the specific impulse and total impulse that these systems produce by using the following equations. First, the mass flow rate ($\dot{m}$) is calculated by using Equation 2.1,

$$\dot{m} = \frac{F_t}{I_{sp} \cdot g_0} \tag{2.1}$$

where F_t is the (nominal) thrust level, I_{sp} is the specific impulse, and g_0 is the gravitational acceleration at sea level. Next, Equation 2.2 is used to calculate the burn time (t_b) of the propulsion system,

$$t_b = \frac{I_{tot}}{F_t} \tag{2.2}$$

where I_{tot} is the total impulse. Combining the two equations allows for calculating the required propellant mass (M_p):

$$M_p = t_b \cdot \dot{m} \tag{2.3}$$

Finally, the dry (M_{dry}) and/or wet (M_{wet}) mass can be calculated by using Equation 2.4.

$$M_{wet} = M_{dry} + M_p \tag{2.4}$$

2.4.2 Creating the dataset

A first step taken is to replace all the performance figures that contain ranges by one value. This allows for creating scatter plots, from which trendlines can be drawn. The first ranges are found for the Aurora ARO thruster, where the thrust and power range between 0.6-4 mN and 2-20 W respectively. These ranges are replaced by a lower-bound (0.6 mN, 2 W for the ARO-Nano), a midpoint (2.3 mN, 11W for the ARO-Micro), and an upper-bound (4 mN, 20 W for the ARMO-Small). By doing this, it is assumed that the thrust and power are approximately linearly related. This makes sense intuitively, as more power will, most likely, result in higher thrust levels.

The same can be done for the ThrustMe RCS system, where the thrust (per nozzle) and total power ranges between 1-4 mN, and 10-30 W respectively. However, this system is quite different compared to the ARO thruster, as it contains 6 nozzles that allow for 6 degrees of freedom attitude control. The power levels of this system include the cases where thrusters fire in pairs, thus delivering a larger thrust force. For this reason, the following data-points are created: a thrust force of 1mN using 10 W of power, a thrust force of 4 mN (2 x 2 mN) using 20 W of power, and a thrust force of 8 mN (2 x 4 mN) using 30 W of power.

The MRJ thrust and power range of 2-10 mN, and 3-15 W respectively can be replaced by a lower-bound (2 mN, 3W), midpoint (6 mN, 9 W) and upper-bound (10 mN, 15 W) when assuming again a linear relation between thrust and system power.

Finally, both the Comet-1000 and the RAMPART propulsion system are not considered in finding relationships between different thruster parameters, as their performance figures do not compare with all other thrusters. This can lead to overfitting of trendlines when these two thrusters are included. However, they can be used to verify trendlines that are a result of all other thrusters through extrapolation.

2.4.3 Finding relationships between thruster performance characteristics

The outcome of the abovementioned steps is a group of 20 datapoints: 12 water resistojet datapoints, and 8 resistojet datapoints that use a different propellant (either R134a, Butane, and Ammonia). These two groups are considered separately in this analysis, as water behaves very different compared to other propellants. This will be evident in the graphs, where a clear distinction between the behaviour of water propellant systems (for some relationships) and systems that make use of R134, butane, and ammonia can be made.

It is proven difficult, and time consuming, to create plots at random to try and find relationships between parameters in this way. For this reason, correlation matrices are used. These correlation matrices contain correlation coefficients that indicate if there is a strong positive (value close to 1) or negative (value close to -1) linear relationship between two parameters. A value close to 0 indicates that there is no (or a weak) linear relationship found [24]. One downside of using such a method is the inability to find non-linear relationships between propulsion system parameters.

$$t = \frac{r\sqrt{n-2}}{\sqrt{1-r^2}} \tag{2.5}$$

Furthermore, a so-called t-score, and p-value can be calculated to determine if the correlation coefficient is statistically significant. These steps are performed in Microsoft Excel by using Equation 2.5 to determine to t-score (where n is the sample size, and r is the correlation coefficient), and the T.DIST.2T function to calculate the p-value. In this research, a relationship between two parameters is deemed significant when the correlation coefficient is larger than 0.8 (or smaller than -0.8), combined with a significance level (p-value) < 0.01. The outcome of this analysis is performed on, as already mentioned, both water propulsion systems and the remaining systems (R134a, Butane, and Ammonia) is shown in Table 2.5 and Table 2.6 respectively. Each cell in these tables contains both the correlation coefficient, and the p-value (in between brackets). The cells that are within the pre-specified range are in bold face [24].

One observation that can be made when looking at Table 2.5 and Table 2.6 is that there are more correlations (with a sufficiently low p-value) found for the systems that do not use water as a propellant. However, this does not necessarily mean that these correlations (that are not found for water propulsion systems) are meaningful or correct as this dataset contains only 8 propulsion systems. Larger sample sizes can provide more reliable estimates of correlation coefficients and its statistical significance. For this reason, it is decided to only include the propulsion characteristics correlations that are found for both the water propulsion systems, and the propulsion systems that use a different propellant.

Table 2.4: (Micro-)resistojet propulsion systems.

Name	Producer	Type	Number of Thrusters	Propellant	Thrust [mN]	Power [W]	Isp [s]	Total Impulse [Ns]	Wet Mass [kg]	Dry Mass [kg]	Volume [U]	System Voltage(s)	Data Interface(s)	Source(s)
ARO-Nano	Aurora	VLM	1	Water	0.6 - 4	2 - 20	100	1	0.030	0.029	0.008			[25]
ARO-Micro	Aurora	VLM	1	Water	0.6 - 4	2 - 20	100	20	0.070	0.050	0.064			[25]
ARO-Small	Aurora	VLM	1	Water	0.6 - 4	2 - 20	100	100	0.300	0.200	0.300			[25]
AQUARIUS	Tokyo University, JAXA	VLM	1	Water	7	20	70	250	1.200	0.800	0.889			[26]
Liquid Water Resistojet	TU Delft	VLM		Water	1.52	5.25	94.4	46.4	0.360	0.310				[27]
Free Molecular Resistojet	TU Delft	FMMR		Water	1.14	4.51	88.1	43.2	0.330	0.280				[27]
PBR-10	Pale Blue	VLM	1	Water	1	6.5	55	50	0.600	0.500	0.500	5, 8	UART, RS422	[14], [28]
PBR-20	Pale Blue	VLM	1	Water	1	20	70	200	1.500	1.300	1.000	5, 8	UART, RS422	[14], [29], [30]
Steam TunaCan Thruster	SteamJet	VLM	1	Water	6	19.9	172	219	0.540	0.410	0.402	9 - 14	RS422, TTL UART	[31], [32], [33]
ThrustMe RCS	ThrustMe	VLM	6	Water	1 - 4	10 - 30	100	400	1.000	*0.592*	1.000	12 - 28	I2C, CAN	[34]
Comet-1000	Bradford Space	VLM	1	Water	17	55	180	1155	1.440	0.740	2.600	8 - 34	RS422/485, NSPv4	[33], [35], [36]
CHIPS - Initial Design	CU Aeruspace, Vacco			R134a	30	30	82	564			1.020		RS422	[8]
CHIPS-180	CU Aeruspace, Vacco			R134a	15	20	67	176	1.027	0.750	0.054		RS422	[9]
CHIPS-500	CU Aeruspace, Vacco			R134a	25	25	69	505	1.835	1.065	1.300		RS422	[9]
CHIPS-1000	CU Aeruspace, Vacco			R134a	31	30	70	1030	3.130	1.617	2.500		RS422	[9]
RAMPART	University of Arkansas			R134a	500	90					1.000			[16]
3U CubeSat Propulsion Module	NanoSpace/ GOMESpace		4	Butane	1	2	81	40	0.350	0.300	0.500			[17]
MRJ	Busek			Ammonia	2 - 10	3 - 15	150	404	*1.525*	1.250	0.810	5		[19]

Table 2.5: Correlation coefficients and p-values (in between brackets) of water-based resistojet systems.

water	**Thrust [mN]**	**Power [W]**	**Isp [s]**	**Total Impulse [Ns]**	**Wet Mass [kg]**	**Dry Mass [kg]**	**Propellant Mass [kg]**	**Volume [U]**	**Thrust/ Power [mN/W]**	**Volumetric Impulse [Ns/U]**
Thrust [mN]	1 (0)									
Power [W]	**0.824 (0.001)**	1 (0)								
Isp [s]	0.455 (0.137)	0.335 (0.287)	1 (0)							
Total Impulse [Ns]	0.535 (0.073)	0.692 (0.013)	0.292 (0.357)	1 (0)						
Wet Mass [kg]	0.311 (0.325)	0.603 (0.038)	-0.206 (0.521)	0.745 (0.005)	1 (0)					
Dry Mass [kg]	0.19 (0.554)	0.533 (0.074)	-0.275 (0.388)	0.578 (0.049)	**0.967 (2.95 $\cdot$ 10^{-7})**	1 (0)				
Propellant Mass [kg]	0.505 (0.094)	0.607 (0.036)	0.004 (0.991)	**0.931 (1.13 $\cdot$ 10^{-5})**	**0.816 (0.001)**	0.642 (0.025)	1 (0)			
Volume [U]	0.295 (0.351)	0.574 (0.051)	-0.154 (0.633)	**0.873 (2.08 $\cdot$ 10^{-4})**	**0.947 (3.14 $\cdot$ 10^{-6})**	**0.849 (4.82 $\cdot$ 10^{-4})**	**0.91 (3.99 $\cdot$ 10^{-5})**	1 (0)		
Thrust/ Power [mN/W]	0.515 (0.087)	-0.015 (0.963)	0.348 (0.268)	-0.182 (0.572)	-0.389 (0.211)	-0.454 (0.138)	-0.141 (0.661)	-0.322 (0.307)	1 (0)	
Volumetric Impulse [Ns/U]	0.603 (0.038)	0.592 (0.043)	**0.823 (0.001)**	0.622 (0.031)	0.123 (0.704)	-0.009 (0.978)	0.402 (0.195)	0.26 (0.415)	0.207 (0.518)	1 (0)

Table 2.6: Correlation coefficients and p-values (in brackets) of the remaining resistojet systems.

other	**Thrust [mN]**	**Power [W]**	**Isp [s]**	**Total Impulse [Ns]**	**Wet Mass [kg]**	**Dry Mass [kg]**	**Propellant Mass [kg]**	**Volume [U]**	**Thrust/ Power [mN/W]**	**Volumetric Impulse [Ns/U]**
Thrust [mN]	1 (0)									
Power [W]	**0.984 (1.05 $\cdot$ 10^{-5})**	1 (0)								
Isp [s]	-0.628 (0.096)	-0.596 (0.119)	1 (0)							
Total Impulse [Ns]	0.736 (0.037)	0.683 (0.062)	-0.135 (0.749)	1 (0)						
Wet Mass [kg]	0.783 (0.021)	0.73 (0.04)	-0.095 (0.822)	**0.993 (7.43 $\cdot$ 10^{-7})**	1 (0)					
Dry Mass [kg]	0.496 (0.211)	0.482 (0.226)	0.334 (0.418)	**0.871 (0.005)**	**0.896 (0.003)**	1 (0)				
Propellant Mass [kg]	**0.852 (0.007)**	0.791 (0.019)	-0.463 (0.247)	**0.938 (0.001)**	**0.926 (0.001)**	0.663 (0.073)	1 (0)			
Volume [U]	0.701 (0.053)	0.631 (0.094)	-0.258 (0.538)	**0.954 (2.30 $\cdot$ 10^{-4})**	**0.956 (2.04 $\cdot$ 10^{-4})**	0.823 (0.012)	**0.976 (3.42 $\cdot$ 10^{-5})**	1 (0)		
Thrust/ Power [mN/W]	**0.965 (1.04 $\cdot$ 10^{-4})**	**0.942 (4.71 $\cdot$ 10^{-4})**	-0.404 (0.321)	0.821 (0.013)	**0.872 (0.005)**	0.766 (0.027)	**0.852 (0.007)**	0.73 (0.04)	1 (0)	

Continued on the next page

Volumetric Impulse [Ns/U]	0.525 (0.181)	0.511 (0.196)	0.333 (0.42)	0.596 (0.119)	0.674 (0.067)	**0.86 (0.006)**	0.439 (0.277)	0.338 (0.413)	0.665 (0.072)	1 (0)

2.4.4 Relationships found between thruster performance characteristics

These correlated performance characteristics, that are found for both types of propulsion systems (water propellant, and other propellants), are: *thrust and power*, *total impulse and propellant mass*, *total impulse and system volume*, *wet and dry mass*, *wet and propellant mass*, *wet mass and system volume*, and *propellant mass and system volume*. These relationships between the system performance characteristics are shown in scatter plots below. Again, the systems are split up into water propellant systems, and systems that make use of a different propellant. Furthermore, trendlines are included for each of the found relationship, including the R^2-value that indicates the fit of the linear curve. A single trendline for both types of systems is provided when both follow the same linear trend (i.e. when the two trendlines overlap).

Thrust vs Power

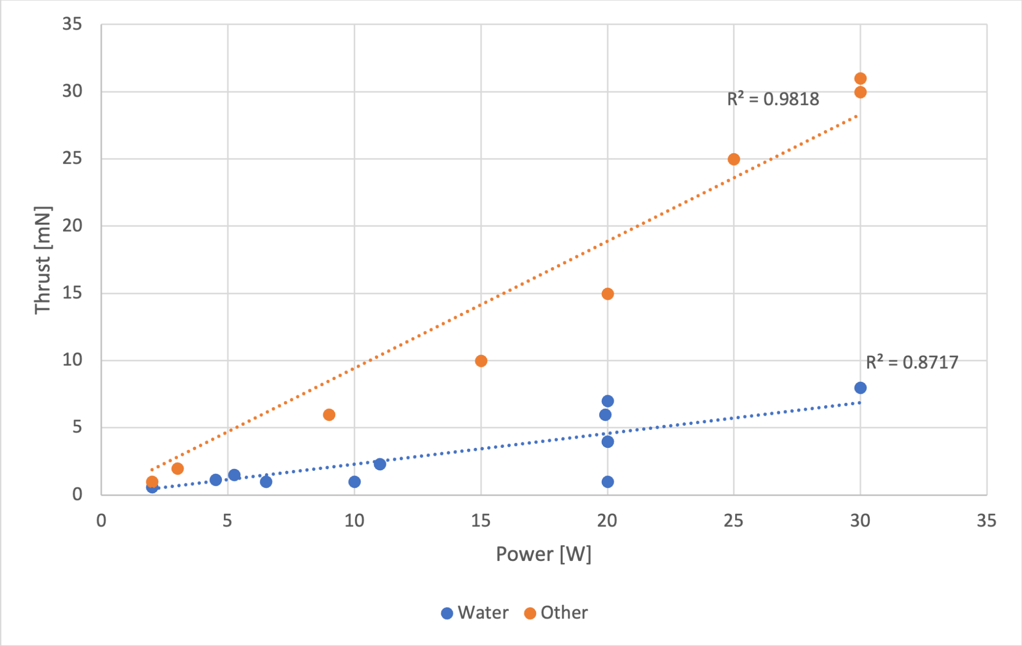

Figure 2.29: Thrust vs power.

Figure 2.29 shows the relationship found between thrust and power. Several observations can be made when looking at the plot. First, it is evident that the water propulsion systems generate a lower thrust for a given system power. This is most likely a result of the higher heat of vaporization of water, thus more power is required to vaporize and heat the propellant. A second observation is that there a several water propellant systems that generate different amounts of thrust at a power level of 20 W. Most notably, there is the system that generates a thrust of only 1 mN whilst using 20 W of power. This is PB-20, the larger variant of the PB-10 system. The PB-10 system provides the same amount of thrust whilst only using 6.5 W of power, and both systems are based on the AQUARIUS thruster. A possible explanation for this increase in power usage for the same thrust level in the PB-20 is the absence of using waste heat from other parts of the spacecraft to vaporize the propellant, and the increase in the systems total impulse of 300 %. The latter requires more propellant that needs heating, and potentially more redundancy in the system, as longer mission durations can be achieved. The statement regarding the use of waste heat from other parts of the system is speculative, as no information on this can be found anywhere, and stems from the fact that the AQUARIUS makes use of waste heat from the on-board communication systems to vaporize the propellant.

The presence of the PB-20 system results in a linear curve fit of water propulsion systems that is less accurate than that of the other propulsion systems, as evident from the R^2-values for both. However, there is still a clear linear relationship between thrust and power for both and can be used to determine the required system power (i.e. the maximum power the system can use) for a given thrust level.

Total Impulse vs Propellant Mass

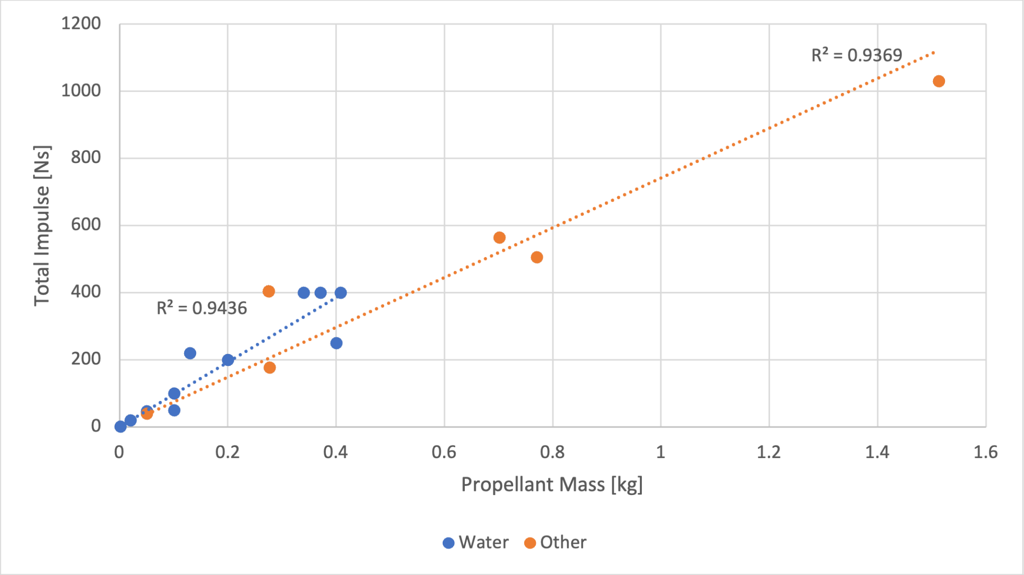

Figure 2.30: Total impulse vs propellant mass.

Figure 2.30 shows the relationships found between the total impulse and the propellant mass. The fact that this relationship is linear is not surprising since the total impulse of the system is a result of the propellant being expelled, and that more propellant allows for a longer thrust duration, hence a larger total impulse. The water-based systems and the other propellant systems follow a different linear trend. This difference is a result of multiple factors, such as differences in vaporization characteristics and molecular mass of the propellants. Furthermore, it can be observed that the current water-based resistojet systems are limited in the total impulse they can deliver when comparing them to the other available systems. One must therefore be careful when extrapolating the linear curve of these systems beyond the data-range, as there is no additional data available to verify its accuracy. However, the accuracy of both curve fits (R^2-values of 0.94 for both system types) allows for the use of this linear relationship to determine the required propellant mass for a given total impulse or vice versa within the data range of both systems.

Total Impulse vs System Volume

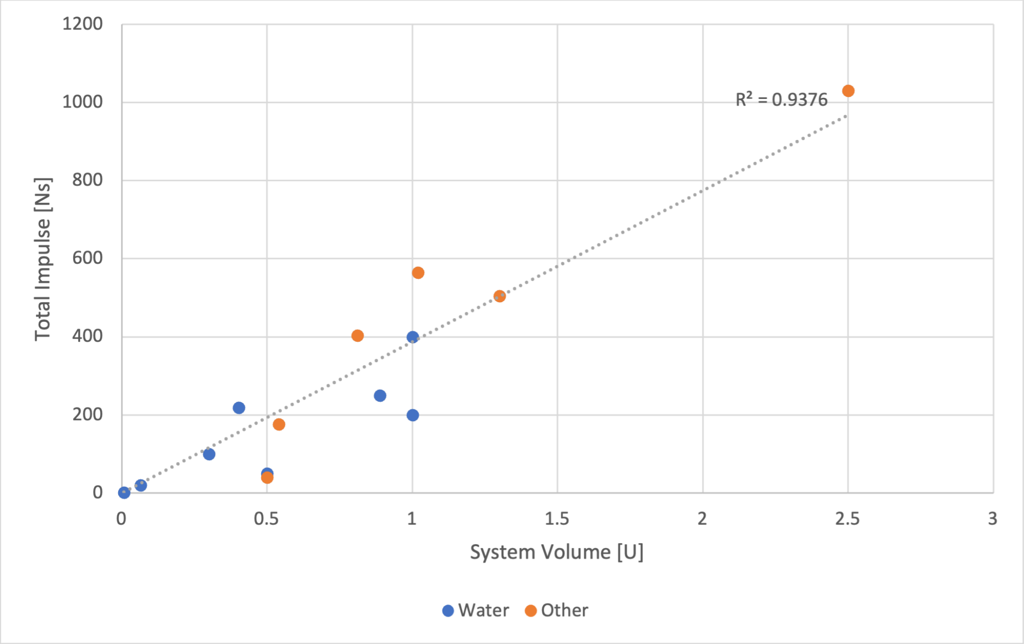

Figure 2.31: Total impulse vs system volume.

The relationship between the total impulse and the system volume is useful to obtain a first estimate of the systems volume for a given total impulse. Figure 2.31 shows that the linear trend of these two parameters is the same for both the water-based systems, as for the systems that use other propellants. Again, one must be cautious when extrapolating the data for water-based systems above a total impulse of 400 Ns, and a system volume of 1 U, as there is no data beyond this point to verify its correctness. The linear trend can be explained by the fact that more propellant is required to achieve a larger total impulse. This increase in propellant requires a larger tank, and results in a larger system value volume. The trendline used in this plot is forced through the origin and, by doing so, results in a R^2-value of approximately 0.94: a good fit.

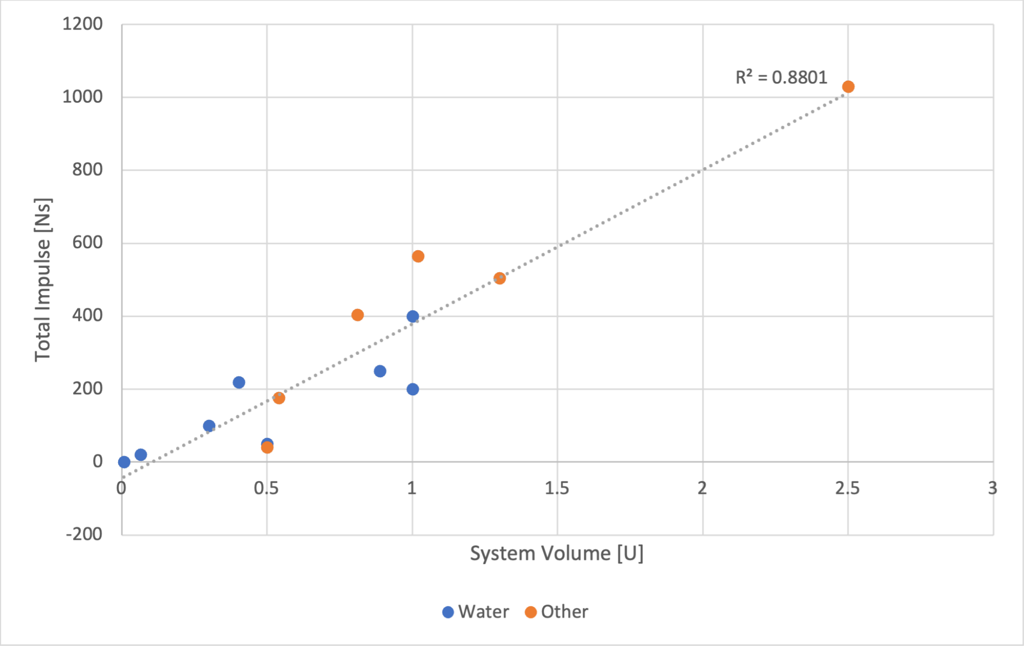

Figure 2.32: Total impulse vs system volume without forcing through origin.

However, an interesting observation can be made when not forcing the trendline through the origin. The R^2-value drops to 0.88, and the linear curve crosses the system volume axis at approximately 0.125, as shown in Figure 2.32. This shows that, for a total impulse of 0, a system volume of approximately 0.125 U is required. This volume could be interpreted as the volume of the system without the propellant tank.

Wet Mass vs System Volume and Propellant Mass vs System Volume

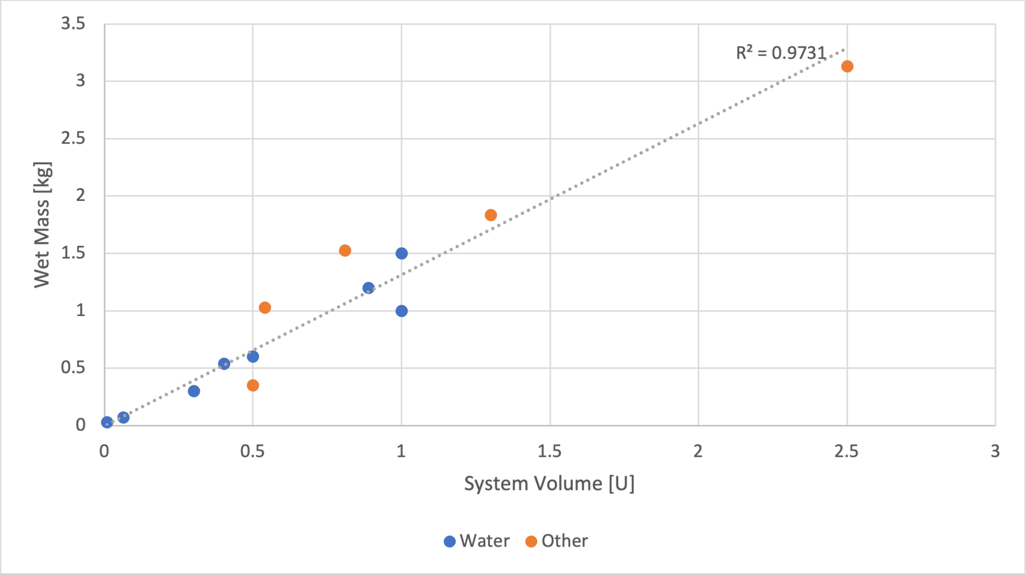

Figure 2.33: Wet mass vs system volume.

Figure 2.33 shows the relationship between wet mass and system volume. An explanation for the linear relation between these parameters is again linked to the propellant tank size that increases with an increase in propellant mass (thus an increase in wet mass). The fit of the linear curve has a R^2-value of 0.97, and the curve is forced through the origin. The latter is done, as a system with no mass can have no volume. However, the influence of the propellant mass on the system volume can not be deduced from this plot. This relationship can be found when looking at Figure 2.34.

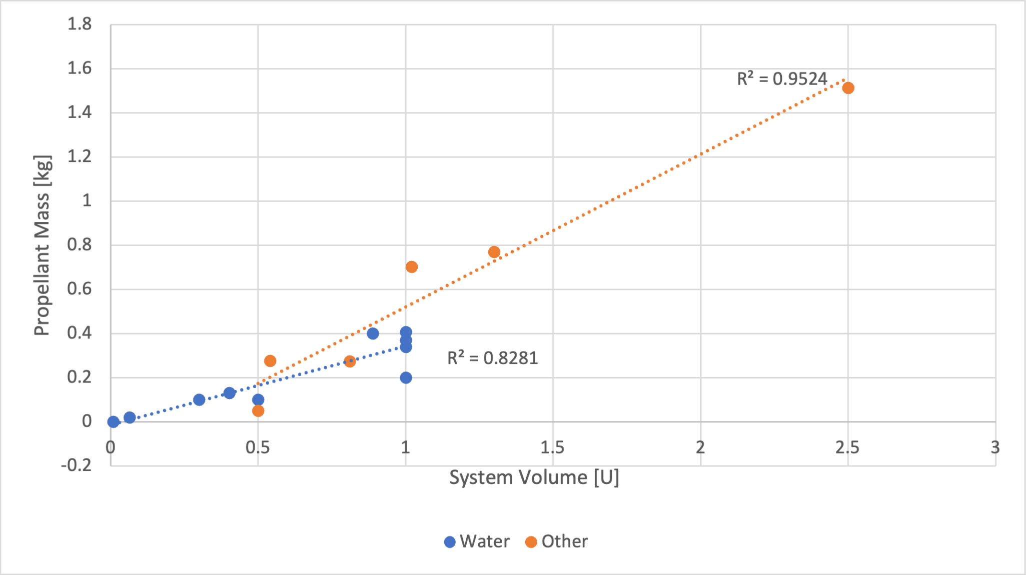

Figure 2.34: Propellant mass vs system volume.

This figure shows that the linear relationship between propellant mass and system volume is different for water-based propulsion systems and propulsion systems that make use of a different propellant. The shallower line for water-based systems is due to the lower density of water with respect to the other propellants, hence more volume is required to store the same amount of propellant. Both curves are not forced through the origin, as the system can still have volume without any propellants; think of the thruster, piping, and electronics. This is indicated in the plot where the curves cross the system volume axis. The system volume axis is crossed at 0.034 U for the water-based systems, and at 0.247 U for the propulsion systems that make use of a different propellant. It is curious that there is an order of magnitude difference between the two types of systems when looking at the intersection of the system volume axis. This is possibly a result of the inclusion of more novel water-based propulsion systems compared to the other systems, where state-of-the-art MEMS based production methods are being used. These state-of-the-art techniques lead to smaller, lighter systems in general. As a final note, on must be cautious when extrapolating the water-based system curve beyond a system volume of 1 U, as there is no data to verify these estimates.

Wet Mass vs Dry Mass and Wet Mass vs Propellant Mass

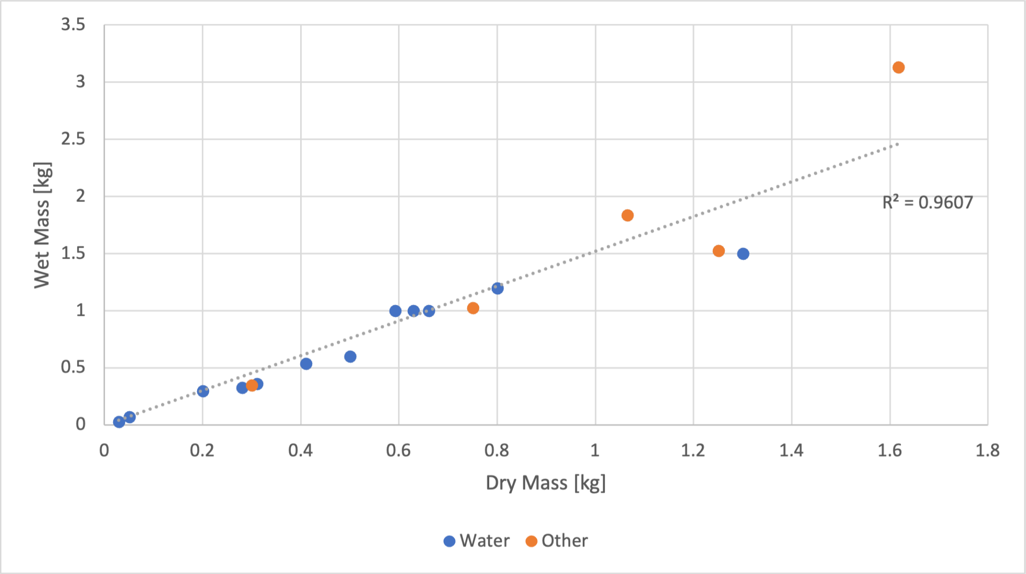

Figure 2.35: Wet mass vs dry mass.

Figure 2.35 shows the linear relation between the wet and dry mass that holds for both water-based propulsion systems, and the systems that make use of another propellant. However, this one linear relationship that holds for both types of systems can be misleading, as the wet and dry mass values lie close to each other. This is due to the fact that the propellant mass fraction is low for most systems, and will automatically result in this linear relationship. More interesting observations can be made when looking at the relationship between wet mass and propellant, as shown in Figure 2.36.

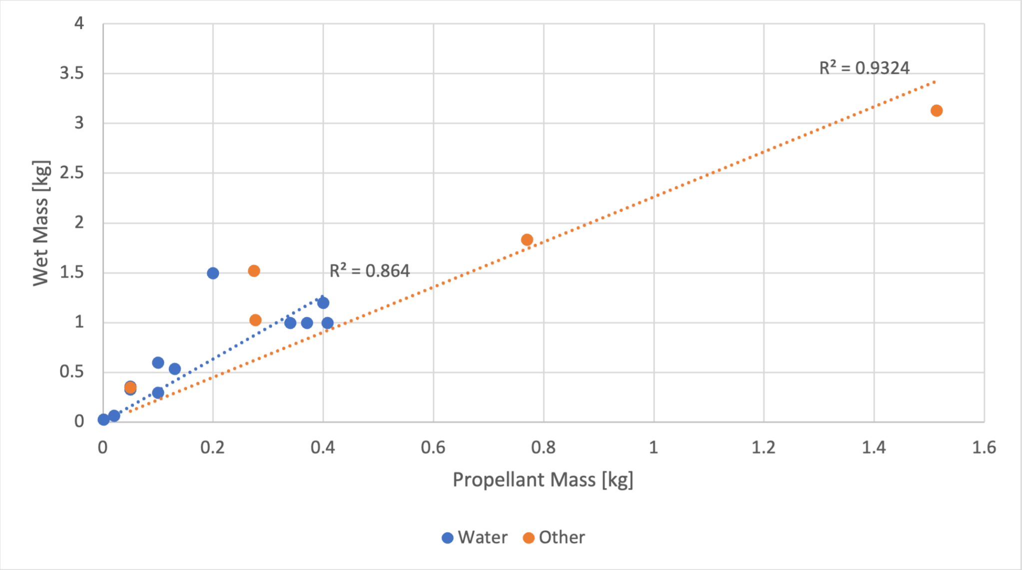

Figure 2.36: Wet mass vs propellant mass.

It can be seen that the water-based systems follow a different trend than the other systems. This was not visible in the previous wet vs dry mass plot. One could argue that it would be more interesting to plot dry mass as function of propellant mass. However, this relationship can also be deduced from Figure 2.36 by subtracting the propellant mass (value on the x-axis) from the wet mass, and is therefore omitted from this study. As with all other plots discussed in this section, one must be cautious when using the linear relation of water-based systems when extrapolating beyond the data-range, as there is no data available to verify its accuracy.

2.4.5 Discussion of Results

Table 2.7 gives an overview of all found linear relationships between the resistojet propulsion system characteristics. The last column, named applicability, provides the value of the most extreme data entry (the one with the highest value for both characteristics that are being investigated). It must be noted that the relationship found can be used to extrapolate to values outside of the sample entries, but one must realise that the linear relationship might not be accurate outside these bounds.

The equations found can be used to estimate the budgets (power, volume, mass) for a given, yet to be specified, mission that makes use of a resistojet propulsion system.

Table 2.7: Fitted relationships between resistojet propulsion system parameters.

	Relationship	**Sample Size**	**Fit (R^2-value)**	**Equation**	**Applicability**
1	Thrust (F_t) vs System Power (P) of water-based resistojet systems.	12	0.87	$F_t = 0.2291 \cdot P$	For F < 8 mN, P < 30 W.
2	Thrust vs System Power of non-water-based resistojet systems.	8	0.98	$F_t = 0.9437 \cdot P$	For F < 31 mN, P < 30 W.
3	Total Impulse (I_{tot}) vs Propellant Mass (M_p) of water-based resistojet systems.	10	0.94	$I_{tot} = 961.0 \cdot M_p$	For I_{tot} < 400 Ns, M_p < 0.4 kg.
4	Total Impulse vs Propellant Mass of non-water-based resistojet systems.	6	0.94	$I_{tot} = 741.0 \cdot M_p$	For I_{tot} < 1030 Ns, M_p < 1.5 kg.
5	Total Impulse vs System Volume (V) when forced through origin.	14	0.94	$I_{tot} = 387.1 \cdot V$	Water: I_{tot} < 400 Ns, V < 1 U. Other: I_{tot} < 1030 Ns, V < 2.5 U.
6	Total Impulse vs System Volume without forcing through origin.	14	0.88	$I_{tot} = 422.7 \cdot V - 44.3$	Water: I_{tot} < 400 Ns, V < 1 U. Other: I_{tot} < 1030 Ns, V < 2.5 U.
7	Wet mass (M_{wet}) vs System Volume.	13	0.97	$M_{wet} = 1.315 \cdot V$	Water: M_{wet} < 1.5 kg, V < 1 U. Other: M_{wet} < 3.1 kg, V < 2.5 U
8	Propellant Mass vs System Volume of water-based resistojet systems.	10	0.83	$M_p = 0.3553 \cdot V - 0.012$	For M_p < 0.4 kg, V < 1 U.
9	Propellant Mass vs System Volume of non-water-based resistojet systems.	6	0.95	$M_p = 0.6910 \cdot V - 0.171$	For M_p < 1.5 kg, V < 2.5 U.
10	Wet Mass vs Dry Mass (M_{dry}).	17	0.96	$M_{wet} = 1.521 \cdot M_{dry}$	Water: M_{wet} < 1.5 kg, M_{dry} < 1.3 kg. Other: M_{wet} < 3.1 kg, M_{dry} < 1.6 kg.
11	Wet Mass vs Propellant Mass of water-based resistojet systems.	12	0.86	$M_{wet} = 3.166 \cdot M_p$	For M_{wet} < 1.5 kg, M_p < 0.4 kg.
12	Wet Mass vs Propellant Mass of non-water-based resistojet systems.	5	0.93	$M_{wet} = 2.262 \cdot M_p$	For M_{wet} < 3.1 kg, M_p < 1.5 kg.

2.5 Conclusion

This chapter aims to answer the three research questions that have been stated in Section 2.1, and as a result, achieve the objective of the literature study: "to investigate the current state-of-the-art micro-resistojet propulsion systems composition of small satellites." The scarcity of detailed information regarding current micro-resistojet propulsion systems lead to some difficulties with providing a complete answer to all research questions, as will be discussed within some of the questions. Many, if not all, companies choose to only publish (often incomplete) performance figures of their state-of-the-art systems, and not provide any detailed information on the systems composition and integration with the rest of the spacecraft.

The systems that did specify their composition, and some of the interfaces with the rest of the spacecraft, are older systems (such as the MRJ by Busek), or systems that are used for proof of concept by both universities and/or companies. The latter is the case for the CHIPS and Pale Blue propulsion systems that provides details on system configuration for the initial concept, but not for their newest systems that are a result of iterating on these initial designs. However, including these designs in this investigation is still useful, as iterations on the designs are often small, and their general composition remains similar.

2.5.1 What is the current state-of-the-art regarding micro-resistojet propulsion systems in small satellites, and why are these current configurations chosen?

There are three types of micro-resistojet propulsion systems used, namely the warm gas thrusters, the vaporizing liquid thrusters (VLM), and the low pressure micro-resistojets, also known as the free molecular micro-resistojets (FMMR). These systems make use of a variety of propellants, of which R134a, R236-fa, and water are the most popular. The popularity of these propellants stems from their non-toxic, and non-flammable nature. Furthermore, the self-pressurization capability of R134a and R236-fa allows for a simplified feed system, as no separate pressurization system is required. Water permits low pressures within the feed system when compared to high-pressure gas systems. This lower pressure simplifies the feedlines, as soft tubes can be used. Two other propellant that are included in this literature study are ammonia and butane.

The performance of the different propulsion systems is linked to the propellant that is used. Water-based systems achieve thrust levels between 0.6 and 17 mN whilst using 2-55 W of power. The specific impulse ranges between 55 and 180 s. R134a-based systems achieve thrust levels between 15 and 500 mN, whilst using 20-90 W of power. The specific impulse ranges between 70 and 82 s. Finally, the butane and ammonia system generate a thrust level between 1 and 10 mN, whilst using 2-15 W of power. The specific impulse ranges between 81 and 150 s. The performance details, and their link with the propellant, are further elaborated on in Subsection 2.5.2.

The micro-resistojet propulsion systems are all similar when talking about the configuration, as all systems contain a propellant tank, piping, valves, (resistive) heating elements, and a nozzle (either expansion slots or a convergent/divergent nozzle). The propellant is stored in a propellant tank. This tank can be heated when a self-pressurizing propellant is used and allows for maintaining a constant temperature level in the tank when part of the propellant vaporizes. Furthermore, porous membranes are sometimes used for self-pressurizing systems in the propellant tank, and act as both a propellant phase separator that ensures that only vaporized propellant enters the feed system, and as a coarse propellant filter. Feed dryers also ensure that no liquids enter the feed system. Bladder tanks can be used for pressure fed systems. The bladder functions as a barrier between the pressurant and propellant, and only allows for propellant to enter the feed system.

Propellant starts flowing towards the nozzle when the thruster valve(s) open. Some systems also have a shutoff-valve that permanently opens as soon as the satellite is in orbit. This is a safety feature that ensures the system cannot fire before and during launch. Pressure and/or temperature sensors in the feed system ensure that the conditions for correct thrusting are met by measuring the pressure and temperature of the propellant in the piping. These sensors work in unison with the valves and heating systems, and ensure a proper mass flow rate, and state of the propellant. Some novel VLM's separate the thrust chamber and the heating chamber by using a separate vaporization chamber. This allows for the vaporization of propellant before a manoeuvre, rather than vaporizing propellant during a manoeuvre. This feature allows for the use of waste heat from the rest of the spacecraft, and negates most of the fluid dynamic complications that result from two-phase flow.

The (vaporized) propellant then flows to the thruster, where the propellant is heated, accelerated, and expelled through a convergent/divergent nozzle. This step is different for the low-pressure micro-resistojets (also knows as FMMR). For these systems, propellant enter the thruster in its transitional or free molecular regime. This allows for the use of heated expansion slots, rather than a more traditional convergent/divergent nozzle. Propellant is heated and accelerated through collisions with these heated slot walls. The use of heated expansion slots negates the challenges that come with using convergent/divergent micro-nozzles, such as flow losses for Reynolds Numbers below 1000, and flow instabilities due to the two-phase flow in the heating chamber.

2.5.2 What design parameters have the most significant impact on the propulsion system performance, and how can they be adjusted to balance efficiency, mass, and complexity?

This answers to this research question is mainly based on Section 2.4, where performance characteristics of propulsion systems are plotted against each other with the goal of finding linear relationships between these characteristics.

The first, and most obvious, design parameter is the choice of propellant. Thrust levels, system power, and total impulse are dependent on what type of propellant is used. This is reflected in the different linear trends are that found for water-based system, and systems that make use of another propellant when looking at, for example the thrust vs power, and the total impulse vs propellant mass plot. Figure 2.29 shows the relationships found between thrust and power. It can be seen that the achievable thrust levels of water-based systems is significantly lower than that of the other systems, and that more power is required to achieve similar thrust levels. The latter is due to the high latent heat of vaporization of water, as explained in subsubsection 2.4.4. Figure 2.30 shows the relationships found between the total impulse and propellant mass. It can be observed that the water-based systems, despite the previously mentioned downsides, achieve a higher total impulse per unit of propellant mass. However, this total impulse is limited to 400 Ns. Systems that make use of R134a, butane, and ammonia, achieve total impulses up to 1030 Ns: significant higher when compared to water-based systems. These systems are therefore more useful for longer missions and/or missions that require higher thrust levels.

Another design parameter that significantly impacts the propulsion system performance is the available system volume. The system volume limits the total achievable impulse, and the maximum allowable wet and dry mass, as shown in Figure 2.31, Figure 2.32, and Figure 2.33. These linear relationships are valid for both the water-based systems, and the systems that makes use of a different propellant. However, these linear relationships are different for water-based systems and the other systems when looking at the propellant mass as function of system volume, as shown in Figure 2.34. The shallower slope of the water-based systems is a result of the lower density of water compared to (most of) the other propellants.

There are more relationships found between thruster parameters, such as the relationship between wet and dry mass, and between wet and propellant mass. Furthermore, the dry mass can be deduced from the wet mass and propellant mass, the wet mass can be deduced from the dry mass and propellant mass, and the propellant mass can be deduced from the wet mass and dry mass. This gets complicated, as each of these calculations results in a different value for all masses, as there are many different methods to get to the two starting values, from which the third unknown is calculated. This is visualised in Figure 2.37, that visualizes how the total impulse, volume, propellant mass, wet mass, and dry mass are related through the linear relationships found in Subsection 2.4.5.

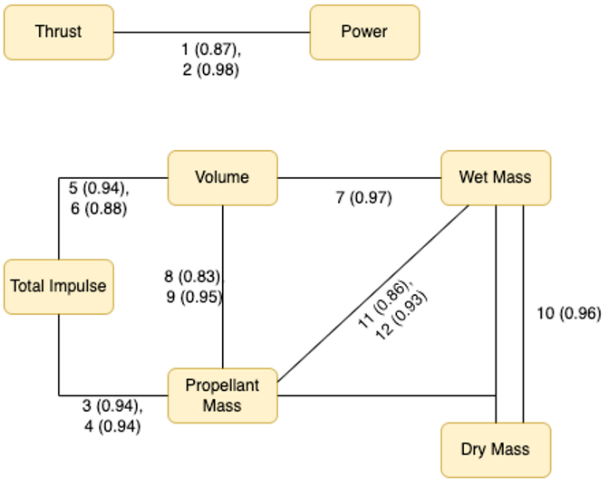

Figure 2.37: Propulsion system parameters linked through linear relationships.

The equation number and the R^2-value (the value in between brackets) are indicated between the different system parameters. The above-mentioned problem of getting to a value by following different path becomes clearer when looking at this figure. For example, there are 8 (!) different path that one can follow to estimate the dry mass of the system when starting with a value for the total impulse. To overcome this problem, one must not only look at the different paths that can be followed, but also include the physical link between the parameters. To illustrate this: it makes more sense to, when starting at the total impulse, estimate the propellant mass by applying equation 3 or 4, rather than first estimating the volume by using equation 5 or 6, and then use equation 8 or 9 to estimate the propellant mass. Propellant mass and total impulse have a direct relationship that can be explained, as was done in subsubsection 2.4.4. Another way of looking at the problem is to include the R^2-value when choosing the path. Most often, the path that results in the highest combined R^2-value (through multiplication) provides the most accurate estimate of the specific parameter.

Part of the research question touches upon adjusting the design parameters to balance efficiency, mass, and complexity. The propulsive efficiency (ratio of thrust over power) is a so-called figure of merit, and is represented as the slope in

Figure 11.6b. There were no other linear relationships found from which efficiencies, such as volumetric efficiency, could be deduced. Furthermore, relationships between total impulse and mass are explained above, as well as the relationships between the wet, dry, and propellant mass. The complexity of the system is not discussed, as it is difficult to graph. One could make the case that smaller systems are more complex, as they require a great deal of miniaturization. However, larger systems often require more parts, such as valves, sensors, and filters that ultimately result in a complex system. The balancing of efficiency, mass, and complexity is proven difficult, and was not performed. Not only because of the previously mentioned difficulties, but also because different missions require a unique design that results from one specific balance. The equations from Subsection 2.4.5, combined with Figure 2.37 can be used to perform this balancing of efficiency and mass.

2.5.3 What are the existing configurations and rationale behind the mechanical, electrical, and thermal interfaces between micro-resistojet propulsion systems and the rest of the spacecraft, and what factors influence the selection of these specific interface configurations in current state-of-the-art designs?

The answer to this research question is based on both Section 2.3 and Table 2.4, where the mechanical, electrical, and thermal interfaces are outlined. The mechanical interface between the propulsion module and the spacecraft bus must survive all load cases throughout the mission duration. The most demanding load case is imposed on the system during launch. The assembled propulsion system is often enclosed in a smooth box that allows for easy integration with the rest of the spacecraft. The outer non-length dimensions of this box mostly align with the standardized dimensions of the CubeSat or PocketQube. The system is fastened using mounting holes that are commonly located in accordance with the CS14 and PQ9 standard. The number of mounting holes varies per design, and ranges between 4 and 12 for the systems that have been investigated in this literature study. The range of attachment points is most likely linked to mass of the system, the location of the holes, and the launcher that is used. However, this link between the load cases, and the location and number of mounting points is not found in literature.

The electrical interfaces consists of both the power and communication interface. Table 2.4 provides an overview of some of these interfaces. The propulsion system voltages range between 5 and 34 V. Some of the systems also allow for a custom supply voltage. Several data interface protocols are used, namely UART, TTL UART, RS422, RS485, I2C, CAN, and NSPv4. The most popular protocol used, based on the systems that are investigated in this literature study, is the RS422.

The literature found on the resistojet systems that are discussed in this study did not provide any information on thermal interfaces between the propulsion system and the satellite bus. The only thermal interface that is touched upon is the use of waste heat of the communication subsystem to vaporize propellant in a separate vaporization chamber. This is most likely achieved through use of thermal straps. However, this is not verified in literature.

Research Plan 3

This chapter contains the need statement, the research objective and intermediate goals, and the research questions with their respective sub-questions. The chapter is concluded with a draft timeline of this thesis.

3.1 Need Statement

Advancements in technology miniaturization allows for the use of smaller form factor satellites for space missions that could previously only be performed by larger ones. The range of possible missions for these smaller spacecrafts can be extended through the use of a micro-propulsion system. The use of such a system would allow these smaller form factor satellites to achieve and maintain lower orbits, change the orbit, extend the mission duration, or to perform an End-Of-Life manoeuvre to reduce space debris by ensuring a fast deorbit.

The TU Delft is one of the institutions that researches these micro-propulsion systems. The existing efforts include the development of a vaporizing liquid micro-resistojet (VLM) thruster combined with a demonstrator system design intended for application in PICO satellites [20]. However, there's currently no comprehensive design for the entire propulsion system, including interfaces, suitable for integration into a small spacecraft format, based on this VLM thruster. In essence, a design capable of executing an operational mission, rather than solely a demonstrative one, is absent.

3.2 Research Objective

The absence of a TU Delft-designed VLM propulsion system is the basis for the following research objective:

"Designing a modular micro-resistojet propulsion system that is capable of delivering three distinct total impulse levels, based on a pre-existing VLM thruster developed by the TU Delft, with a focus on integration into a CubeSat configuration."

The intermediate goals of this thesis are:

- Compile a list of requirements necessary for designing the propulsion system.
- Perform a trade-off between different propellant options to determine the most suitable choice for optimal performance of the system.
- Design the individual components of the propulsion system with a focus on efficiency and compatibility.
- Generate a CAD model that illustrates the layout and configuration of the system.
- Perform structural analysis the ensure the integrity and durability of the propulsion system under various operating conditions.
- Conduct a thermal analysis to assess heat dissipation and temperature regulation within the propulsion system components.

3.3 Research Questions

The following research questions and sub-questions are directed towards achieving the research objective and its associated intermediate goals:

1. ***What are suitable requirements for a VLM propulsion system?***
    - What missions can be flown with a VLM propulsion system, and how do these missions dictate the requirements?
    - What are the constraints acting on the propulsion system?

2. ***What is the best propellant to meet the propulsion system requirements?***
    - How does the requirement of total impulse influence the choice of propellant?
    - How does the choice of propellant influence the required input power and thrust level?
    - How does the choice of propellant influence the propellant mass of the system?
    - How does the choice of propellant influence the required system volume?
    - How does the choice of propellant influence the material selection of the feed system?
    - How does the choice of propellant influence the required temperature levels within the propulsion system?
3. ***What propulsion system architecture would most effectively meet the system requirements?***
    - What components must be present in the propulsion system?
    - How does the use of a modular system influence the design of the propulsion system?
    - What trade-offs are performed for each of the propulsion system components?
    - How does each component of the propulsion system contribute to meeting the overall system requirements?
    - How does the selected propulsion system architecture integrate with the rest of the spacecraft?
    - How does the propulsion system architecture comply with relevant regulatory and safety standards?

3.4 Thesis Timeline

A preliminary timeline of the thesis can be found in Figure 3.1, and is based on the intermediate goals that have been presented in Section 3.2.

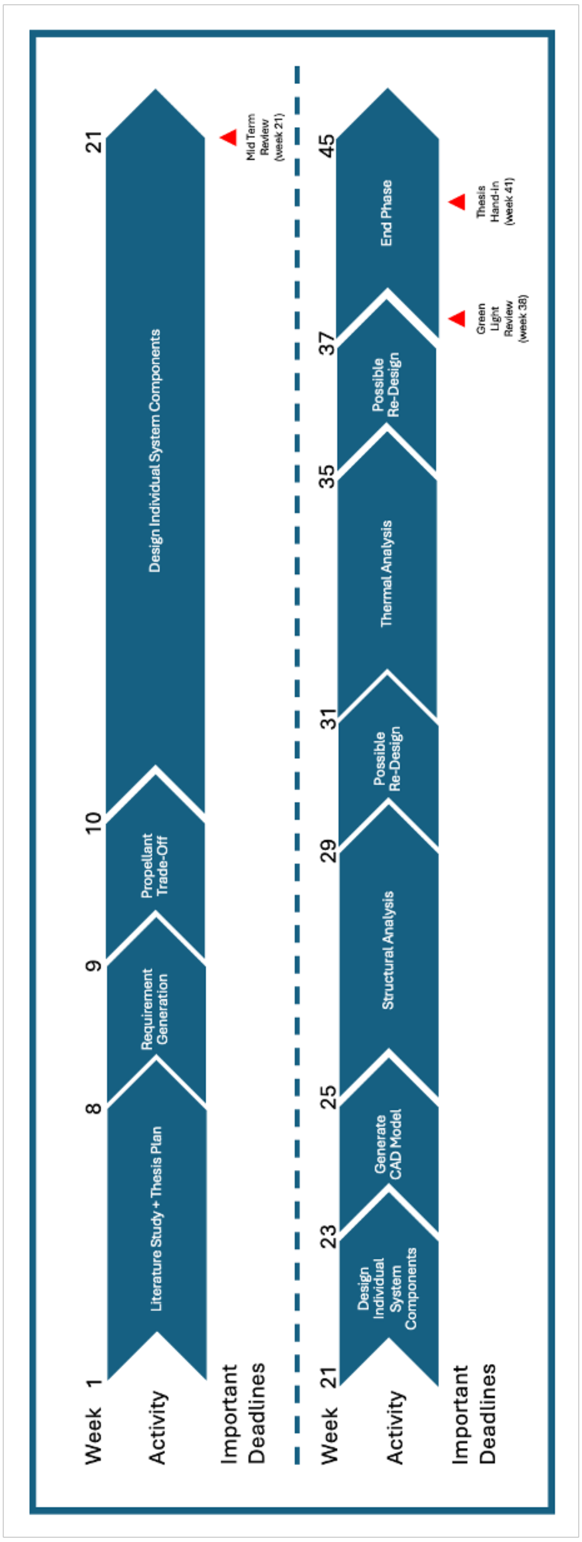

Figure 3.1: Draft timeline of this thesis.

Thruster Definition and System Requirements

4

The goal of this thesis is to design a micro-resistojet propulsion system around an existing VLM thruster developed by TU Delft. This chapter outlines the thruster specifications in Section 4.1. This is followed by the propulsion system requirements, including their rationales, in Section 4.2.

4.1 Thruster Specifications

The latest VLM thruster design information, from 2019, describes a technology demonstrator intended for one of the first Delfi-PQ satellites. This design is used in this thesis to calculate system performance metrics, including thrust, specific impulse, mass flow rate, and input power. The VLM thruster is built on a silicon MEMS chip where one side of the thruster is covered by a glass layer to allow for optical access to the flow. The heating chamber makes consists of serpentine channels, also known as diamond pillars, where molybdenum electrical resistance wires are used to heat the propellant. The vaporized propellant enters the convergent-divergent nozzle, with a throat area of 45 x 100 µm, whereafter the propellant is expelled. Run tests lasting up to 3000 seconds demonstrated the thruster's controllability and stability in terms of mass flow, chamber pressure, and input power [20]. The use of a Pulse Width Modulation approach for the thrust valve opening allowed for controllable pressure in the heating chamber [37]. A technical drawing of the housing for the MEMS thruster chip is shown in Figure 4.1, from which the outer dimensions and the location of the attachment points can be seen.

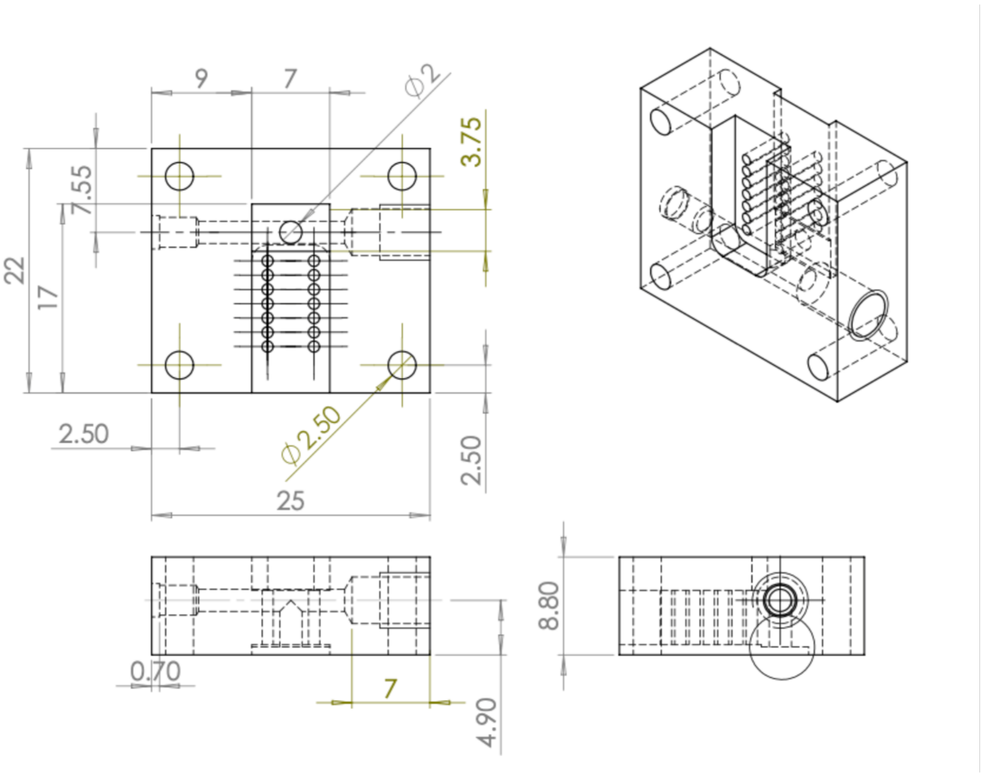

Figure 4.1: Technical drawing of the VLM thruster housing.

An example of the thruster chip is shown in Figure 4.2, whereas the fully assembled thruster can be seen in Figure 4.3.

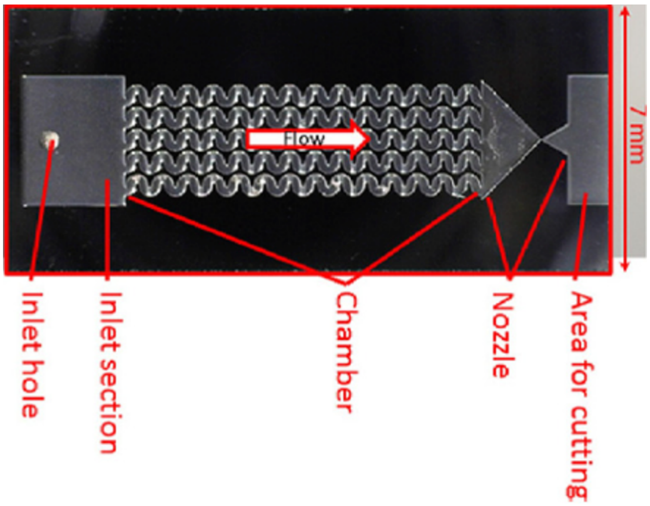

Figure 4.2: Close-up view of a MEMS thruster chip [21].

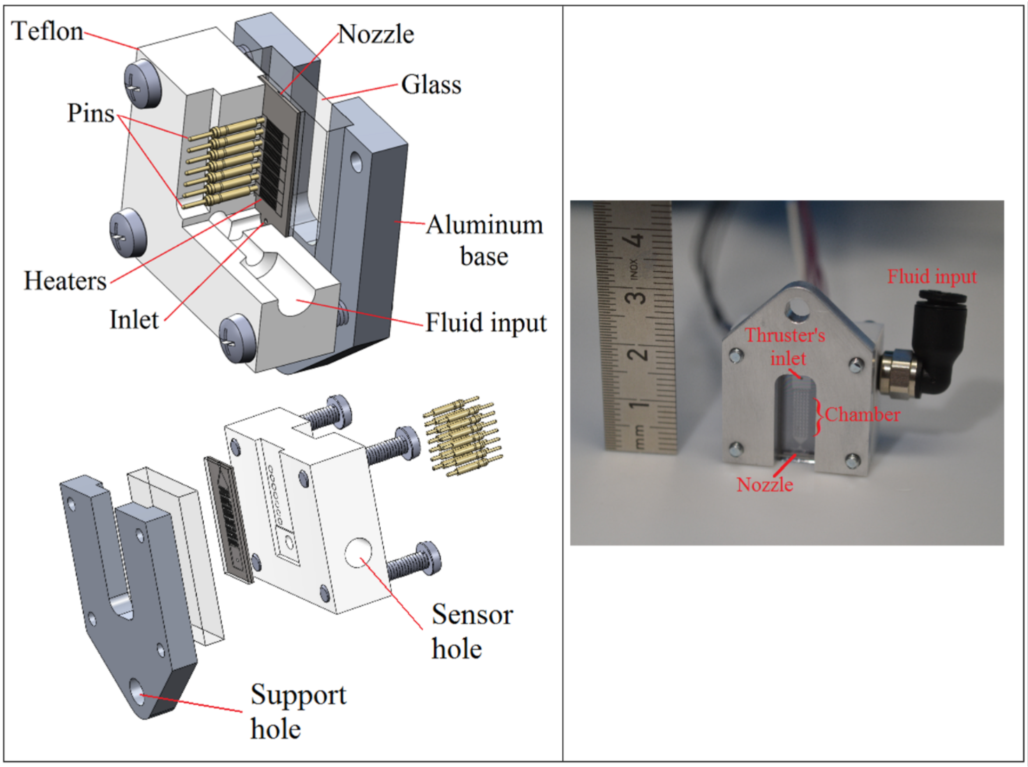

Figure 4.3: Integrated thruster assembly [21].

There is currently a student working on a re-design of the VLM thruster for test purposes. These design updates are not considered in this thesis, as this would require many system design iterations. However, a conceptual redesign of the thruster housing is proposed later in this thesis to reduce its outer dimensions. The specifications of the thruster used in this thesis are summarized in Table 4.1.

Table 4.1: Thruster specifications [20][21].

Property	**Value**
Thruster Mass [g]	20
Housing Dimensions [mm] (height x width x thickness)	32 x 25 x 8.8
Chip Dimensions [mm] (height x width x thickness)	17 x 7 x 0.9
Throat Area [m^2]	$4.5 \cdot 10^{-9}$
Area Ratio [-]	11

4.2 System Requirements

The starting point for the design of a micro-resistojet propulsion system is a list of requirements, including their rationales. These requirements include the required system performance, power budget, mass budget, and volume budget, as well as structural and thermal considerations.

Both PocketQubes and CubeSats are viable candidates for integrating the micro-resistojet propulsion system as part of their spacecraft design. However, PocketQubes are severely power limited, which result in low achievable thrust levels. These low thrust levels, combined with a long burn duration to achieve any significant impulse bit, lead to large gravity losses. The PocketQube is no longer under consideration in this thesis for these reasons.

The list of requirements can be found in Table 4.2, where some requirements contain multiple values. These values, separated with a "/" indicate the values for the differently sized systems (from 0.5 U - 1.5 U). Moreover, several requirements include a TBD, as they depend on trade-offs and design choices made later in this thesis. These requirements will be updated throughout the design process. The compilation of requirements draws inspiration from the "Main requirements for the Delfi-PQ micro-propulsion demonstration payload [20]."

Table 4.2: List of requirements to start the design of a micro-resistojet propulsion system.

Requirement ID	**Requirement**	**Rationale**
PROP-SYST-1	The propulsion system shall be compatible with multiple propellant tank sizes.	See Subsection 4.2.1.
PROP-SYST-2	The total size of the propulsion system shall be within 0.5 U/ 1 U / 1.5 U.	See Subsection 4.2.2.
PROP-SYST-3	The total wet mass of the propulsion system at launch shall be not exceed 0.7 kg / 1.35 kg / 2.0 kg.	See Subsection 4.2.3.
PROP-SYST-4	The power consumption of the propulsion system shall not exceed 25 W.	See Subsection 4.2.4.
PROP-SYST-5	The propulsion system shall function for at least <*TBD*> months.	-
Performance Requirements		
PROP-PERF-1	The propulsion system shall deliver a total impulse of 200 Ns / 400 Ns / 600 Ns.	See Subsection 4.2.5.
PROP-PERF-2	The propulsion system shall deliver a maximum thrust of 5.7 mN.	See Subsection 4.2.6.
PROP-PERF-3	The propulsion system shall deliver a minimum thrust of 0.5 mN.	See Subsection 4.2.7
PROP-PERF-4	The propulsion system shall operate on a supply voltage of <*TBD*> V .	-
Functional Requirements		
PROP-FUNC-1	The propulsion system shall use <TBD> as a propellant.	Design choice.
PROP-FUNC-2	The propulsion system shall have at least an idle and full thrust mode.	Allows for performing manoeuvres.
Interface Requirements		
PROP-INT-1	The mechanical interface between the propulsion system and the satellite shall be complaint with the CubeSat CS14 interface standard.	Allows for integration in any CubeSat that adheres to this standard.
PROP-INT-2	The propulsion system shall stay in a temperature range between <*TBD*> °C and <*TBD*> °C.	-
PROP-INT-3	The electrical interface between the propulsion system and the satellite shall be compliant with the CubeSat CS14 interface standard.	Allows for integration in any CubeSat that adheres to this standard.
PROP-INT-4	The propulsion system shall allow for filling and draining of propellant at any time when the satellite is accessible to human operators.	Allows for testing.
Reliability, Availability, Maintainability, and Safety (RAMS) Requirements		
PROP-RAMS-1	The pressure within the propulsion system shall not exceed 10 bar.	Maximum allowable pressure in the thruster [38].

Continued on next page

Requirement ID	Requirement	Rationale
PROP-RAMS-2	The materials used in the propulsion system shall be compatible with the chosen propellant.	Required for the system to function properly.
PROP-RAMS-3	The materials used in the propulsion system shall not be flammable, toxic, or hazardous to the satellite and operators.	General safety standards.

4.2.1 Rationale PROP-SYST-1

A modular design is proposed to optimize the range of scenarios in which the system can be utilized. The modularity lies in the use of differently sized propellant tanks that can be connected to the same thruster assembly. The volume budget of a micro-resistojet propulsion system is largely taken up by the propellant tank. As a first approximation, it is assumed that the propellant tank occupies the entire volume budget.

4.2.2 Rationale PROP-SYST-2

This requirement is based on the linear relationship found in Chapter 2 between the total impulse and system volume of micro-resistojet propulsion systems. Equation 4.1 shows this relationship,

$$I_{tot} = 387.1 \cdot V \tag{4.1}$$

where I_{tot} is the total impulse in Ns, and V is the system volume in U. Applying this relationship to the three chosen total impulse values of 200 Ns, 400 Ns, and 600 Ns (as will be discussed in Subsection 4.2.5), yield an approximate required system volume of 0.5 U, 1 U, and 1.5 U respectively.

4.2.3 Rationale PROP-SYST-3

This requirement is based on the linear relationship found in Chapter 2 between system volume and wet mass of micro-resistojet propulsion systems. Equation 4.2 shows this relationship,

$$M_{wet} = 1.315 \cdot V \tag{4.2}$$

where M_{wet} is the system wet mass. Applying this relationship to the three system volumes of 0.5 U, 1 U, and 1.5 U, results in a wet mass of 658 g, 1315 g, and 1973 g respectively. These values are rounded up to the nearest 50 g, which result in a maximum allowable wet mass of 700 g, 1350 g, and 2000 g.

4.2.4 Rationale PROP-SYST-4

Larger CubeSats can generate an average satellite power in the neighbourhood of 40 W, and have a peak power generation of up to 100 W [39]. It is assumed that a maximum of 25 W be used by the propulsion system during a burn. This is approximately 63 % of the average satellite power, and 25 % of the peak power. One can argue that the relatively high fraction of the average power is problematic and would leave little room for powering the rest of the spacecraft. However, as the duty cycle of the propulsion system is aimed to be small to minimize gravity losses, it can be assumed that the power generation of the satellite is somewhere in between the 40 W average power, and 100 W peak power generation, and it would lead to sufficient remaining power for the rest of the bus.

This power requirement suggests that the propulsion system can only be integrated in larger spacecraft. However, this requirement states the maximum power that the system can use. The system power can be reduced, which will result in lower achievable thrust levels, as will be explained in Subsection 4.2.6.

4.2.5 Rationale PROP-PERF-1

One application of a micro-resistojet propulsion system is orbital altitude maintenance in Low-Earth-Orbit (LEO) [40]. The orbital lifetime of a 3U CubeSat, with a ballistic coefficient of 164 is estimated by using the interactive excel sheet provided by SMAD [41]. The results of this estimated during a solar maximum are shown in Table 4.3.

Table 4.3: Orbital lifetime (in months) of a 3U CubeSat with a ballistic coefficient of 164 without propulsion.

Orbital Altitude [km]	100	200	300	400	500	600	700	800	900	1000
Orbital Lifetime [months]	0.0	0.1	1.5	7.1	29.8	331.7	1409.6	4742.7	14016.4	36736.0

A propulsion system allows for a prolonged mission duration. To explore the significance of total impulse values in enhancing a spacecraft mission, the analysis focused on determining the required impulse for maintaining orbital altitude.

The required impulse per year to maintain a circular orbit can also be estimated by using the interactive excel sheet from SMAD [41] and is shown for the same 3U CubeSat during a solar maximum in Table 4.4.

Table 4.4: Required Impulse per Year to Maintain a Circular Orbit.

Orbital Altitude [km]	100	200	300	400	500	600	700	800	900	1000
Required Total Impulse [Ns/year]	12070656	8052	907	172	41	11	3	1	0.4	0.2

Elliptical orbits are also considered, as they allow spacecraft to achieve a low altitude at perigee during which measurements can be taken whilst not decaying as quickly as they would when they are continuously at these lower altitudes. The required impulse to maintain these altitudes are estimated by interpolating the atmospheric density used in the SMAD excel template [41]. Next, a relationship between time and orbital radius is generated by using the equations for the mean anomaly, eccentric anomaly, and the mean motion. The results of this are shown in Table 4.5

Table 4.5: Estimated required impulse (in Ns/year) to maintain elliptical orbit.

	Perigee [km]				
Apogee [km]	100	200	300	400	500
100					
200	1082632				
300	741774	9924			
400	600037	6641	630		
500	517294	5306	423	88	
600	461358	4549	335	60	19
700	420268	4044	285	47	13
800	388412	3677	253	40	10
900	362761	3394	229	35	9
1000	341518	3167	211	32	8

As already mentioned, the results in these tables are based on estimates, and can include errors. One of these estimation errors can be seen in Table 4.5 for the 200x300 km orbit. The required impulse per year for this orbit is higher than the required impulse for a circular 200 km orbit, as shown in Table 4.4. One must realise that these estimates on required total impulse are not meant for the detailed design of a mission, but merely being used to determine what range of total impulse is deemed useful for satellite missions at LEO.

The required total impulse per year ranges anywhere between 0.2 Ns/year and 12 MNs/year. Current micro-resistojet systems can provide a total impulse between 1 and 1155 Ns, of which water-based systems are generally on the lower end, and non-water-based systems on the higher end of this scale (Table 2.4). It has been determined that, when considering both the total impulse range of existing micro-resistojet propulsion systems, and the required total impulse to maintain orbital altitudes in LEO, total impulse values of *200* Ns, *400* Ns, and *600* Ns are deemed beneficial and practical for CubeSat missions.

Now, to illustrate the utility of these three distinct total impulses, a potential mission scenario is outlined for two of them. First, a 200 Ns system can maintain a circular orbit at 400 km for almost 14 months. The orbit would decay, without the use of a propulsion system, within approximately 7 months. The 200 Ns system enables a mission duration increase of 200%.

Second, a 600 Ns system could be used to extend a mission at an orbital altitude of 200 km. This orbit would decay, for the specified 3U CubeSat, within 4 days. The use of the 600 Ns system allows for an increased mission duration of approximately 27 days: an increase of 675 %.

4.2.6 Rationale PROP-PERF-2

This requirement is based on the linear relationship found in Chapter 2 between thrust and system power. Equation 4.3 shows this relationship,

$$F_t = 0.2291 \cdot P \tag{4.3}$$

where F_t is the thrust force, and P is the system power. The maximum power of 25 W, as specified in Subsection 4.2.4, results in a maximum achievable thrust of approximately 5.7 mN. Subsection 4.2.4 mentioned that the system power can be reduced in order to be compatible with smaller spacecraft. Equation 4.3 shows the linear relationship found in the literature study between the system power and achievable thrust. This relationship suggests that the thrust decreases linearly by simply reducing the input power. The validity of this relationship is checked through a more mathematical approach that considers not only the heating power, but also different pressure and temperature levels in the chamber.

First, Equation 4.4 is used to determine the relationship between heating power and chamber pressure,

$$P_h = \frac{p_c \cdot A_t}{\sqrt{\frac{R_A}{M_W} \cdot T_c}} \cdot \sqrt{\gamma \left(\frac{1+\gamma}{2}\right)^{\frac{1+\gamma}{1-\gamma}}} \cdot \left[c_{pL} \cdot (T_{boil} - T_0) + L_h + c_{pG} \cdot (T_c - T_{boil})\right] \tag{4.4}$$

where P_h is the available heating power, A_t is the throat area, R_A is the universal gas constant, M_W is the molar mass of the propellant, γ is the specific heat ratio, T_c is the chamber temperature, T_{boil} is the propellant boiling temperature, T_0 is the initial propellant temperature (assumed to be 283.15 K), c_{pL} is the constant pressure specific heat of the liquid propellant, c_{pG} is the constant pressure specific heat of the gaseous propellant, and L_h is the latent heat of vaporization of the propellant. This relationship is applied to three chamber pressure levels (2, 5, and 10 bar), and two chamber temperatures (400 K and 550 K) whilst using water as a propellant [20]. The results of this analysis can be found in Figure 4.4, where a clear linear relationship between the heating power and chamber pressure is found for both temperature levels.

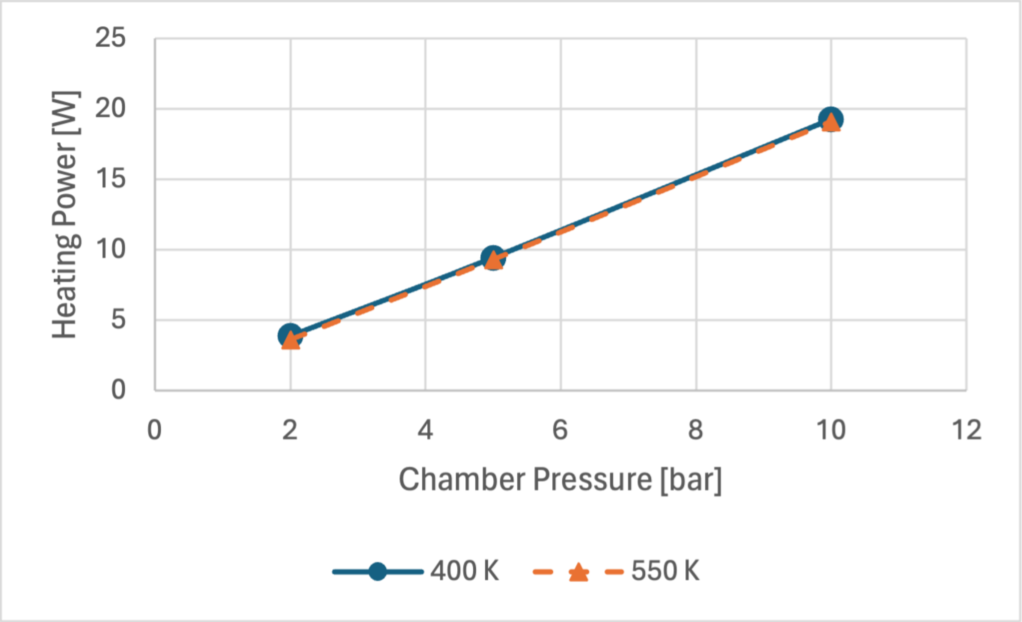

Figure 4.4: Heating Power as function of Chamber Pressure.

Second, a relationship between thrust and chamber pressure is to be found. This is achieved through the following steps, that are performed again for the three chamber pressure levels (of 2, 5, and 10 bar), and two chamber temperatures (of 400 K and 550 K). First, the mass flow rate is calculated by using Equation 4.5,

$$\dot{m} = \frac{p_c \cdot A^*}{\sqrt{\frac{R_A}{M_W} \cdot T_c}} \cdot \Gamma \tag{4.5}$$

where $\dot{m}$ is the mass flow rate, and Γ is the Vandenkerckhove function. The latter can be calculated by using Equation 4.6.

$$\Gamma = \sqrt{\gamma \left(\frac{1+\gamma}{2}\right)^{\frac{1+\gamma}{1-\gamma}}} \tag{4.6}$$

Next, the pressure ratio is to be found. This ratio can be found using Equation 4.7,

$$\frac{A_e}{A^*} = \frac{\Gamma}{\sqrt{\frac{2\gamma}{\gamma-1} \cdot \left(\frac{p_e}{p_c}\right)^{\frac{2}{\gamma}} \cdot \left[1 - \left(\frac{p_e}{p_c}\right)^{\frac{\gamma-1}{\gamma}}\right]}} \tag{4.7}$$

where A_e is the nozzle exit area, and p_e is the nozzle exit pressure. This equation can be solved for the pressure ratio by using the know value for the area ratio of 11 [42]. The pressure ratio can now be used to determine the exit pressure, and the area ratio allows to calculate the nozzle exit area when assuming a nozzle throat area of 45 x 100 µm [20].

Now, the jet velocity can be calculated using Equation 4.8,

$$v_e = \sqrt{\frac{2\gamma}{\gamma - 1} \cdot \frac{R_A}{M_W} \cdot T_c \cdot \left[1 - \left(\frac{p_e}{p_c}\right)^{\frac{\gamma-1}{\gamma}}\right]} \tag{4.8}$$

where v_e is the jet velocity, by using the pressure ratio that resulted from Equation 4.7. Finally, the thrust can be calculated using Equation 4.9,

$$F_t = \dot{m} \cdot v_e + A_e \cdot (p_e - p_a) \tag{4.9}$$

where F_t is the achieved thrust level, and p_a is the atmospheric pressure. The latter is assumed to be zero, as the system operates in a vacuum. The results of this analysis for the three chamber pressures, and two chamber temperatures is are shown in Figure 4.5.

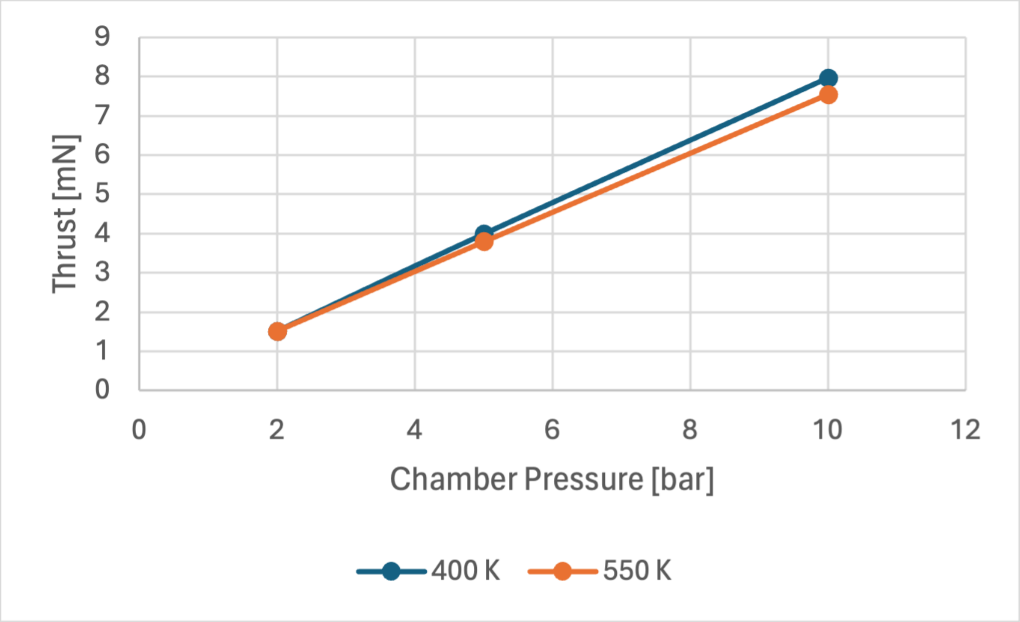

Figure 4.5: Thrust as function of Chamber Pressure.

The last step is to link the linear relation between heating power and chamber pressure, and thrust and chamber pressure. This results in the linear relationship between thrust and heating power. This relationship can be changed into a relationship between the thrust and input power by assuming a system efficiency of 50%. The result of this analysis can be found in Figure 4.6.

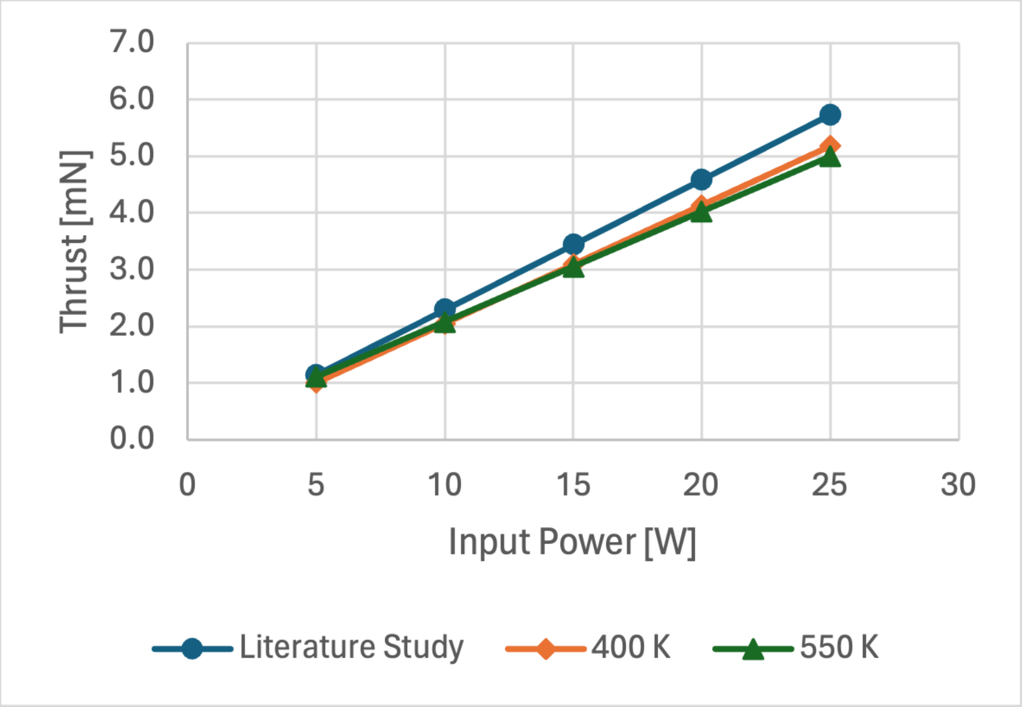

Figure 4.6: Thrust as function of Input Power.

This figure includes the linear relationship between thrust and power that was found in the literature study. The thrust levels for a chamber temperature of 400 K and 550 K are similar to the thrust levels found using the linear approximation that resulted from the literature study. This confirms the accuracy of the simplified approximation derived from the literature.

Subsection 4.2.4 and the start of this section mentioned the decrease in input power, (and the accompanied decrease in thrust) to allow for integration in smaller spacecraft. The following example is provided to quantify the results found in this section. Consider a 3U CubeSat that provides an average power of 12 W, of which 40 % (or approximately 5 W) can be used by the propulsion system. The 5 W input power results in a maximum achievable thrust by this micro-resistojet propulsion system of approximately 1.1 mN.

4.2.7 Rationale PROP-PERF-3

The requirement on the minimum thrust level is necessary to limit the required burn time to perform a manoeuvre. The burn time must be limited to minimize the gravity losses. The minimum thrust level of 0.5 mN is calculated by using the following approach and makes use of several assumptions that will be stated throughout this section.

The case of maintaining a circular orbit between 100 km and 1000 km is investigated. First, the orbital period is calculated for each orbital altitude which can be used to calculate how many orbits are completed within 1 year. Second, the required impulse per orbit to maintain a specific altitude can be calculated by simply dividing the value of required impulse per year (can be found in Table 4.4) by the number of orbits per year. It is assumed that the spacecraft performs a burn every orbit.

Now, the required impulse (that the propulsion system must deliver every orbit), thrust, and burn time are connected through the following expression,

$$I_{bit} = F_t \cdot t_b \tag{4.10}$$

where I_{bit} is the required impulse per orbit, and t_b is the burn time. The minimum required thrust can now be calculated for each altitude by assuming a range of burn times, in this case between 5 and 10 minutes [43][44]. The result of this analysis can be found in Figure 4.7.

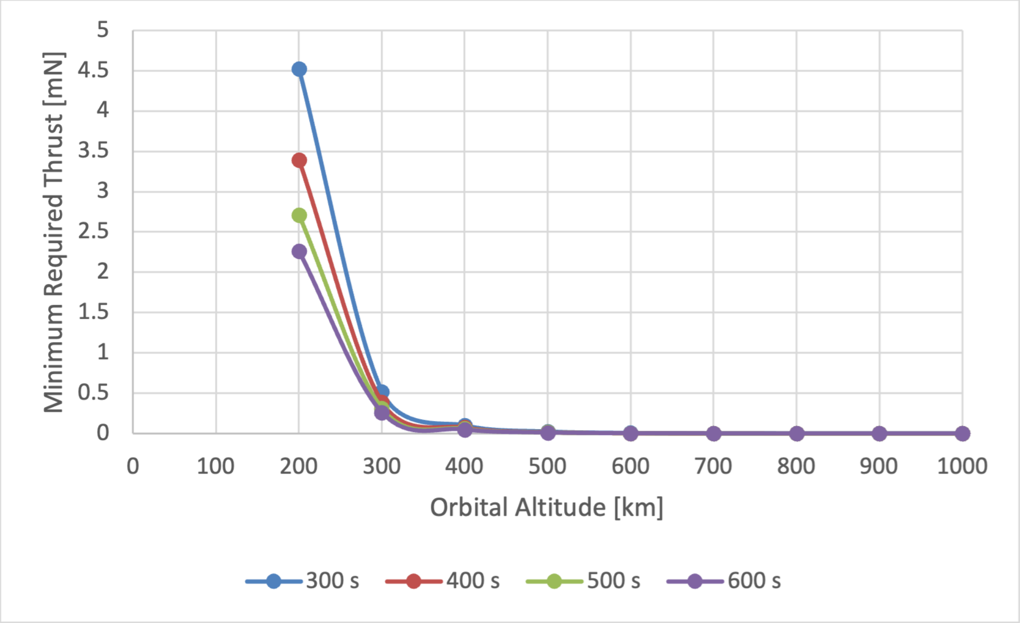

Figure 4.7: Minimum Required Thrust as function of Orbital Altitude

It must be noted that the results for the 100 km orbit are not included in this figure, as they are very large compared to the rest of the values. When taking into account that the maximum impulse the system can deliver is 600 Ns, and looking at Table 4.4, one could argue that orbital maintenance below an orbital altitude of 300 km is not feasible as a result of the large required impulse per year. Orbits above this altitude require a minimum thrust of at most 0.5 mN. This case can be found at an orbital altitude of 300 km, and a burn time of 5 minutes (or 300 seconds).

Propellant Trade-Off 5

This chapter describes the trade-off process for picking a suitable propellant for the VLM propulsion system, and is based on previous work [42]. The previously outlined VLM thruster, designed by the TU Delft to work with water, questions the need for a propellant trade-off. Nevertheless, a trade-off is conducted to confirm the advantages of water over other commonly used propellants in VLM propulsion systems. First, the considered propellants and trade-off methodology are outlined in Section 5.1. This is followed by the results of each trade-off criterion in Section 5.2. The winner of the trade-off, including a sensitivity analysis can be found in Section 5.3. Finally, the conclusions are outlined in Section 5.4.

5.1 Propellant Selection and Trade-off Methodology

This section will first discuss what propellants are included in the propellant trade-off in Subsection 5.1.1, after which the trade-off criteria are outlined in Subsection 5.1.2. Finally, the trade-off methodology is explained in Subsection 5.1.3.

5.1.1 Propellant options

The starting point of a propellant trade-off is the selection of suitable propellants. Chapter 2 discusses the current state-of-the-art micro-resistojet propulsion systems. These systems use water, ammonia, butane, R134a, and R236fa as propellants. The utilization of these propellants highlights their potential and justifies their inclusion in this propellant trade-off analysis. Table 5.1 provides a summary of useful propellant properties.

Table 5.1: Propellant properties [45]

Propellant	Water	Ammonia	Butane	R134a	R236fa
Chemical Formula	H_20	NH_3	C_4H_{10}	$C_2H_2F_4$	$C_3H_2F_6$
Molar Mass [g/mol]	18.0153	17.0305	58.1222	102.0309	152.0384

5.1.2 Trade-off criteria

The five propellants are compared against each other based on four trade-off criteria: system density, performance, flammability, and health risk.

System Density

The system density refers to the density of the propellant under storage conditions, namely a tank pressure of 10 bar and a temperature of 293.15K. The densities are then compared against each other. Higher density at storage conditions is favourable, as this will result in a smaller system.

Performance

The performance of each propellant is analysed by examining their relationships between achievable thrust level as a function of chamber pressure, achievable thrust level as a function of heating power, specific impulse as a function of heating power, and the achievable impulse per volume of propellant as a function of heating power. The relationships found for each propellant are integrated into one plot per relationship which allows for comparing the different propellants.

Ideal rocket theory allows for estimating these relationships. The following calculations are performed for each propellant for chamber pressures between 2 and 5 bar, and for two chamber temperatures. It is important to note that every combination of chamber pressures and temperatures must vaporize the propellant for the thruster to operate effectively.

The thrust F_t and the specific impulse I_{sp} can be calculated using Equation 5.1 and Equation 5.2 respectively,

$$F_t = \dot{m}v_e + (p_e - p_a)A_e \tag{5.1}$$

$$I_{sp} = \frac{F_t}{\dot{m}g_0} \tag{5.2}$$

where $\dot{m}$ is the mass flow rate, v_e is the jet velocity, p_e is the exit pressure, p_a is the ambient pressure, A_e is the nozzle exit area, and g_0 is the gravitational acceleration at sea level. The required heating power can now be calculated using Equation 5.3,

$$P_h = \dot{m}\Delta H \tag{5.3}$$

where ΔH is the change in enthalpy with respect to a baseline temperature of 283.15K. The change in enthalpy is dependent on both the chamber pressure and chamber temperature. The mass flow rate can be calculated using Equation 5.4,

$$\dot{m} = \frac{p_c \cdot A_t}{\sqrt{\frac{R_A}{M_W} \cdot T_c}} \cdot \Gamma \tag{5.4}$$

where p_c is the chamber pressure, A_t is the nozzle throat area, R_A is the universal gas constant, T_c is the chamber temperature, M_W is the molecular mass of the propellant, and Γ is the Vandenkerckhove function. The Vandenkerckhove function can be calculated using Equation 5.5,

$$\Gamma = \sqrt{\gamma \cdot \left(\frac{1+\gamma}{2}\right)^{\frac{\gamma+1}{\gamma-1}}} \tag{5.5}$$

where γ is the specific heat ratio and is dependent on both the chamber temperature and chamber pressure.

The nozzle expansion ratio, the ratio between the nozzle exit area and the nozzle throat area, can be calculated using Equation 5.6.

$$\frac{A_e}{A_t} = \frac{\Gamma}{\sqrt{\frac{2\gamma}{\gamma-1} \cdot \left(\frac{p_e}{p_c}\right)^{\frac{2}{\gamma}} \cdot \left[1 - \left(\frac{p_e}{p_c}\right)^{\frac{\gamma-1}{\gamma}}\right]}} \tag{5.6}$$

Solving Equation 5.6 for the pressure ratio (the ratio of nozzle exit pressure to nozzle chamber pressure) allows for calculating the jet velocity by using Equation 5.7.

$$v_e = \sqrt{\frac{2\gamma}{\gamma-1} \cdot \frac{R_A}{M_W} \cdot T_c \cdot \left[1 - \left(\frac{p_e}{p_c}\right)^{\frac{\gamma-1}{\gamma}}\right]} \tag{5.7}$$

Finally, the achievable impulse per volume of propellant $\left(\frac{I_{sc}}{V_p}\right)$ can be calculated using Equation 5.8,

$$\frac{I_{sc}}{V_p} = I_{sp} \cdot g_0 \cdot \rho_p \tag{5.8}$$

where I_{sc} is the achievable impulse, V_p is the propellant volume, and ρ_p is the propellant density at storage conditions. This relationship is derived from combining Equation 5.9,

$$\Delta V = I_{sp} \cdot g_0 \cdot \frac{M_p}{M_{sc}} \tag{5.9}$$

where it is assumed that the propellant mass (M_p) is sufficiently small compared to the spacecraft mass (M_{sc}), and Equation 5.10,

$$I_{sc} = \Delta V \cdot M_{sc} \tag{5.10}$$

where ΔV is the achievable velocity increment.

Flammability

The flammability of a propellant is included in the trade-off, as it effects the reliability of the propulsion system, the spacecraft in which the propulsion system is integrated, and any other vehicle that is in close proximity to the propulsion system throughout its lifetime. The latter is especially relevant for a piggy-back launch, where the main payload can be endangered when using a flammable propellant.

Health Risk

The health risk refers to the propellant's toxicity and is considered in this trade-off because of the additional safety measures required when handling toxic propellants. The use of non-toxic propellants allows for easier handling of the system during both the testing and integration phases and is therefore preferred.

5.1.3 Trade-off methodology

Now that the trade-off criteria have been established, the trade-off methodology can be outlined. Each criterion is assigned a trade-off weight, ranging from 1 to 6, where 1 signifies the criterion is of low importance, and 6 denotes the criterion is highly significant. One lecturer and three MSc students (from the Space Engineering track) contributed their trade-off weights, and the weight assigned to each criterion is determined by averaging the results. This approach guarantees the absence of any bias in establishing the individual weights.

Each trade-off criterion is evaluated for all propellants. This leads to a score assigned to each propellant based on the evaluation. The scores are categorized into three groups: positive, neutral, and negative, and correspond to scores of 1, 0, and -1 respectively.

The scores for each category are multiplied by their respective weights and then summed for each propellant. The winner of the trade-off, therefore, the propellant selected for the design of the VLM micro-resistojet propulsion system, is the one with the highest weighted score.

5.2 Results

The results are outlined as follows. First, Subsection 5.2.1 discusses the trade-off weights, followed by system density in Subsection 5.2.2. Subsection 5.2.3 covers performance, while Subsection 5.2.4 addresses both flammability and health risks.

5.2.1 Trade-Off Weights

One professor and four master students provided their trade-off weights for each criterion. The results are summarized in both Table 5.2 and Figure 5.1.

Table 5.2: Weight factors provided by each participant, including the average weight factor ($\overline{WF}$) and standard deviation (σ_{st}).

Criterion	**Professor**	**Student 1**	**Student 2**	**Student 3**	**Student 4**	$\overline{WF}$	σ_{st}
System Density	6	5	3	5	5	4.8	1.10
Performance	5	6	5	6	6	5.6	0.55
Flammability	2	3	1	2	2	2.0	0.71
Health Risk	4	4	2	3	4	3.4	0.89

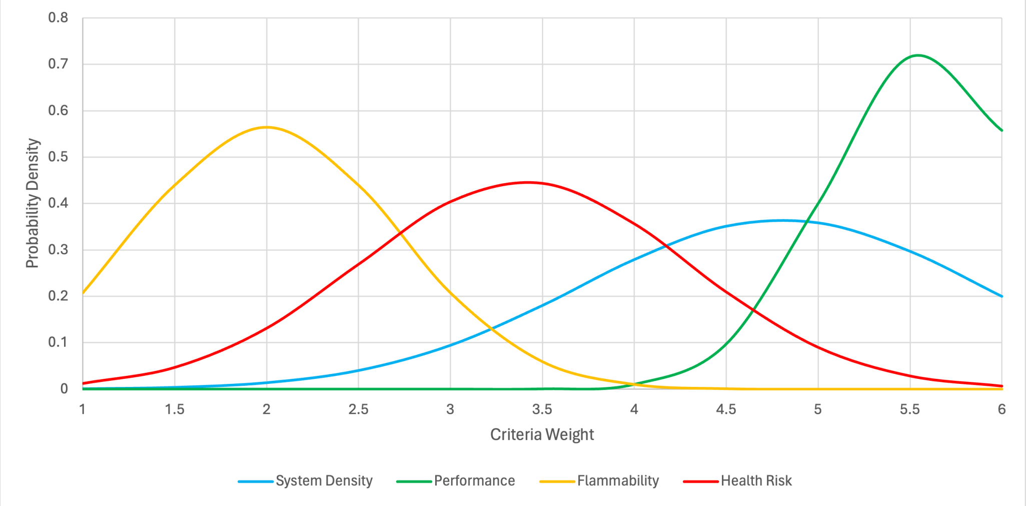

Figure 5.1: Distribution of the provided trade-off weights for each criterion.

Figure 5.1 is included to provide a clearer overview of the distribution of the trade-off weights for each criterion. It can be observed that there is a clear consensus regarding the performance and flammability, as indicated by the small standard deviations. However, there is a wider range of weights observed for system density, health risk, and compatibility. The health risk is centered around the average weight factor of 3.5, whereas the system density is leaning more towards the higher end of the scale.

5.2.2 System Density

The propellant densities at 293.15 K are shown for a range of storage pressures in Figure 5.2.

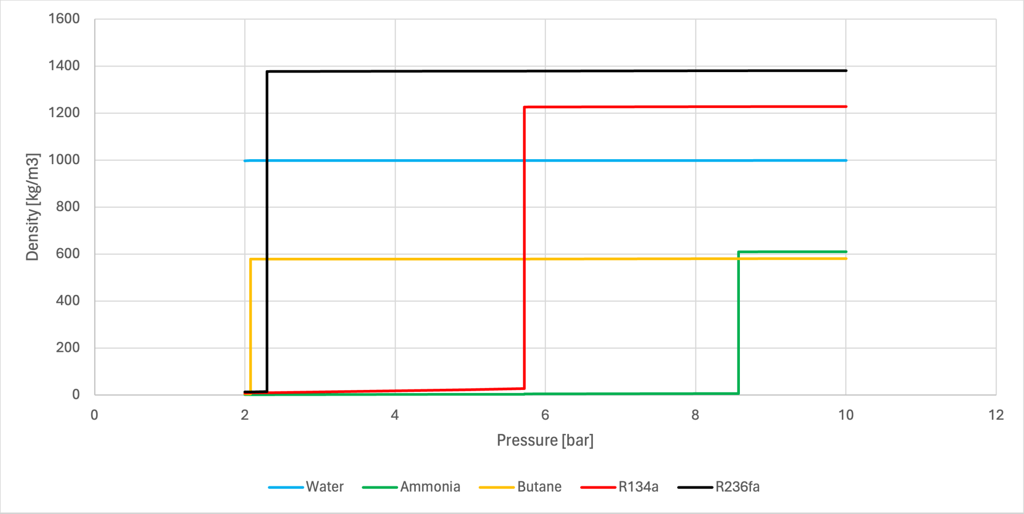

Figure 5.2: Propellant density as a function of pressure at 293.15 K [45].

The densities at the assumed storage pressure of 10 bar and temperature of 293.15 K range between 580 and 1380 kg/m^3. The sudden increases in density signify a phase transition from vapor to liquid. Notably, water is the only propellant that remains in the liquid phase throughout the entire investigated pressure range. Propellants with a higher density at the given storage conditions are the preferred option, as they will reduce the required tank volume and, consequently, the volume of the propulsion system. The evaluation of each propellant density is outlined in Table 5.3.

Table 5.3: Propellant evaluation based on the density at storage conditions (10 bar, 293.15K).

Propellant	**Water**	**Ammonia**	**Butane**	**R134a**	**R236fa**
System Density	Neutral (0)	Negative (-1)	Negative (-1)	Positive (+1)	Positive (+1)

5.2.3 Performance

Pressure and Temperature Ranges

The performance of each propellant is investigated at two chamber pressures, namely 2 bar and 5 bar, and at two chamber temperatures. The latter varies for each propellant, based on the boiling point of the propellant at the given chamber pressure, and the available information on the propellant properties for a given temperature. The minimum chamber temperature must be above the boiling point for the thruster to operate. The maximum chamber temperature is either set at 550 K (equal to the average maximum temperatures that are commonly found in literature for VLMs [42]) or at the highest value where all chemical properties remain provided by NIST [45].

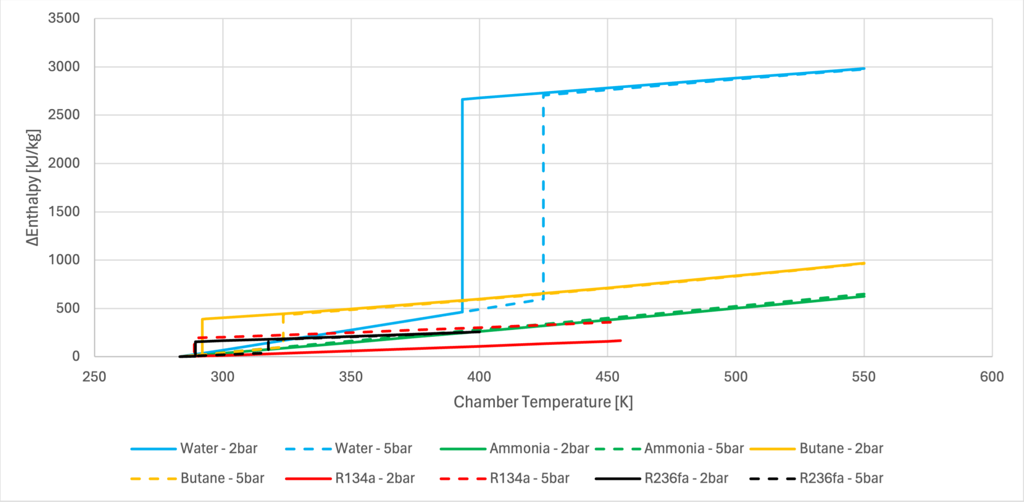

Figure 5.3: Changes in enthalpy as a function of chamber temperature.

Figure 5.3 shows the change in enthalpy, from a baseline temperature of 283.15 K, as a function of the chamber temperature. The sudden jumps in enthalpy indicate that the boiling point is reached and marks the minimum required chamber temperature at which the thruster must operate for a given propellant and chamber pressure. It can be observed that the boiling point is delayed when increasing the chamber pressure. The minimum chamber temperature for each propellant in this analysis is set to the nearest rounded-up value to 25 above the boiling point at a chamber pressure of 5 bar. This adjustment ensures that the propellant's boiling point is reached for both chamber pressures in this comparative analysis. The maximum chamber temperatures can be found at the endpoints of the graph. Table 5.4 provides an overview of the minimum and maximum temperatures used in the analysis for each propellant.

Table 5.4: Upper and lower-bound chamber temperatures.

Propellant	**Minimum Chamber Temperature [K]**	**Maximum Chamber Temperature [K]**
Water	425	550
Ammonia	300	550
Butane	325	550
R134a	300	455
R236fa	325	400

Thrust as function of chamber pressure

The relationship between thrust and chamber pressure can be found by combining Equation 5.1, Equation 5.4, Equation 5.6, and Equation 5.7, and using an nozzle expansion ratio of 11, a nozzle throat area of $4.5 \cdot 10^{-9}$ m^2 as specified in Section 4.1, and assuming that the system operates in a perfect vacuum (p_a = 0 Pa). Figure 5.4 shows the result of this analysis.

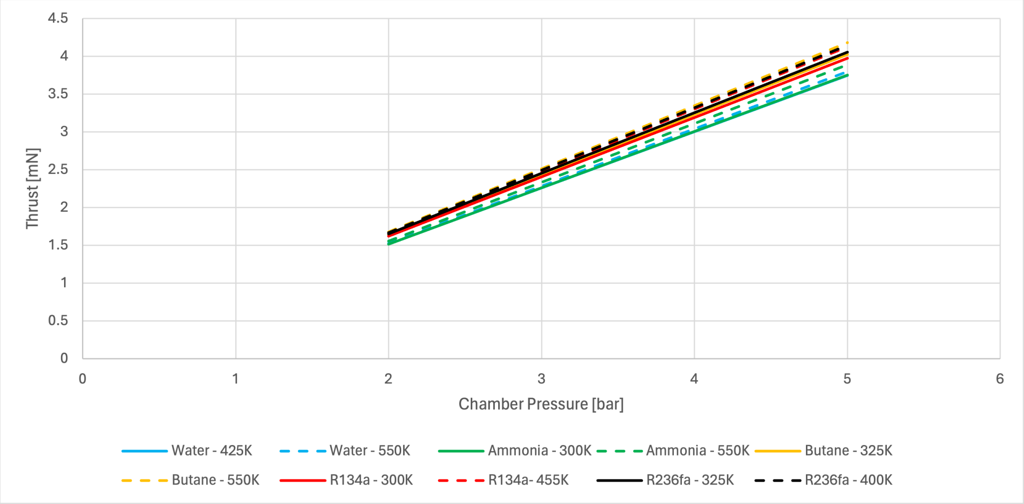

Figure 5.4: Thrust level as function of chamber pressure.

It can be observed that as the chamber temperature rises, there is a corresponding increase in thrust at a constant chamber pressure, and greater thrust is achieved at higher chamber pressures. The effect of temperature on the thrust level is significantly smaller than that of pressure. This distinction becomes more evident when looking at Figure 5.5,

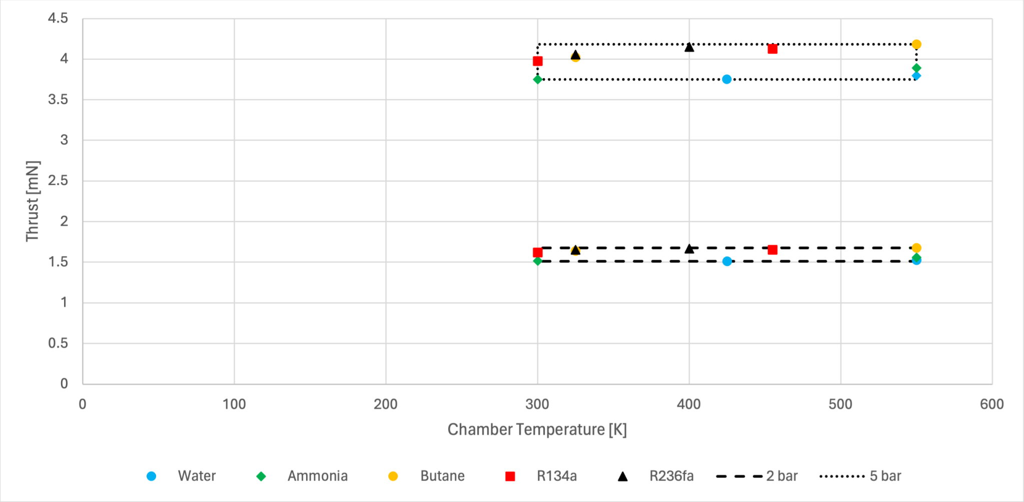

Figure 5.5: Thrust level as function of chamber temperature.

where the thrust is shown as a function of the chamber temperature. An increase in the chamber temperature at a constant pressure result in a much smaller increase in thrust compared to the thrust increase achieved by raising the chamber pressure while maintaining a constant chamber temperature. Furthermore, Figure 5.4 shows that the performance of each propellant is similar, and that the difference in thrust level at each chamber pressure differs at most 0.5 mN.

Thrust as function of heating power

The relationship between thrust and heating power can be found by combining Equation 5.1, Equation 5.3, Equation 5.6, and Equation 5.7. Figure 5.6 shows the results of this analysis.

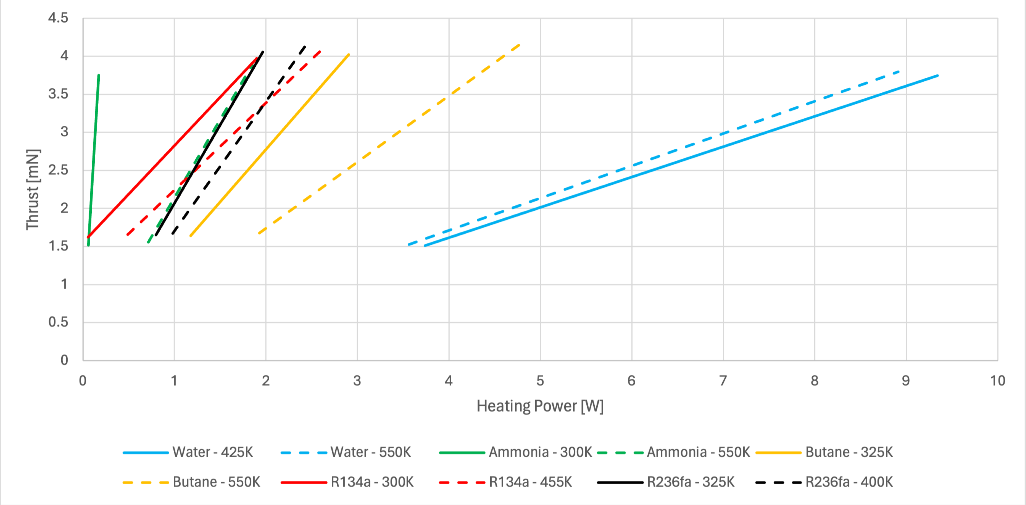

Figure 5.6: Thrust level as function of heating power.

Large differences between the different propellants can be found here. The best performing propellant is the one that achieves the larger thrust level at the smallest required heating power. Ammonia at a chamber temperature of 300 K is the best-performing propellant based on this criterion. An interesting observation is that only water benefits from a higher chamber temperature, as evident from the increase in thrust at a given heating power. All other propellants see a decrease in thrust at a given heating power when increasing the chamber temperature. This can be explained when realising that the thrust is proportional to the square of the chamber temperature and inversely proportional to the change in enthalpy. For water, it's observed that the ratio of the square of the chamber pressure to the change in enthalpy increases with an increase in chamber temperature, whereas a decrease is observed for the other propellants.

Specific impulse as function of heating power

The relationship between the specific impulse and the required heating power can be found by combining Equation 5.1, Equation 5.2, Equation 5.3, Equation 5.6, and Equation 5.7. The result of this analysis is visualized in Figure 5.7.

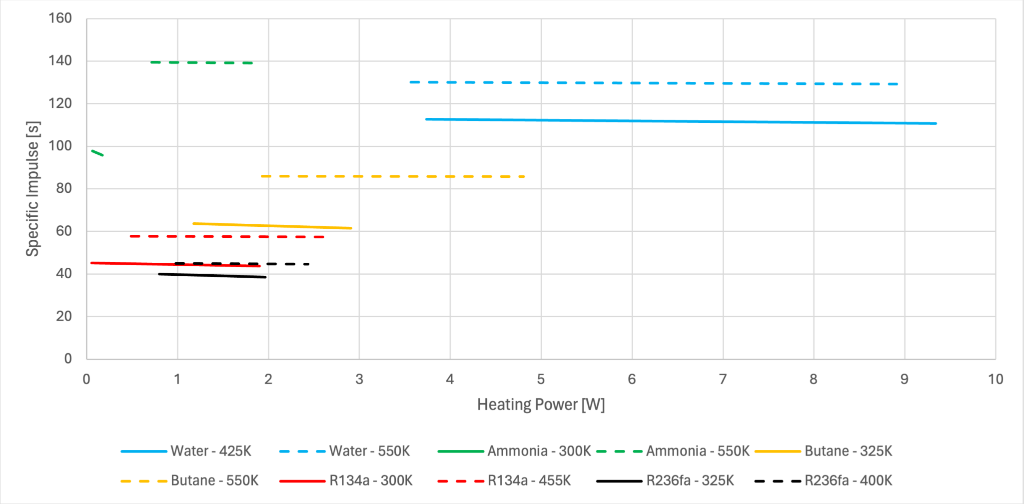

Figure 5.7: Specific impulse as function of heating power.

It can be observed that the specific impulse increases when increasing the chamber temperature, and that the achievable specific impulse shows minimal variation with changes in heating power for a constant chamber temperature. The best performing propellant, assuming that there is no requirement on the available heating power, is the one with the highest specific impulse. Ammonia and water achieve the best result based on this criterion.

Achievable impulse per volume of propellant as function of heating power

The final performance parameter examined is the achievable impulse per volume of propellant as a function of the required heating power. This correlation integrates both the system's performance and the necessary propellant volume to achieve that particular performance level. Such analysis is essential because a propellant may excel, for instance, in terms of specific impulse, yet demand a substantially larger propellant volume compared to a slightly less effective system. The relationship between these two parameters is found by combining Equation 5.3, Equation 5.4, and Equation 5.8, and by using the propellant densities at storage conditions as specified in Subsection 5.2.2. Figure 5.8 shows the results of this analysis.

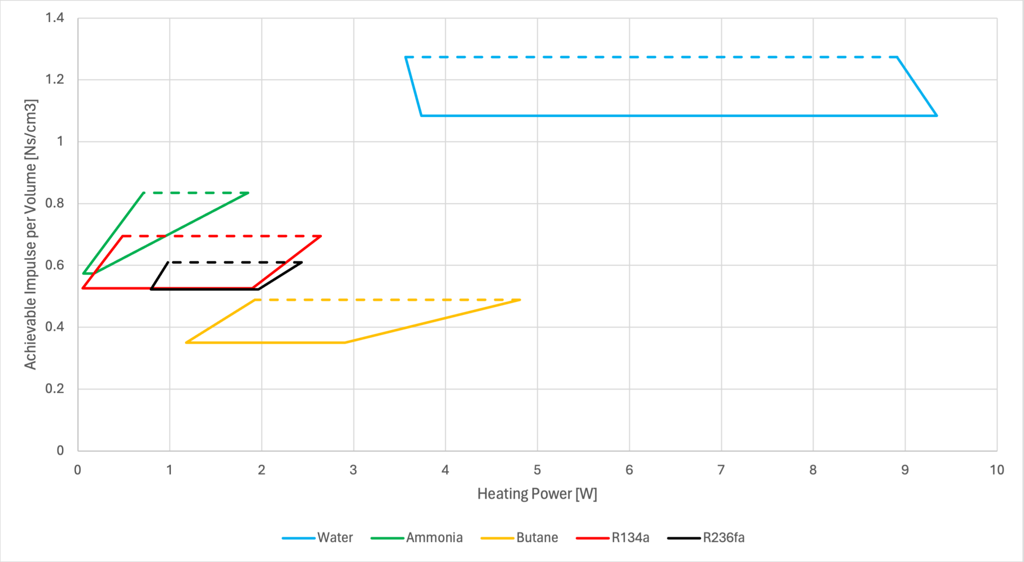

Figure 5.8: Achievable impulse per volume of propellant as function of heating power.

The horizontal dashed lines represent the conditions at maximum chamber temperature, whereas the horizontal solid lines represent the conditions at the minimum chamber temperature. These two lines are connected for each propellant to show the range of possible combinations of achievable impulse per volume of propellant as a function of the heating power. It can be observed that the achievable impulse per volume of propellant increases with an increase in chamber temperature, whereas the heating power has little influence on this parameter at a constant chamber temperature. In the absence of constraints on available heating power, the optimal propellant is determined by the one that achieves the highest achievable impulse per volume of propellant. In this case, water emerges as the top performer.

Performance Evaluation

Water is identified as the top-performing propellant, followed by ammonia, both receiving a "positive" score. This determination is based on their elevated attainable specific impulse and their high achievable impulse per volume of propellant, as shown in Figure 5.7 and Figure 5.8 respectively. The remaining propellants are awarded a “neutral” score, despite their poor performance in both the attainable specific impulse, and impulse per volume of propellant, as they can achieve larger thrust levels for a given chamber pressure, as evident from Figure 5.4. Furthermore, the attainable thrust levels of these propellants require a significantly lower heating power when compared with water, as shown in Figure 5.6. These favourable characteristics result in a “neutral” score, as they still demonstrate the capability to deliver good performance. The results of the performance evaluation are summarized in Table 5.5.

Table 5.5: Propellant evaluation based on their performance.

Propellant	**Water**	**Ammonia**	**Butane**	**R134a**	**R236fa**
Performance	Positive (+1)	Positive (+1)	Neutral (0)	Neutral (0)	Neutral (0)

5.2.4 Flammability and Health Risk

The results of both the flammability and health risk analysis are combined in one section, as they are both based on the so-called National Fire Protection Association (NFPA) Diamond. This diamond provides information on the health risks, flammability, and instability/reactivity of a material by assigning a numerical rating between 0 and 4 to each category. A rating of 0 represents minimal hazards and/or risks, whereas a rating of 4 indicates that there are significant hazards and/or risks. An example of an NFPA diamond is shown in Figure 5.9 [46]. NFPA ratings for each propellant are provided in Table 5.6.

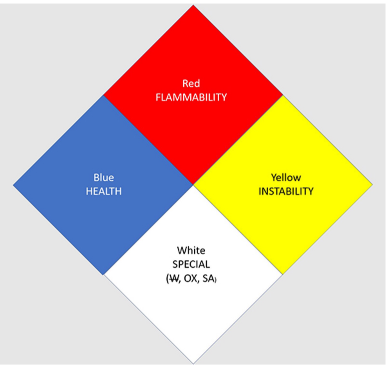

Figure 5.9: An example of a NFPA diamond [46].

Table 5.6: NFPA ratings for each propellant.

Propellant	**Health Risk**	**Flammability**	**Instability/Reactivity**
Water	0	0	0
Ammonia [47]	3	1	0
Butane [48]	1	4	0
R134a [49]	2	1	0
R236fa [50]	1	0	1

The associated evaluation scores for the following NFPA ratings are as follows: a rating of 0 and 1 corresponds to a "positive" score, a rating of 2 corresponds to a "neutral" score, and a rating of 3 and 4 corresponds to a "negative" score. The outcome of this evaluation is provided in Table 5.7.

Table 5.7: Propellant evaluation based on their flammability and health risk.

Propellant	**Water**	**Ammonia**	**Butane**	**R134a**	**R236fa**
Flammability	Positive (+1)	Positive (+1)	Negative (-1)	Positive (+1)	Positive (+1)
Health Risk	Positive (+1)	Negative (-1)	Positive (+1)	Neutral (0)	Positive (+1)

5.3 Trade-off Outcome and Sensitivity Analysis

This section presents the outcome of the trade-off in Subsection 5.3.1, and is followed by a sensitivity analysis in Subsection 5.3.2.

5.3.1 Trade-off Outcome

Now, the propellant evaluations for each trade-off category are combined into one table, and a weighted score is computed for each propellant, as illustrated in Table 5.8.

Table 5.8: Propellant evaluation outcome.

Propellant	Water	Ammonia	Butane	R134a	R236fa
System Density	0	-1	-1	1	1
Performance	1	1	0	0	0
Flammability	1	1	-1	1	1
Health Risk	1	-1	1	0	1
Weighted Score	11	-0.6	-3.4	6.8	10.2

Weight Factor
4.8
5.6
2.0
3.4

Water wins the trade-off with a weighted score of 11, followed closely by R236fa. The variance in performance and system density, along with the differences in weight factors, contributed to this outcome. The small difference in the weighted scores of both water and R236fa suggests that both propellants can be seen as winners, as a slight variation in either the criteria weights, or the assigned criteria scores could result in R236fa gaining the edge in the trade-off. A sensitivity analysis is performed on this trade-off to investigate the effects of changing both the weights and assigned scores.

5.3.2 Sensitivity Analysis

A sensitivity analysis is performed to ensure the robustness of the trade-off. The outcome of the trade-off is affected by both the trade-off weight factors, and the assigned scores for each trade-off criterion. Small variations in both the weight factors and scores could lead to a drastic change in the outcome of the trade-off and suggests that the trade-off is flawed. This sensitivity analysis verifies the robustness of the trade-off by varying both the assigned trade-off weight factors, and the trade-off scores.

The trade-off weight factors are determined by averaging the input from several participants. This resulted in an average weight factor and a standard deviation. Now, the trade-off weight factor for each criterion is split into three: the average weight minus one standard deviation, the average weight, and the average weight plus one standard deviation. These three weight factors for each criterion are then combined with the other trade-off criteria that have also been split into three parts. This results into 81 unique trade-off weight vectors, as shown in Table 5.9, that can be used in the sensitivity analysis. It must be noted that the maximum allowable weight factor is 6, and that any weight factor above this value is rounded down to 6.

Table 5.9: Possible variations for the trade-off weight vectors.

Criterion	Weight Vector 1	Weight Vector 2	Weight Vector 3	Weight Vector ...	Weight Vector 81
System Density	$\overline{WF}$ - σ	$\overline{WF}$	$\overline{WF}$ + σ	...	$\overline{WF}$ + σ
Performance	$\overline{WF}$ - σ	$\overline{WF}$ - σ	$\overline{WF}$ - σ	...	$\overline{WF}$ + σ
Flammability	$\overline{WF}$ - σ	$\overline{WF}$ - σ	$\overline{WF}$ - σ	...	$\overline{WF}$ + σ
Health Risk	$\overline{WF}$ - σ	$\overline{WF}$ - σ	$\overline{WF}$ - σ	...	$\overline{WF}$ + σ

The assigned trade-off scores can also be varied slightly. The reason for doing this is that there are only three possible scores: a positive, neutral, or negative score. Assigning such scores to represent values like propellant density, performance, flammability, and health risk leaves room for interpretation that can result in an incorrect trade-off result. The following changes in the assigned scores are proposed.

The propellant densities at storage conditions are initially split into three groups, where the two best performing propellant (R134a and R236fa) received a positive score, the two worst performing propellants (ammonia and butane) received a negative score, and the one in the middle (water) received a neutral score. However, one could argue that both R134a and R236fa should receive a neutral score, as they are in the liquid state under these storage conditions. As a result of this increase, the initial neutral score of water can be raised to a positive score, as water is closer in density to R134a and R236fa than to ammonia and butane. Additionally, water is also liquid at low storage pressures, which allows for a more compact system at these lower pressures.

The performance is initially split into two groups, where both water and ammonia received a positive score, and the remaining propellant received a neutral score. An argument can be made that ammonia should receive a neutral score, as the achievable impulse per volume of propellant is comparable to that of R134a, R236fa, and butane.

Both the flammability and health risk are split into three groups based on the NFPA ratings. Initially a rating of 0 and 1 received a positive score, a rating of 2 received a neutral score, and a rating of 3 and 4 received a negative score. However, one can argue that only propellants with a NFPA rating of 0 should receive a positive score as any score higher than this has actual flammability and health concerns. A NFPA rating of 1 would then receive a neutral score.

Now that both the variation in trade-off weight factors and assigned scores are explain, the sensitivity analysis can be performed. The 81 unique weight factor vectors are applied to first the original trade-off scores which results in 81 trade-off outcomes. Next, only one of the trade-off category scores is varied at a time whereas the remaining trade-off scores keep their original values. This is done to investigate the sensitivity of the trade-off outcome to changing the scores of one trade-off criteria at a time. Finally, the trade-off is performed when all the criteria scores are changed to their new values. The outcome of this sensitivity analysis is shown in Table 5.10.

Table 5.10: Frequency of propellant wins in sensitivity analysis.

Propellant	**Original Scores**	**New Density Scores**	**New Performance Scores**	**New Flammability Scores**	**New Health Risk Scores**	**All New Scores**	**Total Wins**
Water	63	81	63	63	81	81	432
Ammonia	0	0	0	0	0	0	0
Butane	0	0	0	0	0	0	0
R134a	0	0	0	0	0	0	0
R236fa	18	0	18	18	0	0	54
Total	81	81	81	81	81	81	486

Water wins the trade-off 432 out of 486 times, whereas R236fa wins the remaining 54 trade-offs. R236fa takes second place when water wins the trade-off. The average difference between the weighted scores is approximately 4 in this case. Furthermore, water takes second place when R236fa wins the trade-off. The average difference between their weighted scores is only 0.58 which shows that R236fa barely wins these trade-offs.

The combination of both the frequency which water wins the trade-offs in this sensitivity analysis and the small difference in weighted trade-off scores between water and R236fa when R236fa wins indicates that water is the winner of the trade-off. Furthermore, it also shows the robustness of the trade-off method and outcome.

5.4 Conclusion

This chapter outlined the trade-off between five propellants that can be used in a VLM propulsion system. The trade-off was based on four trade-off criteria, namely the system density, the performance, the flammability of the propellant, and the health risk. Each criterion was assigned a weight between 1 (least significant) and 6 (most significant), derived from input provided by a professor and four students. The performance of each propellant for the four criteria was evaluated and scored. These scores were then multiplied by the averaged weight for each criterion and summed up. The propellant with the highest weighted score emerged as the winner of the trade-off.

A sensitivity analysis was performed to verify the robustness of the trade-off, and the validity of the outcome. The trade-off weights were varied within one standard deviation from the mean which resulted in 81 unique trade-off weight vectors. Furthermore, the assigned scores for each propellant in the different trade-off categories were varied slightly. The trade-off was performed, using the 81 unique weight vectors, whilst changing only one of the trade-off category scores at a time. Furthermore, the trade-off was performed, using the 81 unique weight vectors, whilst using the original scores, and whilst all the trade-off category scores were changed. Water won 432 out of the 486 trade-offs, whereas R236fa won the remaining 51 trade-offs. Furthermore, when water won the trade-off, the runner up was R236fa, and when R236fa won, water came in second. The average difference in weighted scores between the first and second place when water won the trade-off is approximately 4 which indicated that water won by a large margin in these cases. This difference in weighted scores was only 0.58 when R236fa won, which showed that even if R236fa won, it did so by only a small margin.

In summary, water emerges as the most favourable propellant for use in the VLM propulsion system. It not only outperformed other propellants by a significant margin in most trade-offs but also consistently ranked as a very close second when R236fa won the trade-off. With the propellant now identified, requirement *PROP-FUNC-01* can be updated accordingly: "The propulsion system shall use **water** as a propellant."

Feed System Trade-off

6

This chapter outlines the trade-off between a blow-down feed system, a pressure regulated feed system, and a hybrid feed system. First, the performance of the thruster is summarized in Section 6.1, followed by the types of feed systems and pressurants in Section 6.2. Next, the trade-off methodology and results are described in Section 6.3 and Section 6.4 respectively. The winner of the trade-off is determined in Section 6.5, where-after the assumption of isothermal expansion is verified in Section 6.6. The chapter is concluded in Section 6.7, whereas a recommendation for future work is described in Section 6.8.

6.1 Propellant Performance

The propellant used in the design of the VLM thruster is water, as it won the trade-off as described in Chapter 5. Information on the performance of the propellant as function of the chamber pressure is required to design the propulsion system, as the performance of the propellant influences the required mass and volume budgets of both the propellant and, when using a pressurized feed system, pressurant.

The ideal performance of the propellant as a function of the chamber pressure is calculated using the equations from Subsection 5.1.2. The outcome of this analysis is summarized in the following figures, where the relationships between thrust (Figure 6.1a), mass flow rate (Figure 6.1b), specific impulse (Figure 6.2a), required heating power (Figure 6.2b), and the chamber pressure can be seen. Furthermore, the propellant density as a function of the chamber pressure, at a constant (storage) temperature of 293.15 K, can be found in Figure 6.3.

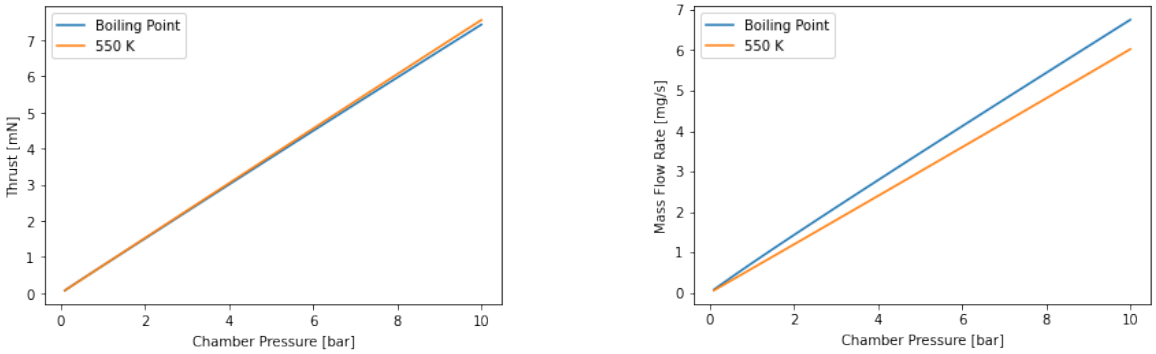

(a) Achievable thrust levels as function of chamber pressure.

(b) Achievable mass flow rates as function of chamber pressure.

Figure 6.1: Thruster performance figures.

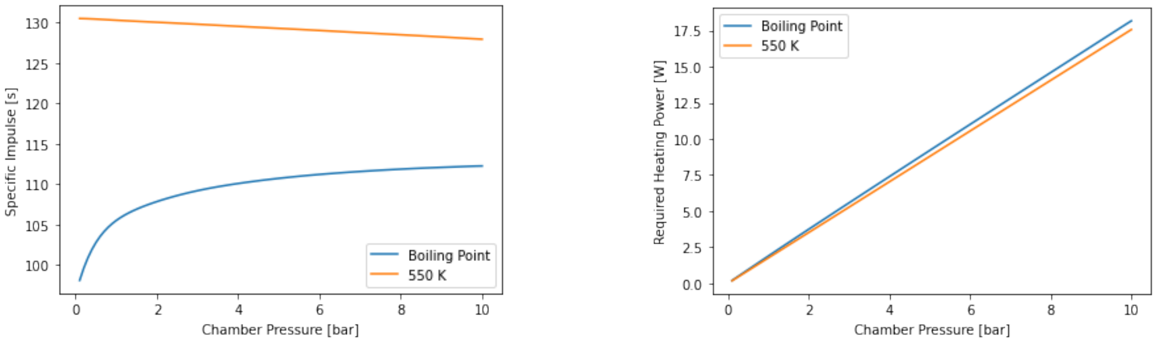

(a) Achievable specific impulse as function of chamber pressure.

(b) Required heating power as function of chamber pressure.

Figure 6.2: Thruster performance figures.

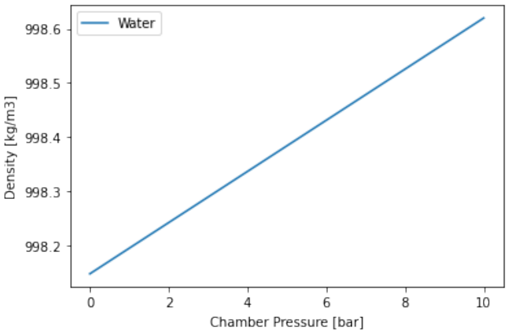

Figure 6.3: Propellant density as function of chamber pressure.

6.2 Feed System Types and Pressurants

The propellant feed system guides propellant from the propellant tank to the thruster at the required rate. There are two principal types of feed system, namely pressurized systems, and pump-fed systems [51]. Simplified schematics of all feed system types can be found in Figure 6.4.

6.2.1 Blow-Down

The pressurized systems consist of both a blow-down system, and a pressure regulated system. The pressurant in a blow-down system is stored in the propellant tank and is separated from the propellant by a membrane. This ensures that the pressurant gas cannot dissolve in the propellant, and that the pressurant gas stays within the propellant tank. The physical separation of the pressurant and propellant requires a separate fill/drain valve for both substances. The pressure in the tank drops as propellant leaves the tank. This results in a decrease of the systems performance, as the mass flow rate decreases with a decrease in pressure [51].

6.2.2 Pressure Regulated

The pressurant in a pressure regulated system is stored in a separate tank at pressures up to several hundred bar. A pressure regulated, located between the pressurant tank, and propellant tank, ensures a constant pressure in the propellant tank. This constant propellant tank pressure allows for a stable performance of the system: the mass flow rate and thrust are constant throughout the mission duration [51].

6.2.3 Hybrid Feed System

The hybrid feed system is a combination of the blow-down feed system, and the pressure regulated system. Both the propellant and pressurant are stored in one tank, separated by a membrane as is done for a blow-down system. However, there is a pressure regulator, located between the propellant tank and thrust chamber, which ensures that the propellant enters the chamber at a constant pressure and with a constant mass flow rate. This results in a system that produces a constant thrust level throughout the mission duration.

6.2.4 Pump-Fed

Pump-fed systems use, as the name suggest, a pump to move propellant from the propellant tank to the thruster. The propellant tanks can be pressurized slightly to prevent cavitation in the pump, and to support the propellant tank walls. The pump requires a separate energy source for it to function. The pump-fed system is not considered in this thesis, as it is deemed too complex for use in a CubeSat propulsion system [51][5].

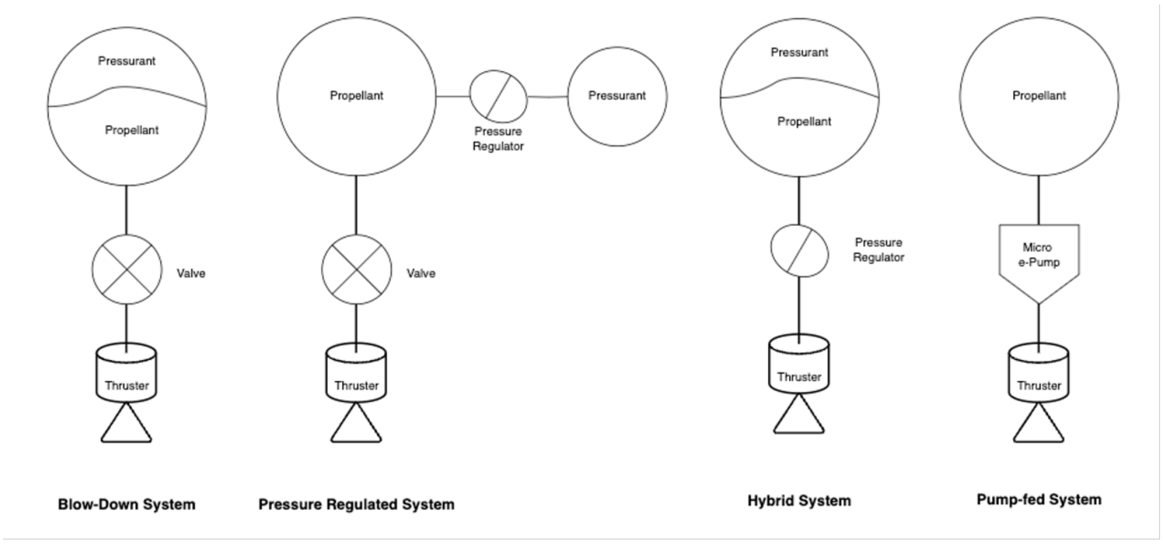

Figure 6.4: Feed system types (inspired by [51][52]).

6.3 Trade-off Methodology

This section outlines the trade-off methodology, starting at the assumptions made. This is followed by the overall trade-off strategy, and trade-off criteria.

6.3.1 Assumptions

Several assumptions are made in this trade-off. First, it is assumed that the temperature of the propellant in the chamber is at the boiling point for each chamber pressure value. This results in conservative values for the systems performance, as both the thrust and specific impulse for each chamber pressure are the smallest for each chamber pressure, and both the mass flow rate and required heating power are the largest for each chamber pressure.

Second, it is assumed that there are no pressure losses between the propellant tank and the thrust chamber. This assumption is made, as the pressure losses tend to be small in micro-propulsion systems, and information on the piping is unavailable at this point. Furthermore, any existing pressure losses over the piping can easily be added to the tank pressures when the piping is designed.

Finally, it is assumed that the expansion of the pressurant is isothermal at a tank temperature of 293.15 K. This assumption is made, as the mass flow rate of the propellant is small (Figure 6.1b). The small mass flow rate results in a slow expansion of the pressurant during which heat can be exchanged with the environment.

6.3.2 Trade-off Methodology

The trade-off between the blow-down, pressure regulated, and hybrid feed system is performed for a test case in which the propulsion system must deliver a total impulse of 200 Ns: the smallest system that is to be designed in this thesis.

The winner of the trade-off is the feed system type that performs best in the following four trade-off categories: performance, mass, volume, and reliability, whilst adhering to the requirements posed in Section 4.2.

The following requirements must be met:

- *PROP-SYST-2*: "The total size of the propulsion system shall be within 0.5 U."
- *PROP-SYST-3*: "The total wet mass of the propulsion system at launch shall not exceed 0.7 kg."
- *PROP-SYST-4*: "The power consumption of the propulsion system shall not exceed 25 W."
- *PROP-PERF-2*: "The propulsion system shall deliver a maximum thrust of 5.7 mN."
- *PROP-PERF-3*: "The propulsion system shall deliver a minimum thrust of 0.5 mN."
- *PROP-RAMS-1*: "The pressure within the propulsion system shall not exceed 10 bar."

6.3.3 Trade-off Criteria

Performance

The performance criterion reflects the achievable thrust levels of all three feed system types, where the best performing feed system is the one that delivers the largest thrust levels. Higher thrust is regarded as an indicator of better performance because it allows for faster manoeuvres and more effective orbit adjustments. The fundamental difference between the blow-down system and the pressure regulated systems is that the thrust in blow-down systems drops as propellant is expelled whereas the thrust remains constant in a pressure regulated system.

Blow-Down Feed System
The achievable thrust levels for the blow-down system are calculated as a function of the ratio of the final tank pressure over the initial tank pressure. The final tank pressure is fixed at 0.65 bar to comply with the requirement on the minimum thrust of 0.5 mN, whereas the initial tank pressure is varied between 0.65 bar and 7.64 bar. The 7.64 bar is again chosen to comply with the requirement on the maximum thrust of 5.7 mN.

Pressure Regulated Feed System
The achievable thrust levels for the pressure regulated system are calculated as a function of the ratio of the final pressurant tank pressure over the initial pressurant tank pressure. Furthermore, a pressure factor of 2 between the final pressurant tank pressure and the propellant tank pressure is used. This pressure differential between both tanks is required for the pressure regulator to function properly [51]. The initial pressurant tank pressure is fixed at 10 bar to comply with the requirement on the maximum allowable pressure within the propulsion system, whereas the final tank pressure is varied between 1.3 and 10 bar. The final tank pressure cannot drop below 1.3 bar, as a minimum of 0.65 bar (1.3/2) is required in the propellant tank to comply with the minimum thrust requirement. Unlike the blow-down system, the initial tank pressure of 10 bar will satisfy the maximum thrust requirement, as the pressure factor of 2 limits the maximum tank pressure to 5 bar.

Hybrid Feed System
The achievable thrust levels for the hybrid feed system are calculated as a function of the ratio of the initial tank pressure over the final tank pressure. As with the pressure regulated system, a pressure factor of 2 is applied between the final tank pressure, and the thrust chamber pressure to ensure proper functioning of the pressure regulator. The initial tank pressure is fixed at 10 bar to comply with the requirement on the maximum allowable pressure within the propulsion system, whereas the final tank pressure is again varied between 1.3 and 10 bar. The pressures of 1.3 and 10 bar are selected for the same reasons as in the pressure regulated system.

Mass

The mass criterion reflects the required propellant and pressurant mass for each of the feed system types, where the best performing feed system is the one that requires the least amount of fluid mass to achieve the total impulse of 200 Ns.

Blow-Down Feed System
An iterative calculation is to be applied for the blow-down feed system, as the thrust and mass flow rate drop with the decrease in propellant tank pressure. This decrease in performance results in a decreased impulse bit per iteration and, as a result, an increase in required propellant and pressurant mass per iteration. This iterative approach is visualized in Figure 6.5.

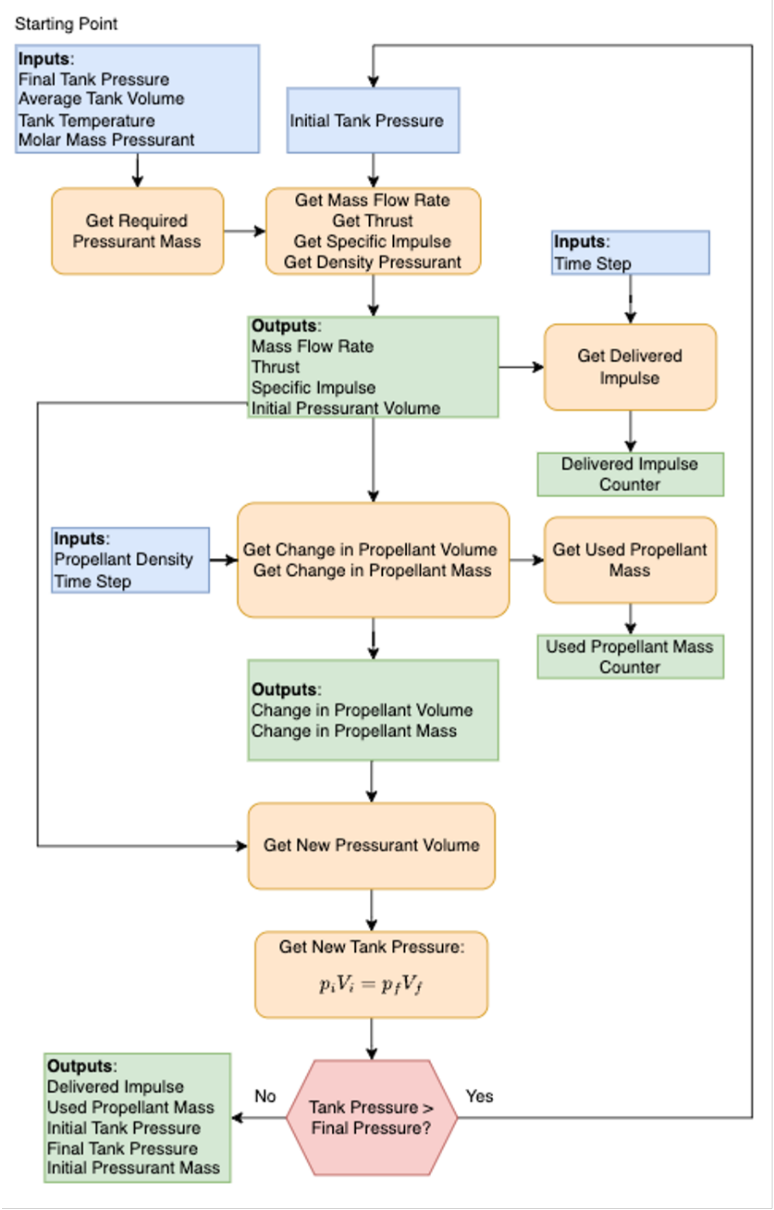

Figure 6.5: Iterative program loop that calculates the required propellant and pressurant mass for a blow-down system.

The final tank pressure, the tank volume, the constant tank temperature, and the molar mass of the pressurant are the starting point of the calculation. The required pressurant mass can now be calculated using Equation 6.1,

$$M_{pres} = \frac{p_{tank_f} \cdot V_{tank}}{R_{pres} \cdot T_{tank}} \tag{6.1}$$

where p_{tank_f} is the final tank pressure of 0.65 bar, V_{tank} is the tank volume, R_{pres} is the gas constant of the pressurant, and T_{tank} is the temperature in the tank [51]. The final tank pressure of 0.65 bar is chosen, as this delivers the minimum required thrust level of 0.5 mN.

The next input is the initial tank pressure. This pressure ranges between the aforementioned 7.64 bar and 0.65 bar and is used to determine the instantaneous mass flow rate, thrust, specific impulse, density of the pressurant, and the volume that the pressurant occupies by using the figures from Section 6.1.

The impulse bit per iteration can be calculated by multiplying the instantaneous thrust by the time step per iteration, in this case 10 seconds. This impulse bit is added to the so-called 'Delivered Impulse Counter,' and keeps track of the total delivered impulse. The decrease in the propellant mass can be calculated by multiplying the instantaneous mass flow rate with the time step per iteration. The decrease in mass is added to the so-call "Used Propellant Mass Counter," which keeps track of the total required propellant mass. Furthermore, the decrease in propellant volume can be calculated by dividing the decrease in propellant mass by the density of the propellant at the current tank pressure.

Now, the volume that was previously occupied by the propellant is now filled by the pressurant. This increase in pressurant volume results in a decrease in the overall tank pressure, and can be calculated using Equation 6.2,

$$V_{pres_f} = V_{pres_i} \cdot \frac{p_{tank_i}}{p_{tank_f}} \tag{6.2}$$

where p_{tank_i} in the initial tank pressure, V_{pres_i} is the initial pressurant volume, and V_{pres_f} is the final tank pressure (or the new instantaneous pressure in the tank).

This new tank pressure is compared with the final tank pressure of 0.65 bar. The tank pressure is updated to this new tank pressure when it is larger than 0.65 bar and the loop is repeated until the new tank pressure is equal to the desired final tank pressure. The outputs of this iterative loop are the total delivered impulse, the required propellant mass, the initial tank pressure, the final tank pressure, and the initial pressurant mass.

One problem that arises with this method is that the loop must be performed for each initial tank pressure between 0.65 and 7.64 bar, and for each propellant tank volume within a set range. The total delivered impulse varies for each propellant tank volume and must equal the required total impulse of 200 Ns. Now, rather than looping over all possible propellant tank volumes within a range, the following approach is used and summarized in Figure 6.6.

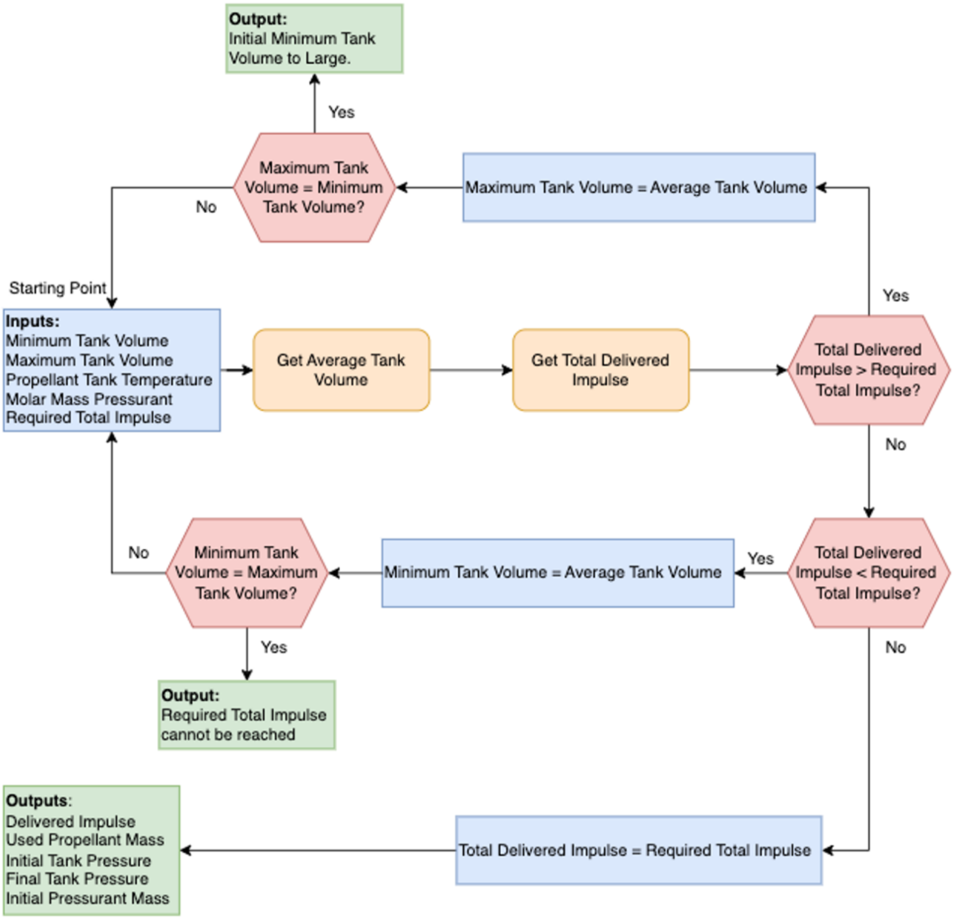

Figure 6.6: Iterative program loop that calculates the required propellant and pressurant mass for a blow-down whilst varying the tank volume.

A minimum tank volume and maximum tank volume are used as inputs for the iterative loop. These volumes are set to 0 and 2.5 dm^3 respectively as an initial guess. The average of these two tank volumes is used as an input in the “Get Total Delivered Impulse” function that is described above, combined with the propellant tank temperature, molar mass of the pressurant, and the total required impulse.

The calculated delivered impulse for the specific average tank volume is compared with the required total impulse. The initial estimate on the propellant tank is too large when the delivered impulse is larger than the required impulse, and the initial guess on the maximum tank volume is replaced by the value of the average tank volume. Next, a check is performed to ensure that the maximum tank volume is not equal to the minimum tank volume. In theory, this should not be possible, as the delivered impulse is larger than the required impulse, hence the minimum tank volume would not have been updated throughout the iterative loop. When the new maximum tank volume is not equal to the minimum tank volume, the loop is repeated, and a new (and smaller) average tank volume is used.

The average tank volume is too small, or the required total impulse is reached when the calculated total delivered impulse is not larger than the required total impulse. The minimum tank volume is set to the average tank volume when the total delivered impulse is smaller than the required impulse, as a larger average tank volume is required to reach the desired total impulse. Next, a check is performed to ensure that the minimum tank volume is equal to the maximum tank volume. The initial guess on the maximum tank volume is not able to deliver the required total impulse when this situation occurs. The loop is repeated with the larger average tank volume when the minimum tank volume is not equal to the maximum tank volume.

The required total impulse is reached when the total delivered impulse is not larger, and not smaller, than the required total impulse. The outputs of this iterative loop are the total delivered impulse, the required propellant mass, the initial tank pressure, the final tank pressure, and the initial pressurant mass.

Pressure Regulated Feed System

Determining the required propellant and pressurant mass for a pressure regulated system does not require an iterative calculation, as the pressure within the propellant tank remains constant throughout the mission duration. The method of calculating the required propellant and pressurant mass is visualized in Figure 6.7.

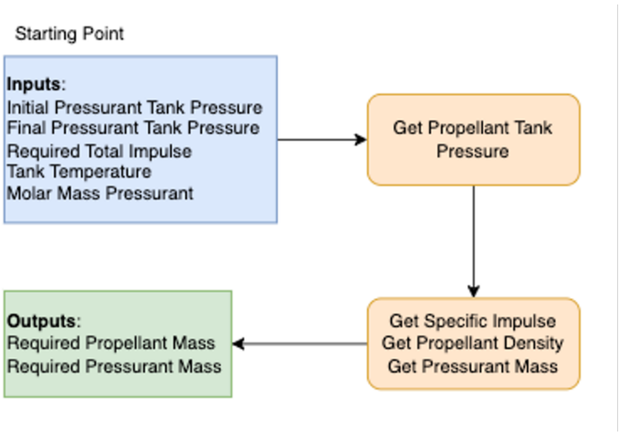

Figure 6.7: Program loop that calculates the required propellant and pressurant mass for a pressure regulated system.

The initial pressurant tank pressure, the final pressurant tank pressure, the required total impulse, the constant tank temperature (of both the pressurant tank and propellant tank), and the molar mass of the pressurants are the starting point of the calculation. The initial pressurant tank pressure is fixed at 10 bar, as this is the maximum allowable pressure within the propulsion system, whereas the final pressurant tank pressure is varied between 1.3 and 10 bar. The propellant tank pressure is calculated by dividing the final pressurant tank pressure by a factor 2. This pressure factor of 2 is necessary to ensure the proper functioning of the pressure regulator that is located between the pressurant tank and the propellant tank.

Next, the specific impulse and propellant density are determined for the given propellant tank pressure by using the relationships that are visualized in Section 6.1. The required propellant mass can be calculated by using Equation 6.3,

$$M_p = \frac{I_{tot}}{g_0 \cdot I_{sp}} \tag{6.3}$$

where I_{tot} is the required total impulse, I_{sp} is the specific impulse, and g_0 is the gravitational acceleration at sea level. Finally, the required pressurant mass can be calculated by using Equation 6.4,

$$M_{pres} = \frac{p_{tank} \cdot V_{tank}}{R_{pres} \cdot T_{tank}} \cdot \left[\frac{1}{1 - \frac{p_{pres_f}}{p_{pres_i}}} \right] \tag{6.4}$$

where p_{tank} is the pressure in the propellant tank, V_{tank} is the propellant tank volume, R_{pres} is the gas constant of the pressurant, T_{tank} is the constant propellant tank temperature, p_{pres_f} is the final pressurant tank pressure, and p_{pres_i} is the initial pressurant tank pressure [51].

Hybrid Feed System

As for the pressure regulated feed system, determining the required propellant and pressurant mass for the hybrid system does not require an iterative calculation. The pressure regulated ensures that the pressure in the thrust chamber remains constant throughout the operational lifetime of the propulsion system. The method of calculating the required propellant and pressurant mass is visualized in Figure 6.8.

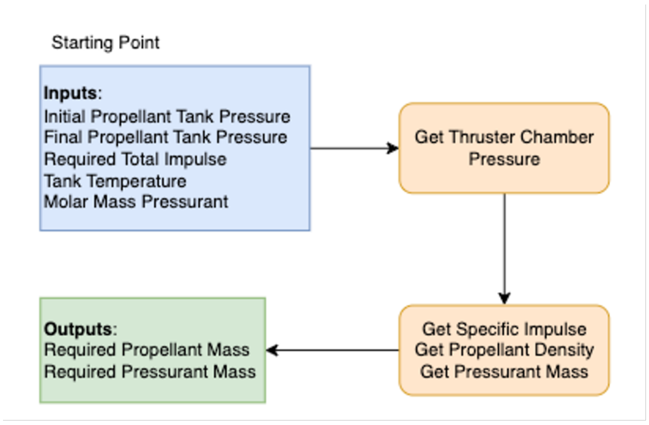

Figure 6.8: Program loop that calculates the required propellant and pressurant mass for a hybrid system.

The initial and final propellant tank pressure, the required total impulse, the constant tank temperature, and the molar mass of the pressurants are the inputs for the calculation. The initial tank pressure is fixed at 10 bar, like the pressure regulated system, whereas the final pressurant tank pressure is varied between 1.3 and 10 bar. First, the thruster chamber pressure is calculated by dividing the final propellant tank pressure by a factor of 2. As previously explained, this factor of 2 is necessary to ensure the proper functioning of the pressure regulator.

Next, the propellant and pressurant densities are determined at the storage conditions (10 bar and 293.15 K). Furthermore the specific impulse is determined by using the relationship that is visualized in Figure 6.2a. Now, the required propellant mass can be calculated by using Equation 6.3, as was done for the pressure regulated system.

Finally, the required pressurant mass can be calculated by using Equation 6.1, as was done for the blow-down system. However, this equation must be rewritten as the tank volume is not known in advance. The derivation of the required pressurant mass is shown in Equation 6.5,

$$
\begin{aligned}
M_{pres} = \rho_{pres_i} \cdot V_{pres_i} &= \frac{p_{tank_f} \cdot V_{tank}}{R_{pres} \cdot T_{tank}} \\
\rho_{pres_i} \cdot V_{pres_i} &= \frac{p_{tank_f} \cdot (V_p + V_{pres_i})}{R_{pres} \cdot T_{tank}} \\
\left(\rho_{pres_i} - \frac{p_{tank_f}}{R_{pres} \cdot T_{tank}} \right) \cdot V_{pres_i} &= \frac{p_{tank_f} \cdot V_p}{R_{pres} \cdot T_{tank}} \\
V_{pres_i} &= \frac{p_{tank_f} \cdot V_p}{\rho_{pres_i} \cdot R_{pres} \cdot T_{tank} - p_{tank_f}} \\
M_{pres} = \rho_{pres_i} \cdot V_{pres_i} &= \frac{\rho_{pres_i} \cdot p_{tank_f} \cdot V_p}{\rho_{pres_i} \cdot R_{pres} \cdot T_{tank} - p_{tank_f}}
\end{aligned}
\tag{6.5}
$$

where ρ_{pres_i} is the initial pressurant volume at storage conditions (10 bar and 293.15 K), and V_p is the required propellant volume which can be obtained from the required propellant mass that is calculated in the previous step.

Volume

The volume criterion reflects the required propellant and pressurant volume for each of the feed system types, where the best performing feed system is the one that requires the least amount of fluid volume to achieve the desired total delivered impulse of 200 Ns.

Blow-Down Feed System

The required propellant and pressurant volume for the blow-down feed system can be calculated by using the calculated propellant and pressurant masses from the mass trade-off criterion. The required propellant volume can be calculated by dividing the propellant mass by the density of the propellant at the initial tank pressure that is used in the iterative loop described in the previous section. The same can be done for the pressurant by dividing the required pressurant mass by its density at these storage conditions.

Pressure Regulated Feed System
The required propellant and pressurant volume for the pressure regulated system can also be calculated by using the calculated propellant and pressurant masses from the mass trade-off criterion. The required propellant volume can be calculated by dividing the required propellant mass by the density of the propellant at tank pressure that is used in calculating the required propellant and pressurant mass. The required pressurant volume can be calculated by dividing the required pressurant mass by its density at the initial pressurant tank pressure of 10 bar, and tank temperature of 293.15 K.

Hybrid Feed System
The propellant and pressurant volume for the hybrid feed system can be calculated by dividing the required propellant and pressurant mass, obtained in the mass criterion, by their respective densities at the storage conditions: an initial propellant tank pressure of 10 bar, and at a constant tank temperature of 293.15 K.

Reliability

The reliability of the feed system types is compared by quantifying the difference in required propulsion system components. The link between the reliability of the system, and the number of components can be found in Equation 6.6,

$$R = e^{-t_m \cdot \sum_{n=0}^{i} \lambda_i} \tag{6.6}$$

where λ_i is the failure rate of each individual component, and t_m is the mission duration in years [53]. Feed system types with a high reliability are preferred.

A failure rate of 1 in 1000 per component per year (or 0.001) is assumed for each component, as failure rates for individual propulsion system components are difficult to find. This value is equal to double the typical failure rate of an entire spacecraft (equal to $5 \cdot 10^{-4}$ failures per year [51, p. 341]), and is considered as conservative, as a spacecraft consists of many parts. Furthermore, a mission duration of 5 years is assumed.

6.4 Trade-off Results

This section outlines the results that are obtained by following the methodology as described in the previous section. First, the performance criterion will be discussed, followed by the fluid mass, volume, and system reliability.

6.4.1 Performance

The achievable thrust levels are plotted in Figure 6.9a and Figure 6.9b for the blow-down, pressure regulated, and hybrid feed system.

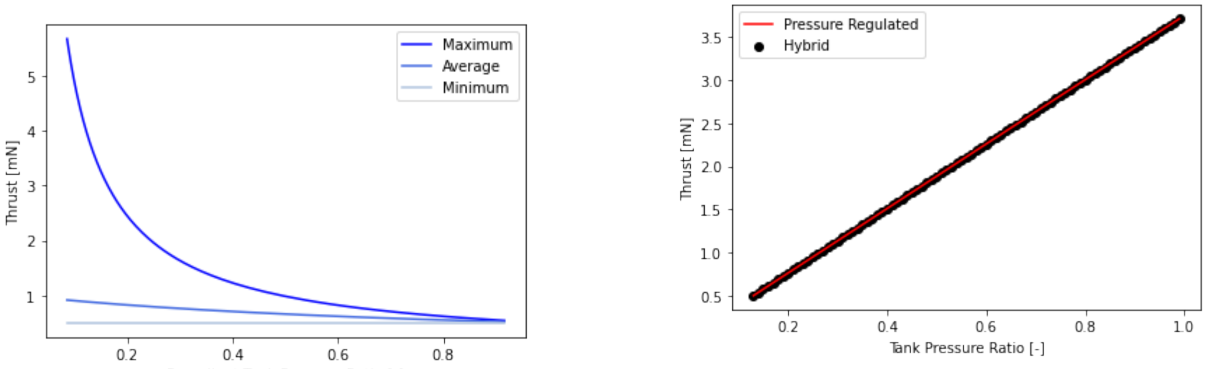

(a) Achievable thrust levels as a function of the propellant tank pressure ratio for the blow-down feed system.

(b) Achievable thrust level as a function of the pressurant tank pressure ratio for both the pressure regulated and hybrid feed system.

Figure 6.9: Thrust as a function of the tank pressure ratio.

Blow-Down Feed System
The achievable thrust levels for the blow-down system are plotted (in Figure 6.9a) as a function of the propellant tank pressure ratio: the ratio of the final propellant tank pressure over the initial propellant tank pressure. The final propellant tank pressure is fixed at 0.65 bar, as this ensures the lower bound achievable thrust of 0.5 mN. The initial tank pressure is varied between 0.65 and 7.64 bar. The latter is the maximum allowable pressure in the tank, as this delivers the upper bound thrust requirement of 5.7 mN. The figure includes the maximum achievable thrust, the average thrust, and the

minimum achievable thrust. The maximum achievable thrust is reached at the initial propellant tank pressure, whereas the minimum achievable thrust is reached at the final tank pressure of 0.65 bar. The average thrust represents the thrust provided on average throughout the mission duration for each propellant tank pressure ratio. The achievable thrust levels decrease with an increase in the pressure ratio. This can be explained when looking at Figure 6.1a, where a decrease in achievable thrust is shown as the chamber pressure drops. The maximum achievable thrust level is equal to the minimum achievable thrust level when the pressure ratio is equal to 1. As expected, the maximum achievable thrust levels occur at the smallest pressure ratio when the initial tank pressure is at the maximum allowable pressure of 7.64 bar, and the final tank pressure is set to 0.65 bar. A maximum thrust of 5.7 mN, an average thrust of 0.91 mN, and a minimum thrust of 0.5 mN is reached at this pressure ratio. The average thrust is noticeably lower than the maximum achievable thrust, which can be attributed to the rapid decrease in thrust early in the propulsion system's life cycle. This rapid drop in thrust is illustrated in Figure 6.10, where the thrust level is plotted against the burn duration for an initial tank pressure of 7.64 bar and a final tank pressure of 0.65 bar.

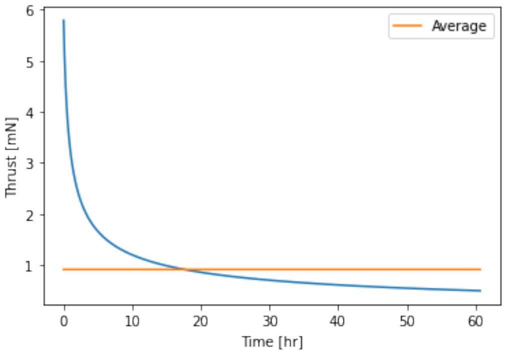

Figure 6.10: Achievable thrust as a function of the burn time for a propellant tank pressure ratio of 0.085.

Pressure Regulated Feed System
The achievable thrust levels for the pressure regulated system are plotted (in Figure 6.9b) as a function of the pressurant tank pressure ratio: the ratio between the final pressurant tank pressure over the initial pressurant tank pressure. The initial pressurant tank pressure ratio is fixed at 10 bar, as this is the maximum allowable pressure within the propulsion system, whereas the final pressurant tank pressure is varied between 1.3 and 10 bar. The pressure in the propellant tank is a factor 2 lower than the final pressure in the pressurant tank to ensure the proper functioning of the pressure regulator. It can be seen that the thrust increases linearly with an increase in the pressurant tank pressure ratio. This relationship can be explained when looking again at Figure 6.1a, where an increase in pressure results in an increased thrust. An increase in the pressurant tank pressure ratio results in an a larger final pressurant tank pressure and, as a result of this, a larger propellant tank pressure and achievable thrust. The maximum achievable thrust of 3.75 mN is reached at a final pressurant tank pressure of 10 bar, or a propellant tank pressure of 5 bar. However, one must realise that this value cannot be reached, as the initial and final pressurant tank pressure are equal. There is no pressure drop possible within the pressurant tank in this specific instant, so the required volume of pressurant will increase significantly as will be shown in Subsection 6.4.3.

Hybrid Feed System
The achievable thrust levels for the hybrid feed system are plotted (in Figure 6.9b) as a function of the propellant tank pressure ratio: the ratio between the final and initial propellant tank pressure. The initial propellant tank pressure is fixed at 10 bar, whereas the final propellant tank pressure is varied between 1.3 and 10 bar. The pressure regulator, now located in between the propellant tank and thrust chamber, requires a pressure drop of a factor of 2 between the final tank pressure and constant chamber pressure to function properly. The achievable thrust level increases linearly as the pressure ratio rises. This behaviour is also seen and explained for the pressure regulated system. As with the pressure regulated system, a theoretical maximum thrust level of 3.75 mN can be achieved as the pressure ratio approaches a value of 1: the initial and final tank pressure are equal. This ratio cannot be reached in practise as the situation remains static. However, a final pressure very close to the initial tank pressure is possible if the required pressurant mass and volume remain within the mass and volume budgets.

6.4.2 Mass

Verification of the Iterative Blow-Down Calculation

The iterative calculation for the blow-down feed system is verified first, to ensure that the results shown in this section are correct and allow for a comparison between the two feed system types.

Table 6.1: Thruster performance as estimated by the ideal rocket theory [54].

Parameter	**Value**	**Unit**
Thrust	2.5 - 0.5	mN
Mass Flow Rate	1.9 - 0.4	mg/s
Pressure	5 - 1	bar
Required Total Impulse	64.8	Ns
Propellant Mass	0.050	kg

Table 6.1 shows the thruster performance of a blow-down system as estimated by ideal rocket theory [54]. The thrust, pressure, and mass flow rate have an upper and lower-bound value. It is assumed that both the mass flow rate and thrust decrease linearly with the decrease in pressure, as this linear relationship was found in Section 6.1. These linear relationships, combined with the initial tank pressure of 5 bar, and final tank pressure of 1 bar, are used as input in the iterative loop. The propellant tank volume is varied until the desired total impulse of 64.8 Ns was reached, which occurred at a required propellant tank volume of 63.3 cm^3. Furthermore, a propellant mass of approximately 50 grams is required to achieve this total impulse, and is in line with the stated required propellant mass in Table 6.1.

Required fluid mass as a function of the pressure ratio

As with the achievable thrust levels for the three feed system types, the required pressurant and propellant mass is plotted as a function of the pressure ratios. The results of the calculations, whilst using both helium and nitrogen as pressurants, are shown in Figure 6.11, Figure 6.12, and Figure 6.13 for the blow-down, pressure regulated, and hybrid feed system respectively. The achievable thrust levels are also included in the graphs to allow for determining the achievable performance in case of a mass budget limitation.

Blow-Down Feed System

The required fluid (propellant and pressurant) mass for the blow-down system increases with an increase in the propellant tank pressure ratio, as shown in Figure 6.11. This can be explained by the fact that an increase in this ratio results in a smaller pressure differential at the start of the mission. This smaller pressure differential requires more pressurant mass to deliver the same total impulse of 200 Ns, as the mass flow rate at the start is lower than when the initial tank pressure is larger. The required pressurant mass will increase to infinity as the tank pressure ratio approaches a value of 1, as the system is stagnant, and no propellant can be moved through a drop in pressure. This situation is not included in the chart, as the initial guess for the maximum allowable tank volume was chosen to be 2.5 dm^3 as explained in the trade-off criterion. The minimum required fluid mass occurs at the pressure ratio of approximately 0.085, where also the maximum achievable thrust levels are reached. Furthermore, helium is the best performing pressurant, as the required fluid mass is lower for every pressure ratio than when using nitrogen.

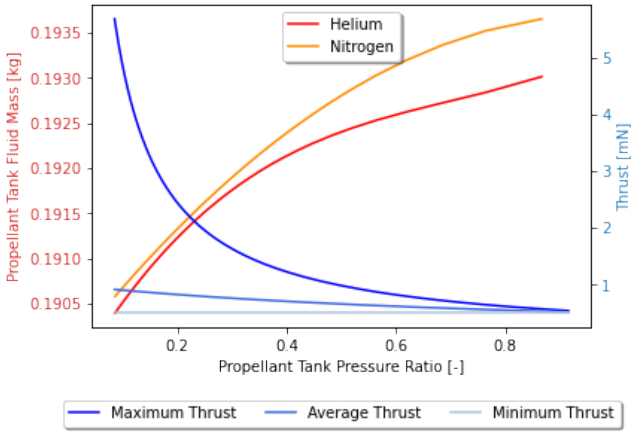

Figure 6.11: Required fluid mass as a function of the propellant tank pressure ratio for the blow-down feed system.

Pressure Regulated Feed System

The required fluid mass for the pressure regulated system initially decreases for an increase in the pressurant tank pressure ratio, followed by an increase as the pressure ratio approaches a value of 1. The initial decrease of the required fluid mass can be explained when looking at the achievable specific impulse as a function of the chamber pressure ratio (Figure 6.2a). The final tank pressure and, as a result the chamber pressure, increases for an increase in the pressure ratio. The increased chamber pressure is accompanied by an increase in the achievable specific impulse, and a decrease in the required propellant mass. However, the amount of pressurant required increases with a growing pressure ratio, as there is a lower pressure differential throughout the lifetime of the propulsion system. The increase in the required pressurant outweighs the decrease in the required propellant mass as the pressure ratio approaches a value of 1, resulting in a steep increase in the total required fluid mass. The pressurant mass will increase to infinity at a pressure ratio of 1, as there is no pressure to force the propellant out of the tank. As with the blow-down system, using helium as a pressurant results in a smaller required fluid mass, with the minimum mass occurring at a pressure ratio of approximately 0.9.

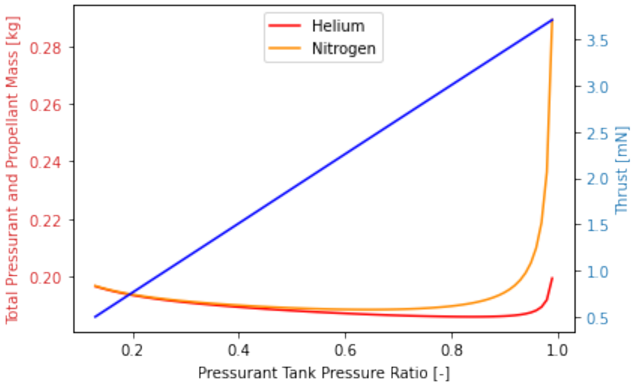

Figure 6.12: Required fluid mass as a function of the pressurant tank pressure ratio for the pressure regulated feed system.

Hybrid Feed System

The required fluid mass for the hybrid feed system follows a similar trend as the pressure-regulated system. An increase in pressure ratio, in this case the pressure ratio within the propellant tank as both pressurant and propellant are stored in one tank, results in an initial decrease of the required fluid mass followed by a steep increase as the pressure ratio approaches a value of 1. The initial decrease is again a result of the increase in the specific impulse, resulting in a lower required propellant mass whereas the steep increase of the required fluid mass is again linked to the lower pressure differential within the tank. The latter results in an exponential increase in the required pressurant mass to deliver the total impulse of 200 Ns. Like the blow-down and pressure regulated system, using helium as a pressurant results in a smaller, but measurable, decrease in the total required fluid mass.

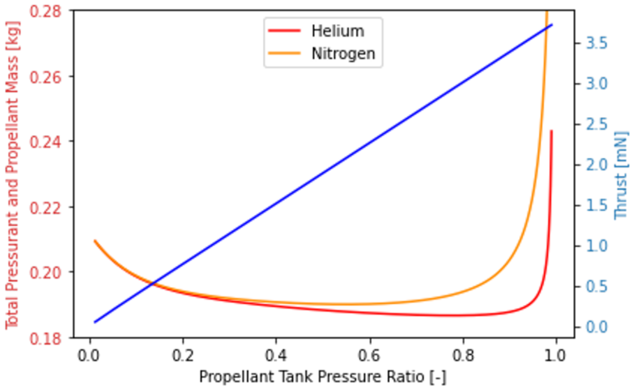

Figure 6.13: Required fluid mass as a function of the pressurant tank pressure ratio for the hybrid feed system.

6.4.3 Volume

The total required propellant and pressurant volume are plotted as a function of the tank pressure ratio in Figure 6.14, Figure 6.15, and Figure 6.16 for the blow-down, pressure regulated, and hybrid feed system respectively. The fill ratio, defined as the ratio of the required propellant volume over the total tank volume, is also included in the graphs to give an indication of the storage efficiency for each feed system type as a function of the pressure ratios.

Blow-Down Feed System

The required tank volume for the blow-down feed system increases with an increase in pressure ratio, as can be seen in Figure 6.14. An interesting observation is that the required volume increases exponentially, whereas the required fluid mass slope for an increasing pressure ratio flattens. This exponential increase in volume is a result of the significant increase in the required pressurant mass at higher pressure ratios to achieve the total impulse of 200 Ns. The lower density of the pressurant mass results in a significant increase in the tank volume. As with the mass criterion, the lowest tank volume occurs at the smallest pressure ratio. Furthermore, it can be observed that the required fluid volume remains the same when using either helium or nitrogen as pressurant, whereas there was a difference in the required fluid mass. The larger mass when using nitrogen as pressurant is compensated by the higher density of the pressurant while the lower mass when using helium as pressurant is offset by its smaller density. Finally, the maximum allowable pressure ratio is limited to a value of approximately 0.62 by the volume requirement of 0.5 dm^3.

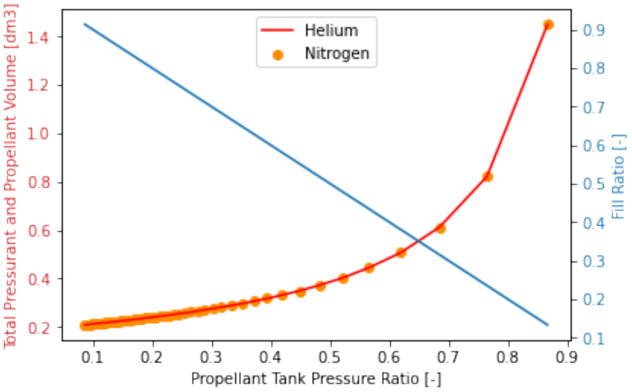

Figure 6.14: Required fluid volume as a function of the propellant tank pressure ratio for the blow-down feed system.

Pressure Regulated Feed System

The required pressurant and propellant volume for the pressure regulated system also increases exponentially with an increase in the pressurant tank pressure ratio, as shown in Figure 6.15. The explanation of this is the same as for the blow-down system, where a larger pressure ratio, resulting in a lower pressure differential, requires more pressurant mass to deliver the same total impulse of 200 Ns. The required fluid volume ranges between approximately 0.2 and 9.5 dm^3, which greatly surpasses the volume requirement of 0.5 dm^3. The maximum allowable pressure ratio is therefore limited to 0.77 for both pressurants. This limitation on the pressure ratio also enforces a limit on the maximum achievable thrust level, as can be seen in Figure 6.9b. Finally, it can be observed that the fill ratio decreases significantly as the pressurant tank pressure ratio increases. This is a result of the large increase in required pressurant when the pressure ratio rises.

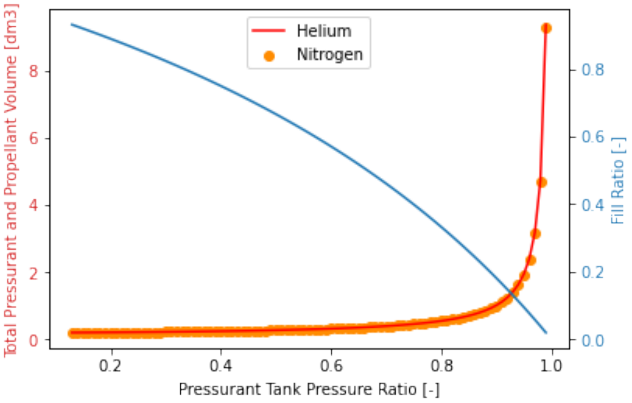

Figure 6.15: Required fluid volume as a function of the propellant tank pressure ratio for the pressure regulated feed system.

Hybrid Feed System

As with the blow-down and pressure regulated system, the required fluid volume for the hybrid system increases exponentially with an increase in the propellant tank pressure ratio, as can be seen in Figure 6.16. This can again be attributed to the sharp rise (to infinity) in the required low-density pressurant at higher pressure ratios. There is again no difference in the required volume when using either helium or nitrogen whereas there was a small but noticeable difference in the required fluid mass. The higher density of nitrogen compensates for the larger required pressurant mass while the lower density of helium offsets the smaller mass requirement. The hybrid system is, like the pressure regulated system, volume limited where the maximum allowable propellant tank pressure ratio is 0.62 for both pressurants. Finally, it can be observed that the fill ratio decreases as the pressure ratio increases. This can again be attributed to the increase in required pressurant volume as the pressure ratio rises.

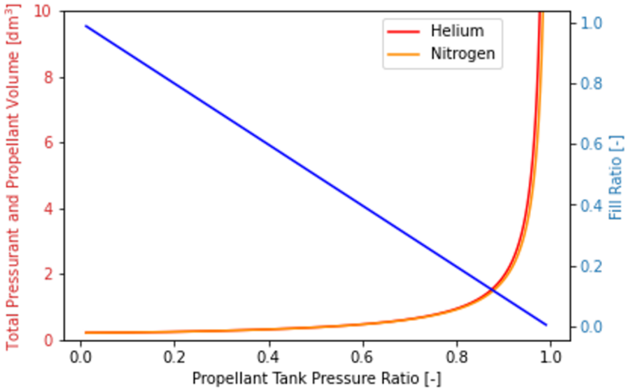

Figure 6.16: Required fluid volume as a function of the propellant tank pressure ratio for the hybrid feed system.

6.4.4 Reliability

A pressure regulated and hybrid feed system requires more components to function properly than a blow-down system. Only components that have a realistic change of failing are included in this trade-off, whereas additional components, such as piping, screws, and washers, that are unlikely to fail are excluded. The included additional components for the pressure regulator are an extra tank, filter, isolation valve, pressure relieve valve, and a pressure regulator. For the hybrid system, only an additional pressure regulator are included as there is no separate pressurant tank for the hybrid feed system.

The reliability relationship can be written for the blow-down, pressure regulated, and hybrid feed system. The difference (or decrease) in reliability when using a pressure regulated or hybrid system, rather than a blow-down system can be calculated by subtracting the relationship for the reliability of the pressure regulated or hybrid system from the blow-down system as shown in Equation 6.7,

$$\Delta R = e^{-t_m \cdot \sum_{n=0}^{\#_{bd}} \lambda_i} - e^{-t_m \cdot \sum_{n=0}^{\#_{pr/hy}} \lambda_i} \tag{6.7}$$

where t_m is the mission duration in years, $\#_{bd}$ is the number of components in a blow-down system, $\#_{pr/hy}$ is the number of components in a pressure regulated/hybrid system, and λ_i is the failure rate of each individual component. This equation can be simplified, as the failure rate per component is assumed to be at a constant value of 0.001. Furthermore, the equation can be simplified by assuming that the number of components in a pressure regulated system is equal to the number of components in a blow-down system plus the additional 5 components mentioned before. The result of these simplifications can be seen in Equation 6.8,

$$\Delta R = e^{-t_m \cdot \#_{bd} \cdot \lambda_i} \cdot \left(1 - \frac{1}{e^{t_m \cdot \Delta_{pr/hy} \cdot \lambda_i}}\right) \tag{6.8}$$

where $\Delta_{pr/hy}$ is the additional components required for the pressure regulated/hybrid system. This relationship can be plotted for a range of blow-down system components, as is shown in Figure 6.17.

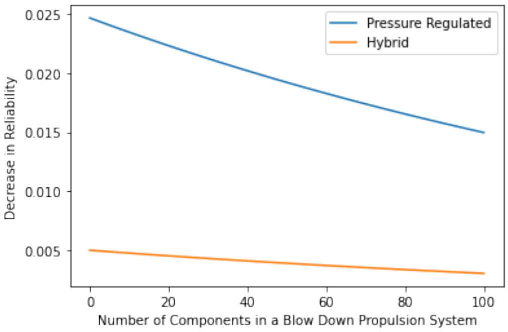

Figure 6.17: The decrease in reliability for using a pressure regulated or hybrid feed system over a blow-down system as function of the number of components within a blow-down system.

It can be seen that, whilst assuming a constant failure rate of 0.001 failures per year per component and a mission duration of 5 years, the maximum decrease in the reliability is approximately 0.025 for the pressure regulated system, and 0.005 for the hybrid system. These decreases in reliability occurs when a blow-down system consists of 0 components, which is not feasible. Furthermore, the decrease in reliability reduces as the number of components within a blow-down system increases. The fact that both the maximum reduction in reliability is low (0.025 and 0.005), and that the decrease in reliability reduces with an increased number of components leads to conclusion that the reliability of the three feed systems can be considered similar.

6.5 Trade-off Outcome and Required Fluid Storage per System

This section describes the trade-off outcome, followed by the required fluid storage per total achievable impulse.

6.5.1 Trade-off Outcome

The blow-down and pressure regulated systems are analysed for its performance, required fluid mass, required fluid volume, and reliability.

The performance of the blow-down system decreases with an increase in the tank pressure ratio, where the maximum achievable thrust levels are obtained at the lowest pressure ratio of 0.085. The maximum, average and minimum achievable thrust levels are 5.7 mN, 0.91 mN, and 0.5 mN respectively, and are all compliant with the requirements on the minimum and maximum achievable thrust.

The performance of the pressure regulated system increases with an increase in the pressure ratio, where the maximum achievable thrust of 3.75 mN is achieved at a theoretical pressure ratio of 1. As discussed in the previous section, this pressure ratio can never be reached, as any pressure ratio larger than 0.77 violates the requirement on the maximum allowable volume. The maximum achievable thrust is, as a result of volume requirement, limited to approximately 2.9 mN.

Like the pressure regulated system, the performance of the hybrid feed system increases with an increase in pressure ratio, where the maximum achievable thrust of 3.75 mN is achieved at the same theoretical pressure ratio of 1. However, as with the pressure regulated system, a pressure ratio of 1 can never be achieved due to the limitation on the maximum allowable system volume of 0.5 U. The volume limitation restricts the pressure ratio to 0.62 for both pressurants, resulting in a maximum achievable thrust of approximately 2.4 mN.

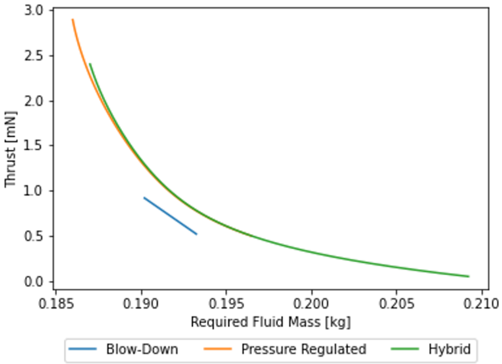

Figure 6.18: Achievable thrust level as a function of the required fluid mass.

Figure 6.18 shows the achievable thrust levels as a function of the required fluid mass. A first observation that can be made from this figure is that the required fluid mass does not meaningfully differ between the three feed system types. However, the blow-down system performs worse in terms of achievable thrust. There is only a small difference in achievable thrust levels for each fluid mass between the pressure regulated and hybrid feed system.

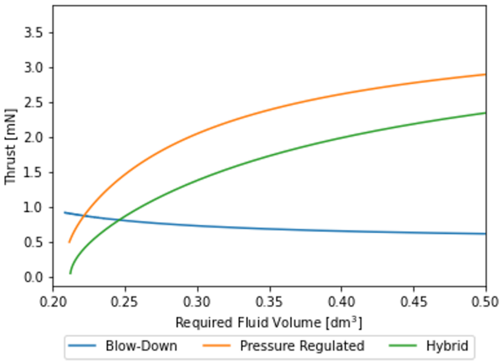

Figure 6.19: Achievable thrust level as a function of the required fluid volume.

As was mentioned before, both the pressure regulated and hybrid feed systems are volume limited in terms of achievable thrust levels, as their achievable thrust increases with an increase in the fluid volume. Figure 6.19 shows the performance of all three feed systems as a function of the required fluid volume. The blow-down system outperforms both the pressure regulated and hybrid feed systems for smaller fluid volumes, but quickly becomes a worse option as the fluid volume increases. Both the pressure regulated, and hybrid feed system are comparable in terms of achievable thrust per fluid volume.

The reliability of the three feed systems is considered to be the same, as only a few additional components are required for both the pressure regulated and hybrid feed systems compared to the blow-down system. The reliability of these systems is not significantly affected by the inclusion of these extra parts.

The three feed systems are comparable in terms of the required fluid mass and volume whereas the maximum achievable thrust of the blow-down system is significantly lower than that of the pressure regulated and hybrid feed system. The fact that these three systems are performing similar is not a surprise, as all three systems are used in propulsion systems. It is therefore difficult to pick a clear winner.

The fact that the blow-down system achieves the lowest thrust is reason for its elimination from the trade-off. This leaves the pressure regulated and hybrid feed system which are both volume limited in terms of their performance. The pressure regulated system does achieve a higher thrust per required fluid volume, but does require a separate tank to store the pressurant. This results in a small decrease in reliability, and an increase in the required material and volume. The need for additional material volume can potentially decrease the performance of the pressure regulated system below that of the hybrid system, as this trade-off was only performed for the required fluid volume. The small decrease in reliability, combined with the potentially large decrease in system performance in terms of thrust per volume, is reason for eliminating the pressure regulated feed system from the trade-off.

The last part of the trade-off is to choose which pressurant to use for the hybrid feed system. It was shown in Figure 6.13 that the required fluid mass is lower when using helium as pressurant. This mass discrepancy increased for an increasing pressure ratio. However, the hybrid feed system is volume limited which puts a limit of 0.62 on the maximum allowable pressure ratio. The difference in mass at this pressure ratio is small and can therefore be seen as insignificant. Furthermore, the required fluid volume for both pressurants is the same for all pressure ratios, as was shown in Figure 6.16. It does not matter what pressurant is used in the hybrid feed system when looking at the required fluid mass and volume. However, helium is more prone to leakages as its molecule size is smaller than that of nitrogen. Nitrogen is therefore chosen as the pressurant in this feed system. The trade-off results are summarized in Table 6.2, where the winner of the trade-off is indicated in **bold face** font.

Table 6.2: Trade-off results per category.

Feed System Type	Blow-Down		Pressure Regulated		**Hybrid**	
Pressurant	Helium	Nitrogen	Helium	Nitrogen	Helium	**Nitrogen**
Performance/ Thrust [mN]	0.61 - 0.92	0.61 - 0.91	0.5 - 2.9	0.5 - 2.9	0.5-2.35	**0.5-2.36**
Mass [g]	190.3 - 190.2	190.5 - 190.1	209.2 - 186.0	209.2 - 189.1	196.5 - 187.1	**196.8 - 190.2**
Volume [dm^3]	0.500 - 0.208	0.500 - 0.208	0.211 - 0.500	0.211 - 0.500	0.226-0.500	**0.226-0.500**
Reliability [-]	Best	Best	Good	Good	Better	**Better**

6.5.2 Required Fluid Storage per System

The hybrid system is to be used for the design of the VLM propulsion system. The propulsion system must deliver three total impulse levels of 200 Ns, 400 Ns, and 600 Ns, as per requirement *PROP-PERF-1*: “The propulsion system shall deliver a total impulse of 200 Ns / 400 Ns / 600 Ns.“

The worst-case scenario is assumed in the trade-off, where the chamber temperature is kept at the boiling temperature of the propellant for each chamber pressure. However, as can be seen in Section 6.1, the performance of the system increases with an increase in the chamber temperature. All calculations that have been performed for the 200 Ns system at the boiling point of the propellant in the trade-off have been repeated for all three total impulses at both the boiling point of the propellant and at a chamber temperature of 550K, whilst using nitrogen as the pressurant. The required fluid mass and volume depends on the fill ratio, as was shown previously. This fill ratio (F_i) is linked to the so-called blow-down (B) ratio through the following equation [51].

$$B \approx \frac{1}{1 - F_i} \tag{6.9}$$

Assuming a blow-down ratio of 4, the required fill ratio is 0.75. This blow-down ratio is chosen to ensure compatibility with all possible propellant management devices (PMDs). There are two types of PMDs: positive expulsion devices (PEDs) and surface tension devices (STDs), as will be explained in Chapter 8. The aim is to maximize the fill fraction as this will minimize the required tank volume. The lowest blow-down ratio that is compatible with both PEDs and STDs is 4, resulting in a maximum fill ratio of 0.75 [55]. The system can deliver a continuous thrust of 0.95 mN at this fill ratio, where the initial and final tank pressure are 10 bar and 2.5 bar respectively. The results of the calculations, performed at both chamber temperatures (the boiling point, and 550 K) while using the fill ratio of 0.75 are summarized in Table 6.3.

Table 6.3: Required propellant and pressurant mass and volume per delivered total impulse.

Total Impulse [Ns]	200		400		600	
Temperature	Boiling Point	550 K	Boiling Point	550 K	Boiling Point	550 K
Propellant Mass [g]	192	157	384	313	576	470
Pressurant Mass [g]	0.737	0.602	1.475	1.204	2.212	1.806
Propellant Volume [dm^3]	0.192	0.157	0.384	0.314	0.577	0.47
Pressurant Volume [dm^3]	0.064	0.0523	0.128	0.105	0.192	0.157
Total Mass [g]	193	157	385	314	578	472
Total Volume [dm^3]	0.256	0.209	0.512	0.419	0.769	0.627
Fill Ratio [-]	0.75	0.75	0.75	0.75	0.75	0.75

A first observation that can be made is that the required mass and volume for both the propellant and pressurant increases linearly with an increase in the required total impulse level. This behaviour is expected, as the achievable total impulse is a function of the available propellant mass, and the specific impulse.

A second observation is the significant decrease (of approximately 18%) in the required mass and volume for both the propellant and the pressurant when increasing the chamber temperature to 550 K. Furthermore, the required heating power decreases as the chamber temperature increases, as shown in Figure 6.2b. This is a result of the decrease in the mass flow rate when increasing the chamber temperature.

It is decided that the chamber temperature, thus the temperature of the propellant within the thrust chamber, is to be maintained at a constant temperature of 550 K due to the decrease in required fluid mass and volume. This decrease in both mass and volume allows for a more flexible design space for the rest of the system.

6.6 Verification of the Isothermal Expansion Assumption

A first indication on the correctness of the isothermal expansion assumption can be seen when looking at the fraction of the required pressurant mass over the required propellant mass (from Table 6.3) for the hybrid system. The temperature of the pressurant cannot significantly affect the temperature of the propellant, as there is a lot more propellant than pressurant in terms of mass: the propellant has a larger thermal mass. Thus, even if the expansion is not isothermal, the resulting change in temperature of the pressurant as the pressure drops will not influence the tank temperature in any meaningful way, as the thermal mass of the propellant is larger.

This can also be shown mathematically for all three feed system types. The change in internal energy per gram (ΔU) of both the propellant and pressurant can be calculated by using Equation 6.10,

$$\Delta U = \frac{C_v}{M_W} \cdot (T_{ini} - T_{fin}) \tag{6.10}$$

where C_v is the specific heat at constant volume, T_{ini} is the initial temperature, T_{fin} is the final temperature, and M_W is the molar mass of the fluid. Furthermore, the final temperature of the fluid can be calculated, when assuming isentropic expansion, by using Equation 6.11,

$$T_{fin} = T_{ini} \cdot \left(\frac{p_f}{p_i}\right)^{\frac{\gamma-1}{\gamma}} \tag{6.11}$$

where γ is the specific heat ratio [51]. Equation 6.12, where M_p is the required propellant mass in grams and M_{pres} is the required pressurant mass in grams, can be used when assuming that no energy is lost to the environment, and that the propellant and pressurant are perfectly mixed.

$$
\begin{aligned}
M_{pres} \cdot \Delta U_{pres} &= M_p \cdot \Delta U_p \\
M_{pres} \cdot \left[\frac{C_{v_{pres}}}{MW_{pres}} \cdot \left(T_i \cdot \left(1 - \left(\frac{p_f}{p_i} \right)^{\frac{\gamma-1}{\gamma}} \right) \right) \right] &= M_p \cdot \left[\frac{C_{v_p}}{MW_p} \cdot (T_i - T_f) \right] \\
\frac{M_{pres}}{M_p} \cdot \frac{C_{v_{pres}}}{C_{v_p}} \cdot \frac{MW_p}{MW_{pres}} \left(T_i \cdot \left(1 - \left(\frac{p_f}{p_i} \right)^{\frac{\gamma-1}{\gamma}} \right) \right) &= (T_i - T_f)
\end{aligned}
\tag{6.12}
$$

This equation can be solved for the change in propellant temperature within the propellant tank ($T_i - T_f$) for all three feed system types as a function of the ratio of the final tank pressure over the initial tank pressure, whilst using the variables summarized in Table 6.4. The results of this analysis are visualized in Figure 6.20.

Table 6.4: Input values for verifying the isothermal expansion assumption.

Variable	**Value**	**Unit**
$C_{v_{helium}}$	12.5	J/(mol·K)
$C_{v_{nitrogen}}$	20.8	J/(mol·K)
C_{v_p}	75.3	J/(mol·K)
MW_{helium}	4.0026	g/mol
$MW_{nitrogen}$	28.0134	g/mol
MW_p	18.0153	g/mol
γ_{helium}	1.66	-
$\gamma_{nitrogen}$	1.41	-
T_i	293.15	K

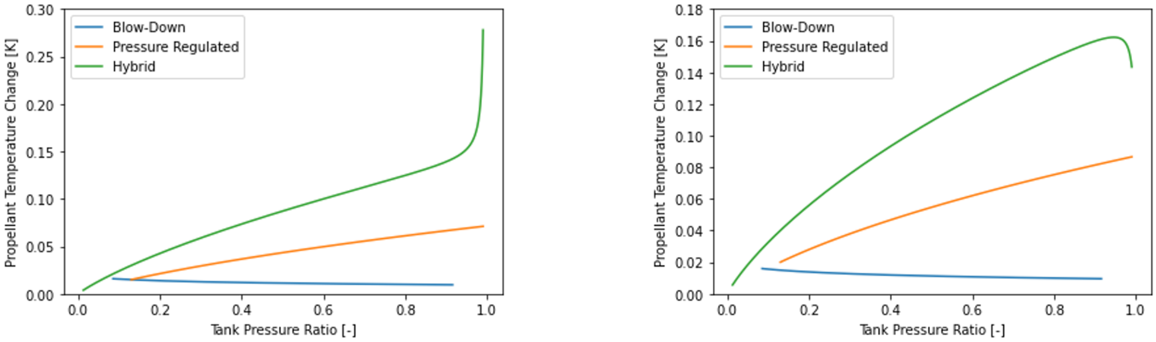

(a) Helium as pressurant.

(b) Nitrogen as pressurant.

Figure 6.20: Decrease in propellant temperature as a function of the tank pressure ratio.

The maximum deviation of the propellant temperature observed for the hybrid system, when using helium as the pressurant, is just 0.28 K. This temperature drop occurs at a pressure ratio approaching 1 and can be explained by the notion that the required pressurant mass increases to infinity. Consequently, the mass fraction of the required pressurant mass over the required propellant mass also increases to infinity, leading to a significant temperature drop in the propellant. This behavior is expected for all feed system types as the tank pressure ratio approaches 1.

An interesting observation is the behavior of the hybrid system using nitrogen as a pressurant, where the change in propellant temperature appears to drop at a pressure ratio of 1. This can be explained by looking at Equation 6.5, where the denominator drops towards zero and becomes negative for large pressure ratios. This drop towards zero and eventual transition to negative values results in a discontinuity, followed by an infeasible negative required pressurant mass. The minor propellant temperature change for all feed systems confirms the validity of the isothermal expansion assumption. However, the mathematical approach assumed that the propellant and pressurant are perfectly mixed at all times. This is most likely not the case as there is often a barrier between both fluids, and could lead to the formation of small ice crystals within the propellant itself. Nevertheless, the formation of ice crystals is still highly unlikely, as the pressurant expands slowly, resulting in a gradual temperature drop. The large thermal mass of the propellant can compensate for this slow drop in the pressurant temperature, ensuring that the temperatures of both the pressurant and propellant remain constant.

6.7 Conclusion

This chapter outlined the trade-off between the blow-down, pressure regulated, and hybrid feed system where both helium and nitrogen were investigated as possible pressurants. The trade-off was based on four criteria, namely the performance, mass, volume, and reliability. It was decided that the winner of the trade-off is the system that performed best in all categories whilst adhering to the requirements posed in Chapter 4.

The blow-down system can deliver a continuously decreasing thrust from 5.7 to 0.5 mN. These thrust levels are in-line with the requirements on the minimum and maximum thrust levels and are achieved for an initial tank pressure of 7.64 bar, and a final tank pressure of 0.65 bar. However, the average thrust that is delivered by the blow-down system is only 0.91 mN, as the thrust level rapidly decreases in the first 5 hours of the total burn duration.

The pressure regulated system is limited to a maximum achievable thrust of 2.9 mN, which is significantly higher than the average thrust provided by the blow-down system. The achievable thrust of the pressure regulated system is limited by the final pressure within the pressurant tank, as the constant pressure within the propellant tank is assumed to be equal to half of this final pressure. The required pressurant mass and volume increases with an increase in the final pressurant tank pressure, where the volume budget is limiting this pressure.

The hybrid system can deliver a maximum thrust of approximately 2.4 mN as it is, like the pressure regulated system, volume limited. It was shown that the performance of the pressure regulated and hybrid system are similar in terms of thrust per fluid mass and volume while having a comparable relative reliability with respect to the blow-down system.

The hybrid feed system won the trade-off, as it does not require an additional tank to store pressurant in. The need for an additional tank increases the required tank material and volume, and negatively impacts the already volume-limited feed system. Nitrogen was preferred over helium as helium is more prone to leakage whilst only requiring an insignificantly reduced fluid mass over the use of nitrogen. A summary of the trade-off results can be found in Table 6.2.

The calculations for the hybrid system were repeated for total impulse levels of 200 Ns, 400 Ns, and 600 Ns at both the propellant boiling point and 550 K, using nitrogen as the pressurant. A clear linear relationship was observed between the required masses and volumes and the total impulse. Additionally, increasing the chamber temperature from the propellant's boiling point to 550 K resulted in approximately an 18% reduction in the required masses and volumes. The total required fluid masses were calculated as 157 g, 314 g, and 472 g for the 200 Ns, 400 Ns, and 600 Ns systems, respectively. These masses corresponded to total volumes of 0.209 L, 0.419 L, and 0.627 L. A detailed breakdown of the required fluid masses and volumes for each system is provided in Table 6.3.

6.8 Recommendation

The trade-off methodology and results allow for continuing the design process of the VLM propulsion system, as the performance of the system, including the required propellant mass, propellant volume, pressurant mass, and pressurant volume are now know at two operating temperatures. However, one must realise that these values are the result of equations that assume the ideal performance of the thruster. In practise, the thruster will never reach these performance figures, as losses occur due to inefficiencies in the system. An investigation in the relationship between ideal rocket theory and practise is required to obtain more accurate values for the performance and, as a result, the required fluid masses, and volumes. Finding the link between ideal rocket theory and the real performance of the thruster is left for future work.

7

Design Budgets

It is good practise to start the design of any space-related hardware by establishing a volume, mass and power budget, as an increase in any of these parameters results in an increase in cost. This chapter will outline the design envelope of the three propulsion systems by first discussing the volume and power budget in Section 7.1, followed by the mass budget in Section 7.2.

7.1 Volume and Power Budget

Requirements *PROP-SYST-2* and *PROP-SYST-4* restrict respectively the volume and power that the three propulsion systems can use. It is proven difficult to allocate both volume and power budgets across various system component categories for the three systems, as there are no existing relationships found in literature for electrothermal propulsion systems. Furthermore, the lack of detailed volume and power breakdowns from existing micro-resistojet systems makes generating such budgets impossible and highly speculative at best. It is therefore decided to not generate detailed volume and power budgets. The decision not to define specific power and volume budgets prior to the design phase necessitates careful monitoring of these parameters during the design process to ensure they remain within acceptable limits.

However, a limit must be placed on the design envelope in terms of system width before starting the design to ensure compatibility with the CubeSat architecture. Requirement *PROP-SYST-2* states: “The total size of the propulsion system shall be within 0.5 U / 1.0 U / 1.5 U.” Furthermore, requirement *PROP-INT-1* states: “The mechanical interface between the propulsion system and the satellite shall be compliant with the CubeSat CS14 standard.” The combination of these two requirements limits the maximum allowable system width to 92 x 92 mm^2 as imposed by the CS14 PCB layout shown in Figure 7.1. This limit is enforced throughout the design of the propulsion systems to ensure easy integration with any CubeSat that adheres to the CS14 standard. Furthermore, the axis system as indicated in Figure 7.1 is used for the remainder of the design process.

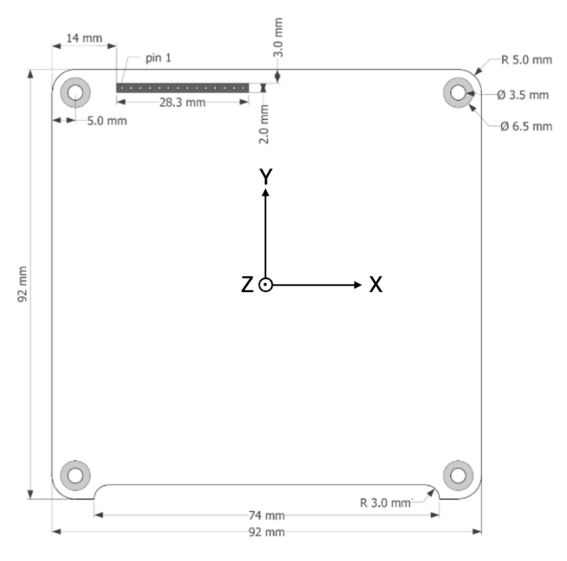

Figure 7.1: CS14 Printed Circuit Board Outline [23].

7.2 Mass Budget

The mass budget must provide a usable mass for each of the VLM propulsion components. A VLM propulsion system consists of a thruster, propellant tank, piping, structures and mounts, and controls and wiring. The maximum allowable wet masses are 700 grams, 1350 grams, and 2000 grams for the 200 Ns, 400 Ns, and 600 Ns propulsion system respectively, as specified in requirement *PROP-SYST-3*. The required fluid mass, both the propellant mass and pressurant mass, have been specified in Chapter 6. These values are multiplied by a safety factor of 1.25 to compensate for any non-ideal behaviour in the thruster, and to allow for an expulsion efficiency smaller than 100 %. The dry mass can be calculated by simply subtracting the required fluid mass from the wet mass. This dry mass is divided by a factor of 1.3 to create a mass budget for structures and general mounting hardware (10 % of the system net dry mass), control systems and wiring harnesses (5 % of the system net dry mass), and a margin for unforeseen system growth (15 % of the system net dry mass) [56]. Furthermore, as specified in Section 4.1, the thruster mass is estimated to be 20 grams. Given that the most recent specifications for the thruster, that contains both the VLM and LPM, are from 2019 [20], and a redesign is currently in progress, a safety factor of 2 is applied to this value. The thruster mass is consistent across all three systems, as the propulsion design's modularity is achieved through tank sizing rather than the inclusion of multiple thrusters. Finally, the tankage mass can be calculated by subtracting the mass of the thruster, the structures and mounts, and the controls and wiring from the system dry mass. This tankage mass includes the mass of the propellant tank, the feed lines, the valves, and the flow control systems [56]. The mass budgets for the 200 Ns, 400 Ns, and 600 Ns VLM propulsion systems can be found in Table 7.1

Table 7.1: Mass budgets for the 200 Ns, 400 Ns, and 600 Ns propulsion systems.

Component	**200 Ns**	**400 Ns**	**600 Ns**
Wet Mass [g]	700	1350	2000
Propellant Mass [g]	197	393	589
Dry Mass [g]	503	957	1411
Structures and Mounts [g]	39	74	109
Controls and Wiring [g]	19	37	54
Thruster Mass [g]	40	40	40
Tankage [g]	347	696	1045
Design Margin [g]	58	110	163

8 Propellant Tank Design

This chapter outlines the design of the propellant tank. First, a list of requirements is generated in Section 8.1. Next, different propellant tank shapes and materials are discussed in Section 8.2, followed by an outline of propellant management devices in Section 8.3. A summary of the considered tank shapes and propellant management devices is visualized in Section 8.4. A trade-off between the different tank shapes and materials is performed in Section 8.5, and is followed by the mechanical interface design in Section 8.6. The propellant management device trade-off is performed in Section 8.7, and is followed by the detailed propellant management design in Section 8.8. Next, the compliance with the generated requirements is discussed in Section 8.9, after which the chapter is concluded in Section 8.10.

8.1 Requirements

Table 8.1: Propellant storage device requirements.

Requirement ID	Parent Requirement	Requirement	Rationale
PROP-TANK-01	PROP-PERF-1	The propellant tank shall store a usable fluid volume of 0.263 L / 0.526 L / 0.788 L ± 2%.	Required fluid volume with a 25% margin to compensate for non-ideal performance of the thruster, volume taken up by propellant management devices (PMDs), and an expulsion efficiency smaller than 100%.
PROP-TANK-02	PROP-INT-2	The propellant tank shall not exceed the 92 x 92 mm (XY) boundaries.	Outer dimensions of a CS14 Printed Circuit Board (see Figure 7.1).
PROP-TANK-03	PROP-SYST-2	The propellant tank height (Z) shall not exceed 50 mm / 100 mm / 150 mm.	From propulsion system volume budgets of 0.5 U / 1.0 U / 1.5 U.
PROP-TANK-04	PROP-SYST-3	The total mass of the tankage shall not exceed 347 g / 695 g / 1043 g.	Taken from the mass budget as described in Chapter 7.
PROP-TANK-05	PROP-INT-2	The propellant tank shall allow for a propellant and pressurant temperature range between 283 K and 323 K.	Design choice: a wide operating temperature range allows for a less restrictive design of the thermal management system.
PROP-TANK-06	PROP-RAMS-1	The propellant tanks shall survive a maximum expected operating pressure of 10 bar.	See Subsection 8.1.1.
PROP-TANK-07	PROP-RAMS-3	The propellant tank shall have a design factor of safety of 1.25 for yield.	Design Safety Factor from SMAD, given that one flight unit of a fleet is tested to 1.25 times the limit load [41].
PROP-TANK-08	PROP-RAMS-3	The propellant tank shall have a design factor of safety of 1.4 for ultimate load.	Design Safety Factor from SMAD, given that one flight unit of a fleet is proof tested to 1.25 times the limit load [41].
PROP-TANK-09	PROP-INT-2, PROP-RAMS-1	The pressure and temperature within the propellant tank shall be electronically monitored.	Necessary for the thermal management system, and allows for sensing the propellant level within the tank.
PROP-TANK-10	PROP-RAMS-3	The propellant tank shall leak before burst.	Prevents a sudden end-of-life of the propulsion system, damaging of the spacecraft, and injuring of operators.

Continued on next page

Requirement ID	Parent Requirement	Requirement	Rationale
PROP-TANK-11	PROP-INT-3	The propellant tank shall allow for filling and draining of both the propellant and pressurant.	Allows for testing.
PROP-TANK-12	PROP-RAMS-2	The propellant tank material shall be compatible with gaseous nitrogen and liquid water.	Required for the system to function properly.
PROP-TANK-13	PROP-PERF-1	The propellant tank shall ensure that no pressurant enters the thruster.	Premature end-of-life when pressurant leaves the tank.
PROP-TANK-14	PROP-PERF-1	The propellant tank shall allow for an expulsion efficiency of at least 95%.	Design choice.
PROP-TANK-15	PROP-INT-1	The propellant tank shall be mechanically integrated within the propulsion system according to the CS14 interface standard.	Allows for integration within any CubeSat that adheres to this standard.
PROP-TANK-16	PROP-INT-3	The propellant tank shall be electrically integrated within the propulsion system according to the CS14 interface standard.	Allows for integration within any CubeSat that adheres to this standard.
PROP-TANK-17	PROP-SYST-5	The propellant tank shall survive an axial acceleration of 8.5g.	Falcon 9 specification for payloads lighter than 1.81 tonnes [57, p. 18].
PROP-TANK-18	PROP-SYST-5	The propellant tank shall survive a lateral acceleration of 3g.	Falcon 9 specification for payloads lighter than 1.81 tonnes [57, p. 18].
PROP-TANK-19	PROP-SYST-5	The minimum resonant frequency of the mechanical interface between the propellant tank and the main structure of the propulsion system shall be larger than 35 Hz.	Falcon 9 specification for secondary structures [57, p. 17].

8.1.1 P-TANK-06 rationale

The requirement for a maximum expected operating pressure of 10 bar limits the tank pressure during nominal operating conditions. This maximum of 10 bar is reached when the tank temperature hits the maximum allowable value of 323 K at the Beginning of Life (BOL), with the tank at its highest fill level. System performance was previously calculated (in Chapter 6) based on a BOL pressure of 10 bar. However, under nominal BOL conditions, when the tank temperature is at 293 K, the pressure within the tank is lower. This allows the tank temperature at BOL to increase from 293 K to 323 K while keeping the pressure below the 10-bar limit but will result in a decrease in system performance in terms of the mass flow rate.

The increase in tank pressure as a function of the tank temperature rise can be calculated using the following method. The volumetric expansion of the propellant (ΔV_p) as function of the temperature increase can be calculated using:

$$\Delta V_p = V_p \beta_p \left(T_2 - T_1\right) \tag{8.1}$$

where V_p is the volume of propellant in the tank, β_p is the coefficient of volumetric thermal expansion of the propellant, T_2 is the new tank temperature, and T_1 is the nominal tank temperature equal to 293 K. As the propellant expands, it reduces the volume available to the pressurant gas. The new volume of pressurant gas (V_{g_2}) at temperature T_2 is:

$$V_{g_2} = V_{tank} - \left(V_p + \Delta V_p\right) \tag{8.2}$$

where V_{tank} is the volume of the tank. The new pressure of the pressurant gas, hence the new pressure in the tank (p_2), can be estimated using the ideal gas law:

$$p_2 = p_1 \frac{V_{g_1}}{V_{g_2}} \frac{T_2}{T_1} \tag{8.3}$$

where p_1 is the initial pressurant pressure and V_{g_1} is the initial volume that the pressurant occupies at the nominal temperature. Combining Equation 8.1, Equation 8.2, and Equation 8.3, and realising that the initial gas volume is equal to the tank volume minus the propellant volume gives the following relationship:

$$p_2 = p_1 \frac{V_{tank} - V_p}{V_{tank} - V_w \left[1 + \beta_p \left(T_2 - T_1\right)\right]} \frac{T_2}{T_1} \tag{8.4}$$

This relation can be further simplified by rewriting the propellant volume in terms of the fill ratio F_i:

$$p_2 = p_1 \frac{1 - F_i}{1 - F_i \left[1 + \beta_p \left(T_2 - T_1\right)\right]} \frac{T_2}{T_1} \tag{8.5}$$

It is interesting to notice that the pressure increase as a result of a temperature rise is independent of the volume of the tank itself. The final attribute to the pressure increase as a function of the tank temperature is the vapor pressure (P_v) of the propellant. This pressure can be estimated using the Magnus equation [58]:

$$P_v = 610.94 \exp\left(\frac{17.625 \left(T_2 - 273.15\right)}{\left(T_2 - 273.15\right) + 243.04}\right) \tag{8.6}$$

The tank pressure at the maximum tank temperature can be calculated by summing Equation 8.5 and Equation 8.6:

$$p_2 = p_1 \frac{1 - F_i}{1 - F_i \left[1 + \beta_p \left(T_2 - T_1\right)\right]} \frac{T_2}{T_1} + 610.94 \exp\left(\frac{17.625 \left(T_2 - 273.15\right)}{\left(T_2 - 273.15\right) + 243.04}\right) \tag{8.7}$$

Solving Equation 8.7 for the tank pressure at the nominal tank temperature (p_1) gives:

$$p_1 = \left[p_2 - 610.94 \exp\left(\frac{17.625 \left(T_2 - 273.15\right)}{\left(T_2 - 273.15\right) + 243.04}\right)\right] \cdot \left[\frac{1 - F_i}{1 - F_i \left[1 + \beta_p \left(T_2 - T_1\right)\right]}\right] \cdot \frac{T_1}{T_2} \tag{8.8}$$

Applying Equation 8.8 for water and nitrogen as respectively propellant and pressurant at the maximum tank temperature of 323 K and a fill ratio of 0.75 gives a BOL tank pressure of approximately 8.75 bar at the nominal operating temperature of 293 K. This results in a maximum achievable thrust level of 0.8 mN at a mass flow rate of 0.7 mg/s at these nominal conditions.

8.2 Tank Shapes and Materials

There are various tank shapes used in propulsion systems, including spherical, cylindrical, toroidal, and cono-spheroidal (peer) shapes. The latter is used for rotating spacecraft, as the combination of rotation and the peer-like shape forces propellant to the tank outlet [51]. This thesis will investigate three tank commonly used shapes, namely spherical, cylindrical, and rectangular tanks. Spherical tanks are optimal in terms of mass efficiency, whereas rectangular-shaped tanks are optimized for the efficient use of the design volume. Cylindrical tanks provide a balance between mass optimization, due to their resistance to internal pressure, and volume optimization. Furthermore, cylindrical tanks can have hemispherical, elliptical, and flat end caps.

Commonly used materials for liquid propellant tanks are aluminium, titanium, stainless steel, and pre-stressed composites. Composites can offer a mass reduction of more than 60% due to their high strength to weight ratio [51]. However, due to the relatively low pressure within the propellant tank of 10 bar, the need for a liner material (usually titanium or steel), and the complexity of manufacturing, resulting in this material not being included in this thesis. Furthermore, the inability to access the internal structure after manufacturing limits the choice of the propellant management device later in the design. The materials considered in this thesis are aluminium 6061-T6, 304L Stainless Steel, Titanium Grade 5, and Inconel-718, and are all compatible with both liquid water and gaseous nitrogen. Inconel-718 is commonly used in high-temperature environments, such as nozzles. It is included here for its high tensile yield and ultimate tensile strength. The material properties are summarized in Table 8.2.

Table 8.2: Material properties

Material	Aluminium 6061-T6	304L Stainless Steel	Titanium Grade 5	Inconel - 718
UNS Code	A96061	S30403	R56400	N07718
Tensile Strenght, Yield [MPa]	276	210	880	1100
Tensile Strenght, Ultimate [MPa]	310	564	950	1375
Density [kg/m^3]	2700	8000	4430	8190
Specific Heat Capacity [J/(kg·K)]	896	500	560	435
Thermal Conductivity at 293 K [W/(m·K)]	166	15	6.7	11.1
Thermal Diffusivity [$\cdot 10^{-6}$ m^2/s]	68.7	3.8	2.7	3.1
Minimum Sheet Thickness [mm]	0.2	0.02	0.15	0.15
Minimum Wall Thickness for drawn, seamless tube [mm]	0.5	0.3	0.3	0.5
Source(s)	[59][60][61]	[62][63][64]	[65][66][67]	[68][69][70]

The thermal diffusivity (α_{th}) is calculated by using Equation 8.9,

$$\alpha_{th} = \frac{k}{\rho \cdot C_p} \tag{8.9}$$

where k is the thermal conductivity, ρ is the density of the material, and C_p is the specific heat capacity.

The minimum sheet thickness and drawn seamless tube wall thicknesses are obtained from companies that provide these products. It must be noted that the wall thicknesses of the drawn seamless tubes are often linked to the tube diameter, where smaller wall thicknesses are only achievable for pipes with a small diameter. It is assumed that the stated wall thicknesses of the seamless tube can be achieved for an outer diameter of 92 mm.

8.3 Propellant Management Devices

This section presents the positive expulsion devices (PEDs) in Subsection 8.3.1, followed by the surface tension devices (STDs) in Subsection 8.3.2.

8.3.1 Positive Expulsion Devices

Bladder

A bladder is a balloon-like membrane that either stores the liquid propellant or pressurant. The balloon is deflated over the mission duration when propellant is stored inside the bladder, whereas the bladder is inflated when the pressurant is stored inside. To achieve the most efficient use of the tank volume, the fully extended bladder is shaped to precisely fit in the tank. Making bladders smaller than the tank can result in damage by excessive stretching. This stretching occurs when filling the bladder with propellant at the start of the mission, or during the mission when the pressurant is stored within the balloon-like membrane. Bladders that exceed the tank volume are in danger of being damaged by folding creases. In general, the durability of the bladder is influenced by the folding. Bladders cannot collapse to near-zero internal volume without creasing, stretching, or shrinking. This material deformation results in tangential membrane strains, transverse shearing strains, and localized bending strains. Another concern regarding bladders is the permeability of the membrane material. Permeating propellant into the ullage decreases the total deliverable impulse, whereas permeating pressurant into the propellant dilutes the propellant and results in a pressure loss within the tank [71].

Diaphragm

Unlike bladders, diaphragms allow both the propellant and pressurant to be in contact with the propellant tank. The thin membrane divides the tank into two compartments and is fastened to the outermost edge of the tank. Diaphragms can either be completely reversed upon themselves or start from an intermediate shape and be shaped by the pressure within the tank to its final shape. A reversing diaphragm is required when only one diaphragm is used, whereas convoluting diaphragms are used in a dual diaphragm setup. Convoluting diaphragms are folded such that there is no stretching or shrinking within the material. Like bladders, there are concerns regarding the creasing in the diaphragm material as a result of the folding. Furthermore, the shape of the diaphragm is affected by the required fastening to the tank's periphery. Small ribs on the outside of the diaphragm can be used to keep the diaphragm away from the tank wall, which significantly improves the expulsion efficiency when compared to smooth diaphragms. The minimum expulsion efficiencies of smooth and ribbed hemispherical diaphragms are 84 % and 99.7 % respectively [71].

Piston

Pistons are solid devices that traverse the length of the tank. Like diaphragms, the tank is exposed to both propellant and pressurant. Bellows or sealing rings are used to ensure that the pressurant and propellant are continuously separated. Pistons can either be free-floating or are held by mechanical actuation devices. A round shape is often used for the cross section perpendicular to the direction of motion as this allows for both an easy fit within the tanks, and a good seal between the tank walls and the piston. A flat, cylindrical, convex, or concave shape can be used in the longitudinal direction. However, flat pistons are not often used as they are prone to cocking without proper guiding. The tank walls can be used as a guide for cylindrical pistons when using a length of at least $\frac{5}{8}$ the tank diameter. Convex and concave pistons are used in tanks with non-flat end caps to maximize the volumetric efficiency.

One of the major challenges of piston expulsion devices is maintaining a good seal between the piston and tank wall without excessive friction. The seal must prevent leakage past the piston and remove all propellant from the wall when traversing the tank. Another challenge is preventing the cocking of the piston. Center guides and peripheral guides can be used when the piston length is below the previously stated $\frac{5}{8}$ of the tank diameter. Disadvantages of using these types of guides include the need for sealing, the need for exact alignment, and the straightness of the guide itself [71]. An example of a bladder, diaphragm, and piston tank is shown in Figure 8.1

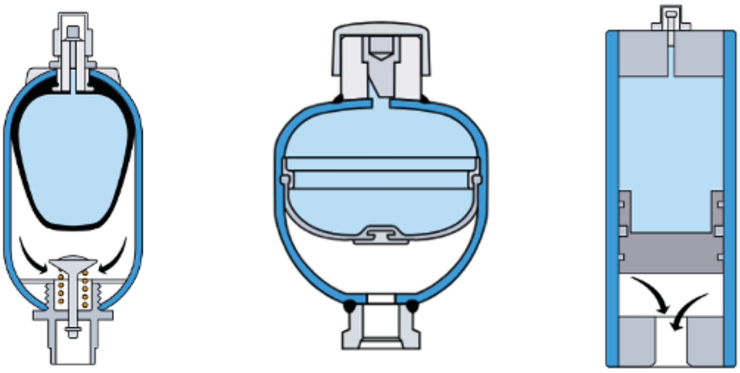

Figure 8.1: Example of a bladder tank (left), diaphragm tank (middle), and piston tank (right) [55].

8.3.2 Surface Tension Devices

Communication Devices

Communication PMDs can move propellant from the propellant tank to the tank outlet in any direction through use of vanes or galleries. Vanes are thin metal plates that can be used to lift propellant under low acceleration conditions and are located along the tank walls or within the tanks. Liquids adhere to these sheet metal structures and communicate the liquid from a free-floating pool to the tank outlet. The firing of the thruster moves the liquid pool to the tank wall, where the vanes communicate the propellant to the tank outlet. The use of vanes is limited to thrusters that provide low accelerations to the spacecraft. Major advantages of using vanes include their ability to provide propellant to the thruster continuously for any burn duration and direction, while also being lightweight and low cost [72].

Galleries are used when the acceleration levels are high. They consist of porous channel elements that run along the tank walls. As with vanes, they communicate the liquid from propellant pool to the tank outlet. The porous element ensures that only the liquid enters the enclosed channels, whereas the gas remains within the tank. The liquid can enter these channels when the propellant pool is moved to the tank wall by firing the thruster. This type of PMD works if the hydrostatic losses and flow losses do not exceed the porous element bubble point. Gallery PMDs are the most capable of PMDs, but are heavier, more complex, less reliable, and less efficient than other PMDs [72]. An example of a vane and gallery is shown in Figure 8.2.

Figure 8.2: Example of vanes (left) and galleries (right) [72].

Control Devices

There are two types of control PMDs: partial control and total control (or slosh control). Partial control PMDs retain a fraction of the propellant over the tank outlet whereas the remaining liquid is free. This is achieved through (a combination of) traps, trough and sponges. Total control PMDs retain all propellant through a large, compartmented trap, and are used when slosh control is of concern. Porous barriers are used to compartment the trap [51].

Traps hold liquid within its solid wall structure by a porous element covered trap inlet window. The porous element allows for the retention of propellant at higher acceleration than sponges. There are several trap configurations, including cylindrical, clam shell, and bulkhead traps. Traps are not suitable for repeated orbital manoeuvres, as they are not passively refillable during zero-g coast and are typically used for a single manoeuvre. Some traps can be refilled during a high acceleration settling manoeuvre [72].

Sponges consist of closely spaced metal panels, located over a trap or tank outlet. There are three types of sponges, namely radial, fan, and accordion sponges, each with their unique flow characteristics and manufacturing difficulties. Propellant clings to the tapered space between the panels and forces any bubbles in the sponge outboard. Sponges can be used for repeated manoeuvres, such as station keeping, and are refillable during zero g coasts or a settling acceleration. They are highly reliable, as they are open devices like vanes which do not rely on porous elements. This allows for refilling after any acceleration environment [72].

Troughs, in contrast to other PMDs, do not rely on surface tension forces to retain liquid. There are several through configurations, including radial, cylindrical, conical, inverted cone, and tubular troughs. They use the hydrostatic force of a liquid in an acceleration field to control propellant. The ratio of retained propellant over the total trough volume is small, making these PMDs relatively heavy and expensive. Like sponges, most troughs are refillable, but at higher accelerations and at low mass and cost efficiency. Non-refillable troughs, like tubular troughs, are more efficient [72]. Examples of a combination of a cylindrical trap and sponge, sponge, and a trough are shown in Figure 8.3.

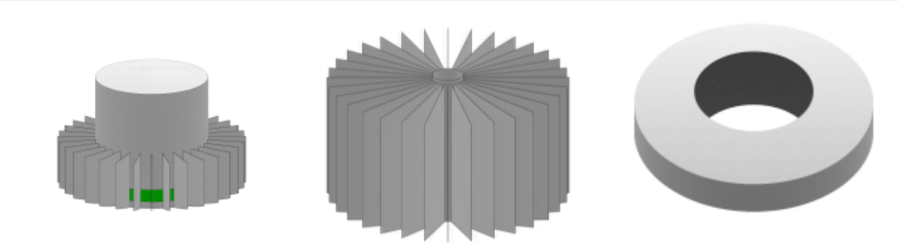

Figure 8.3: Example of a combination of cylindrical trap and sponge (left), sponge (middle), and a trough (right) [72].

8.4 Shape and Propellant Management Devices Design Option Tree

This section summarizes the different propellant tank configuration options for this thesis by means of a design option tree (DOT). The DOT, shown in Figure 8.4, outlines the different tank shapes and propellant management devices that can be used to store and control propellant within a propulsion system. The materials used, namely aluminium 6061-T6, 304L stainless steel, grade 5 titanium, and Inconel-718 have been omitted from this DOT to limit its size.

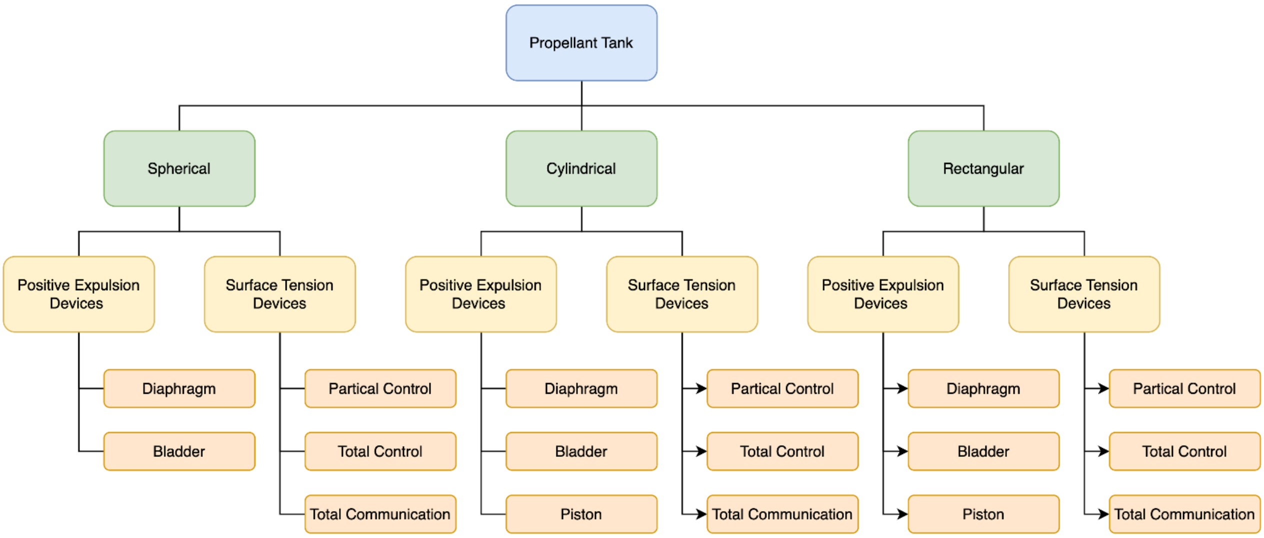

Figure 8.4: Design option tree of the tank shape and propellant management devices.

8.5 Tank Shape and Material Trade-off

This section outlines the trade-off for both the propellant tank shape, and the tank material. These two are combined, as they both influence each other. First, assumptions made are outlined in Subsection 8.5.1, followed by the initial elimination of tank shape options in Subsection 8.5.2 and trade-off criteria in Subsection 8.5.3. The trade-off results are presented in Subsection 8.5.4 whereas the trade-off is concluded in Subsection 8.5.5

8.5.1 Assumptions

Three assumptions are made during this trade-off. First, it is decided to use only one propellant tank, as employing multiple propellant tanks in a small system leads to a significant portion of unusable space occupied by the tank walls. Additionally, it results in an increase in system dry mass due to the need for multiple feed lines, and it complicates the system by requiring multiple valves, filters, propellant management devices, and pressure and temperature measurement devices.

Second, it is assumed that a single tank shape is used for all three tank sizes: either all spherical, cylindrical, or rectangular. The tank maximum outer dimension is limited to 92 mm in the XY-plane, while their height (in the Z-direction) can vary between 0 mm and 150 mm (for the largest propulsion system). This assumption is made to simplify the design of the propulsion systems.

Finally, it is assumed that the dominant load on the tank is the internal pressure within the propellant tank. Any other load cases will be considered during the detailed design phase of the propellant tank.

8.5.2 Initial Eliminations

Spherical tanks are eliminated, as the tank diameter of the larger systems exceeds the maximum dimension of 92 mm, as described in requirement *PROP-TANK-02*.

Cylindrical tanks with hemispherical end caps are eliminated, as the radius and height of each tank size will differ. This complicates the design of the mechanical interface of the tank with the rest of the propulsion system. Furthermore, the use of hemispherical end caps results in an increase in the required tank height, as part of the design volume is not occupied by the tank.

Cylindrical tanks with elliptical end caps are eliminated, as different elliptical end caps are required for each propulsion system due to the different tank volumes. This significantly increases the complexity of the tank designs. As with the hemispherical end caps, the use of elliptical end caps results in an increase in the required tank height, as part of the design volume is not occupied by the tank.

8.5.3 Trade-off Criteria

The two remaining tank shapes for the trade-off are the rectangular tank, and the cylindrical tank with flat end caps. They are compared against each other by three trade-off criteria: shell mass, tank height, and the manufacturability. These criteria are dependent on the material used, and is the reason why both the tank shape and tank material are traded-off simultaneously. The rectangular tank is shown in Figure 8.5, whereas the cylindrical tank with flat end caps is visualized in Figure 8.6. The outer dimension of both tank shape bottom plates (L_o, W_o, and D_o) are constrained by the PCB dimensions of 92 x 92 mm^2.

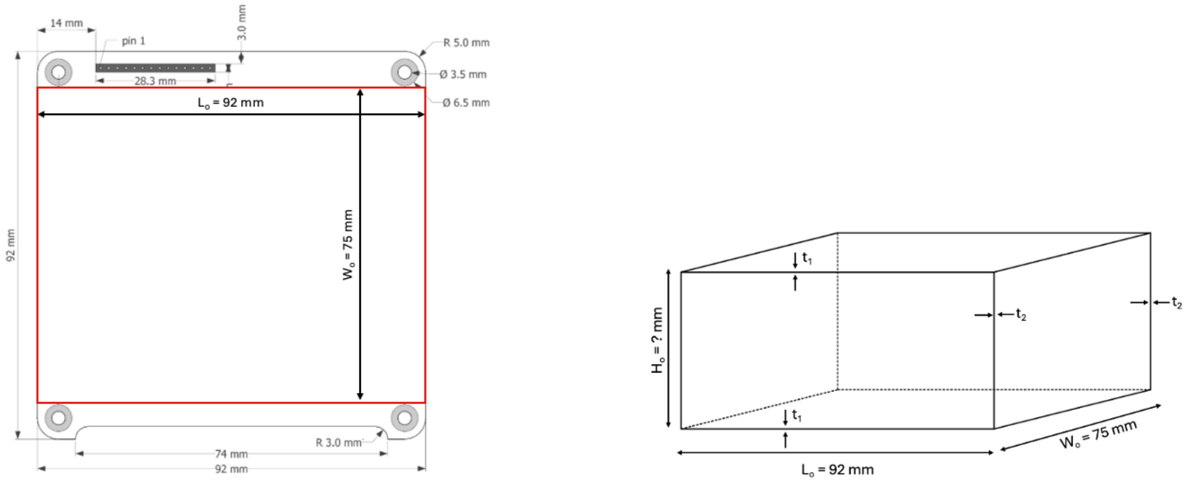

(a) Cross Section on PCB. (b) Isometric View.

Figure 8.5: Rectangular Propellant Tank

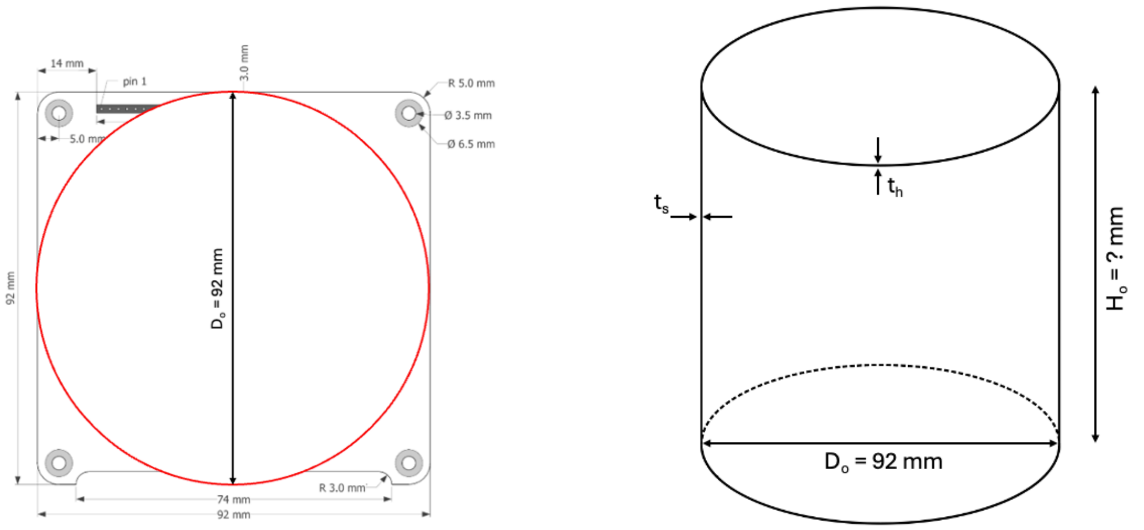

(a) Cross Section on PCB. (b) Isometric View.

Figure 8.6: Cylindrical Propellant Tank with flat end caps

Shell Mass and Tank Height

The shell mass and tank height criteria are combined, as they are dependent on each other by the thickness of the tank walls. The optimal combination of tank shape and material is the one with the lowest shell mass and tank height, as this allows for greater flexibility in designing the rest of the propulsion system.

Rectangular Tank

The shell mass and tank height of an internally pressurized rectangular propellant tank are calculated by following the ASME Boiler and Pressure Vessel Code for the design procedures for pressure vessels of non-circular cross section [73], and approach as outlined in [74]. The rectangular tank has two axis of symmetry for both the L_o x H_o (from now on called face A) and W_o x H_o (face B) planes, as shown in Figure 8.5b. It is assumed that the two opposite sides may have a wall thickness different than that of the other side. The cross section of face A is shown in Figure 8.7.

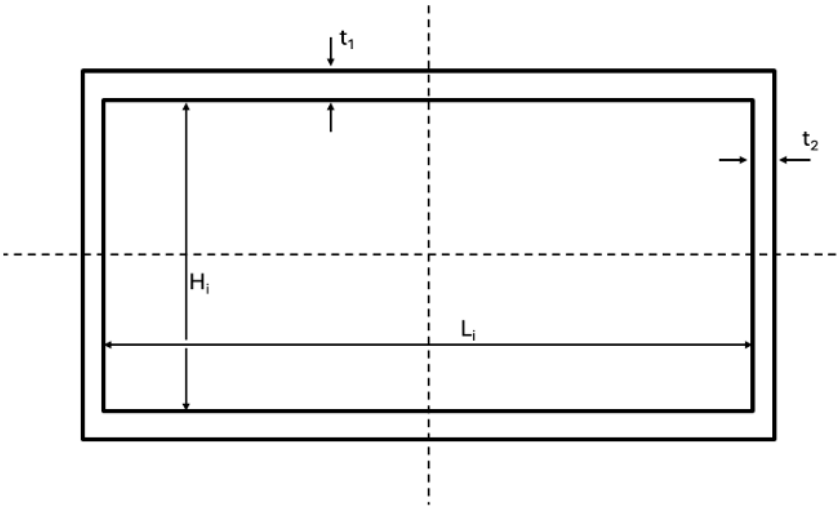

Figure 8.7: Cross section of face A.

The following design procedure is performed for both face A and B, of which face A is outlined in this section. The symmetry of this face allows to perform the analysis on one fourth of the cross section. The starting point of this analysis is to compute the reaction forces and moments T_P, T_R, M_P, and M_R to the internal pressure p_{tank}. These forces and moments are per unit of depth, which in the case of face A is per unit of W_o. Figure 8.8 shows the free body diagram of the tank section PQR.

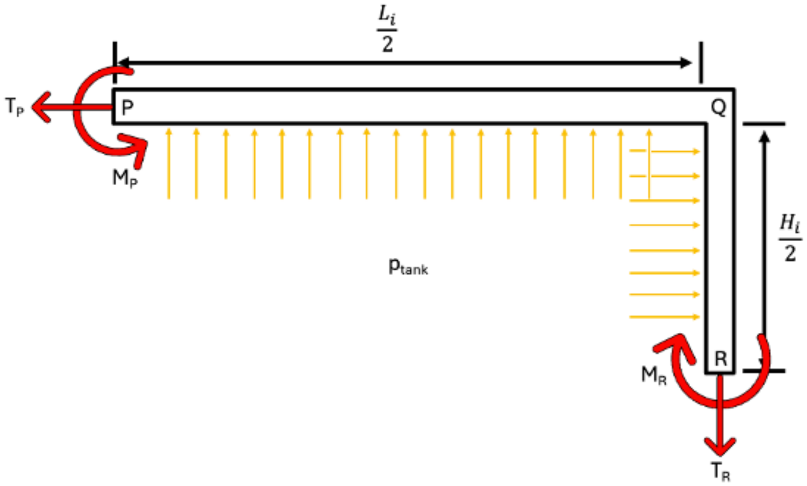

Figure 8.8: Free body diagram of tank section PQR.

The reaction forces T_P and T_R can be calculated by applying a force equilibrium in the horizontal and vertical direction:

$$\sum F_h = 0 \qquad \rightarrow \qquad T_P = p_{tank} \cdot \frac{H_i}{2} \tag{8.10}$$

$$\sum F_v = 0 \qquad \rightarrow \qquad T_R = p_{tank} \cdot \frac{L_i}{2} \tag{8.11}$$

A moment equilibrium can be applied around, for example, point P:

$$\sum M_P = 0 \qquad \rightarrow \qquad M_P + M_R + p_{tank} \cdot \frac{H_i^2}{8} - p_{tank} \cdot \frac{L_i^2}{4} + p_{tank} \cdot \frac{L_i^2}{8} = 0 \tag{8.12}$$

An additional equation is required to obtain all reaction forces and moments. This equation is obtained from Castigliano's Theorem. This theorem states that the slope at any point in the structure is given by:

$$\phi = \frac{\delta U_{st}}{\delta M_b} \tag{8.13}$$

where U_{st} is the total elastic strain energy of the system, and M_b is the applied bending moment. The total elastic strain energy for bending is given by:

$$\int \frac{M_b^2 \cdot dx}{2 \cdot E \cdot I} \tag{8.14}$$

where E is the Young's modulus, and I is the moment of inertia. The moment of inertia is calculated by:

$$I = \frac{t_s^3}{12} \tag{8.15}$$

where t_s is the skin thickness. The slope at point P and R must be equal to zero to satisfy the symmetry boundary condition. The slope at point P is considered here, and used to obtain the additional equation that is required:

$$\phi_p = \frac{\delta U}{\delta M_P} = 0 \quad \rightarrow \quad \int_0^{\frac{H_i}{2}} \frac{M_{QR} \delta M_{QR}}{\delta M_P} \left(\frac{dx}{I_2}\right) + \int_0^{\frac{L_i}{2}} \frac{M_{PQ} \delta M_{PQ}}{\delta M_P} \left(\frac{dx}{I_1}\right) = 0 \tag{8.16}$$

where M_{PQ} and M_{QR} are the bending moments along PQ and QR respectively. The forces and moments along PQ and QR are summarized in Table 8.3, where the direction x_1 is from P to Q and x_2 is from Q to R.

Table 8.3: Forces and moment distributions along PQ and QR.

PQ	$F_h = p_{tank} \cdot \frac{L_i}{2}$ $F_v = p_{tank} \cdot x_1$ $M_{PQ} = M_R - p_{tank} \cdot \frac{x_1^2}{2}$
QR	$F_h = p_{tank} \cdot \frac{H_i}{2} - p_{tank} \cdot x_2$ $F_v = p_{tank} \cdot \frac{L_i}{2}$ $M_{QR} = M_R - p_{tank} \cdot \frac{H_i^2}{8} - p_{tank} \cdot \frac{x_2}{2} + p_{tank} \cdot \frac{L_i \cdot x_2}{2}$

Now, the reaction moments at P and R can be calculated by substituting the force and moment distributions in Equation 8.16:

$$M_p = \frac{p_{tank}}{12} \cdot \left[1.5 \cdot L_i^2 - H_i \cdot \left(\frac{1 + \alpha^2 K}{1 + K}\right)\right] \tag{8.17}$$

$$M_R = \frac{p_{tank} \cdot H_i^2}{12} \cdot \left[1.5 - \left(\frac{1 + \alpha^2 K}{1 + K}\right)\right] \tag{8.18}$$

where

$$\alpha = \frac{L_i}{H_i} \quad ; \quad k = \frac{I_2}{I_1} \cdot \alpha$$

The stress in both PQ and QR can now be calculated as function of the skin thickness by realising that the total stress (S_T) is the sum of the membrane stress (S_m) and bending stress (S_b). The membrane stress is constant throughout the length of the section, whereas the bending stress is maximum at point P and R. The total stresses at point P and R can be calculated:

$$\begin{aligned} (S_T)_P &= (S_m)_P + (S_b)_P \\ &= \frac{p_{tank} \cdot H_i}{2 \cdot t_1} + M_P \cdot \frac{t_1}{2 \cdot I_1} < \sigma_m \end{aligned} \tag{8.19}$$

$$\begin{aligned} (S_T)_R &= (S_m)_R + (S_b)_R \\ &= \frac{p_{tank} \cdot L_i}{2 \cdot t_2} + M_R \cdot \frac{t_2}{2 \cdot I_2} < \sigma_m \end{aligned} \tag{8.20}$$

These equations are applied for all possible combinations of wall thicknesses (t_1 and t_2) between 1 and 10 mm. The total stress within PQ and PR cannot exceed the maximum allowable stress (σ_m). Stress concentration factors are not included in the above equations, as the formulas have been validated through independent computer analysis [73]. All possible combinations of t_1 and t_2 that do not exceed the maximum allowable stress, and the maximum allowable tank height are stored. The internal tank height (H_i) is calculated by:

$$H_i = \frac{V_{tank}}{(L_o - 2 \cdot t_2) \cdot (W_o - 2 \cdot t_2)} \tag{8.21}$$

where V_{tank} is the internal tank volume. The external tank height (H_o) is calculated by:

$$H_o = H_i + 2 \cdot t_1 \tag{8.22}$$

This procedure is repeated for face B. The combinations of t_1 and t_2 that satisfy both the maximum allowable stress and the maximum allowable tank height for face A and B (thus the overlap between both faces) are considered for the mass calculation. This is done, as the tank must survive both the stresses calculated for face A and face B. Now, the mass of the tank shell (M_{tank}) can be calculated:

$$\begin{aligned} M_{tank} &= \rho_{mat} \cdot [L_o \cdot H_o \cdot W_o - L_i \cdot H_i \cdot W_i] \\ &= \rho_{mat} \cdot [L_o \cdot H_o \cdot W_o - (L_o - 2 \cdot t_2) \cdot (H_o - 2 \cdot t_1) \cdot (W_o - 2 \cdot t_2)] \end{aligned} \tag{8.23}$$

where ρ_{mat} is the density of the tank material.

Cylindrical Tank with Flat End Caps

The mass and height of the cylindrical tank with flat end caps is calculated by following the AMSE Boiling and Pressure Vessel Code [75, p.35-36]. An internally pressured cylindrical tank experience both a longitudinal and a circumferential stress within its tank walls, where the longitudinal stress is half that of the circumferential stress. The design of the tank must therefore be based on the circumferential stress. The circumferential stress (σ_c) can be calculated by using Equation 8.24,

$$\sigma_c = \frac{p_{tank} \cdot D_m}{2 \cdot t_s} \tag{8.24}$$

where p_{tank} is the pressure within the propellant tank, D_m is the mean diameter of the cylinder, and t_s is the skin thickness. This equation can be rewritten to calculate the required skin thickness as function of the outer diameter (D_o) and the maximum allowable stress (σ_m), as shown in Equation 8.25.

$$t_s = \frac{p_{tank} \cdot D_o}{2\sigma_m + p_{tank}} \tag{8.25}$$

Next, the inner diameter can be calculated by subtracting twice the skin thickness from the outer diameter. Furthermore, the internal height (H_i) of the cylinder can be calculated by using Equation 8.26,

$$H_i = \frac{4 \cdot V_{tank}}{\pi \cdot D_i^2} \tag{8.26}$$

where V_{tank} is the tank volume, and D_i is the internal tank diameter. The required head thickness (t_h) can be calculated by using Equation 8.27,

$$t_h = D_i \sqrt{\frac{C \cdot p_{tank}}{\sigma_m \cdot E_j}} \tag{8.27}$$

where C is a factor that depends on the method of attachment to the shell, and E_j is the joint efficiency. An attachment factor of C = 0.33 is assumed, and is applicable for a welded joint where the minimum skin thickness of the seamless shell must be a factor 1.25 larger than the calculated skin thickness from Equation 8.25. This method of fastening the head to the shell in shown in Figure 8.9. A joint efficiency of 1 is assumed, and is applicable when a full radiographic examination of the weld is performed.

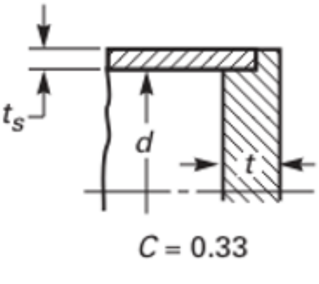

Figure 8.9: Welded connection between the cylindrical shell and the flat end cap [75, p. 35].

The external tank height (H_o) can now be calculated by adding the required head thickness twice to the internal tank height as was calculated in Equation 8.26. Finally the required tank mass (M_{tank}) can be calculated:

$$\begin{aligned} M_{tank} &= \rho_m \cdot (V_{shell} + V_{head}) \\ &= \rho_{mat} \cdot \left(\pi \cdot D_i \cdot t_s \cdot H_o + \frac{\pi \cdot D_i^2 \cdot t_h}{2} \right) \end{aligned} \tag{8.28}$$

where ρ_{mat} is the density of the tank material, V_{shell} is the required material volume of the seamless tube, and V_{head} is the required material volume of the flat end caps.

Manufacturability

Manufacturability takes into account both the ease of creating the specific tank shape and the method used for manufacturing the tank, which depends on the chosen material. These methods include the material's weldability, machinability, and suitability for additive manufacturing techniques. The optimal combination of tank shape and material, in terms of manufacturability, is one that facilitates easy creation of the tank shape and is compatible with the most manufacturing methods.

8.5.4 Results

Maximum Allowable Stress

Before going to the calculation results of both the shell mass and tank height for the rectangular and cylindrical propellant tank, it is important to explain what is meant by the maximum allowable stress (σ_m) within the tank walls.

As stated in requirement *PROP-TANK-07* and *PROP-TANK-08*, the tank shall have a design factor of safety (FoS) of 1.25 for yield, and 1.4 for ultimate load. The smallest allowable stress within the structure, that is a result of dividing both the tensile yield strength (σ_y) by the factor of safety for yield (FoS_y), and the ultimate tensile strength (σ_u) by the factor of safety for ultimate load (FoS_u) is to be used as the maximum allowable stress within the propellant tanks. By doing this, it is ensured that the structure can survive a yield load and an ultimate load. The definition of the maximum allowable stress is:

$$\sigma_m = min\left(\frac{\sigma_y}{FoS_y} \quad ; \quad \frac{\sigma_u}{FoS_u}\right) \tag{8.29}$$

The maximum allowable stress for each material is summarized in Table 8.4.

Table 8.4: Maximum allowable stress for each material.

Material	**Aluminium 6061-T6**	**304L Stainless Steel**	**Titanium Grade 5**	**Inconel - 718**
σ_y [MPa]	276	210	880	1100
σ_u [MPa]	310	564	950	1375
FoS_y [-]	1.25			
FoS_u [-]	1.4			
σ_y/FoS_y [MPa]	220.8	168.0	704.0	880.0
σ_u/FoS_u [MPa]	221.4	402.9	678.6	982.1
σ_m (Design Case) [MPa]	220.8 (Yield)	168.0 (Yield)	678.6 (Ultimate)	880.8 (Yield)

Shell Mass and Tank Height

Rectangular Tank

The intermediate steps of the calculation for a titanium propellant tank for the 200 Ns propulsion system is outlined. Figure 8.10 shows the required tank wall thicknesses for both face A (in blue) and face B (in red).

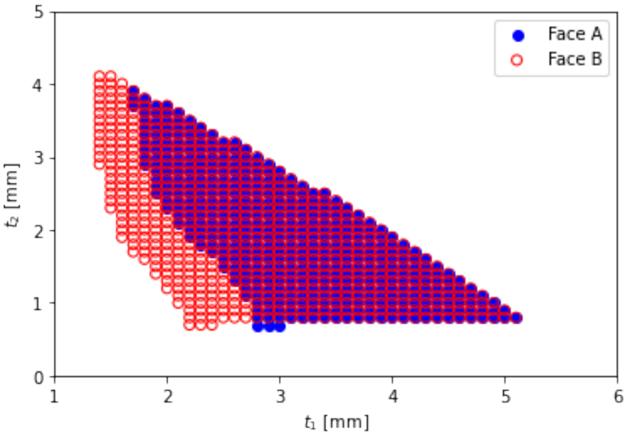

Figure 8.10: Possible wall thicknesses to survive the internal pressure load.

It can be seen that face B can survive the internal pressure load with smaller wall thicknesses than face A. This can be explained by the smaller length of face B (75 mm vs 92 mm), which results in a lower reaction moment at point P and a lower membrane stress in point R (see Figure 8.8). However, both face A and face B must withstand the internal pressure load. Therefore, only the tank thickness combinations that satisfy the requirements for both faces can be included in the shell mass and tank height calculation. Figure 8.11 shows the overlap in the required tank thicknesses for both face A and face B, where the point of minimum mass and height in indicated in red.

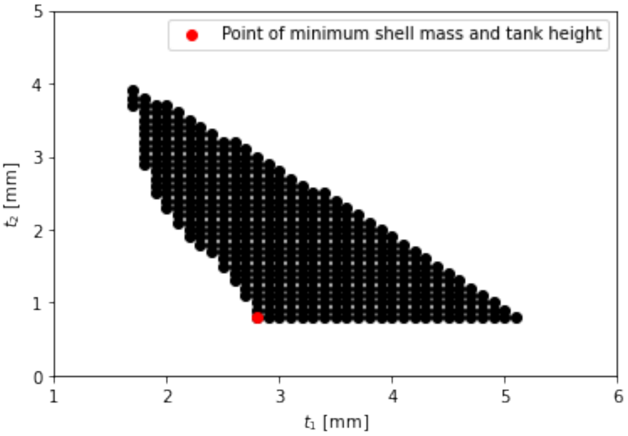

Figure 8.11: Overlapping wall thicknesses of both face A and face B

These steps are performed for all three propulsion systems for which the outcomes are summarized in Table 8.5. The values in the table entries separated by a '/' correspond to the 200 Ns (0.5 U), 400 Ns (1.0 U) , and 600 Ns (1.5 U) respectively, whereas the N.A. indicate that the use of that material for a specific system exceeds both the mass and height budgets and cannot be used.

Table 8.5: Rectangular tank shell mass and height.

Material	**Aluminium 6061-T6**	**304L Stainless Steel**	**Titanium Grade 5**	**Inconel-718**
t_1 [mm]	N.A / 4.1 / N.A.	N.A. / N.A. / N.A.	2.8 / 1.9 / 4.2	2.5 / 1.9 / 3.2
t_2 [mm]	N.A / 3.6 / N.A.	N.A. / N.A. / N.A.	0.8 / 1.8 / 2.8	0.7 / 1.5 / 2.5
Shell Mass [g]	N.A / 437 / N.A	N.A. / N.A. / N.A.	218 / 334 / 777	358 / 546 / 1221
Tankage Mass Budget [g]	347 / 696 / 1045	347 / 696 / 1045	347 / 696 / 1045	347 / 696 / 1045
Percentage of Mass Budget	N.A. / 63 % / N.A	N.A. / N.A. / N.A.	63 % / 48 % / 75 %	103 % / 79 % / 117 %
Tank Height [mm]	N.A / 99.7 / N. A	N.A. / N.A. / N.A.	45.3 / 87.2 / 139.7	44.5 / 85.6 / 135.8
Height Budget [mm]	50 / 100 / 150	50 / 100 / 150	50 / 100 / 150	50 / 100 / 150
Percentage of Height Budget	N.A. / 100% / N. A.	N.A. / N.A. / N.A.	91 % / 87 % / 93 %	89 % / 86 % / 91 %

Based on the data in Table 8.5, it can be concluded that titanium is the only material suitable for a rectangular propellant tank. This is because the mass and external tank height for all three systems (the 200, 400, and 600 Ns) fall within the allocated mass and height budget. An interesting observation is that the 400 Ns system utilizes the lowest percentage of the mass and height budget. This is due to the cubic shape of the propellant tank, which results in similar membrane and bending stresses in the lid, side panels, and bottom. Consequently, this leads to a relatively uniform wall thickness and a lower overall shell mass, and tank height.

Aluminium 6061-T6 can only be used for the 400 Ns system, where more than 60 % of the mass budget is used, and almost the entire height budget. Furthermore, it is impossible to use 304L stainless steel, as both the tank mass and external tank height exceed their respective budgets. Finally, Inconel-718 can only be used for the 400 Ns system, as the shell mass for both the 200 Ns and 600 Ns surpasses the allocated mass budgets.

Cylindrical Tank with Flat End Caps

The results of the cylindrical tank with flat end caps are summarized in Table 8.6, where the values in the table entries, separated by a '/' correspond to the 200 Ns (0.5 U), 400 Ns (1.0 U), and 600 Ns (1.5 U) respectively.

Table 8.6: Cylindrical tank shell mass and height.

Material	Aluminium 6061-T6	304L Stainless Steel	Titanium Grade 5	Inconel-718
Skin Thickness [mm]	0.5	0.35	0.3	0.5
Head thickness [mm]	3.6	4.1	2.1	1.8
Shell Mass [g]	143 / 158 / 174	462 / 494 / 527	138 /153 / 168	240 / 287 / 334
Tankage Mass Budget [g]	347 / 696 / 1045	347 / 696 / 1045	347 / 696 / 1045	347 / 696 / 1045
Percentage of Mass Budget	41 % / 23 % / 17 %	133 % / 71 % / 50 %	40 % / 22 % / 16 %	69 % / 41 % / 32 %
Outer Height [mm]	47.7 / 88.1 / 128.4	48.4 / 88.6 / 128.6	44.3 / 84.4 / 124.3	44.1 / 84.5 / 124.8
Height Budget [mm]	50 / 100 / 150	50 / 100 / 150	50 / 100 / 150	50 / 100 / 150
Percentage of Height Budget	95 % / 88 % / 86 %	97 % / 89 % / 86 %	89 % / 84 % / 83 %	88 % / 85 % / 83 %

A first observation that can be made is that the required skin and head thickness is independent of the performance (in terms of delivered total impulse) of the propulsion system. Aluminium 6061-T6, titanium grade 5, and Inconel-718 are suitable materials for a cylindrical tank with flat end caps, as both the mass and tank height are within the allocated budgets for all three systems. 304L stainless steel cannot be used for a cylindrical tank, as the mass of the smallest system exceeds the tankage mass budget by 33 %.

A second observation is that, unlike the rectangular tank, the portion of the mass and height budget used decreases as the system size increases. This is due to the cylindrical shape's greater efficiency in withstanding internal pressures compared to the rectangular tank.

The critical design case is that of the smallest system, as it uses the largest portion of the mass and height budget. In this scenario, aluminium and titanium have similar mass requirements, whereas the required tank height is larger for aluminium. Inconel-718 has the highest shell mass, while the external tank height is comparable to that of titanium.

Manufacturability

The manufacturability of a titanium rectangular tank, and a cylindrical tank that is made aluminium, titanium, and Inconel-718 is considered here. The other combinations of tank shape and materials are not included, as these combinations resulted in the exceeding of the allocated shell mass and/or height budget.

Tank Shape

With regards to the ease of creating the tank shape, it is clear that a cylindrical tank is the easiest to manufacture, as the shell wall thickness and head thickness do not change between the system sizes (Table 8.6). The fact that the shell and head thickness does not change with the system size allows for the use of the same cylindrical tube and plate for each tank, where only the length of the cylindrical tube varies.

The wall thicknesses of the titanium rectangular tank vary for each system size (Table 8.5). This variation increases the complexity of manufacturing the tank, as it necessitates multiple tube and plate thicknesses and/or different machining and additive manufacturing programs for each system size.

Aluminium 6061-T6

Aluminium 6061 is an aluminium alloy that contains both silicon and magnesium. This alloy can be welded using gas welding, manual metal arc welding (MMA), metal inert gas welding (MIG), tungsten inert gas welding (TIG), resistance welding, and brazing. Most used welding methods are MIG welding, TIG welding, and friction stir welding (FSW). The latter is applicable to almost all aluminium alloys but requires full accessibility of the welding interface. Aluminium is sensitive to thermal cracking of the weld as the heat affected zone (HAZ) cools. A filler material can be used to provide additional material to fill the gaps and prevent cracking by supplying alloying substances. It is important to realise that the structure of the aluminium is always altered by the heat of welding, where the rapid cooling affects the structure of the material away from that produced by a normal heat treatment. The joint efficiency, defined as the ultimate tensile strength of the weld over the ultimate tensile strength of the base material, indicates the decrease in the weld's mechanical properties [76]. Joint efficiencies of up to 80 % are realised when using FSW [77].

Furthermore, aluminium 6061-T6 can be easily machined, as it does not contain high silicon (Si) contents (above 7.5 % weight) or hard silicon carbide (SiC) and aluminium oxide (Al2O3) particles. A cutting fluid is the be used to prevent excessive heating and sticking to the cutting surface [78], where mineral oil can be used as a cutting fluid for micro-milling [79].

Finally, aluminium 6061 is unsuitable for additive manufacturing techniques that involve high thermal gradients along the build direction of the structure, such as laser powder bed fusion (LPBF). The high thermal gradients result in excessive porosity and the formation of solidification cracking [80]. However, there is promising research performed on friction stir powder additive manufacturing. This method of additive manufacturing reduces the thermal gradient along the build direction which enhances the microstructure and mechanical properties when compared to LPBF [81].

Titanium Grade 5
Titanium, and titanium alloys (such as Ti-6Al-4V, also known as titanium grade 5) are readily weldable by fusion welding processes. These include gas-tungsten arc welding (GTAW), gas-metal arc welding (MIG), plasma arc welding (PAW), electron-beam welding (EBW), laser-beam welding (LBW), friction welding (FRW), resistance welding (RW), diffusion welding (DW), explosive welding (EW), and brazing. One problem with welding titanium is that the heated area easily reacts with oxygen and nitrogen in the air, which affects the mechanical properties. Proper shielding from air during arc welding is essential to prevent this issue. The metal is not exposed to air when using resistance welding methods such as spot welding and seam welding, making these techniques generally suitable for titanium. Pressure welding, welding by using inert gases or welding without heat are the preferred welding methods for titanium, as there is no interaction possible between the metal and the air. Gas-tungsten arc welding is found to be the best way to weld titanium, as it is safe, cheap, does require high welding skills, and has a wide range of applications [82].

Titanium alloys, including Ti-6Al-4V, are inherently difficult to machine due to its low thermal conductivity. However, several strategies allow for enhancing the machinability. These strategies include: the use of effective cooling strategies, process design, optimization of process parameters, and the selection of appropriate cutting tools including the use of coatings [83]. Features as small as 0.2 mm x 0.05 mm can be milled when using a tungsten carbine flat end mill with a titanium-aluminium-nitride coating [84].

Titanium alloys are suitable for additive manufacturing techniques, where laser powder bed fusion (LPBF) can produce minimum wall thicknesses of 0.1 mm, where overhang structures can attain a minimum wall thickness of 0.3 mm and an inclination angle of up to 60 degrees [85]. The machinability of laser powder bed fusion also increases in terms of its mechanical properties, cutting force, roughness, and burr formation [86].

Inconel-718
Inconel-718 can be welded by laser welding (LW), electron beam welding (EBW), gas tungsten arc welding (GTAW), friction welding (FW), and metal inert gas welding (MIG). However, liquation cracking (or micro fissuring) and fusion zone cracking are problematic in Inconel-718 weldments, despite the reputed possession of good weldability. Pre and post weld heat treatments minimise the liquation cracking in the heat affected zone (HAZ) [87].

Inconel-718 is one of the most difficult-to-machine materials, as the high amount of heat generated at the tip of the cutting tool results in significant tool wear. The high temperatures lead to work material adhering to the cutting tool. The use of flood cooling cannot be applied at high cutting speeds due to the formation of a heat transfer hindering bubble barriers, whereas the use of a low cutting speed decreases the productivity. High pressure cooling can be applied to higher cutting speeds but requires severe environmental obligations and laws for the disposal of these cutting fluids [88].

Like Ti-6Al-4V, Inconel-718 can be additively manufactured using laser powder bed fusion (LPBF). This method of additive manufacturing allows for minimum wall thicknesses of approximately 0.1 mm, and an inclination angle up to 45 degrees [85]. A study demonstrated that laser powder bed fusion can be utilized to manufacture pressure vessels capable of withstanding internal pressures up to 50 bar, with wall thicknesses varying from 0.5 to 2 mm [89].

8.5.5 Conclusion

The four possible tank shape and material combinations are a rectangular tank made from grade 5 titanium, and a cylindrical tank made from either aluminium 6061-T6, grade 5 titanium, or Inconel-718. The rectangular tank design was included in the trade-off due to its efficient use of the XY design space when compared to a cylindrical tank. However, this tank shape requires a large wall thickness due to the shapes inefficiency to withstand internal pressures. This increase in wall thicknesses, when compared to the cylindrical tank designs, results in a larger required internal and external tank height. Furthermore, the required shell mass for the larger systems (1.0 U and 1.5 U) exceeds that of the cylindrical options, whereas the shell mass of the smallest system is comparable to that of the cylindrical tank made from Inconel-718: the heaviest of the cylindrical designs. Finally, the manufacturability of the rectangular shape is more complex than the cylindrical one, as the required wall thickness varies for each system size. Using a uniform wall thickness for all designs would simplify manufacturability but would exceed the allocated mass and height budgets. Therefore, the rectangular tank made from grade 5 titanium is discarded.

As shown in Table 8.6, the most critical design case for a cylindrical tank is that of the smallest system, where the largest portion of the mass and height budget are used. The Inconel-718 cylindrical tank design uses almost 70 % of the mass budget, which does not allow for much design space for the rest of the tankage system. Both the aluminium and titanium cylindrical tanks are possible options when looking at the used mass and height budgets, of which the titanium tank uses the smallest percentage of the allocated mass and height budget.The fact that almost the entire height budget is taken up by the tank height results in this being the most critical trade-off parameter. This makes the cylindrical tank made of titanium grade 5 the winner of the trade-off regarding the shell mass and tank height criteria.

With respect to the manufacturability criterion. The inconel-718 option was discarded due to the tank shell mass for the smallest system, and is therefore not considered here. The manufacturability of an aluminium 6061-T6 and titanium grade 5 tank are comparable, and do not influence the outcome of the trade-off in any way. As for aluminium 6061-T6, it can be welded and machined, whereas the use of additive manufacturing methods is still a point of research. Grade 5 titanium can also be welded and machined. However, grade 5 titanium is much more difficult to machine due to its low thermal conductivity. This decreased machinability can be mitigated through several strategies, such as the selection of appropriate cutting tools, and the use of coatings. Finally, grade 5 titanium can be additively manufactured through laser powder bed fusion.

In conclusion, the cylindrical tank made from grade 5 titanium (Ti-6Al-4V) was the optimal choice due to its combination of low tank shell mass and height, and the versatility in construction methods, including welding, machining, and additive manufacturing. The aluminium 6061-T6 cylindrical tank was discarded for its tank height, whereas the cylindrical tank made of Inconel-718 was discarded due to the high shell mass for the critical design case (the 0.5 U system) and negligible tank height benefits. Finally, the rectangular tank option was rejected due to the combination of both its large shell mass and tank height for all three system sizes. The results of the trade-off are summarized in Table 8.7 for the 0.5 U system, where the winner of the trade-off in indicated in **bold face**.

Table 8.7: Trade-off table for the 0.5 U system.

Tank Shape	Rectangular	**Cylindrical**		
Material	Titanium Grade 5	Aluminium 6061-T6	**Titanium Grade 5**	Inconel-718
Mass Budget Used	63 %	41 %	**40 %**	69 %
Height Budget Used	91 %	95 %	**89 %**	88 %
Manufacturability	Medium	Good	**Good**	Good

It must be noted that all tank options resulted in a significant external tank height, close to the height limit of the entire propulsion system. In the most critical design case, that of the 200 Ns system, only 5.7 mm of the height budget remains for the thruster, piping, and mechanical and electrical interfaces. For the 400 Ns and 600 Ns systems, 15.6 mm and 25.7 mm of the height budget remain, respectively. These large external heights are a consequence of the 92 x 92 mm^2 PCB, which was not accounted for when generating the volume requirement, as they were based on the assumption of a 100 x 100 mm^2 XY plane being available for the design. Due to these large external heights, it is possible that some of the system volume requirements may need to be relaxed. Relaxing the requirement on system volume is preferred over using deployables, as deployables significantly decrease system reliability. The possible relaxation of the volume requirement for some of the systems will be addressed in the next phase of the design, where the additional height needed for each system will become clearer. Table 8.8 provides a summary of the three cylindrical tank configurations.

Table 8.8: Propellant tank specifications for the three propulsion systems.

Propulsion System	**200 Ns**	**400 Ns**	**600 Ns**
Shell thickness [mm]	0.3		
Head thickness [mm]	2.1		
Tank outer radius [mm]	46		
Outer tank height [mm]	44.3	84.4	124.3
Tank dry mass [g]	138	153	168
Internal volume [L]	0.263	0.526	0.788

8.6 Mechanical Interface Design of Propellant Tank

The propellant tank must be structurally integrated into the propulsion system. It is decided to make use of the PCB template, where the attachment point holes must line up with the holes in the PCB. This allows to make use of four rods to attach the tank at the top and bottom. Four connection points are used at the top, whereas only two are used at the tank bottom. The latter is done to allow for components of the piping to fit next to tank. An example of the mechanical interface layout is shown in Figure 8.12a, where the top connection points are indicated by a purple cross and the bottom connection points are indicated in green. An example of the actual mechanical interface is shown in Figure 8.12b, where w_c is the width of the connection beam, L_{avg} is the average length of the beam, and t_c is the thickness of the beam. This mechanical interface design is used to allow for piping and electrical connections to be routed next to the tank if necessary.

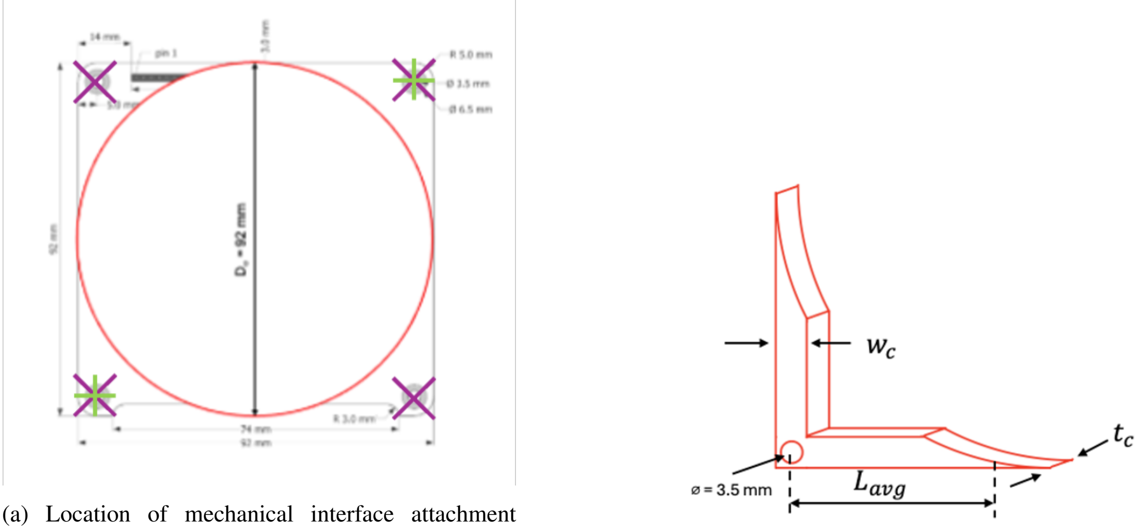

(a) Location of mechanical interface attachment points, with the top attachment points in purple, and the two bottom attachment points in green.

(b) Mechanical interface design.

Figure 8.12: Visualization of the mechanical interface location and design.

The mechanical tank interface must be designed such that it survives the most critical load case: launch. As per requirement *PROP-TANK-17* and *PROP-TANK-18*, the propulsion system must survive lateral loads of up to 3g and axial loads up to 8.5g. Furthermore, the natural frequency of the interface must be larger than 35 Hz, as per requirement *PROP-TANK-19*. A simplified analysis is performed for the design of the mechanical interface due to time constraints and must be verified later using finite element methods. The sizing of the mechanical interfaces for launch load is presented in Subsection 8.6.1, and is followed by the sizing for natural frequency in Subsection 8.6.2. The preliminary design of the mechanical interfaces is concluded in Subsection 8.6.3.

8.6.1 Sizing for Launch Loads

The sizing of the mechanical interface for the launch loads starts by calculating the forces within the connection points. Figure 8.13 shows the free-body diagram (FBD) and kinetic diagram (KD) of the propellant during launch, where θ is the angle of the propulsion system with respect to the launch vehicle. The reaction forces at the connection point between the propellant tank and interface can be solved in the launch vehicle reference frame (subscript 1) using:

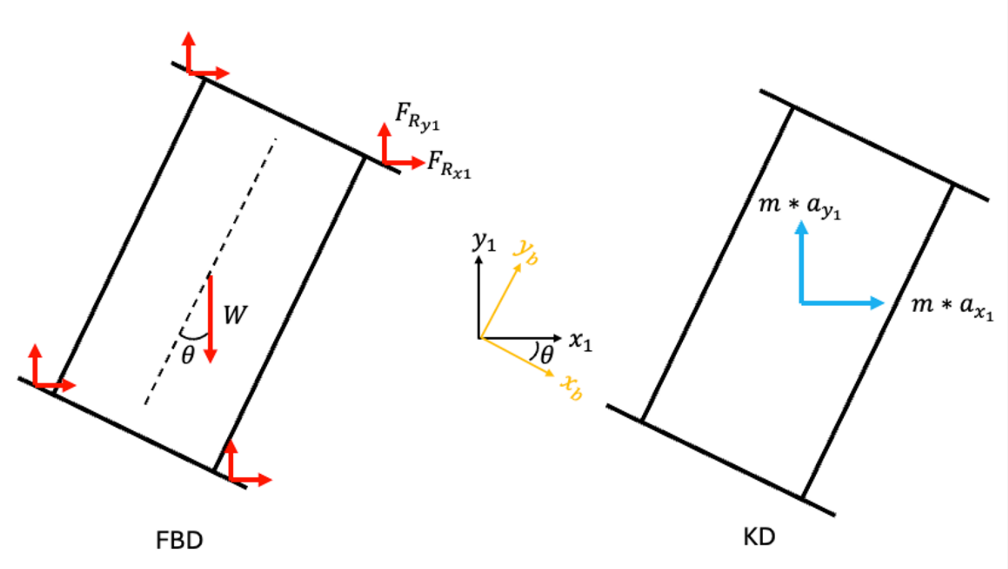

Figure 8.13: Free-body diagram (FBD) and kinetic diagram (KD) of propellant tank during launch.

$$F_{R_{x_1}} = \frac{1}{6} M_{wet} a_{x_1} \tag{8.30}$$

$$F_{R_{y_1}} = \frac{m}{6} \left(a_{y_1} + g_0\right) \tag{8.31}$$

where M_{wet} is assumed to be the wet mass of the entire propulsion system, a_{x_1} is the lateral acceleration equal to $3g_0$, and a_{y_1} is the axial acceleration equal to $8.5g_0$. It is useful, for the design of the mechanical interface, to translate these reaction forces into the body frame (subscript b) of the propulsion system:

$$F_{R_{x_b}} = F_{R_{x_1}} \cos(\theta) - F_{R_{y_1}} \sin(\theta) \tag{8.32}$$

$$F_{R_{x_b}} = F_{R_{x_1}} \sin(\theta) + F_{R_{y_1}} \cos(\theta) \tag{8.33}$$

The results of this calculation for the smallest 200 Ns propulsion system is visualized in Figure 8.14 for three load cases: an axial load, a lateral load, and a combined (both axial and lateral) load. The combined load is the largest and must be used for the design of the mechanical interface. Moreover, the design load is chosen to be at the maximum reaction force in the y-direction. Table 8.9 summarizes the reaction forces for this load case at the connection points within the body frame of the three propulsion systems.

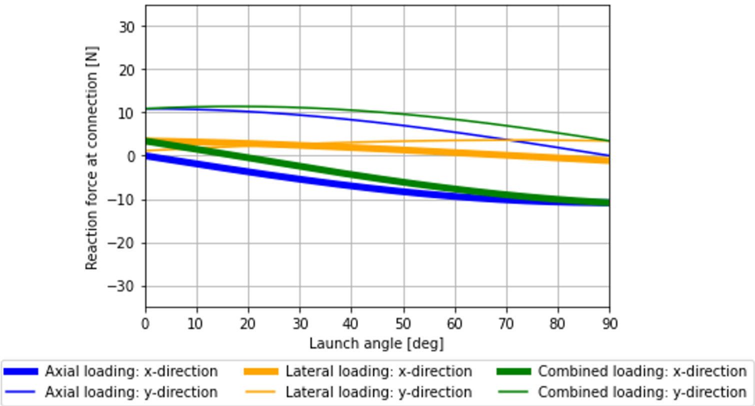

Figure 8.14: Reaction force at the interface between the connecting beam and propellant tank in the reference frame of the 200 Ns propulsion system.

Table 8.9: Reaction forces at the interface between the propellant tank and connecting beam for all three propulsion systems.

Propulsion System	**200 Ns**	**400 Ns**	**600 Ns**
$F_{R_{x_b}}$ [N]	-0.008	-0.016	-0.024
$F_{R_{y_b}}$ [N]	11.4	22.0	32.6

Next, the internal forces and moment in each connection point must be determined as a function of the width and thickness of the interface. It is assumed that both connection beams bear half of the previously calculated reaction forces. The critical load case is when the reaction force $F_{R_{x_b}}$ is acting only in the (negative) x-direction, as this will result in both a maximum axial load and bending moment. The mechanical interface can be decomposed in two beams, as shown in Figure 8.15. An internal force and moment analysis is performed on both beams.

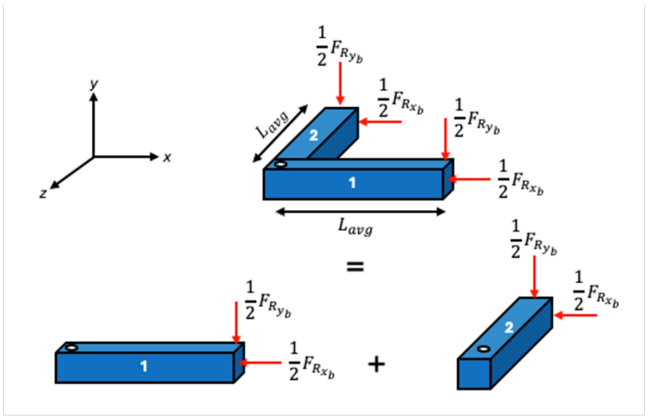

Figure 8.15: Free-body diagram of one (decomposed) mechanical interface.

The free-body diagram of the first beam is shown in Figure 8.16, and is used to solve for the reaction forces and moments at point A:

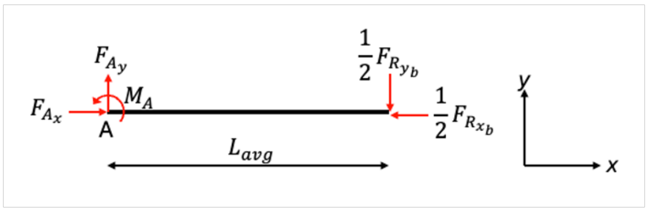

Figure 8.16: Free-body diagram of beam 1.

$$F_{A_x} = \frac{1}{2}F_{R_{x_b}} \tag{8.34}$$

$$F_{A_y} = \frac{1}{2}F_{R_{y_b}} \tag{8.35}$$

$$M_A = \frac{1}{2}L_{avg}F_{R_{y_b}} \tag{8.36}$$

Next, the internal normal force N_i, shear force V_i and bending moment M_i can be calculated as a function of the position along the beam (x):

$$N_i = -\frac{1}{2}F_{R_{x_b}} \tag{8.37}$$

$$V_i = \frac{1}{2}F_{R_{y_b}} \tag{8.38}$$

$$M_i = \frac{1}{2}F_{R_{y_b}}\left(L_{avg} - x\right) \tag{8.39}$$

The internal normal force and bending moment result in a maximum tensile (F_T) and compressive force (F_C) at point A:

$$F_T = \frac{1}{2}\left(\frac{F_{R_{y_b}}L_{avg}}{t_c} - F_{R_{x_b}}\right) \tag{8.40}$$

$$F_C = \frac{1}{2}\left(\frac{F_{R_{y_b}}L_{avg}}{t_c} + F_{R_{x_b}}\right) \tag{8.41}$$

This analysis is repeated for the second beam, where the free-body diagram (Figure 8.17) is used to solve for the reaction forces and moments at point A:

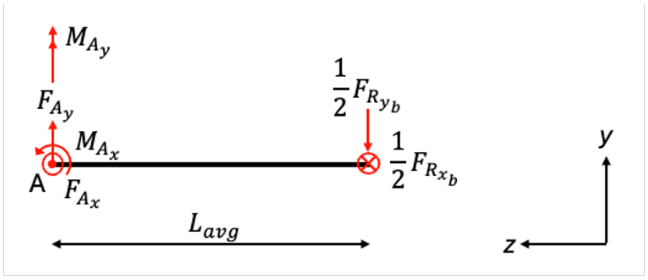

Figure 8.17: Free-body diagram of beam 2.

$$F_{A_x} = \frac{1}{2}F_{R_{x_b}} \tag{8.42}$$

$$F_{A_y} = \frac{1}{2}F_{R_{y_b}} \tag{8.43}$$

$$M_{A_x} = \frac{1}{2}L_{avg}F_{R_{y_b}} \tag{8.44}$$

$$M_{A_y} = -\frac{1}{2}L_{avg}F_{R_{x_b}} \tag{8.45}$$

The internal forces and moments along the beam are (from point A in the negative z-direction):

$$V_{x_i} = \frac{1}{2}F_{R_{x_b}} \tag{8.46}$$

$$V_{y_i} = \frac{1}{2}F_{R_{y_b}} \tag{8.47}$$

$$M_{x_i} = \frac{1}{2}F_{R_{y_b}}\left(L_{avg} - z\right) \tag{8.48}$$

$$M_{y_i} = \frac{1}{2}F_{R_{x_b}}\left(z - L_{avg}\right) \tag{8.49}$$

As with the previous case, the maximum forces and moments are found at point A (where z = 0). The tensile ($F_{T_{xz}}$) and compressive ($F_{C_{xz}}$) forces in the xz-plane are:

$$F_{T_{xz}} = F_{C_{xz}} = \frac{-F_{R_{x_b}}L_{avg}}{2w_c} \tag{8.50}$$

The tensile ($F_{T_{yz}}$) and compressive ($F_{C_{yz}}$) forces in the yz-plane are:

$$F_{T_{yz}} = F_{C_{yz}} = \frac{F_{R_{y_b}}L_{avg}}{2t_c} \tag{8.51}$$

Now, the maximum tensile (σ_T), compressive (σ_C), and shear load (τ) can be calculated using:

$$\sigma_T = \frac{F_T}{A_c} \tag{8.52}$$

$$\sigma_C = \frac{F_C}{A_c} \tag{8.53}$$

$$\tau = \frac{V}{A_c} \tag{8.54}$$

where A_c is the cross-sectional area of the beam. This area is calculated using:

$$A_c = \left(w_c - D_h\right)t_c \tag{8.55}$$

where D_h is the diameter of the hole (3.5 mm) that allows for the connecting rod to pass through. A width (w_c) of 5 mm and thickness (t_c) of 1 mm are used to ensure that the connection rod does not shear out of the mechanical interface. The internal loads for both connection beams are summarized in Table 8.10.

Table 8.10: Internal loads (in MPa) in each mechanical interface.

Propulsion System	**200 Ns**	**400 Ns**	**600 Ns**
Beam 1 [MPa]			
$\sigma_{T_{xy}}$	79.6	153.5	227.5
$\sigma_{C_{xy}}$	79.5	153.5	227.5
τ_{xy}	3.8	7.33	10.87
Beam 2 [MPa]			
$\sigma_{T_{xz}}$, $\sigma_{C_{xz}}$	0.011	0.022	0.033
$\sigma_{T_{yz}}$, $\sigma_{C_{yz}}$	79.6	153.5	227.5
τ_{xz}	0.0027	0.0054	0.008
τ_{yz}	3.8	7.33	10.87

These internal loads are well below the stated tensile yield strength (880 MPa), compressive yield strength (970 MPa), and shear strength (550 MPa) of Ti-6Al-4V. It can be concluded that the launch load will not break the mechanical interface with a width of 5 mm and thickness of 1 mm. Next, the natural frequency of the mechanical interface during launch must be determined.

8.6.2 Sizing for Natural Frequency

The primary axial and lateral natural frequencies of the mechanical interface must be larger than 35 Hz to avoid interaction with the launch vehicle, as per requirement *PROP-TANK-19*. The mechanical interface can be modelled as 12 individual mass-spring systems (6 interfaces, each with 2 beams), where one end of the beam is fixed (at the connection rod), and one is free to move (where the beam attaches to the tank) as shown in Figure 8.18.

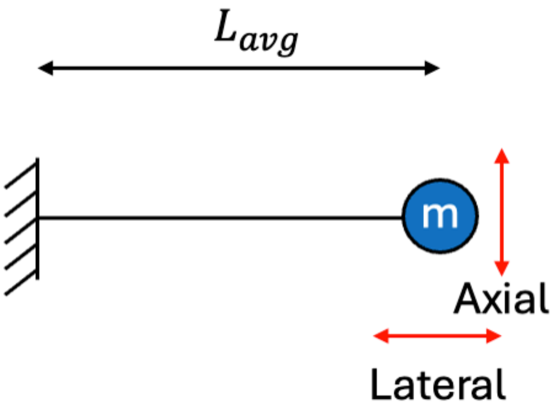

Figure 8.18: Mass spring system representation for one beam of the mechanical interface.

The axial (f_{n_a}) and lateral (f_{n_l}) natural frequency can be calculated using [41]:

$$f_{n_a} = 0.276\sqrt{\frac{EI}{mL_{avg}^3}} \tag{8.56}$$

$$f_{n_l} = 0.160\sqrt{\frac{A_cE}{mL_{avg}}} \tag{8.57}$$

where E is the modulus of elasticity, I is the area moment of inertia of the beam, A_c is the cross-sectional area of the beam, and m is the mass that is attached to each beam. It is assumed that each beam carries one-twelfth of the total wet mass of the propulsion system. It must be noted that these formulas are valid when assuming that the mass is concentrated at the free end of the beam, and that the beam has no mass. In reality, the end of the beam is not free to move, as it is connected to the tank, which in turn is connected to another connection rod. The resulting natural frequencies of this calculation are conservative, as the real configuration is stiffer due to the 6 mechanical interfaces. The axial and lateral natural frequencies for the three propulsion systems, using a beam width of 5 mm and a beam thickness of 1 mm, are summarized in Table 8.11

Table 8.11: Axial and lateral natural frequencies of the mechanical interface for all three propulsion systems.

Propulsion System	**200 Ns**	**400 Ns**	**600 Ns**
Axial natural frequency [Hz]	82.2	59.2	48.6
Lateral natural frequency [kHz]	165	119	97.6

Both the axial and lateral natural frequencies exceed the required 35 Hz, with the lateral acceleration being significantly larger than the axial acceleration. This is intuitive, as it is much easier to bend a square beam than to compress it.

8.6.3 Conclusion

It is concluded that the mechanical interface, consisting of two connected beams per interface with a width of 5 mm and a thickness of 1 mm, can be used for the attachment of the propellant tank to the main structure. This design allows for piping components to be placed next to the tank, and electrical connections to be routed towards the PCB. The internal stresses are well below the maximum allowed stresses, and the natural frequency is in excess of the required 35 Hz in both the axial and lateral direction. A more detailed analysis, using finite element methods, is required to verify these results. The mechanical interface, attached to both flat end caps, is visualized in Figure 8.19.

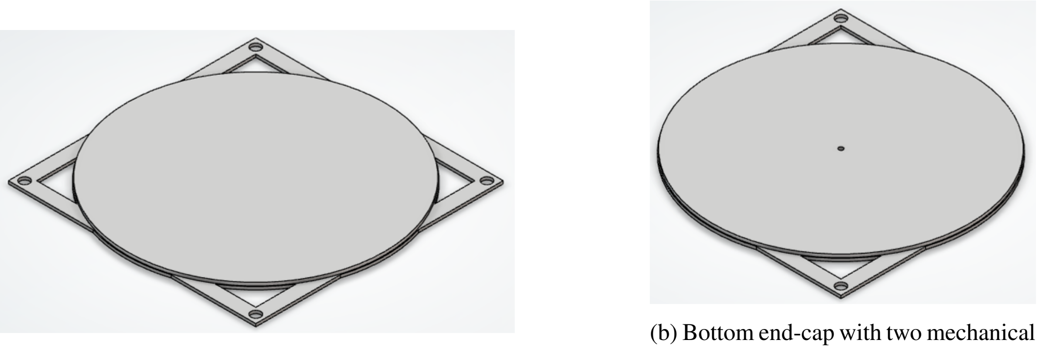

(a) Top end-cap with four mechanical interfaces.

(b) Bottom end-cap with two mechanical interfaces.

Figure 8.19: Visualization of the top and bottom endcaps.

8.7 Propellant Management Device Trade-off

The microgravity environment in space requires the use of propellant management devices within the propellant tank. The most commonly used ones were described in Section 8.3, and included both positive expulsion devices and capillary driven PMDs. This section outlines the qualitative trade-off between the different options based on the advantages, disadvantages, and use-cases for each of the options. A qualitative approach is chosen due to the difficulty in assigning quantitative values such as mass, volume, and reliability to each PMD. The selection of a PMD is not as critical, as both PEDs and STDs are successfully used in satellite propulsion systems, allowing for such a qualitative approach [90]. Table 8.12 summarizes the advantages, disadvantages, and use-cases for each PMD.

Table 8.12: Advantages, disadvantages, and use-cases of propellant management devices.

Name	Advantages	Disadvantages	Types	Use-cases	Sources
Positive Expulsion Devices					
Bladder	Slosh control, no reaction between propellant and pressurant, adaptable to many tank geometries, variable initial ullage gas volumes, small sealing area	Heavy, low expulsion efficiency when folding	Elastomeric	Slosh control, low thrust, high thrust	[71][90][91]
Diaphragm	Slosh control, no reaction between propellant and pressurant, high expulsion efficiency,	Heavy, large sealing area, poor long time wearability when sloshing, high initial ullage gas volume required	Elastomeric, metallic	Slosh control, low thrust, high thrust	
Piston	Slosh control, no reaction between propellant and pressurant, variable initial ullage gas volumes	Complex (sealing, guiding), heavy, risk of jamming	Metallic	Slosh control, low thrust, high thrust	
Surface Tension Devices					
Vanes	Lightweight, inexpensive, low residuals, reliable, low accelerations, low flow rates, omnidirectional, omnidurational	Complex design for liquids with large contact angles	Simple, ribbon, double, combination	Low thrust, zero-g resupply	[72] [90]
Gallery	Omnidirectional, omnidurational, medium accelerations, medium flow rate	Heavy, high cost, high residuals, low reliability	Screen covered channel, tubing with pick ups, liner	Omnidirectional systems, all propellants, smaller tanks and traps	
Sponge	Lightweight, inexpensive, low residuals, reliable, omnidirectional, passively refillable, control of both ullage and liquid, medium acceleration, medium flow rate	Limited burn duration	Radial, fan, accordion	Repeated events, CG control, ullage gas control	
Traps	Lightweight, low residuals, reliable, omnidirectional	Not passively refillable, expensive	Cylindrical, clamshell, bulkhead, venting	One time maneuvres, main engine ignition	
Troughs	Reliable, low residuals, high-g capable, refillable (except tubular)	Heavy (except tubular), high cost, limited directionality, limited use	Tubular, radial, cylindrical	High-g events, repeated higher-g manoeuvres	

8.7.1 Positive Expulsion Devices Advantages and Disadvantages

Two of the main advantages of PEDs over surface tension devices (STDs) is the effective slosh control, and the separation of pressurant from the propellant, where the latter prevents pressurant from reacting with the propellant. A reaction between propellant and pressurant can lead to a loss of pressure in the tank [90].

A bladder can be adapted to many tank shapes, has a small sealing area, and works with various initial ullage gas volumes. However, the fact that the bladder must cover the entire tank volume without excessive stretching makes it heavy. Furthermore, any folding of the bladder can lead to pinhole leaks and/or a reduced expulsion efficiency by trapping part of the propellant within the fold.

The diaphragm allows for a high expulsion efficiency but is also relatively heavy as it must cover the entire inside of the propellant tank. It requires a large sealing area, as it is often fastened to the outer perimeter of the tank at its widest point. Moreover, elastomeric bladders suffer from poor long-time wearability when sloshing, and requires a high initial ullage gas volume.

Pistons, like bladders, allow for variable initial ullage gas volumes, but are complex with regards to sealing and guiding, heavy, and have a significant risk of jamming. The latter makes it a less attractive option over the bladder and diaphragm, as jamming of the piston results in total failure of the propulsion system [90][91].

8.7.2 Surface Tension Devices Advantages and Disadvantages

Vanes are used in low thrust propulsion systems. They are lightweight, inexpensive, reliable, have a high expulsion efficiency, can passively refill, and can accommodate low flow rates in all directions and for all durations. However, the design of vanes is complex for liquids with large contact angles, such as water.

Sponges, like vanes, are inexpensive, reliable, have a high expulsion efficiency, and allow for passive refilling. While they are slightly heavier than vanes, they enable control over both the ullage gas and liquid propellant, thereby offering control over the centre of gravity. Additionally, they can accommodate a medium flow rate and acceleration, but only for a limited duration.

A gallery allows for omnidirectional and omnidurational acquisition of propellant at medium to high flow rates and accelerations. However, they are heavy, expensive, and have a low expulsion efficiency.

Traps are lightweight, reliable, have a high expulsion efficiency, and allow of omnidirectional acquisition of propellant. However, they are expensive and do not allow for passive refilling.

Finally, troughs are reliable where radial and cylindrical troughs can be refilled during high-g events. Downsides of troughs are that they are heavy, expect for tubular ones, expensive, have limited directionality, and can only be used for a limited number of manoeuvres [72].

8.7.3 Evaluating the Necessity of Positive Expulsion Devices

Table 8.12 summarizes the advantages, disadvantages, and use-cases of both PEDs and STDs. The main advantages of PEDs over STDs are their ability to better control propellant sloshing and to provide a physical barrier between the pressurant and propellant, preventing any possible reactions between the two. However, PEDs have some drawbacks, such as significant mass and low expulsion efficiency when folding occurs. Thus, it is important to assess the necessity of slosh control and the physical barrier between pressurant and propellant, as STDs are lighter and more reliable.

Propellant Sloshing Analysis

It was mentioned that PEDs allow for slosh control. It is therefore useful to analyze the slosh behaviour of the propellant within the cylindrical tank and to determine whether this inherent ability of PEDs to control slosh is necessary. Determining the slosh behaviour within a propellant tank can be seen as a standalone thesis topic due to its complexity. A simplified slosh analysis is performed for this reason. The analysis of the slosh behaviour is based on a mass-spring model that is excited by a harmonic translation in the X-direction and a pitching moment about the Y-axis [92]. The fluid can be split into the sloshing mass (M_{sl}) and the stationary mass (M_{st}), where the sum of both is equal to the total propellant mass (M_{prop}):

$$M_{sl} + M_{st} = M_{prop} \tag{8.58}$$

A relationship between the ratio of the stationary mass to the total propellant mass, and the ratio of the propellant height (H_{prop}) to the tank radius (r_{tank}) is found and shown in Figure 8.20.

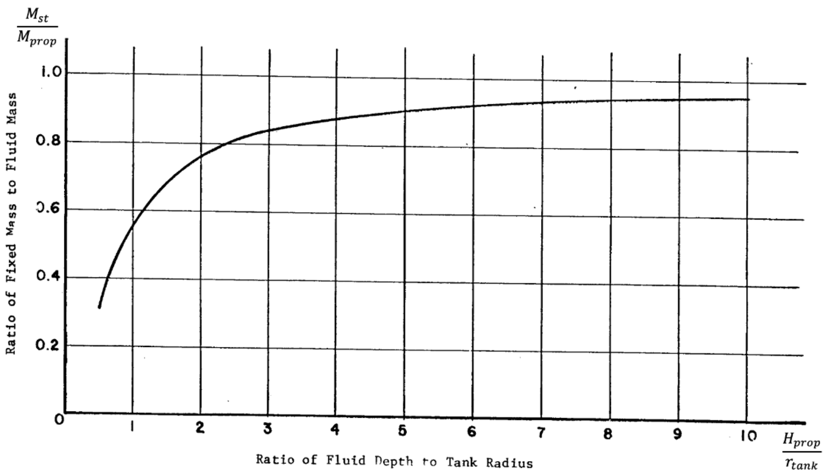

Figure 8.20: Fraction of stationary propellant mass to the total propellant mass as a function of the ratio of the liquid height to tank radius [92].

The ratio of sloshing mass to the total propellant mass can be found by rewriting Equation 8.58:

$$\frac{M_{sl}}{M_{prop}} = 1 - \frac{M_{st}}{M_{prop}} \tag{8.59}$$

Applying this methodology to the three propulsion systems with a fill ratio of 0.75 yields the following results:

Table 8.13: Sloshing propellant mass ratios.

System	**200 Ns**	**400 Ns**	**600 Ns**
Outer tank height [mm]	44.3	84.4	124.3
Head thickness [mm]	2.1		
Inner tank height [mm]	40.1	80.2	120.1
Tank outer radius [mm]	46		
Skin thickness [mm]	0.3		
Tank inner radius [mm]	45.7		
H_{prop}/r_{tank} [-]	0.66	1.3	2.0
M_{st}/M_{prop}	0.44	0.65	0.76
M_{sl}/M_{prop}	0.56	0.35	0.24
M_{prop} [g]	198	395	593
M_{sl} [g]	111	138	142
M_{wet} [g]	700	1350	2000
M_{sl}/M_{wet} [-]	0.16	0.10	0.07

As explain in Chapter 6, a fill ratio of 0.75 is used to ensure compatibility with both PEDs [55] and STDs [93][94]. The sloshing mass fraction decreases with larger propulsion systems. Although these fractions can be significant (0.56 for the smallest system), the ratio of sloshing mass to the propulsion system wet mass (M_{wet}) results into significantly smaller values. These fractions decrease even further when considering that the propulsion systems are integrated into CubeSats. In this context, the wet mass encompasses the entire satellite, leading to a notable reduction in the sloshing mass fraction. This is shown in Figure 8.21, where a mass of 2 kg per U is assumed [95].

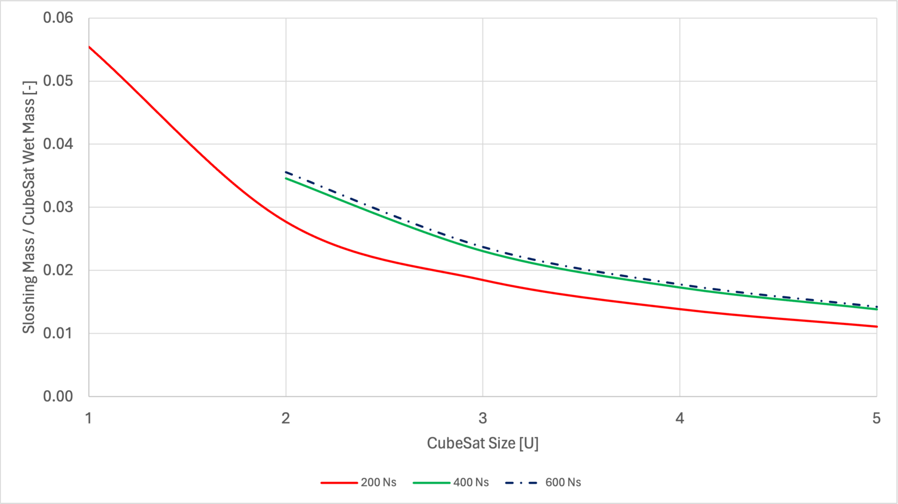

Figure 8.21: Ratio of the sloshing propellant mass to CubeSat wet mass as a function of CubeSat size.

The sloshing mass fraction drops below 0.03 for CubeSats larger than 2 U. The aforementioned analysis is performed at BOL, where the tanks are filled for 75%. However, as the tank empties (when the ratio H_{prop}/r_{tank} decreases), the proportion of sloshing propellant relative to the total propellant increases significantly, as illustrated in Figure 8.20. To ensure that this increase does not cause issues during the mission, further investigation into the impact of the tank emptying on the sloshing mass is necessary. Figure 8.22 depicts the sloshing mass as a function of the fill ratio for the three propulsion systems. It shows that the total sloshing mass decreases as propellant is expelled, with the maximum sloshing mass occurring at BOL. From this, it can be concluded that the BOL is the most critical in terms of propellant sloshing.

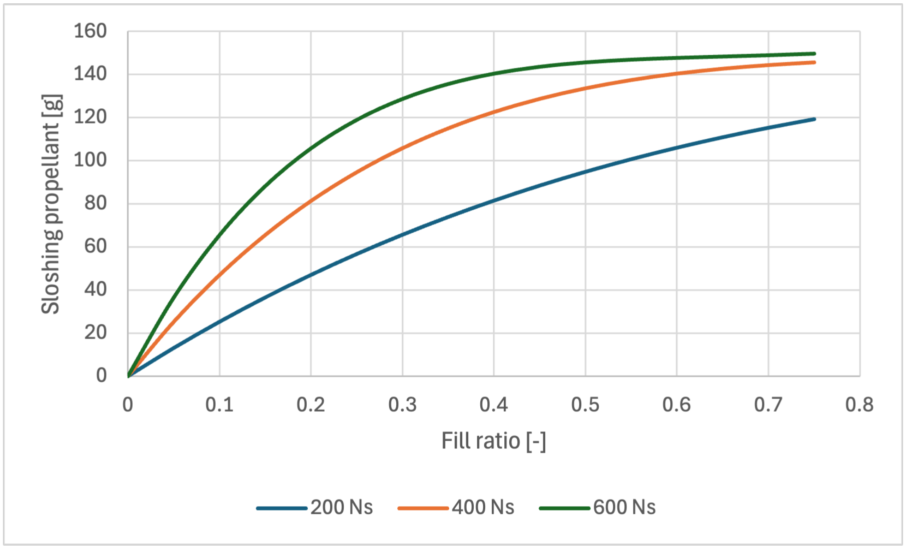

Figure 8.22: Sloshing propellant as a function of the fill ratio.

Another important sloshing parameter is the natural frequency of the slosh motion. The primary focus is on the first natural frequency of the motion since it carries most of the liquid's mass and has the longest period in liquid motion. This first natural frequency (ω_1) can be calculated for a contact angle (θ_c), the angle between the tank wall and the liquid surface boundary, of zero degrees (Equation 8.60) and 90 degrees (Equation 8.61),

$$\omega_1 = 1.61 \cdot \sqrt{\frac{\sigma_s}{\rho_{prop} r_{tank}^2}(1 + 0.789Bo)} \cdot tanh\left(\frac{1.841 H_{prop}}{r_{tank}}\right) \tag{8.60}$$

$$\omega_1 = \sqrt{\left(\frac{3.3893\sigma_s}{\rho_{prop} r_{tank}^3} + \frac{a_r}{r_{tank}}\right) \cdot 1.841 \cdot tanh\left(\frac{1.841 H_{prop}}{r_{tank}}\right)} \tag{8.61}$$

where σ_s is surface tension of the propellant, ρ_{prop} is the density of the propellant, a_r is the relative acceleration of the fluid in its tank, and Bo is the Bond number. The Bond number is defined as:

$$Bo = \frac{\rho_{prop} a_r L_c^2}{\sigma_s} \tag{8.62}$$

where L_c is a characteristic dimension of the tank, in this case the tank radius [96]. A relative acceleration of 10^{-6} g is assumed [41]. The first natural frequencies of the three systems for a contact angle of 0 degrees and 90 degrees are summarized in Table 8.14.

Table 8.14: First natural frequencies of the slosh motion.

System	**200 Ns**	**400 Ns**	**600 Ns**
ω_1 (θ_c = 0 deg) [Hz]	0.040	0.047	0.048
ω_1 (θ_c = 90 deg) [Hz]	0.316	0.343	0.346

The contact angle of water on titanium grade 5 is approximately 35.5 degrees [97]. Assuming a linear increase in natural frequency with contact angle, and using the contact angle of 35.5 degrees, results in a natural frequency of approximately 1 rad/s (or 0.16 Hz) for the three propulsion systems. Linking both the sloshing mass fraction and natural frequency of the slosh motion to the stability of a satellite is difficult as the stability differs for each combination of propulsion system and satellite size. However, the oscillating motion of the propellant within the tank can be represented by a pendulum with a torsional spring and torsional damping from linear system theory:

$$\frac{d^2\psi}{dt^2} + 2\gamma_d\omega_n\frac{d\psi}{dt} + \omega_n^2\psi = 0 \tag{8.63}$$

where ψ is the slosh angle, γ_d is the damping ratio, and ω_n is the natural frequency [96]. The oscillating fluid is damped by viscous stresses when there is no anti-slosh device present, as is the case here. The damping ratio can be calculated using Equation 8.64,

$$\gamma_d = 0.79\sqrt{\frac{\nu}{r_{tank}^2\omega_1}}\left[1 + \frac{0.318}{sinh\left(1.84\cdot\frac{H_{prop}}{r_{tank}}\right)}\cdot\left(1 + \frac{1-\frac{H_{prop}}{r_{tank}}}{cosh\left(1.84\cdot\frac{H_{prop}}{r_{tank}}\right)}\right)\right] \tag{8.64}$$

where ν is the kinematic viscosity of the propellant [98, p. 27]. Using the values provided in Table 8.13 gives damping ratios of 0.705, 0.568, and 0.546 for the 200 Ns, 400Ns, and 600 Ns system respectively. These damping ratios, combined with the natural frequency are used in Equation 8.63. The response (the slosh angle) of the three propulsion systems to an initial angular velocity equal to their respective natural frequencies is visualized in Figure 8.23.

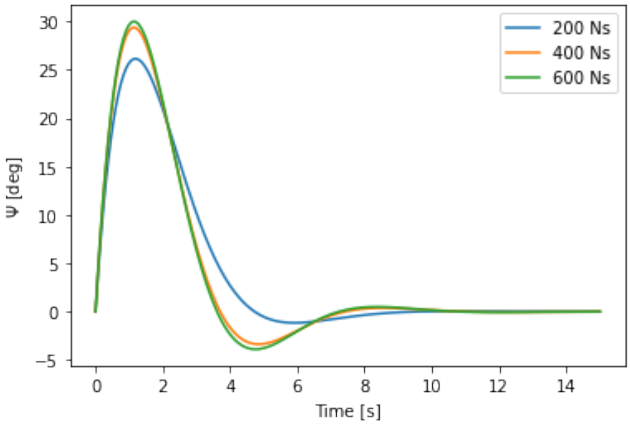

Figure 8.23: Propellant slosh angle after excitation at their first natural frequency.

The sloshing motion of the three system decays to zero within 12 seconds after the excitation of the propellant due to the viscous damping within the tank. This oscillatory decay of the slosh angle is comparable to similar sloshing research [96].

The combination of the small sloshing mass fraction [99], the low natural frequency of the sloshing motion, and the fast decay of the slosh angle after excitation leads to the conclusion that propellant sloshing can be neglected for now. Additionally, the fact that a propulsion system is integrated on a CubeSat dictates the need for an attitude control system (ACS) to be able to perform burns in the correct direction. This ACS can provide additional slosh dampening capabilities. A more detailed slosh analysis is left for future work.

Solubility of Nitrogen in Water

One of the defining differences between PEDs and STDs is that PEDs separate the pressurant from the propellant using a physical barrier. This ensures that there cannot be any chemical reaction between the two. Nitrogen, being an inert gas, does not react with water. However, the solubility of nitrogen in water can be of concern as it may lead to a notable decrease in pressure within the propellant tank.

The solubility of nitrogen (in grams of nitrogen per kg of water) in water is plotted as a function of the temperature within the tank for different tank pressure levels in Figure 8.24. It can be seen that the solubility increases with an increase in tank pressure, and decreases with an increase in tank temperature.

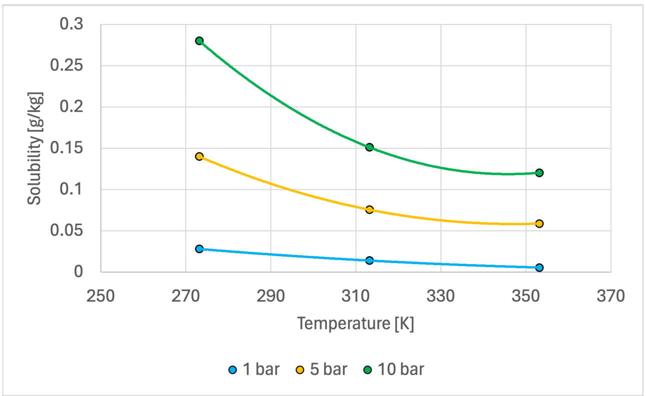

Figure 8.24: The solubility of nitrogen in water as a function of the tank temperature [100].

The amount of nitrogen (M_{N_2}) that is dissolved in water can be calculated using Equation 8.65,

$$M_{N_2} = S \cdot M_{prop} \tag{8.65}$$

where S is the solubility and M_{prop} is the propellant mass. The required pressurant and propellant masses for each system size are summarized in Table 8.15.

Table 8.15: Required pressurant and propellant mass for each system.

System	**200 Ns**	**400 Ns**	**600 Ns**
Pressurant Mass [g]	0.756	1.51	2.27
Propellant Mass [g]	197	394	590

The results of applying Equation 8.65 to the three systems can be found in Table 8.16, where a linear increase of the amount of dissolved nitrogen as a function of the tank pressure and delivered impulse can be seen for all three systems.

Table 8.16: The maximum amount of dissolved nitrogen (in grams) in water at 293.15 K as a function of tank pressure.

System	**200 Ns**	**400 Ns**	**600 Ns**
1 bar	0.0040	0.0080	0.0120
5 bar	0.0201	0.0401	0.0601
10 bar	0.0401	0.0802	0.1201

The pressure drop within the propellant tank as a result of the nitrogen dissolving in water can be calculated using the ideal gas law:

$$p_{tank} \cdot V_{tank} = \frac{M_{pres}}{M_W} \cdot R_A \cdot T_{tank} \tag{8.66}$$

where p_{tank} is the pressure in the tank, V_{tank} is the tank volume, M_{pres} is the pressurant mass, M_W is the molar mass of the pressurant, R_A is the universal gas constant, and T_{tank} is the temperature within the tank. The pressure drop within the tank (Δp_{tank}) as a result of the nitrogen dissolving in water can be calculated using Equation 8.67 when assuming that the density of the propellant does not change when the pressurant is dissolved, and that the temperature within the tank remains constant.

$$\Delta p_{tank} = p_{tank_i} \cdot \left(\frac{M_{pres_f}}{M_{pres_i}} - 1 \right) \tag{8.67}$$

The pressure drop as a result of nitrogen dissolving in water is plotted as function of the initial tank pressure in Figure 8.25.

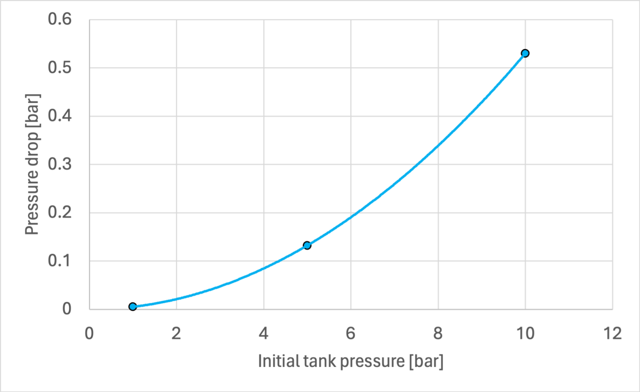

Figure 8.25: Decrease in tank pressure when nitrogen dissolves in water as a function of the initial tank pressure.

The pressure drop increases for an increase in initial tank pressure, where a maximum pressure drop of 0.53 bar (or 5.3 %) is calculated for an initial tank pressure of 10 bar (the maximum expected operating pressure). This drop in tank pressure is significant but can be negated by simply adding more nitrogen to the tank as soon as the water is fully saturated with the pressurant. Since nitrogen is non-reactive with water and nitrogen gas can be added to compensate for the pressure drop in the tank caused by its low solubility, a physical barrier between the pressurant and propellant is not strictly necessary.

8.7.4 Conclusion

The advantages, disadvantages and use-cases of both PEDs and STDs were outlined in this section. PEDs provide slosh control and ensure that no reaction between pressurant and propellant is possible, whereas STDs are generally lighter and more reliable.

The winner of the qualitative trade-off, and the PMD used for the propulsion system in this thesis, is a combination of vanes and a sponge. Vanes can continuously access and move propellant towards to sponge, and is compatible with the relatively low mass flow rates and acceleration environment of the VLM propulsion system. The sponge is used to hold propellant over the tank outlet, and ensures that only liquid can enter the feed system. Both PMD types are reliable, lightweight, inexpensive, passively refillable in zero-g, allow for omnidirectional movement of propellant, and can be made from thin sheet metal such as grade 5 titanium. The combination of vanes and a sponge is previously used in mission such as the Lunar Flashlight Mission [101].

The PEDs did not win the trade-off, as slosh control and a physical barrier between pressurant and propellant are not required. Furthermore, their large mass, low expulsion efficiency when folding, possibility of leaking, and high complexity (of the piston PMD) are deemed unfavourable. Gallaries were not chosen due to their large mass, high cost, low expulsion efficiency and poor reliability. Traps did not win the trade-off, as they both expensive and not passively refillable. The latter results in that they are only used for one-time manoeuvres such as main engine ignition. Finally, troughs did not win the trade-off as they are heavy, expensive, and often used in high-g environments where they can be passively refilled.

8.8 PMD Design

This section present the design of the propellant management devices. The sponge is designed in Subsection 8.8.1, followed by the vane design in Subsection 8.8.3.

8.8.1 Sponge Design

Governing equations

A sponge makes use of the surface tension forces of the propellant to ensure gas free delivery of propellant to the thruster in zero-g. Propellant will remain within the sponge when the surface tensions forces are balanced by the hydrostatics and the flow losses through the panels. The sponge will start leaking when the hydrostatics and flow losses do not balance the surface tension forces. The pressure drop (ΔP) over the liquid-gas interface as a result of the surface tension forces are defined by the Laplace equation:

$$\Delta P = P_{gas} - P_{liquid} = \sigma_a \left(\frac{1}{R_1} + \frac{1}{R_2} \right) \tag{8.68}$$

where σ_a is absolute surface tension of the propellant and R_1 and R_2 are the principal radii of curvature of the surface [102]. The pressure difference within the liquid between the lower and upper side of the sponge as a result of the surface tension forces (ΔP_{st}) can be estimated using [103]:

$$\Delta P_{st} = P_{low} - P_{up} = \left[P_{gas} - \sigma_a\left(\frac{1}{R_{low}}\right)\right] - \left[P_{gas} - \sigma_a\left(\frac{1}{R_{up}}\right)\right] \\ = \sigma_a\left(\frac{1}{R_{up}} - \frac{1}{R_{low}}\right) \tag{8.69}$$

This approximation comes with errors associated to the one-dimensionality of the approach, but are accepted as they greatly simplify the design process. The surface tension pressure difference is opposed only by the hydrostatic pressure difference when assuming that the flow losses are negligible. This results in the following relationship [103]:

$$\sigma_a\left(\frac{1}{R_{up}} - \frac{1}{R_{low}}\right) = \rho_{prop}a(z_{up} - z_{low}) \tag{8.70}$$

where ρ_{prop} is the propellant density, a is the lateral acceleration to which to sponge is subjected, and (z_{up} – z_{low}) is the total height of the propellant within the sponge relative to the acceleration vector. This equation can be rewritten in terms of the principal radii of curvature for a radial sponge when assuming that R_{up} and R_{low} are equal to one half the sponge panel gap [103]:

$$\sigma_a\left(\frac{1}{R_{up}} - \frac{1}{R_{low}}\right) = \frac{\rho_{prop}a}{sin\left(\frac{\pi}{N_p}\right)}\left(R_{up} + R_{low}\right) \tag{8.71}$$

where N_p is the number of radial panels. A radial sponge is chosen for this thesis, as it fits well within the cylindrical propellant tank. Equation 8.70 can also be written in terms of the radial distance from the center of the sponge to the propellant surface:

$$\frac{\sigma_a}{sin\left(\frac{\pi}{N_p}\right)}\left(\frac{1}{r_{up}} - \frac{1}{r_{low}}\right) = \rho_{prop}a(r_{up} + r_{low}) \tag{8.72}$$

where r_{up} and r_{low} are the upper and lower radial distance to the sponge center. A schematic overview of a radial sponge, including the previously indicated radii can be found in Figure 8.26.

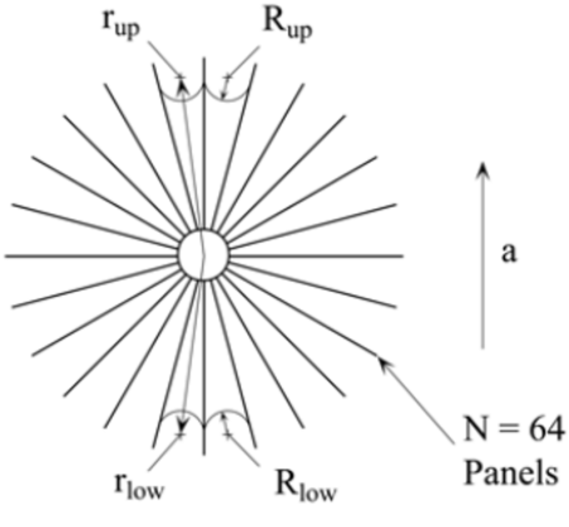

Figure 8.26: Top view of a sponge [103].

Sponge design procedure

The design of the sponge is an iterative procedure where the goal is to achieve a maximum deliverable propellant volume at minimal sponge mass. The maximum deliverable propellant volume must be equal to the required propellant holding volume (V_{man}) to perform a manoeuvre. The latter is calculated using:

$$V_{man} = FoS_m\frac{\dot{m}t_b}{\rho_{prop}} \tag{8.73}$$

where $\dot{m}$ is the mass flow rate, t_b is the required burn time per manoeuvre, and FoS_m is a safety factor. A safety factor of 2 is often used for the required propellant holding volume [103].

The iterative design procedure starts by assuming a sponge configuration, where the design variables are: the panel gap at the sponge interior (g_{inner}, the panel gap at the sponge exterior (g_{outer}), a number of radial sponge panels (N_p), and a panel thickness (t_p). The minimum value allowed for the external panel gap is constrained to 1 mm as a result of manufacturing capabilities whereas the minimum panel gap must be larger than zero to allow propellant to enter the sponge's inner cylinder [103]. Given the inner panel gap, outer panel gap, panel thickness, and number of panels, the inner ($r_{s_{inner}}$) and outer sponge radius ($r_{s_{outer}}$) can be calculated:

$$r_{s_{inner/outer}} = \frac{N_p \left(t_p + g_{inner/outer}\right)}{2\pi} \tag{8.74}$$

The sponge outer radius is constrained by the internal radius of the tank (R_{tank_i}), as there must be a gap between the sponge and tank wall to prevent propellant leaking towards the wall. A gap of 25 mm is used in literature for a 100 mm radius sponge, from which the following relationship between the maximum allowed sponge outer radius ($r_{s_{max}}$), sponge outer radius and internal tank radius is deduced [103]:

$$\begin{aligned} r_{s_{max}} &= R_{tank_i} - \frac{1}{4} r_{s_{outer}} \\ &= R_{tank_i} - \frac{1}{4}\frac{N_p \left(t_p + g_{outer}\right)}{2\pi} \\ &= R_{tank_i} - \frac{N_p \left(t_p + g_{outer}\right)}{8\pi} \end{aligned} \tag{8.75}$$

The limit acceleration (a_{limit}), the acceleration below which pressurant gas can be ejected from the sponge such that no propellant becomes isolated within the sponge, can be calculated for the given sponge configuration:

$$\begin{aligned} a_{limit} &= \frac{dg}{dz}\frac{\sigma_a}{\rho_{prop}}\frac{2}{g_{outer}^2} \\ &= \left(\frac{g_{outer} - g_{inner}}{r_{s_{outer}} - r_{s_{inner}}}\right)\frac{\sigma_a}{\rho_{prop}}\frac{2}{g_{outer}^2} \\ &= \frac{2\pi}{N_p}\frac{\sigma_a}{\rho_{prop}}\frac{2}{g_{outer}^2} \end{aligned} \tag{8.76}$$

where $\frac{dg}{dz}$ is the change in gap size along the length of the radial sponge panel. Exceeding this limit acceleration will result in the isolation of propellant within the sponge which will reduce the deliverable propellant volume per manoeuvre. It is important to realise that the limit acceleration of a sponge can differ from the accelerations that the sponge encounters throughout its lifetime. It is decided that the limit acceleration of the sponge design must always be larger than the mission acceleration (the maximum lateral acceleration that the sponge is expected to encounter), as this ensures a sufficient amount of propellant is available for a manoeuvre.

An observation that can be made from Equation 8.75 and Equation 8.76 is that a smaller exterior panel gap is preferred, as this results in both a larger allowed sponge radius and higher limit acceleration. The larger sponge radius means more propellant can be stored within the sponge per unit height, while the higher limit acceleration ensures that the propellant stays adhered to the sponge at greater lateral accelerations.

The propellant surface that is held within the sponge at the limit acceleration can be calculated by applying Equation 8.70 to any point on the surface of the propellant in the sponge [103]:

$$\frac{\sigma_a}{R} - \rho_{prop} a z = \frac{\sigma_a}{R_0} - \rho_{prop} a z_0 \tag{8.77}$$

where R_0 and z_0 are respectively the radius of curvature and the location from the sponge center of a specific liquid surface within the sponge. A substitution for R and z can be made for a radial sponge in terms of the radial distance of the propellant surface to the center of the sponge (r) and the angle relative to the acceleration vector (ϕ) [103]:

1. For $r < r_s$:

$$R = r sin\left(\frac{\pi}{N_p}\right) - \frac{t_p}{2} \tag{8.78}$$

$$z = r cos(\phi) \tag{8.79}$$

2. For $r > r_s$:

$$R = r_s \tag{8.80}$$

$$z = r_s cos(\phi) \tag{8.81}$$

The propellant that is held within the sponge is constrained by the radius of curvature at the bottom of the sponge (R_{low}). The sponge will be isolated from the leak path (the tank wall) when this radius of curvature is equal to one half the gap between the sponge exterior and the wall. As previously mentioned, this wall gap was approximated to be one-fourth the sponge outer radius (from Equation 8.75). Equation 8.77 is applied for values of z_0 ranging from the inner to the outer radius of the sponge and solved for the radial distance r and the radius of curvature R as a function of the angle ϕ. The maximum allowable value for z_0 is the one when a radius of curvature equal to one-eighth the sponge outer radius is reached at the bottom of the sponge (at $\phi = \pi$). The propellant surface for this maximum value of z_0 is obtained by integrating Equation 8.77 over the entire sponge angle (between 0 and 2π). The sponge height (h_s) required to hold the previously calculated propellant volume (from Equation 8.73) can be calculated by simply dividing the propellant volume by the propellant surface within the sponge.

The calculated propellant surface is based on Equation 8.70 that assumed negligible flow losses within the sponge. These results are therefore only valid when these losses are negligible. The flow losses can be estimated by assuming a steady flow through a constant width slot. This estimation will only provide the order of magnitude of the losses, as the real sponge slots taper. The flow velocity of the propellant within the sponge must be low enough such that the sum of the flow loss head (H_{loss}) and the dynamic head (H_{dyn}) are much less than the surface tension head (H_{st}) [103]:

$$\begin{aligned} H_{loss} + H_{dyn} &<< H_{st} \\ \frac{24}{Re}\frac{L_p}{g_{avg}}\frac{u^2}{2} + \frac{u^2}{2} &<< \frac{\sigma_a}{\rho_{prop}}\frac{2}{g_{avg}} \end{aligned} \tag{8.82}$$

where L_p is the length of a sponge panel, g_{avg} is the average slot width, u is the flow velocity, and Re is the Reynolds number. The latter can be calculated using Equation 8.83 [103],

$$Re = \frac{\rho_{prop} u L_p}{\mu} \tag{8.83}$$

where μ is the dynamic viscosity of the propellant.

In general, the calculated propellant surface is valid for flow velocities at which the losses are more than 10 times smaller than the surface tension head. The maximum allowable flow velocity (u_{max}) within the sponge in then given by rewriting Equation 8.82:

$$\begin{aligned} \left(1 + \frac{24}{Re}\frac{L_p}{g_{avg}}\right)\frac{u_{max}^2}{2} &= \frac{1}{10}\left(\frac{\sigma_a}{\rho_{prop}}\frac{2}{g_{avg}}\right) \\ u_{max} &= \sqrt{\frac{\left(\frac{\sigma_a}{\rho_{prop}}\frac{2}{g_{avg}}\right)}{5\left(1 + \frac{24}{Re}\frac{L_p}{g_{avg}}\right)}} \end{aligned} \tag{8.84}$$

The maximum allowable volumetric flow rate (Q_{max}) is calculated by [103]:

$$Q_{max} = u_{max} h_s g_{s_i} N_p \tag{8.85}$$

whereas the required volumetric flow rate (Q_{req}) is determined by using:

$$Q_{req} = \frac{\dot{m}}{\rho_{prop}} \tag{8.86}$$

The calculated sponge dimensions are valid as long as the required volumetric flow rate is below the maximum allowable volumetric flow rate.

Finally, the mass of the sponge (M_s) can be estimated using Equation 8.87,

$$M_s = \rho_t t_p h_s N_p \left(r_{s_o} - r_{s_i}\right) \tag{8.87}$$

where ρ_t is the density of the sponge material (Ti-6Al-4V). This entire procedure is performed for a range of sponge outer radii and number of radial sponge panels.

Verification of the sponge design procedure

It is important to verify the design procedure that was outlined above. More specific, the method of calculating the propellant surface within the sponge at a given acceleration must be checked, as this affects both the sponge dimensions and mass. This is done by applying the methodology to two sponge examples: the one on which the calculations are based [103], and one that makes use of OpenFOAM to investigate sponge propellant holding at different accelerations for the REXUS mission [104]. The inputs for both sponges are summarized in Table 8.17.

Table 8.17: Sponge examples used for verification [103][104].

	PMD Technology	**REXUS**
Propellant	NTO	PDMS
Number of panels	128	18
Sponge outer radius [m]	0.102	0.011
Sponge panel thickness [mm]	0.25	0.5
Inner panel gap [mm]	1	N/A
Limit acceleration [m/s^2]	0.08	1

The propellant surfaces found in the paper of the PMD Technology sponge are visualized in Figure 8.27 for three acceleration levels: below the limit acceleration, at the limit acceleration, and above the limit acceleration. It must be noted that the maximum possible propellant surface at each acceleration level is represented by the largest non-circular shape whereas the two perfect circles represent the inner and outer radius of the sponge. These propellant surfaces are also found when using the methodology that was described previously, as shown in Figure 8.28. The similarities between the paper and the previously outlined methodology confirm that the calculation for the maximum possible propellant surface is accurate.

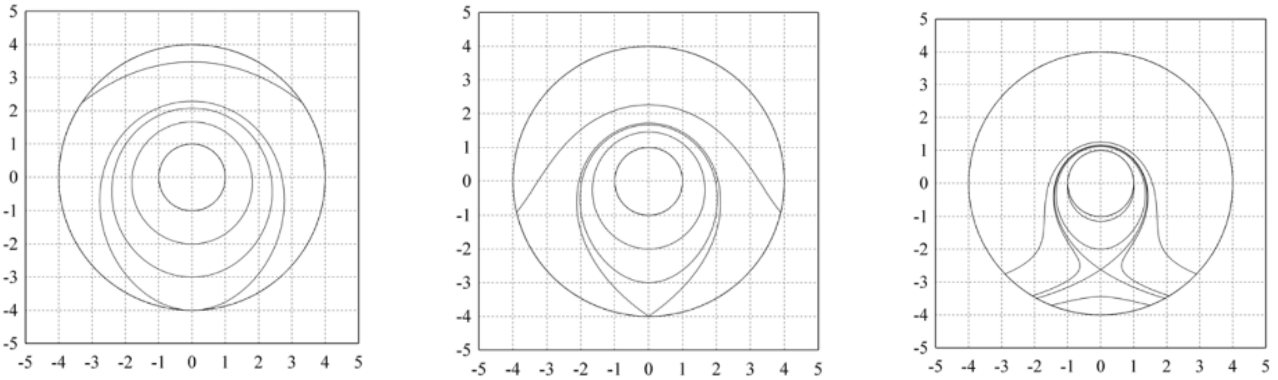

(a) 0.004g (b) 0.0081g (limit acceleration) (c) 0.02g

Figure 8.27: Propellant surfaces for the PMD Technology sponge at different acceleration levels [103].

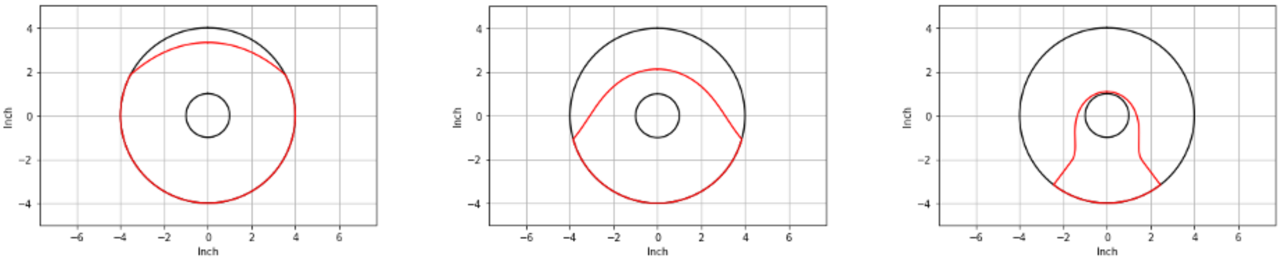

(a) 0.004g (b) 0.0081g (limit acceleration) (c) 0.02g

Figure 8.28: Verification of the propellant surface calculation for the PMD Technology sponge at different acceleration levels where the propellant surface is indicated in red and the sponge radii in black.

Figure 8.29 shows the propellant surfaces within the sponge that are found for the REXUS sponge using OpenFOAM at different acceleration levels. Applying the methodology for calculating the propellant surface within a sponge for different acceleration levels to this sponge results in similar propellant surfaces in terms of their shape and size, as shown in Figure 8.30. The similarities between the OpenFOAM result and the previously described methodology for calculating propellant surfaces within sponges at different acceleration levels confirms the validity of the latter.

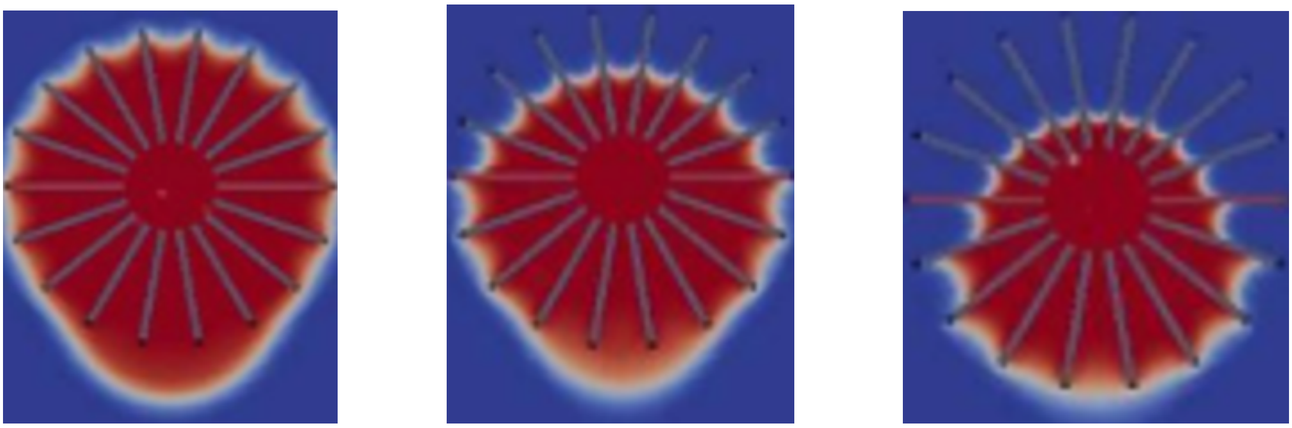

(a) 0.5 m/s (b) 1.0 m/s (limit acceleration) (c) 1.5 m/s

Figure 8.29: Propellant surfaces (in red) for the REXUS sponge at different acceleration levels using OpenFOAM [104].

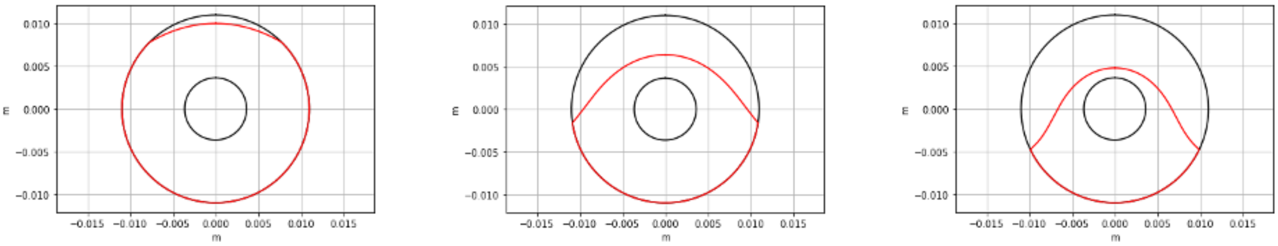

(a) 0.5 m/s (b) 1.0 m/s (limit acceleration) (c) 1.5 m/s

Figure 8.30: Verification of the propellant surface calculation for the REXUS sponge at different acceleration levels where the propellant surface is indicated in red and the sponge radii in black.

8.8.2 Detailed Sponge Design

The required propellant volume per manoeuvre must be calculated to start the iterative design of the sponge. Applying Equation 8.73 for a mass flow rate of 0.7 mg/s (from Subsection 8.1.1), a burn duration of 10 minutes, and a safety factor of 2 results in a required propellant volume of 0.84 mL per manoeuvre. The maximum burn duration of 10 minutes per manoeuvre was chosen in Subsection 4.2.7 to limit gravity losses. All values used for the design of the sponge are summarized in Table 8.18.

Table 8.18: Values used for sponge design.

Parameter	**Value**	**Parameter**	**Value**
Propellant tank characteristics		*Propellant characteristics* [105]	
Tank outer radius [mm]	46	Density [kg/m^3]	998
Tank wall thickness [mm]	0.3	Surface tension [N/m]	0.0728
Sponge characteristics		Dynamic viscosity [Pa·s]	0.001
Outer panel gap [mm]	1	*Mission characteristics*	
Inner panel gap [mm]	0.15	Mass flow rate [mg/s]	0.7
Panel thickness [mm]	0.3	Manoeuvre duration [s]	600
Density Ti-6Al-4V [kg/m^3]	4430	Maximum lateral mission acceleration [g0]	0.007

The outer panel gap of 1 mm is chosen, as it was explained in the previous part that it is beneficial for both the maximum allowable sponge radius and limit acceleration to minimize the outer panel gap. This lower-bound value was set to 1 mm due to manufacturing limitations. The inner panel gap of 0.15 mm is a design choice, and equal to half the thickness of the panel.

With the sponge inner radius, outer radius, and panel thickness chosen, the only remaining design variable is the number of radial sponge panels. It is important to understand the effect that the number of sponge panels has on the propellant surface within the sponge, the sponge height, and mass of the sponge. Figure 8.31 shows the sponge inner, outer, and maximum allowed outer radius of the sponge as a function of the number of sponge panels. Both the inner and outer radius increase with an increase in sponge panels, as the minimum distances between the panels must be maintained, whereas the maximum allowed outer radius decreases for an increase in sponge panels. A maximum of 175 sponge panels can be used, as evident from the intersection between the two outer radii curves.

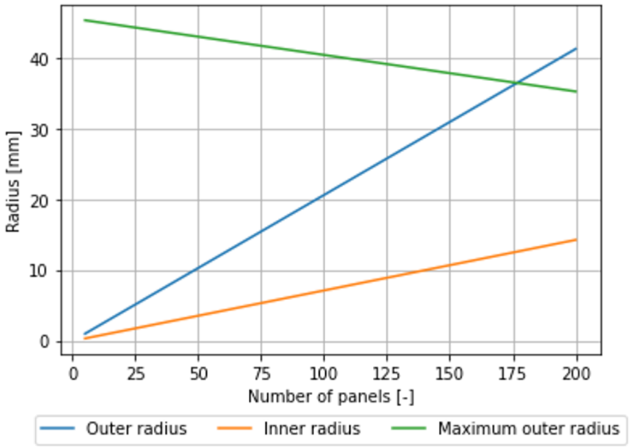

Figure 8.31: Sponge inner and outer radius as a function of the number of radial sponge panels.

Figure 8.32 shows the limit acceleration and propellant surface as a function of the number of sponge panels. The limit acceleration decreases for an increase in sponge panels due to an increased panel length (thus decreasing $\frac{dg}{dz}$ in Equation 8.76) when increasing the amount of sponge panels. The propellant surface within the sponge increases for an increased number of sponge panels as the sponge outer radius increases. The propellant surface within the sponge will increase until the mission acceleration exceeds the limit acceleration and part of the propellant becomes isolated.

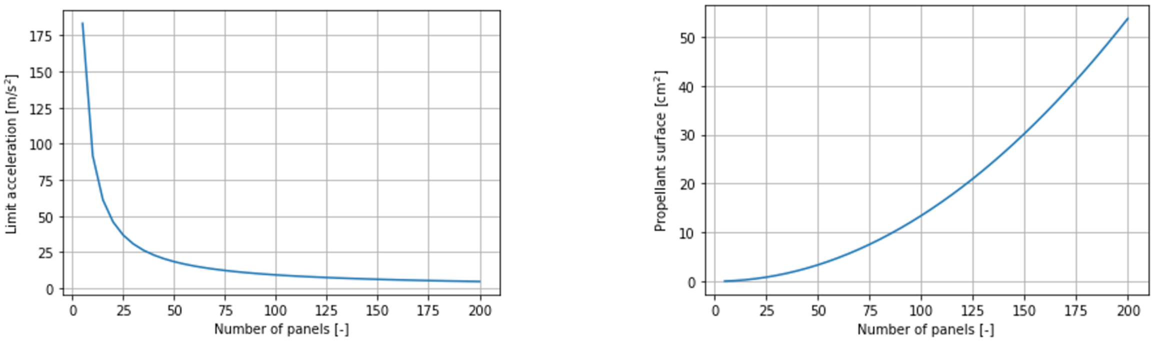

(a) Sponge limit acceleration as a function of the number of radial sponge panels.

(b) Propellant surfaces within sponge as a function of the number of radial sponge panels.

Figure 8.32: Sponge parameter relationships.

Figure 8.33 shows the required sponge height and resulting mass as a function of the number of sponge panels. The required sponge height decreases for an increase in sponge panels, as the propellant surface increased for a growing number of panels. The combination of an increasing sponge outer radius and decreasing sponge height when the number of panels increases results in a net decrease of the sponge mass.

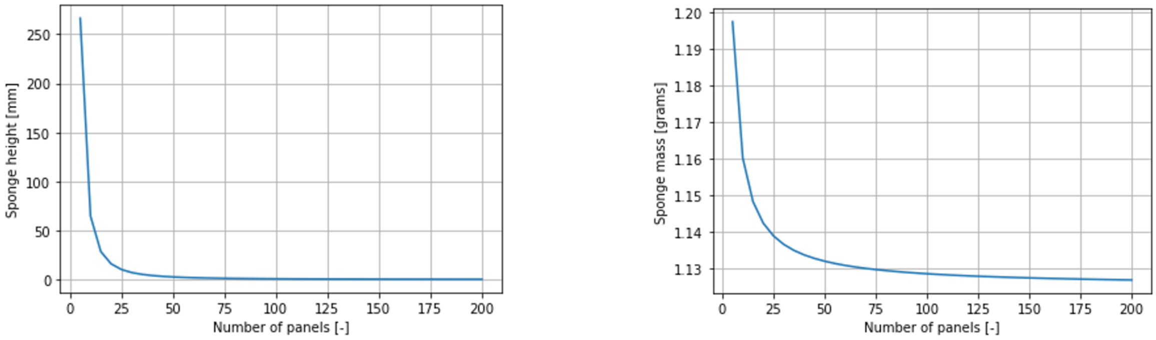

(a) Sponge height as a function of the number of radial sponge panels.

(b) Sponge mass as a function of the number of radial sponge panels.

Figure 8.33: Sponge parameter relationships.

Finally, Figure 8.34 shows the maximum volumetric flow rate within the sponge at which flow losses can be neglected. It can be seen that the maximum volumetric flow rate is larger than the required volumetric flow rate for all sponge configurations. The fact that flow losses can be neglected ensures the validity of the previously found results.

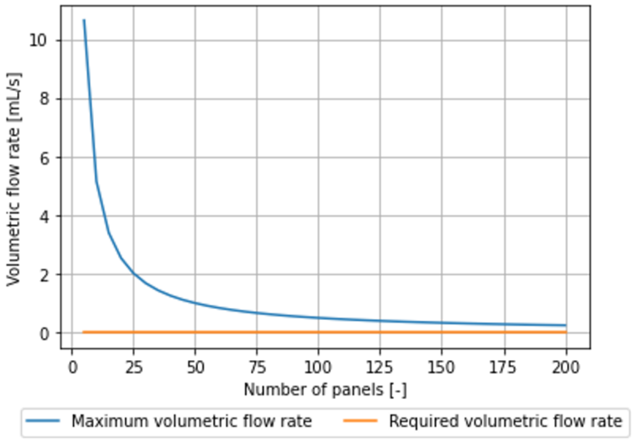

Figure 8.34: Maximum volumetric flow rate and required volumetric flow rate as a function of the number of radial sponge panels.

The question now is, what is the optimum sponge configuration? An increase in sponge panels results in a decreasing limit acceleration and increasing propellant surface with a resulting decrease required sponge height and mass. Increasing the number of panels, until the limit of 175 panels and as long as the limit acceleration is larger than the mission acceleration, seems beneficial. The maximum sponge height is constrained by the internal tank height of the smallest propulsion system. The 200 Ns system has an internal tank height of approximately 40 mm (from Table 8.6) and, as a result, requires a minimum of 14 sponge panels (see Figure 8.33a).

One concern, when increasing the number of sponge panels, is the decrease in required sponge height. The sponge height becomes smaller than the panel thickness when using more than 145 sponge panels which is deemed unfeasible. Propellant might want to adhere to the thickness side of the sponge when the panel height approaches the panel thickness. It is therefore decided that the sponge height must at least be 4 times greater than the panel thickness, resulting in a minimum allowed sponge height of 1.2 mm. Applying this final constraint to the sponge design results in a sponge consisting of 70 radial sponge panels, an outer radius of 14.5 mm, an inner radius of 5 mm, and a height of 1.3 mm. The sponge configuration is summarized in Table 8.19 and shown in Figure 8.35.

Table 8.19: Sponge characteristics

Parameter	**Value**
Number of panels [-]	70
Outer radius [mm]	14.5
Inner radius [mm]	5
Sponge height [mm]	1.3
Panel thickness [mm]	0.3
Panel mass [g]	1.2
Limit acceleration [g0]	1.3

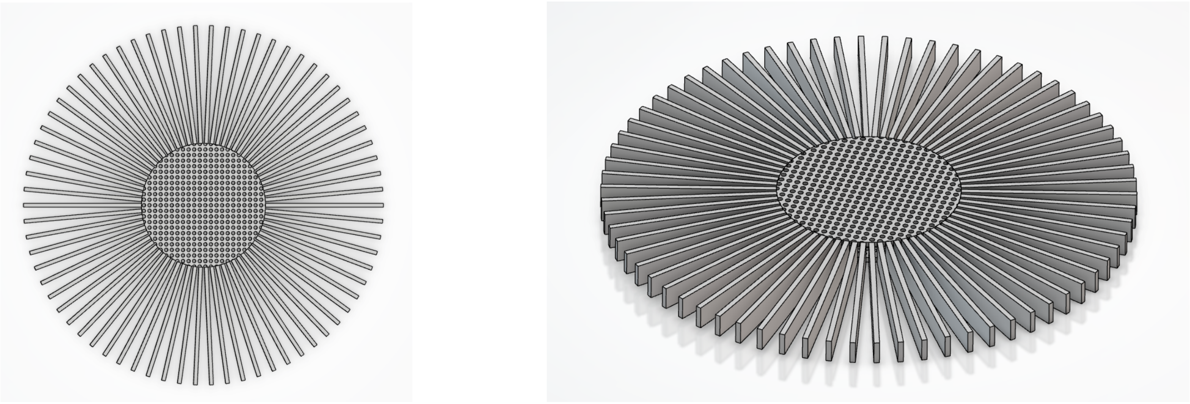

(a) Top view of sponge.

(b) Isometric view of sponge.

Figure 8.35: Final sponge configuration.

The relatively large central tube (with a radius of 5 mm) of the sponge PMD is a result of the 0.15 mm inner panel gap between the radial sponge panels. The resulting inner central tube is too large to rely on surface tension forces or capillary action to prevent gas ingestion. A porous membrane with circular gaps of 0.15 mm (the same dimension as the inner panel gap) is attached to both the top and bottom of the sponge to prevent gas bubbles from entering the feed system [106]. Furthermore, the sponge mass is solely based on the mass of the sponge panels, whereas these panels must be assembled as one unit requiring a fastening method. For simplicity it is assumed that the panels can be rigidly attached to the porous inner sponge membranes.

Both the sponge and the porous membrane cannot allow pressurant gas to enter the feed system. The taper of the sponge panels ensures this functionality for the sponge, but not for the porous membrane. The design of the porous membrane must be checked to ensure this functionality. This is done through determining both the bubble point pressure of the screen and the Flow-Through-Screen (FTS) pressure drop. The bubble point is defined as the maximum allowed pressure differential between the liquid side (inside the sponge) and the gas side (outside the sponge) without gas ingestion into the liquid side of the sponge. In general, gas will not penetrate the porous membrane as long as the FTS pressure loss (ΔP_{FTS}) does not exceed the bubble point pressure (ΔP_{BP}). The bubble point pressure of the screen can be calculated using [107, p. 84]:

$$\Delta P_{BP} = \frac{4\sigma cos(\theta_c)}{D_p} \tag{8.88}$$

where σ is the surface tension of the propellant, θ_c is the contact angle of the propellant with the sponge material, and D_p is the pore diameter. The FTS pressure drop is calculated using Equation 8.89 [107, p. 101],

$$\Delta P_{FTS} = \alpha_f \left(\frac{t_{sc}\mu a_s^2}{\epsilon_v}\right) u_p + \beta_f \left(\frac{t_{sc}}{\epsilon_v^2 D_p}\right) u_p^2 \tag{8.89}$$

where α and β are fitting parameters, t_{sc} is the screen thickness, a_s is the surface area to volume ratio of the screen, ϵ_v is the dimensionless void fraction of the screen (i.e. the volume fraction of perforations within the screen), and u_p is the flow velocity of the propellant. The surface area to volume ratio of the screen (a_s) is approximated using [107, p. 100]:

$$a_s \approx \frac{6(1-\epsilon_v)}{D_p} \tag{8.90}$$

whereas the flow velocity (u_p) is calculated using:

$$u_p = \frac{Q_{req}}{\pi r_{s_i}^2} \tag{8.91}$$

where r_{s_i} is the inner radius of the sponge.

The bubble point pressure and FTS pressure drop are 1573 Pa and 0.02 Pa respectively and are found using the values summarized in Table 8.20. Given that the FTS pressure drop is orders of magnitude lower than the bubble point pressure, it can be concluded that the porous membrane with a pore diameter of 0.15 mm effectively prevents gas from entering the feed system.

Table 8.20: Values used to calculate the screen bubble point pressure and FTS pressure drop.

Parameter	**Symbol**	**Value**
Contact angle [°]	θ_c	35.5
Pore diameter [mm]	D_p	0.15
Screen thickness [mm]	t_{sc}	0.3
Viscosity [Pa·s]	μ	0.001
Surface tension [N/m]	σ	0.0072
Dimensionless void fraction [-]	ϵ_v	0.5
Fitting parameter [-] [107, p. 108]	α_f	10
Fitting parameter [-] [107, p. 108]	β_f	0.35

The final consideration of the sponge design is the manufacturing. Small sponges can be manufactured using wire electrical discharge machining (WEDM) where a metallic wire is used to cut a contour in a work piece. This method of manufacturing allows to machine conductive materials of any hardness. Only the diameter of the of the cutting wire limits the amount of detail that can be achieved [108]. Examples of sponges that have been produced using this method are shown in Figure 8.36.

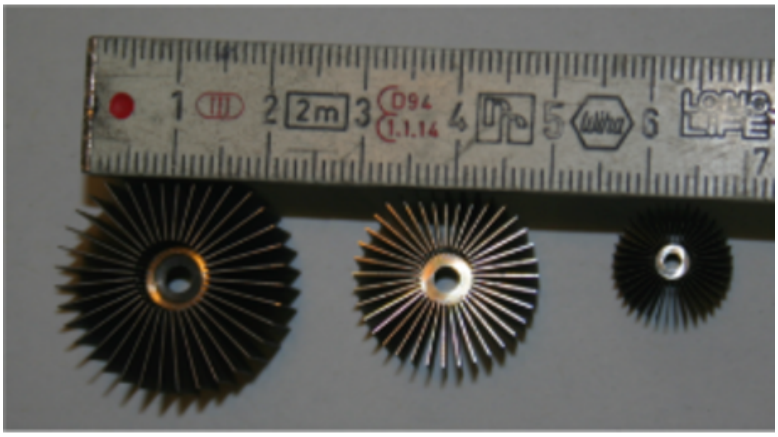

Figure 8.36: Examples of sponges that are manufactured using WEDM [108].

8.8.3 Vane Design

Governing equations

Vanes are used to refill the sponge during the zero-g coast between two consecutive manoeuvres. Propellant can move from the propellant pool towards the sponge along the vane through surface tension forces that provide a driving pressure. This driving pressure is a function of the radii of curvature, and is defined as [109]:

$$\Delta P_{drive} = \sigma \left(\frac{1}{R_D} - \frac{1}{R_U} \right) \tag{8.92}$$

where σ surface tension of the propellant, R_D is the downstream radius of curvature of the propellant along the vane, and R_U is the upstream radius of curvature of the propellant along the vane. This equation shows that propellant flows towards the sponge as long as the upstream radius of curvature is larger than the downstream radius of curvature. Figure 8.37 shows the flow of liquid propellant along a simple vane, where H_V is the vane height, L_V is the length of the vane, and D_V is the distance between two adjacent vanes. The direction of the flow is indicated by blue arrows.

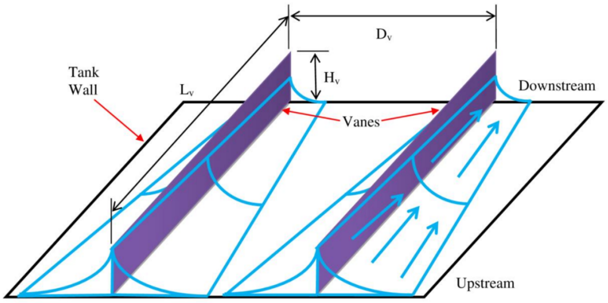

Figure 8.37: Propellant flow along wall mounted vanes [109, p. 577].

The vane design in this thesis is performed whilst assuming steady state, incompressible, and isothermal flow along simple, wall-mounted vanes. The governing equations for steady state flow along a vane are the continuity and momentum equations [109, p. 578]:

$$du = -\frac{\dot{Q}}{A^2}dA \tag{8.93}$$

$$-Adp - 2\rho\nu\dot{Q}\left(\frac{s}{A}\right)^2 dx = \rho_{prop}Audu \tag{8.94}$$

where u is the propellant flow velocity along the vane, ν is the kinematic viscosity, A is the cross-sectional area of the fillet attached to the vane, $\dot{Q}$ is the volumetric flow rate of the propellant along the vane, s is the wetted circumference, and x is the position along the vane. Combining the continuity and momentum equation, substituting the equation of state [110],

$$dp = \sigma\left(\frac{1}{R^2}\right)dR \tag{8.95}$$

and reducing results yields the following equation [109, p. 579]:

$$\frac{dR}{dx} = \frac{FoS_f\frac{2\nu}{\dot{Q}}s^2}{\frac{dA}{dR} - FoS_\sigma\frac{\sigma}{\rho_{prop}}\frac{1}{\dot{Q}^2}\frac{A^3}{R^2}} \tag{8.96}$$

where R is the radius of curvature at a location along the vane (x), FoS_f is the friction multiplier (set to a value of 3), and FoS_σ is a safety factor on the surface tension (set to a value of 2). It is important to realise that both A and s are functions of the radius of curvature, and can differ for different vane heights [109, p. 583]:

1. For $R > H_V$:

$$A = C_VH_V - \frac{R^2}{2}(\theta - \sin\theta) \tag{8.97}$$

$$s = C_V + 2H_V \tag{8.98}$$

where

$$C_V = \sqrt{8H_V\left(R - \frac{H_V}{2}\right)} \qquad ; \qquad \theta = 2\arcsin\left(\frac{C_V}{2R}\right)$$

2. For $R < H_V$:

$$A = 2R^2 - \frac{\pi R^2}{2} \tag{8.99}$$

$$s = 4R \tag{8.100}$$

Equation 8.96 has three unknowns, namely the upstream radius of curvature (R_U), the downstream radius of curvature (R_D), and the volumetric flow rate ($\dot{Q}$). The downstream radius of curvature is constrained by the sponge design, whereas the upstream radius of curvature is constrained by the expulsion efficiency. Given either R_D or R_U and a required volumetric flow rate allow for integrating Equation 8.96 to obtain the radius of curvature as a function of the position along vane ($R(x)$). A fourth-order Runge-Kutta integration method is required, as there is no closed-form solution to this problem.

It is crucial the sponge remains submerged in propellant as the tank is drained to prevent pressurant gas from being ingested into the feed system. In other words, the downstream radius of curvature of propellant along the vane must be sufficiently large to ensure that sponge is fully covered by propellant. The required downstream radius of curvature can be calculated by using a geometric relationship between the chord length based on the height of the vane (C_D), and the chord length based on the height of the sponge (C_S). The sponge is fully submerged when the difference between C_D and C_S is equal to the distance between the vanes. This relationship is given by [109, p. 582]:

$$C_D - C_S = D_V \tag{8.101}$$

$$\sqrt{8H_V\left(R_D - \frac{H_V}{2}\right)} - \sqrt{8H_S\left(R_D - \frac{H_S}{2}\right)} = \frac{2\pi R_S}{N_V}$$

where H_S is the height of the sponge, R_S is the outer radius of the sponge, and N_V is the number of vanes. With the downstream radius known, only the volumetric flow rate is required to perform the integration of Equation 8.96.

The maximum volumetric flow rate along a vane can be determined by calculating the area wave propagation speed. This wave speed cannot be exceeded as this leads to choked flow. The area wave propagation speed (c) is defined as [110]:

$$c = \sqrt{\frac{1}{2}\left(\frac{\sigma}{\rho_{prop}}\right)\frac{1}{R}} \tag{8.102}$$

where an increase in radius of curvature (R) results in a decreasing propagation speed. Multiplying the area wave propagation speed by the cross-sectional area of the fillet (A, obtained from Equation 8.97 or Equation 8.99) provides the maximum volumetric flow rate before choking occurs. It is important to realise that an increase in radius of curvature does decrease the wave area propagation speed, but increases the fillet area. The net effect of increasing the radius of curvature will result in a constant maximum volumetric flow rate after a certain radius of curvature, as will be shown further along this section.

Equation 8.96 can now be integrated with the values for downstream radius of curvature and the maximum volumetric flow rate. This results in a curve that shows the radius of curvature along the vane length. The residual propellant (V_R) attached to the vanes at EoL can be calculated using [109, p. 583]:

$$V_R = N_V \int_0^{L_V} A(x)\,dx \tag{8.103}$$

where L_V is the length of the vane, and A(x) is obtained from inserting $R(x)$ into Equation 8.97 or Equation 8.99. There are two vane lengths used in this thesis, namely vanes that reach the top of the tank, and vanes that reach to half the tank height. The length of the tall vanes are calculated using:

$$L_{V_{long}} = (R_t - R_S) - (H_t - H_V) \tag{8.104}$$

where R_t is the inner rank radius and H_t is the inner height of the tank. The length of the short vanes are calculated using:

$$L_{V_{short}} = (R_t - R_S) - H_V + \frac{H_t}{2} \tag{8.105}$$

Finally, the expulsion efficiency (EE) can be calculated:

$$EE = 1 - \left(\frac{N_{V_{long}} \int_0^{L_{V_{long}}} A(x)\,dx - N_{V_{short}} \int_0^{L_{V_{short}}} A(x)\,dx}{V_{prop}}\right) \tag{8.106}$$

where $N_{V_{long}}$ are the number of long vanes, $N_{V_{short}}$ are the number of short vanes, $L_{V_{long}}$ is the length of the long vanes, $L_{V_{short}}$ is the length of the short vanes, and V_{prop} is the propellant volume in the tank at BOL.

Detailed Vane Design

The goal of the vane design is to refill the sponge whilst achieve an expulsion efficiency larger than 95 % as per requirement *PROP-TANK-14*. As was explained previously, the expulsion efficiency is determined by the propellant residual that remains attached to the vanes at EOL, and is a function of the number of vanes and fluid radius of curvature along the length of the vane. The fluid radius of curvature is calculated by integrating Equation 8.96, where the design variables are the volumetric flow rate, number of vanes used, and the vane height.

The vane height is varied between 1.4 and 5 mm. The upper limit of 5 mm is chosen arbitrarily whereas the lower limit of 1.4 mm is chosen to ensure that the sponge can be fully submerged in propellant. The vane must be taller than the sponge to allow for full sponge submergence when using a small number of vanes. The number of vanes is, as a design choice, varied from 6 to 12.

The volumetric flow rate along the vane is the final design variable needed to integrate Equation 8.96 and compute the expulsion efficiency. This flow rate is constrained by the area wave propagation speed and increases with greater vane height. If this flow rate is exceeded, choked flow occurs. Figure 8.38 displays the choked volumetric flow rate as a function of the propellant's radius of curvature, for vane heights ranging from 1.4 to 5 mm.

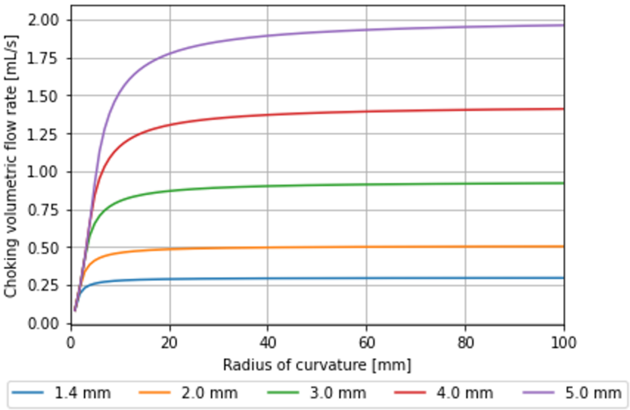

Figure 8.38: Maximum volumetric flow rate before choking as a function of the radius of curvature for different vane heights.

It is evident that the maximum allowable flow rate rises with increasing vane height, and a maximum value is reached after a specific radius of curvature for all vane heights. The smallest vane height presents the limiting case, where a maximum flow rate of 0.3 mL/s can be reached before choking occurs. This volumetric flow rate is applied across all vane configurations considered in this section and can be regarded as conservative.

Now, the downstream radius of curvature for each vane configuration can be calculated using Equation 8.101. This downstream radius, combined with the vane height, number of vanes, and maximum volumetric flow rate, can be used to integrate Equation 8.96 to obtain the radius of curvature along the length of each vane configuration. Plugging this curve ($R(x)$) into the relationship that calculates the cross-sectional area of the propellant allows for calculating the expulsion efficiency for each vane configuration. These steps are performed for both the 6 and 12 vane configuration whilst varying both the vane height and the length of the vanes. There are three vane length configurations chosen, namely to use long vanes that reach the top of the tank, use a combination of long and short vanes, and the use of only short vanes. The latter is only included to investigate what the maximum possible expulsion efficiency of the system is and can never be used in this PMD design as propellant tends to adhere to the connection between the cylindrical tank wall and the flat cap at the top of the tank. Long vanes are required to move this propellant from the crevice to the tank outlet.

The expulsion efficiencies of the 200 Ns propulsion system for the different vane configurations are visualized in Figure 11.6b. Several observations can be made when looking at these figures. First, there is a notable improvement in expulsion efficiency when the vane height is increased from 1.4 mm to 3 mm. However, further increases in vane height beyond 3 mm result in minimal efficiency gains, followed by a slight decrease. Furthermore, the expulsion efficiency increases marginally when using more short vanes over long vanes. An interesting observation is that the expulsion efficiency does not meaningfully increase when going from a 6 vane configuration to a 12 vane configuration for vane heights beyond 3 mm. The use of more vanes does lower the required downstream radius of curvature, with a lower upstream radius of curvature, hence a lower fillet volume clinging to the vane, as a result. This decrease in vane fillet area is compensated for by the use of more vanes. Finally, it is observed that none of the vane heights result in an expulsion efficiency of 95 %, hence the requirement on the expulsion efficiency (*PROP-TANK-14*) is not met for the 200 Ns system. The best performing vane configuration, and the one that will be used in this thesis, is the 6-vane setup consisting of 3 short vanes and 3 long vanes. The use of more vanes, or taller vanes, will not meaningfully increase the expulsion efficiency.

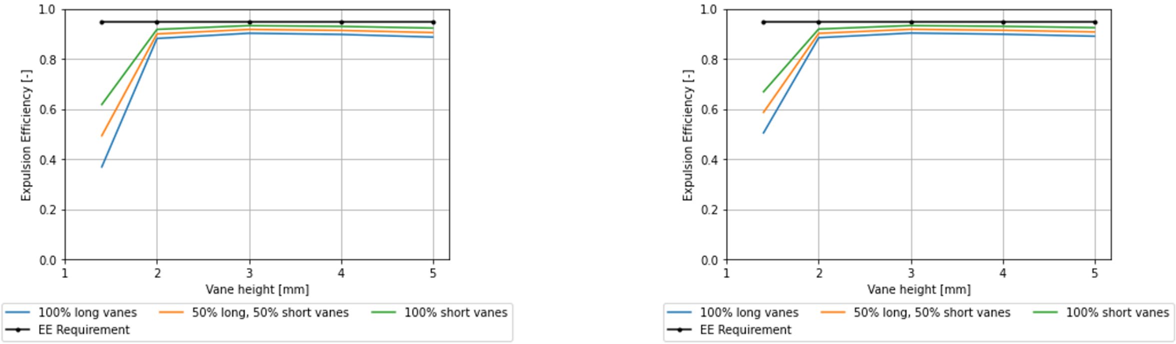

(a) 6-vane configuration

(b) 12-vane configuration

Figure 8.39: Expulsion efficiencies for varying vane heights.

This 6-vane configuration is to be used in all three propulsion systems: the 200 Ns, 400 Ns, and 600 Ns system. The inputs used to obtain the expulsion efficiencies, and the expulsion efficiencies for the three propulsion systems are summarized in Table 8.21. It is important to note that, once again, none of the systems meet the expulsion efficiency requirement, indicating that either the requirement must be slightly relaxed, or the sponge design modified. The lower expulsion efficiencies can be compensated for by taking part of the 25 % margin that was taken on the required propellant and pressurant volume (from *PROP-TANK-01*), so a redesign for the sponge is deemed unnecessary.

Table 8.21: Inputs and outputs of the vane design procedure.

Parameter	**Value**	**Parameter**	**Value**
Sponge characteristics		*Vane characteristics*	
Sponge radius [mm]	14.5	Number of vanes [-]	6
Sponge height [mm]	1.3	Vane configuration [-]	3 short, 3 long vanes
Sponge holding volume [mL]	0.842	Vane height [mm]	3
Propellant characteristics [105]		Vane thickness [mm]	0.5
Density [kg/m^3]	998	Volumetric flow rate [mL/s]	0.25
Surface tension [N/m]	0.0724	Friction safety factor [-]	3
Kinematic viscosity [m^2/s]	$1.002 \cdot 10^{-6}$	Surface tension safety factor [-]	2

Propulsion System	**200 Ns**	**400 Ns**	**600 Ns**
Expulsion efficiency [-]	0.918	0.936	0.942
Length of short vane [mm]	49	69	89
Length of long vane [mm]	69	109	149
Vane mass [g]	2.4	3.5	4.7

Finally, the function of the vanes is to refill the sponge during two consecutive manoeuvres. It is important to investigate what the sponge refill duration is for the given vane configuration. The most limiting case is at EoL where, most likely, only the 3 long vanes can move the propellant from the top of the tank towards the sponge. With the assumed volumetric flow rate of 0.3 mL/s, it will take only one seconds to refill the 0.84 mL sponge volume. The sponge holding volume was based on being able to perform a 10-minute manoeuvre without any refilling. The short refill period (of one seconds), combined with the fact that propellant is forced towards the sponge during a manoeuvre, suggests that the sponge will never fully empty until the end of the mission when all free-floating propellant is expelled.

8.8.4 PMD Design Conclusion

The PMD design, consisting of a 70-panel radial sponge, a membrane with 0.15 mm diameter holes, and 6 vanes was outlined in this section. A summary of the PMD configuration, including the tank volume that the PMD occupies, is provided in Table 8.22. Futhermore, the assembled PMD of the 200 Ns propulsion system is visualized in Figure 8.40. It can be concluded that the PMD design does not occupy a significant portion of the tank volume that could have been used by the propellant.

Table 8.22: Overview of the PMD design.

Propulsion System	**200 Ns**	**400 Ns**	**600 Ns**
Sponge design			
Sponge outer radius [mm]	14.5		
Sponge height [mm]	1.3		
Sponge holding volume [mL]	0.842		
Sponge mass [g]	1.2		
Membrane Design			
Membrane outer radius [mm]	5.0		
Hole diameter [mm]	0.15		
Membrane mass [g]	0.14		
Vane Design			
Length of short vane [mm]	49	69	89
Length of long vane [mm]	69	109	149
Vane Mass [g]	2.4	3.5	4.7
PMD Performance			
PMD volume [mL]	0.81	1.09	1.35
PMD mass [g]	3.74	4.84	6.04
Expulsion efficiency [-]	0.918	0.936	0.942

8.8.5 PMD Design Recommendations

There are several unanswered questions in regard to the design of both the sponge and vanes. First, the effect of the contact angle between the propellant and PMD material (Ti-6Al-4V) has not been considered. The use of large safety factors during the design is meant to compensate for the unknown decrease in performance of the PMD. Testing in zero-g is required to verify the current design.

Second, there is a strange behaviour that, when decreasing the volumetric flow rate below a certain limit along the vane results in a radius of curvature that is smaller at the of top the vane than at the bottom of the vane. This results in a negative driving pressure, hence a flow away from the sponge rather than towards it. Numerous attempts have been made to understand this behaviour, but without success. As with the previous point, testing in zero-g is required to verify the current design, and to investigate this flow-reversal behaviour for smaller volumetric flow rates.

Finally, the configuration of the PMD design is now known, but the method on how to assemble this system is not investigated in great detail. Connecting the different PMD components will likely change the flow characteristics of the propellant along these structures. These effects must be investigated through testing. It was mentioned in the sponge design that the radial sponge panels are connected at the top and bottom by a membrane that was used to prevent gas ingestion through the top and bottom of the sponge's inner cylinder. The vanes are to be equally spaced in an alternating pattern (short vane, long vane, short vane, etc), attached to the tank wall and extend from the tank wall towards the sponge.

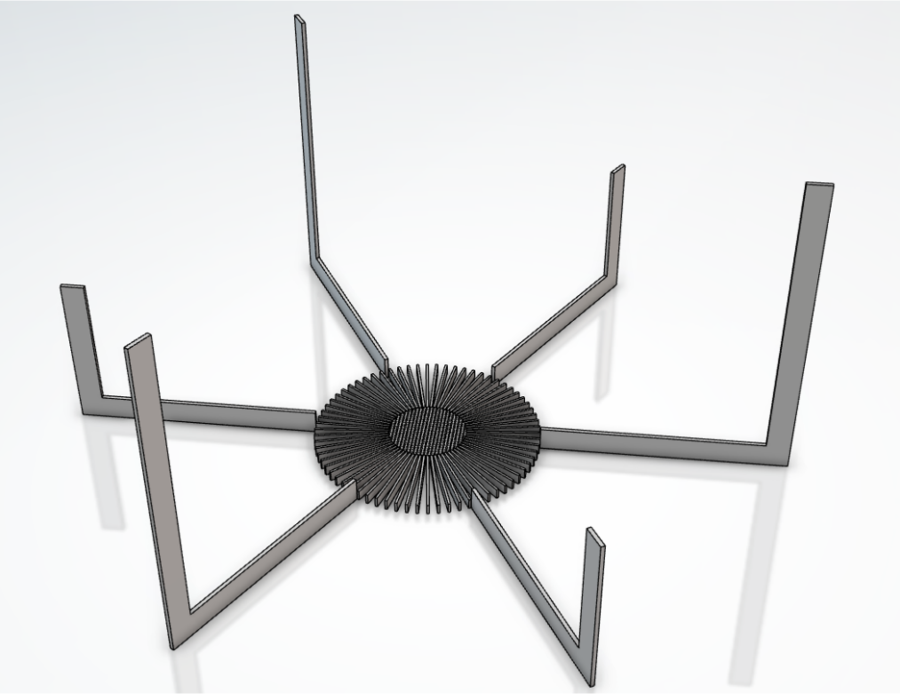

Figure 8.40: Assembled propellant management device of the 200 Ns propulsion system.

8.9 Requirement Compliance

The final stage of the propellant tank design involves verifying whether the 19 requirements outlined at the beginning of this chapter have been fulfilled. Table 8.23 provides a summary of these requirements, indicating whether each one is met, and if not, suggests a potential mitigation strategy.

Table 8.23: Requirement verification table.

Requirement ID	Requirement	Compliant	Explanation	Mitigation Strategy
PROP-TANK-01	The propellant tank shall store a usable fluid volume of 0.263 L / 0.526 L / 0.788 L without failure.	Yes	Tank volume minus PMD volume is within the stated 2% deviation.	Not required.

Continued on next page

Requirement ID	Requirement	Compliant	Explanation	Mitigation Strategy
PROP-TANK-02	The propellant tank shall not exceed the 92 x 92 mm (XY) boundaries.	Yes	Tank outer radius is 46 mm.	Not required.
PROP-TANK-03	The propellant tank height (Z) shall not exceed 50 mm / 100 mm / 150 mm.	Yes	Tank outer heights are: 44.3 mm/ 84.4 mm / 124.3 mm.	Not required.
PROP-TANK-04	The total mass of the tankage shall not exceed 347 g / 695 g / 1043 g.	Yes	Tank masses, including mechanical interface, are: 147 g / 163 g / 179 g.	Not required.
PROP-TANK-05	The propellant tank shall allow for a propellant and pressurant temperature range between 283 K and 323 K.	Partial	Tank can withstand the maximum pressure of 10 bar at 323 K, but no thermal analysis is performed to ensure the temperature does not exceed the upper and lower limits.	Thermal analysis.
PROP-TANK-06	The propellant tanks shall survive a maximum expected operating pressure of 10 bar.	Yes	Tank is sized for this pressure, excluding safety factors.	Not required.
PROP-TANK-07	The propellant tank shall have a design factor of safety of 1.25 for yield.	Yes	Safety factor used in design process.	Not required.
PROP-TANK-08	The propellant tank shall have a design factor of safety of 1.4 for ultimate load.	Yes	Safety factor used in design process.	Not required.
PROP-TANK-09	The pressure and temperature within the propellant tank shall be electronically monitored.	No	Not incorporated in tank design.	Include in piping design.
PROP-TANK-10	The propellant tank shall leak before burst.	No	Not incorporated in tank design.	Include in piping design.
PROP-TANK-11	The propellant tank shall allow for filling and draining of both the propellant and pressurant.	Yes	There is a hole in the tank bottom end-cap to allow for filling and draining of the tank.	Not required.
PROP-TANK-12	The propellant tank material shall be compatible with gaseous nitrogen and liquid water.	Yes	Ti-6Al-4V is compatible with both gaseous nitrogen and water.	Not required.
PROP-TANK-13	The propellant tank shall ensure that no pressurant enters the thruster.	Yes	Sponge design ensures that only liquid can enter the feed system.	Not required.
PROP-TANK-14	The propellant tank shall allow for an expulsion efficiency of at least 95 %.	No	Expulsion efficiencies are: 0.918 / 0.936 / 0.942.	Use part of the 25% design margin that was taken in *PROP-TANK-01*.

Continued on next page

Requirement ID	Requirement	Compliant	Explanation	Mitigation Strategy
PROP-TANK-15	The propellant tank shall be mechanically integrated within the propulsion system according to the CS14 interface standard.	Yes	Mechanical interface is aligned with the CS14 PCB standard.	Not required.
PROP-TANK-16	The propellant tank shall be electrically integrated within the propulsion system according to the CS14 interface standard.	Yes	There is sufficient space for electrics to be routed towards the CS14 PCB standard.	Not required.
PROP-TANK-17	The propellant tank shall survive an axial acceleration of 8.5 g.	Yes	Mechanical interface design is based on this acceleration.	Not required.
PROP-TANK-18	The propellant tank shall survive a lateral acceleration of 3 g.	Yes	Mechanical interface design is based on this acceleration.	Not required.
PROP-TANK-19	The minimum resonant frequency of the mechanical interface between the propellant tank and the main structure of the propulsion system shall be larger than 35 Hz.	Yes	Mechanical interface design is based on this minimum natural frequency.	Not required.

8.10 Conclusion

This chapter outlined the design of the propellant tank, the mechanical interface between the propellant tank and propulsion system structure, and the propellant management device.

A list of 19 requirements was constructed at the start of the design to ensure that the propulsion system could achieve the required performance. This was followed by an outline of the possible tank shapes (spherical, cylindrical, and rectangular), materials (aluminium 6061-T6, 304L stainless steel, grade 5 titanium, and inconel-718), and propellant management devices that were summarized in a design option tree.

This was followed by a trade-off between the different tank shapes and materials, where a cylindrical tank with flat end-caps, made from grade 5 titanium won the trade-off. The mechanical interface was designed to be incorporated in the flat end-cap design, where four interfaces connect the top of the tank to the propulsion system, and two connect the bottom of the tank to the propulsion system. This design choice was made to allow for components to be placed next to the tank.

Next, a trade-off was performed between the previously outlined propellant management devices where a combination of a sponge and vanes won the trade-off. A radial sponge, consisting of 70 sponge panels and two porous membranes, combined with 6 vanes (3 short and 3 long vanes) was designed based on this trade-off. A detailed summary of the tank design is outlined in Table 8.24, where the mass and volume values are taken from the 3DExperience CAD files. The propellant tank designs are visualized in Figure 8.41 and Figure 8.42.

Table 8.24: Propellant tank design specifications.

Propulsion System	200 Ns	400 Ns	600 Ns
Tank Shell Design			
Shape	Cylindrical with flat end-caps		
Material	Ti-6Al-4V		
Shell thickness [mm]	0.3		
Head thickness [mm]	2.1		
Tank outer radius [mm]	46		
Outer tank height [mm]	44.3	84.4	124.3
Tank dry mass [g]	138	153	168
Internal volume [L]	0.263	0.526	0.788

Continued on next page

Mechanical Interface Design			
Configuration	Six L-shaped beams, four on top, two on bottom		
Material	Ti-6Al-4V		
Mass [g]	5		
Sponge Design			
Configuration	Radial sponge consisting of 70 sponge panels		
Material	Ti-6Al-4V		
Outer radius [mm]	14.5		
Inner radius [mm]	5		
Height [mm]	1.3		
Panel thickness [mm]	0.3		
Holding volume [mL]	0.842		
Limit acceleration [g0]	1.3		
Mass [g]	1.2		
Membrane design			
Configuration	Porous membrane on top and bottom of sponge		
Material	Ti-6Al-4V		
Outer radius [mm]	5		
Hole diameter [mm]	0.15		
Mass [g]	0.14		
Vane design			
Configuration	Three short vanes, three long vanes		
Material	Ti-6Al-4V		
Length of short vane [mm]	49	69	89
Length of long vane [mm]	69	109	149
Mass [g]	2.4	3.5	4.7
PMD Performance			
Occupied volume [mL]	0.81	1.09	1.35
Expulsion efficiency [-]	0.918	0.936	0.942

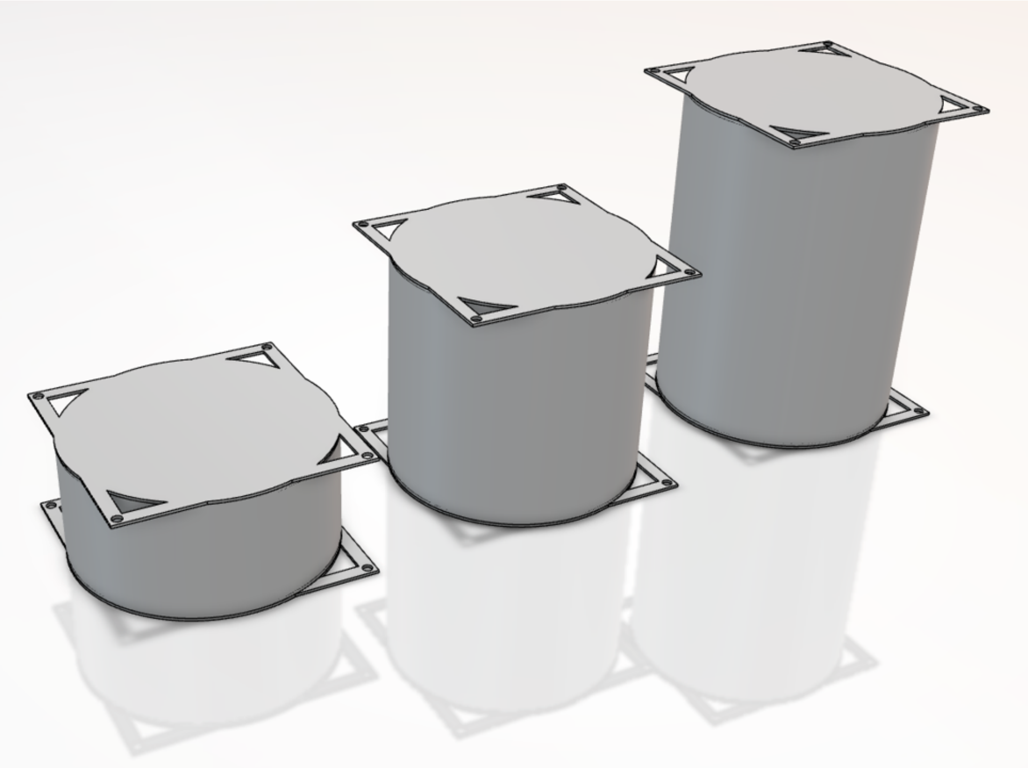

Figure 8.41: Propellant tank assemblies.

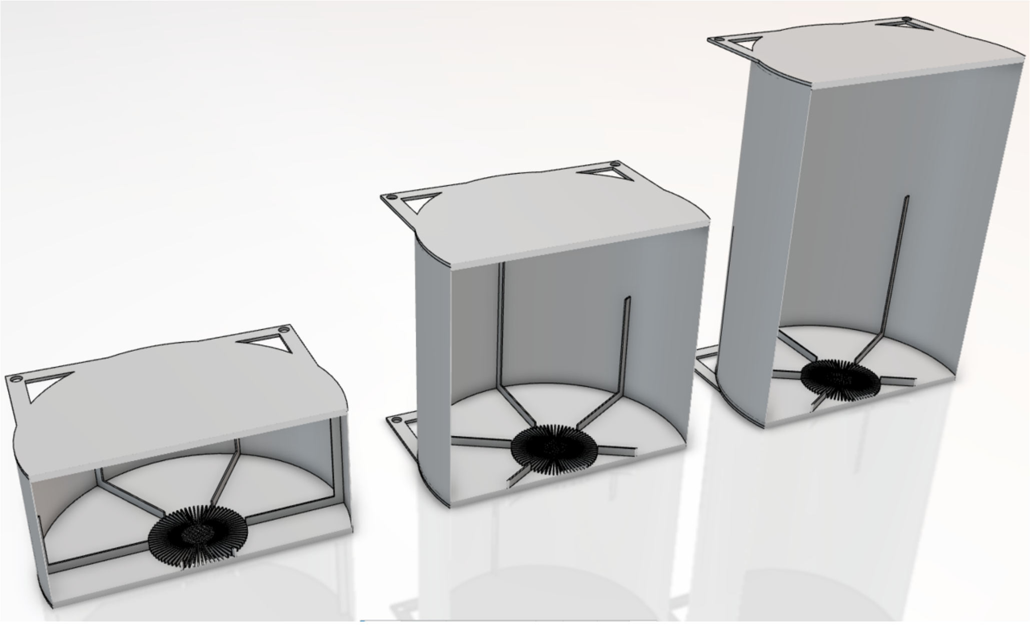

Figure 8.42: Clipped propellant tank assemblies that shows internal structure.

Piping 9

This chapter outlines the piping design for the three propulsion systems. First, a list of requirements is generated in Section 9.1, and is followed by the piping components and layout in Section 9.2. The pressure drop over the thrust path is calculated in Section 9.3, whereas the compliance with the generated requirements is discussed in Section 9.4. Finally, the chapter is concluded in Section 9.5, whereas recommendations are presented in Section 9.6.

9.1 Requirements

A list of requirements is generated to start the design of the piping. Part of these requirements are directly copied from the propellant tank design, as piping is included in the tankage mass and volume budgets. The requirements are summarized in Table 9.1. Values separated by a '/' indicate the values for the different size propulsion systems: 200 Ns, 400 Ns, and 600 Ns.

Table 9.1: Piping requirements.

Requirement ID	Parent Requirement(s)	Requirement	Rationale
PROP-PIPE-01	PROP-PERF-1	The piping shall allow for propellant to flow from the tank towards the thruster.	Propellant must reach the thruster to provide its specified performance.
PROP-PIPE-02	PROP-SYST-1	The configuration of the piping shall be identical across the three system sizes.	Design choice; increases the ease of manufacturing.
PROP-PIPE-03	PROP-SYST-5	The piping shall ensure that no impurities enter the thruster.	Minimizes the risk of blockages that result in loss of performance and failure.
PROP-PIPE-04	PROP-SYST-2, PROP-INT-3	The piping shall not exceed the 92 x 92 mm (XY) boundaries.	A result of the specified volume budgets of 0.5 U, 1.0 U, and 1.5 U.
PROP-PIPE-05	PROP-SYST-2	The tankage height (Z) shall not exceed 50 mm / 100 mm / 150 mm.	A result of the specified volume budgets of 0.5 U, 1.0 U, and 1.5 U.
PROP-PIPE-06	PROP-SYST-3	The total mass of the tankage shall not exceed 347 g / 695 g / 1043 g.	Taken from the mass budget as described in Chapter 7.
PROP-PIPE-07	PROP-RAMS-1	The piping shall survive a maximum expected operating pressure of 10 bar.	Maximum pressure allowed in thruster.
PROP-PIPE-08	PROP-RAMS-3	The lines and fittings shall have a burst safety factor >= 4.	Decreases the risk of propulsion system failure [111].
PROP-PIPE-09	PROP-RAMS-3	All pressure components, other than lines and fittings, shall have a burst safety factor >= 2.5.	Decreases the risk of propulsion system failure [111].
PROP-PIPE-10	PROP-TANK-09	The pressure and temperature of the propellant shall be electronically monitored.	Allows for estimating the remaining propellant in the tank.
PROP-PIPE-11	PROP-TANK-10	The feed system shall leak before burst.	Prevents sudden end-of-life of the propulsion system, damaging of the spacecraft, and injuring of ground personnel.
PROP-PIPE-12	PROP-INT-4	The piping shall allow for filling and draining of both pressurant and propellant.	Allows for testing.

Continued on next page

Requirement ID	Parent Requirement(s)	Requirement	Rationale
PROP-PIPE-13	PROP-RAMS-2	The piping material shall be compatible with gaseous nitrogen, water, and Ti-6Al-4V.	Required for the system to function properly.
PROP-PIPE-14	PROP-INT-1	The piping shall be mechanically integrated within the propulsion system according to the CS14 interface standard.	Allows for integration within any CubeSat that adheres to this standard.

9.2 Piping Components and Layout

The piping consists of a fill/drain valve, a pressure relief valve, a pressure and temperature transducer, a propellant filter, a pressure regulator, a thruster valve, tubing, and connectors. This section discusses the above-mentioned components, including a conceptual re-design of the thruster housing itself, why they are required, where they are placed within the loop, and how they are attached to each other. All components, except some connectors and the conceptual re-design of the thruster housing, are commercial-off-the-shelf (COTS) components. These COTS components are selected without performing an individual trade-off, as was done in the rest of this thesis, between the wide variety of possible options due to time constraints. The main focus of the piping design is to show one possible configuration that allows propellant to flow from the tank to the thruster.

9.2.1 Components

Fill/drain valve

The fill/drain valve, shown in Figure 9.1, is a combination of a solenoid and check valve that was previously used in the LEAP propulsion system. This valve, despite its age (paper dates from 1992), is selected for its lightweight and compact design, as well as its capability to handle both loading and unloading of pressurants and propellants. Newer fill/drain valves with similar functionality tend to have larger component dimensions. The valve has an operating pressure range of 0 to 1500 psi (103 bar), and can withstand pressure surges of up to 5200 psi (358 bar). There are two unknowns regarding this fill/drain valve, namely the material of which it is constructed which might affect its compatibility with the pressurant and propellant and the number of fill/drain cycles without failure. Testing is required to verify the performance of the valve before implementation. The specifications of the fill/drain valve are summarized in Table 9.2.

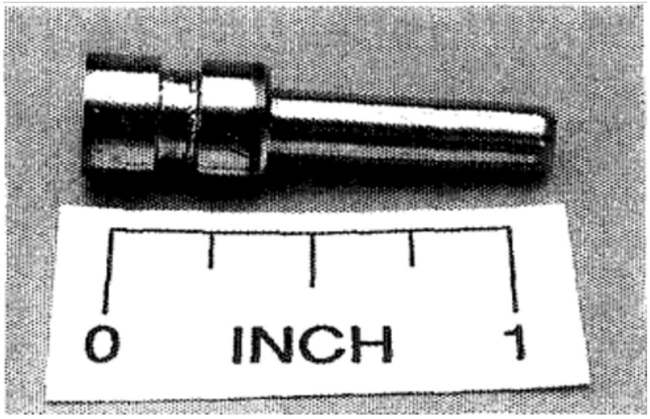

Figure 9.1: Fill/drain valve [112].

Table 9.2: Fill/drain valve specifications [112].

Type	Solenoid/check valve combination
Interface	Precision lapped poppet/seat interface
Working pressure	103 bar
Burst pressure	358 bar
Mass	6.35 g

Pressure relief valve

The screened 250 PRI relief valve, manufactured by The Lee Company, is chosen due to its low mass and small size. This valve is required to ensure that the pressure within the propulsion system does not exceed 10 bar (as per requirement

PROP-PIPE-07). A custom design in terms of the cracking pressure is required, as these are either below (5.5 bar) or above (34.5 bar) the required cracking pressure of 10 bar. The Lee Company offers such customization options for their pressure relief valves, including tailored designs with specific cracking pressures, flow rates, leakage criteria, and material selection [113]. The specifications of the custom relief valve are summarized in Table 9.3.

Table 9.3: Pressure relief valve specifications [114, p. 333].

Manufacturer	The Lee Company
Product number	Custom PRFA2505 series
Material	304L Cres
Minimum cracking pressure	10 bar (custom)
Minimum shutoff pressure	9 bar (custom)
Leakage at minimum cracking pressure	2 mL/min
Mass	4.5 g

A custom housing is required to integrate the relief valve within the propulsion system and to ensure that any expelled propellant is moved away from the internals as to prevent system malfunctions. The relief valve and custom housing are visualized in Figure 9.2.

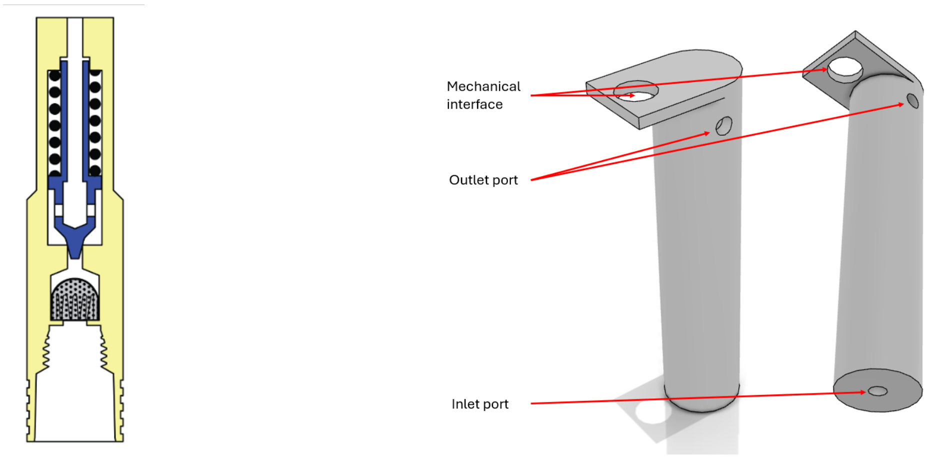

(a) Relief valve [114, p. 333].

(b) Custom relief valve holder.

Figure 9.2: Visualization of the pressure relief valve and custom holder.

Pressure and temperature transducer

The PCM127 sub-miniature pressure and temperature transducer, manufactured by EFE and shown in Figure 9.3, is chosen for its light-weight design and precision. Such a transducer is required to monitor both the pressure and temperature within the propulsion system as per requirement *PROP-PIPE-10*. The specifications of this pressure and temperature transducer are summarized in Table 9.4. A custom elbow connector is used to integrate the transducer.

Figure 9.3: Pressure and temperature transducer [115].

Table 9.4: Pressure and temperature transducer specifications [115].

Manufacturer	EFE
Product number	PCM127S-20bar-SG30-09/1m-D-2-2-BT
Material	316L Stainless Steel
Operating temperature range	-40 - 125 °C
Pressure range (FS)	-1 - 19 bar
Burst pressure	125 % FS
Rated excitation	8 to 16 VDC
Maximum electrical current	10 mA
Output voltage	5 VDC
Mass	10 g

Propellant filter

A propellant filter is essential to prevent impurities from entering the thruster, which could lead to performance degradation and potential malfunction. The 2F series filter with a 0.5 µm pore size, produced by Swagelok and shown in Figure 9.4, has been selected for this design. It is important to note that Swagelok typically offers this filter with inlet and outlet fittings larger than 1/8 inches, whereas the feed system requires fittings with a diameter of 1/16 inches to ensure compatibility with 1/16-inch OD tubing as discussed later in this section. It is assumed that Swagelok can provide 1/16-inch fittings, as they manufacture 1/16 inch OD tubing and other components with this fitting size. The specifications of the propellant filter can be found in Table 9.5.

Figure 9.4: Propellant filter [116].

Table 9.5: Propellant filter specifications (*mass is estimated using the CAD design) [116].

Manufacturer	Swagelok
Product Number	Custom 2F series
Material	316L Stainless Steel
Working pressure	355 bar
Operating temperature range	-28 - 93 °C
Element nominal pore size	0.5 μm
Mass	55 g*

Pressure regulator

The two-stage pressure regulator, manufactured by Beswick Engineering, is chosen as it can maintain a constant outlet pressure for a decaying inlet pressure. A constant outlet pressure of up to 30 psig (2.07 bar) can be achieved, whereas the inlet pressure can be as high as 500 psi (34.5 bar). One unknown regarding this pressure regulator is its compatibility with water. The manufacturer describes the performance of the regulator with compressed air as working medium. Testing is required before integration within the propulsion system to ensure compatibility with liquid water. Two custom elbow connectors are used to connect the regulator to the tubing. The pressure regulator is depicted in Figure 9.5, with its specifications summarized in Table 9.6.

Figure 9.5: Pressure regulator [117, p. 144].

Table 9.6: Pressure regulator specifications [117, p. 144].

Manufacturer	Beswick Engineering
Product number	PRD3-1N2-3-6VIK
Material	316L Stainless Steel
Seal and diaphragm material	Fluorocarbon
Lubrication	Krytox 240AZ
Inlet pressure	up to 34.5 bar
Outlet pressure range	0 to 2.1 bar
Mass	66 g

Solenoid valve

The high-speed solenoid valve, manufactured by The Lee Company, is chosen for its lightweight design and fast response time. This valve is of the normally-closed type, and is used as a thruster valve. The valve is shown in Figure 9.6, with its specifications summarized in Table 9.7.

Figure 9.6: High-speed solenoid valve [114, p. 600].

Table 9.7: High-speed solenoid valve specifications [114, p. 600].

Manufacturer	The Lee Company
Product number	IEPA1221541H
Seal material	Fluorocarbon
Spike/hold voltage	12 / 1.6 VDC
Power at spike/holding voltage	3 / 0.35 W
Maximum operating frequency	500 Hz
Maximum operating pressure	20 bar
Operating temperature range	4 - 125 °C
Life expectancy	$> 10^8$ cycles
Lohm rate	4100 [-]
Internal volume	62 μL
Mass	4.8 g

Tubing and connectors

Swagelok components are used to connect the aforementioned components and integrate them into the propulsion system. For tubing, 1/16 inch (1.6 mm) OD piping with a wall thickness of 0.01 inch (0.254 mm) are used, as this is the smallest tubing that Swagelok offers in terms of the outer diameter. Moreover, using this tube size allows for easy integration with the solenoid valve and other Swagelok piping components. Furthermore, a 1/16 inch OD union cross and tee connector are used. The union cross and tee connectors are visualized in Figure 9.7. The specifications of the tubing and connectors are summarized in Table 9.8.

(a) Union cross connector [118, p. 46].

(b) Union tee connector [118, p. 40].

Figure 9.7: Swagelok connectors.

Table 9.8: Piping and connector specifications (*mass is estimated using the CAD design) [118][119].

Tubing	
Manufacturer	Swagelok
Material	316L Stainless Steel
Outer diameter	1.6 mm
Wall thickness	0.254 mm
Working pressure	386 bar
Linear density	8.59 g/m
Union Cross	
Manufacturer	Swagelok
Material	316L Stainless Steel
Working pressure	386 bar
Mass	32 g*
Union Tee	
Manufacturer	Swagelok
Material	316L Stainless Steel
Working pressure	386 bar
Mass	21 g*

Conceptual thruster housing design

A re-design of the thruster housing is required, as the design that was outlined in Chapter 4 was constructed for testing purposes. The conceptual design of the housing is inspired by the CHIPS superheater cartridge (SHC) that was discussed in Chapter 2. It is assumed that the original chip dimensions remain the same: 17 x 7 x 0.9 mm. The conceptual design is shown in Figure 9.8, where the housing is a simple cylinder with a screw-on top cap.

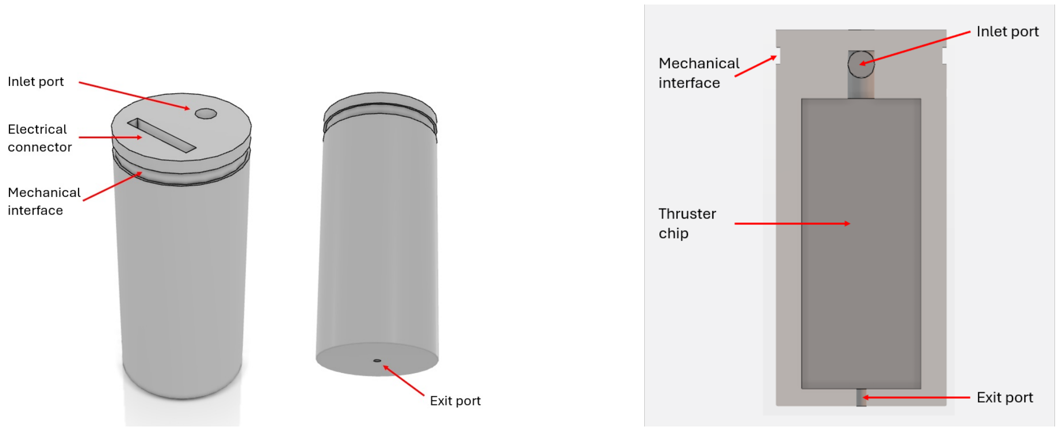

(a) External view.

(b) Clipped view.

Figure 9.8: Conceptual thruster housing design.

The 1.6 mm diameter of the thruster inlet ensures it is compatible with the tubing. A small cylindrical indent (1 mm tall, 0.2 mm depth) between the main thruster body and the screw-on cap allows for the thruster the be fastened to a flat plate. Electrically conductive rings are used to connect the electrical interface of the top cap with the heating elements on the chip itself. The detailed internal structure of the thruster housing, such as the connection between the thruster housing inlet and VLM chip inlet, the connection between the VLM chip outlet and the thruster housing outlet, and the electrical interface between the thruster housing and VLM chip, is left as future work.

9.2.2 Piping Layout and Material Compatibility

A schematic overview of the piping layout, including numbered pipes, can be found in Figure 9.9. These numbers are later used to indicate pressure drops over certain piping sections. The pressure and temperature transducer is placed as close as possible to the propellant tank outlet as to provide accurate readings of the pressure and temperature of the propellant within the tank. This allows for determining the remaining propellant within the tank. The propellant filter is placed in front of the pressure regulator, as a filter can cause a significant pressure drop within the piping. As the pressure regulator allows for a maximum outlet pressure of 2.1 bar, it is deemed beneficial to limit the pressure drop after the regulator as much as possible and maximise the thruster performance. This is done by placing most of the piping components in front of the pressure regulator. Only the thruster valve is placed after the regulator to ensure fast response times. Both the pressure relief valve and fill/drain valve are placed within the loop such that they can be positioned next to the cylindrical propellant tanks. Their functioning is deemed independent of their position within the loop, as long as they are placed in front of the pressure regulator.

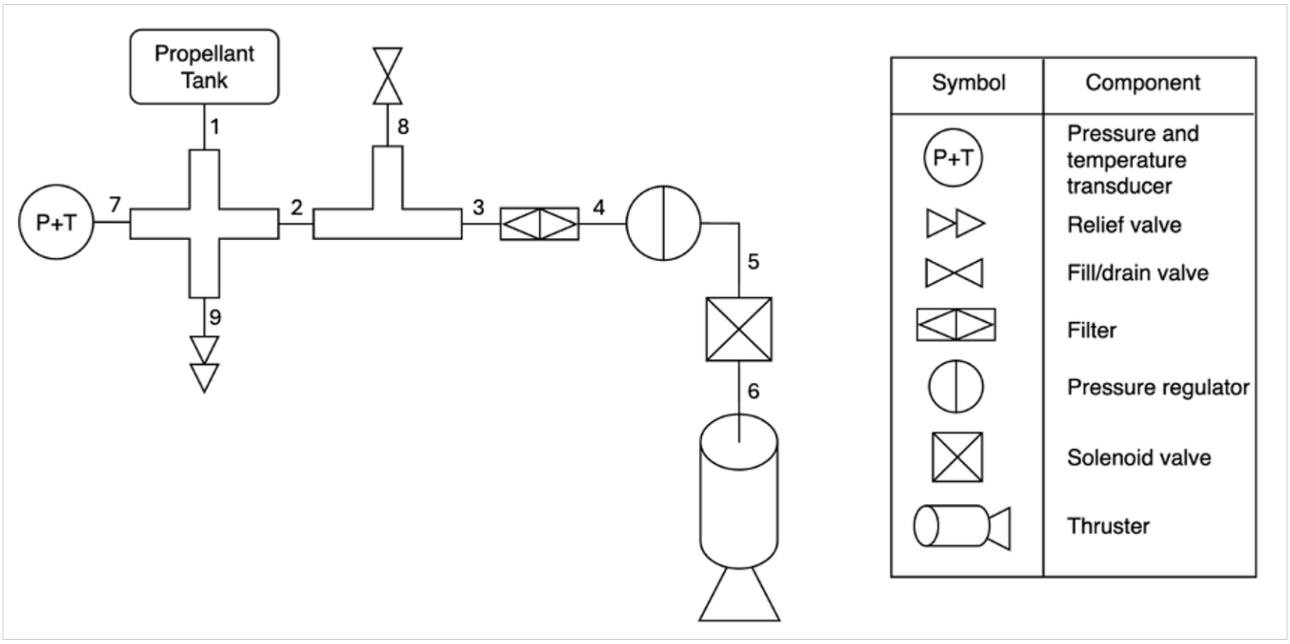

Figure 9.9: Schematic overview of the propulsion system

It is crucial to ensure that the piping materials are compatible with the pressurant (gaseous nitrogen), propellant (water), and tankage materials (Ti-6Al-4V). In terms of compatibility between the dissimilar tankage and piping materials, water can act as an electrolyte between the cathodic titanium and anodic stainless steel. Although titanium and stainless steel are relatively close in the galvanic series (indicating lower galvanic potential), there is still a risk of galvanic corrosion. This risk is increased in conditions with slow or stagnant fluid flow, as is the case here [120]. To minimize galvanic corrosion, it is essential to use demineralized water as propellant, as it contains very few dissolved ions, thereby reducing the conductivity of the solution and slowing the corrosion process. Additionally, a propellant filter is used to remove any particulates from the flow, which may arise from the minimal galvanic corrosion. Finally, 316L stainless steel is compatible with both the pressurant and propellant [121].

9.2.3 3DExperience Model

Figure 9.10 shows the CAD model of the piping, including the custom 92 x 92 mm tray with 4 mechanical interfaces that are conform the CS14 interface standard (as per requirement *PROP-PIPE-14*).

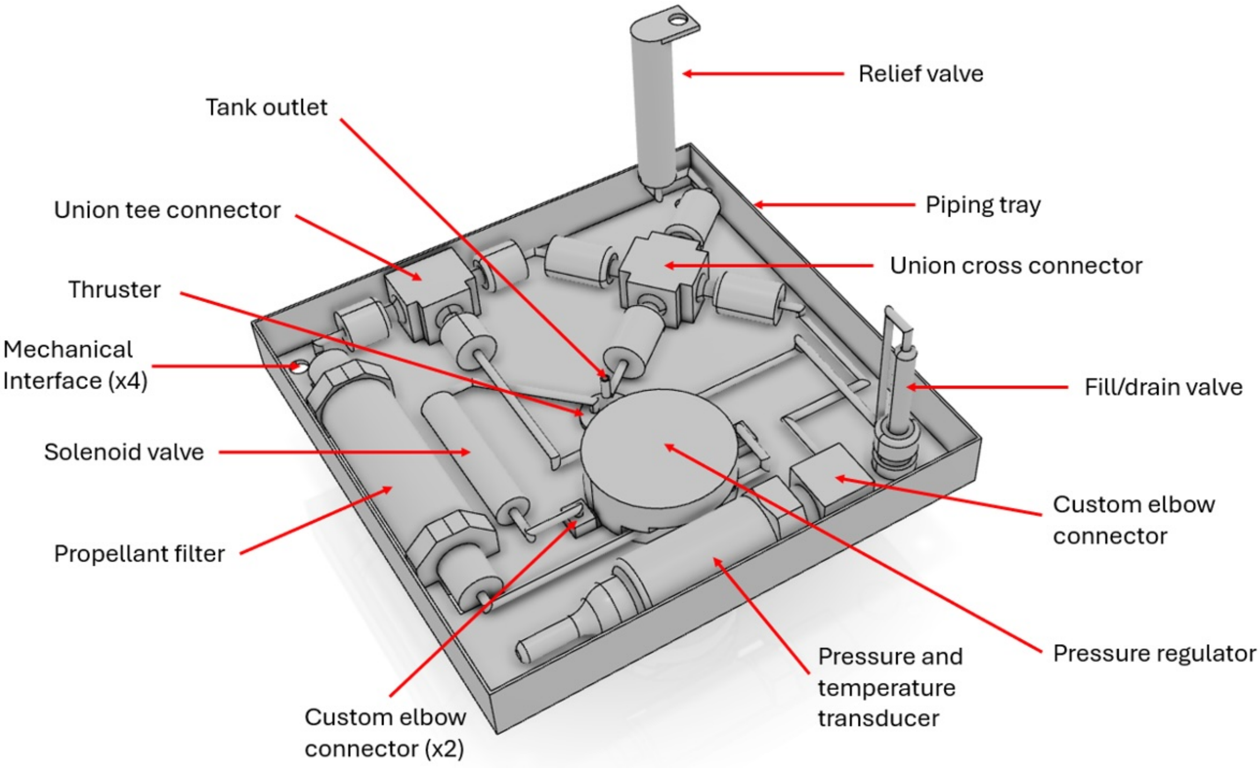

Figure 9.10: Piping CAD model.

9.2.4 Fill/drain and thrust path

The fill path is visualized in Figure 9.11a. First, a vacuum is created within the feed system to ensure that there is no air within the system itself. The propellant is then filled and flows toward the tank by entering the fill/drain valve, then into pipe 8, followed by the tee connector into pipe 2, and finally through the cross connector into pipe 1 and into the tank. It must be noted that the liquid propellant also enters pipe 3, passes through the filter and pressure regulator and is stopped by the thruster valve. Furthermore, propellant flows towards the fill/drain valve and pressure and temperature regulator. After the correct amount of liquid propellant is filled by taking into account the unusable propellant in the piping towards the relief valve and transducer, pressurant is added into the system. There is only one way that this pressurant can flow to: towards the empty space within the propellant tank itself.

The propellant and pressurant are drained by following the same flow path in reverse, where first the propellant is drained, followed by the pressurant. It is possible that both pressurant and propellant leave the tank at the same time, as there is no physical barrier between the two. Adequate steps must be taken to ensure the safety of the ground personnel.

The thrust path can be seen in Figure 9.11b, where propellant leaves the tank and enters the piping. It flows from the tank through the cross connector, tee connector, propellant filter, pressure regulator, and thrust valve towards the thruster.

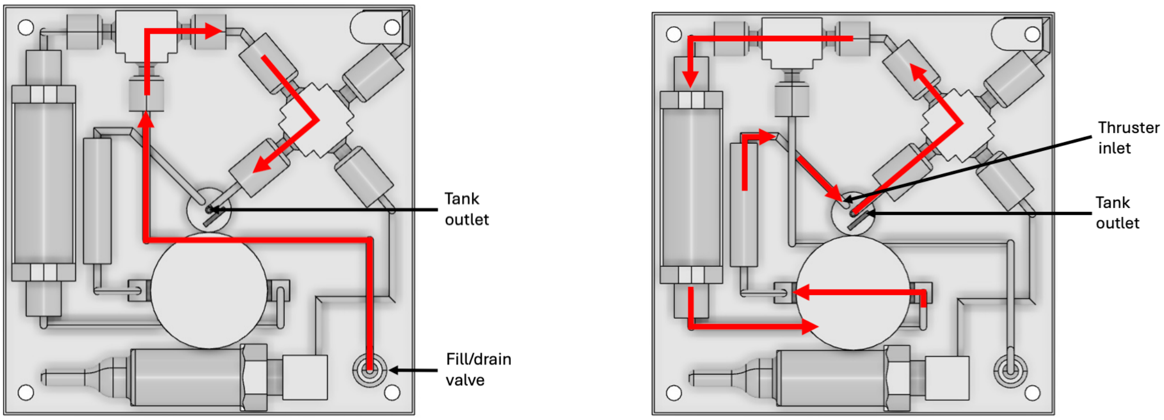

(a) Fill/drain path.

(b) Thrust path.

Figure 9.11: Pressurant and propellant flow paths.

9.2.5 Mass and Power Breakdown

Table 9.9 shows the mass and power breakdown of the piping configuration. The total mass and power are 283 g and 3.16 W respectively. It must be noted that the peak power of the solenoid valve is taken as a worst-case scenario. The power used by the valve is more likely to be closer to its average value of 0.35 W.

Table 9.9: Mass and power breakdown (*mass estimated from CAD model).

Component	**Mass per Unit [g]**	**Power per unit [W]**	**Quantity**	**Total Mass [g]**	**Total Power [W]**
Piping tray	67*	N/A	1	67	N/A
Tubing	8.6	N/A	0.379	3.3	N/A
Propellant filter	55*	N/A	1	55	N/A
Solenoid valve	4.8	3	1	4.8	3
Pressure regulator	66	N/A	1	66	N/A
Pressure regulator connector	2*	N/A	2	4.0	N/A
Pressure and temperature transducer	10	0.16	1	10	0.16
Transducer connector	5*	N/A	1	5.0	N/A
Fill/drain valve	5	N/A	1	5.0	N/A
Cross connector	32*	N/A	1	32	N/A
Tee connector	21*	N/A	1	21	N/A
Pressure relief valve	4.5	N/A	1	4.5	N/A
Pressure relief valve holder	5*	N/A	1	5.0	N/A
Total				**283**	**3.16**

Table 9.10 provides an overview of the tankage mass breakdown. It is clear that the smallest 200 Ns system is significantly over budget. This is a result of the relatively heavy piping tray. Additional cut-out in the piping tray can, combined with utilizing part of the design margin (= 58 grams), can help reduce or potentially eliminate the mass budget overrun.

Table 9.10: Tankage mass breakdown (masses are in grams).

System	**200 Ns**	**400 Ns**	**600 Ns**
Tank shell	138	153	168
PMD	3.74	4.84	6.04
Piping	283		
Total	424	440	457
Tankage mass budget	347	696	1045
Remainder	***-77***	256	588

9.2.6 Volume Breakdown

Figure 9.12 provides a side view of the piping, illustrating that a portion of the piping extends beyond the tray. Table 9.11 details the distances from the top of the piping tray to the bottom of each protruding component, including the tray's bottom.

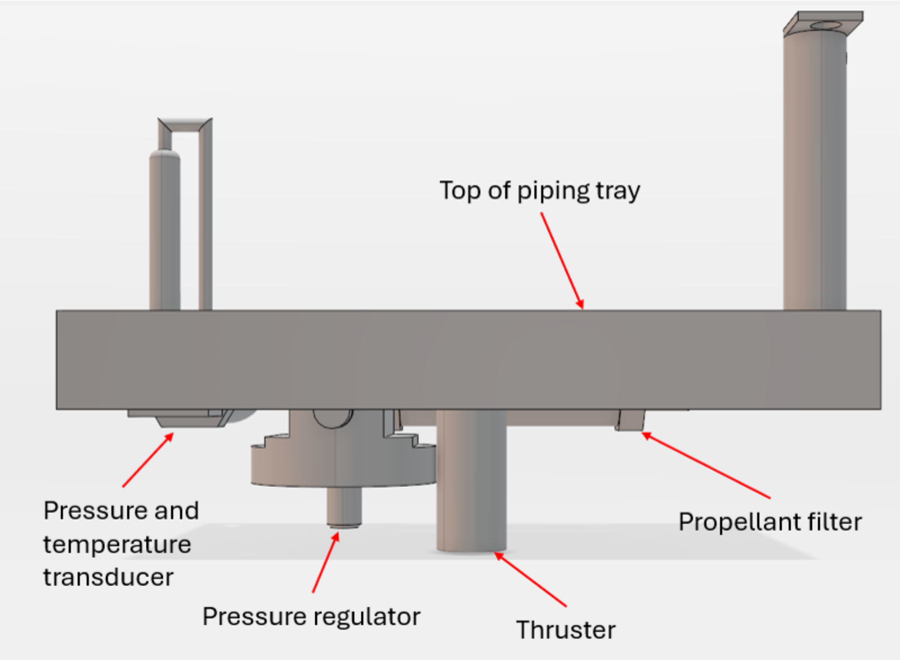

Figure 9.12: Side view of the piping assembly.

Table 9.11: Distances (in mm) from the top of the piping tray to the bottom of each protruding component.

Component	**Distance from top of tray**
Bottom of tray	11.0
Propellant filter	14.8
Transducer	13.5
Pressure regulator	27.9
Thruster housing	31.0

Furthermore, Table 9.12 presents the remaining height budget for the tankage in each of the three propulsion systems. By comparing Table 9.11 and Table 9.12, it is evident that the entire piping assembly exceeds the height budget allocated for the 200 Ns system. For the 400 Ns and 600 Ns systems, only the thruster and pressure regulator surpass the height budgets.

Table 9.12: Residual tankage height budgets for piping assembly.

System	**200 Ns**	**400 Ns**	**600 Ns**
External tank height [mm]	44.3	84.4	124.3
Height budget [mm]	50	100	150
Residual budget [mm]	5.7	15.6	25.7

A TunaCan add-on can partially mitigate the height budget overrun for the 200 Ns system and fully resolve the overruns for the 400 Ns and 600 Ns systems. The remaining overrun for the 200 Ns system is deemed acceptable, as reducing the propellant tank height could lead to a total deliverable impulse below the minimum required 200 Ns, depending on the (currently unknown) thruster losses.

9.3 Pressure drops

Estimating the pressure drop within the piping is required to verify the performance of the propulsion system. The pressure drop over the tubing can be calculated by using the Darcy-Weisbach relation [51, p. 382]:

$$\Delta P = \frac{f}{2}\frac{L_{pipe}}{D_i}\rho_{prop}v^2 \tag{9.1}$$

where f is the friction factor of the pipe, L_{pipe} is the length of the pipe, D_i is the inner diameter of the pipe, ρ_{prop} is the propellant density, and v is the flow velocity. The flow velocity is found using [51, p. 382]:

$$v = \frac{Q}{A_{in}} = \frac{\dot{m}}{\rho_{prop} A_{in}} \tag{9.2}$$

where Q is the volumetric flow rate, A_{in} is the inner cross-sectional area of the pipe, and $\dot{m}$ is the mass flow rate. The mass flow rate, volumetric flow rate, and flow velocity are summarized in Table 9.13.

Table 9.13: Flow within 1/16 inch tubing (the flow rates are taken from Subsection 8.1.1).

Mass flow rate [kg/s]	$6.54 \cdot 10^{-7}$
Volumetric flow rate [m^3/s]	$6.55 \cdot 10^{-10}$
Flow velocity [m/s]	$7.00 \cdot 10^{-4}$

The friction factor value (f) is dependent on the flow regime. This regime is determined by calculating the Reynolds number (Re) of the flow within the tubes [51, p. 457]:

$$Re = \frac{\rho_{prop} v D_i}{\mu} \tag{9.3}$$

where μ is the dynamic viscosity of the propellant. Fully developed, incompressible, laminar flow occurs when the Reynolds number is below 2320, whereas turbulent flow occurs at Reynolds numbers larger than 10,000. Transitional flow is found at Reynolds numbers between 2320 and 10,000. The flow within the 1/16 inch OD piping is, with a Reynolds number of 0.762, in the fully developed, incompressible laminar flow regime. The friction factor is determined using the Poisseuille relationship [51, p.458]:

$$f = \frac{64}{Re} \tag{9.4}$$

resulting in a friction factor of 83.9.

The pressure drop within connectors, such as the cross connector, tee connector, and elbow connectors, and pipe bends can be calculated by using an equivalent length over diameter value (L_{eq}/D_i) within the Darcy-Weisbach relationship. The equivalent length over diameter values for the connectors and pipe bends within the piping of the propulsion system are summarized in Table 9.14.

Table 9.14: Equivalent length over diameter ratios (*linear interpolation between 45° and 90° used) [122].

Connectors	
Tee: straight flow	20
Tee: corner flow	60
Cross: straight flow	20
Cross: corner flow	60
Elbow: 90°	30
Pipe bends	
45°	14
50°	14.6*
60°	15.7*
90°	19

The pressure drop within the piping components can be calculated using two methods: through interpolation and extrapolation of manufacturer provided flow data, and through use of the discharge coefficient. The latter is preferred, as it more accurate. However, some manufacturers, including Beswick Engineering, provide the performance of their components in unspecific units such as standard cubic feet per hour (SCFH) compressed air, without specifying the pressure and orifice area that is required to calculate the discharge coefficient. Interpolation and extrapolation is required, combined with several assumptions, to estimate the performance of the component.

Calculating the pressure drop though the discharge coefficient is done by using [51, p. 235]:

$$\Delta P = \frac{\rho_{prop}}{2} \left(\frac{Q}{C_d A_o} \right)^2 \tag{9.5}$$

where C_d is the discharge coefficient and A_o is the orifice area. The discharge coefficient is either provided by the manufacturer, can be calculated by solving the above-mentioned relationship for the discharge coefficient given a certain volumetric flow rate, orifice area, propellant, and pressure drop, or can be determined from the Lohm rate. The Lee Company specified the Lohm rate (L) of each component, which can be converted to a discharge coefficient using [123, p. 143]:

$$C_d = \frac{0.527}{LA_o} \tag{9.6}$$

where A_o is the orifice area in square inches.

9.3.1 Measurement flow path

The pressure drop between the tank and pressure and temperature transducer must be calculated to determine the real pressure within the propellant tank. It is expected that the pressure drop is negligibly small due to the low flow velocity. However, this must be verified. The flow path between the tank and pressure transducer consists of pipe 1, a cross connector, and pipe 7. The equivalent length over diameter ratios and the total pressure drop are summarized in Table 9.15.

Table 9.15: Pressure loss in measurement flow path.

Component	**L$_{eq}$/D$_i$**	**Quantity**	**$\prod$L$_{eq}$/D$_i$**
Straight pipe	0.916	69.0	63.2
90 deg pipe bed	19	5	95.0
Cross: corner flow	60	1	60.0
Elbow: 90 deg	30	1	30.0
$\sum$ L$_{eq}$/D$_i$ [-]			248
ΔP [Pa]			5.09

It is concluded that the pressure drop between the tank and transducer is negligibly small compared to tank pressure at EOL (2.19 bar).

9.3.2 Pressure relief path

Propellant is expelled through the relief valve when the pressure within the feed system rises beyond 10 bar. The flow path between the tank and pressure relief valve consists of pipe 1, a cross connector, and pipe 9. The equivalent length over diameter ratios and total pressure drop are summarized in Table 9.16.

Table 9.16: Pressure loss in pressure relief flow path.

Component	**L$_{eq}$/D$_i$**	**Quantity**	**$\prod$L$_{eq}$/D$_i$**
Straight pipe	0.916	28.3	25.9
50 deg bend	14.6	1	14.6
90 deg pipe bend	19	3	57.0
Cross: straight flow	20	1	20.0
$\sum$ L$_{eq}$/D$_i$ [-]			118
ΔP [Pa]			2.41

9.3.3 Thrust path

Propellant flows from the tank towards the thruster when the solenoid valve is opened. The flow path can be split into two parts: in front of the pressure regulator and after the pressure regulator. The flow path in front of the pressure regulator consists of pipe 1, a cross connector, pipe 2, a tee connector, pipe 3, a propellant filter, and pipe 4. The flow path after the pressure regulator consists of pipe 5, a solenoid valve, and pipe 6. The pressure drops over the pipes and connectors can easily be calculated by using their equivalent length of diameter ratios, as was done before. However, calculating the pressure drop over the filter, pressure regulator, and solenoid valve requires some additional steps and assumptions.

Propellant filter

Swagelok provides flow data for the propellant filter in the form of the pressure drop within the filter as function of the flow rate. Three data points are provided for each nominal pore size. The data for the 0.5 μm pore size, including a trend line that allows for interpolation and extrapolation, are plotted in Figure 9.13.

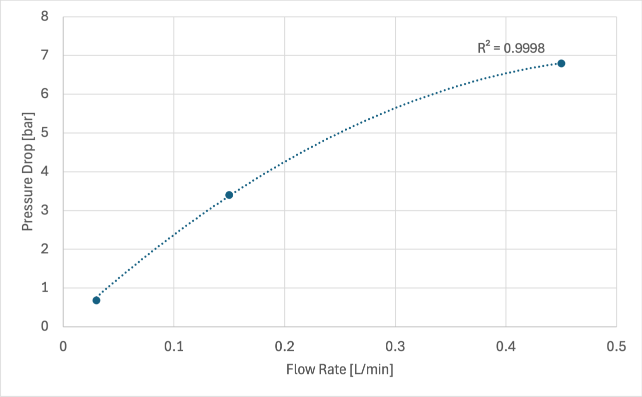

Figure 9.13: Pressure loss as a function of the flow rate through the filter [116].

The total pressure drop over the 0.5 μm filter, for a volumetric flow rate of $3.93 \cdot 10^{-9}$ L/min, is approximately 103 Pa.

Pressure regulator

Beswick Engineering describes the performance of the pressure regulator as a function of the standard cubic feet per hour (SCFH) compressed air. There is no orifice area and air pressure mentioned with these units, which makes calculating the discharge coefficient impossible. Furthermore, as previously mentioned, it was assumed that this pressure regulator works with water as the working fluid, whereas the manufacturer does not specifically specify this to be a working fluid.

Beswick engineering provides two flow curves that relate the regulated pressure (at the outlet) and compressed air flow rate [124]. The goal is to relate the inlet pressure to the outlet pressure for a given flow rate. Two data points are obtained from the two flow curves for the no-flow condition. The no-flow condition is chosen, as the flow rate of the propulsion system is small ($6.55 \cdot 10^{-10}$ m^3/s or $8.33 \cdot 10^{-5}$ CFH). A linear relationship between the two data points is assumed and extrapolated to generate a third data point at the nominal operating pressure of 8.75 bar at BOL. The three data points are used to generate a plot that relates the ratio of inlet pressure over the outlet pressure to the input pressure. This ratio cannot drop below a value of 1, as it is impossible for the regulator to increase the downstream pressure. The relationship between the ratio of the inlet pressure over the outlet pressure as a function of the inlet pressure is shown in Figure 9.14. This relationship can be used to calculate the downstream pressure when the upstream pressure (at the regulator inlet) is known.

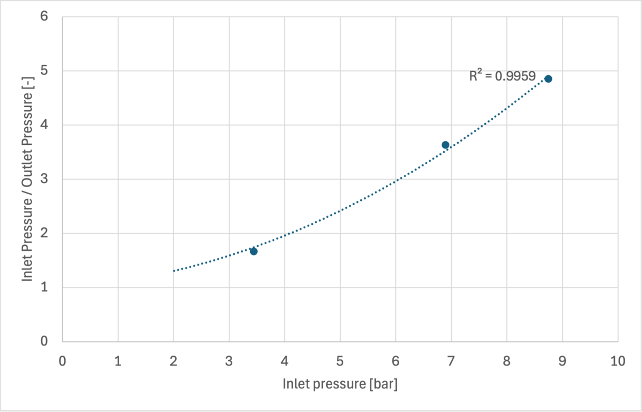

Figure 9.14: Ratio of inlet over outlet pressure as a function of the input pressure.

Solenoid valve

The Lee Company provides the Lohm rate, internal volume, and length of the solenoid valve. These three parameters allow for calculating the discharge coefficient using Equation 9.6. The pressure drop is then calculated using Equation 9.5, and results in a total pressure drop of 0.021 Pa.

Total pressure drop

The total pressure drop over the thrust flow path determines the performance of the propulsion system itself. The mass flow rate, hence thrust, is constant throughout the system lifetime, as it is a pressure regulated system. The worst-case scenario is at EOL, when the inlet pressure at the regulator is the smallest (2.19 bar) as was shown in Figure 9.14 and is to be used for determining the performance of the system. Table 9.17 shows the pressure drops within the piping of the flow upstream and downstream of the pressure regulator.

Table 9.17: Pressure loss over thrusting flow path.

Component	**L_{eq}/D_i**	**Quantity**	**$\prod L_{eq}/D_i$**
Before pressure regulator			
Straight pipe	0.916	101.734	93.2
60 deg pipe bend	15.7	1	15.7
90 deg pipe bend	19	9	171
Cross: corner flow	60	1	60.0
Tee: straight flow	20	1	20.0
Elbow: 90 deg	30	1	30.0
$\sum L_{eq}/D_i$ [-]			390
Propellant filter pressure drop [Pa]			103
ΔP [Pa]			111
Regulator inlet pressure [bar]			2.19
Regulator outlet pressure [bar]			1.62
After pressure regulator			
Straight pipe	0.916	51.012	46.7
45 deg pipe bend	14	1	14.0
90 deg pipe bend	19	5	95.0
Elbow: 90 deg	30	1	30.0
$\sum L_{eq}/D_i$ [-]			186
Solenoid valve pressure drop [Pa]			0.0210
ΔP [Pa]			3.83

It is observed that the pressure drop over the tubing, connectors, valve and filters is negligible compared to the pressure drop over the pressure regulator. It is therefore assumed that the regulator inlet pressure is equal to the EOL tank pressure, namely 2.19 bar. This yields a thrust chamber pressure of 1.62 bar, as the pressure loss between the regulator and thruster is again negligible. The ratio of inlet over outlet pressure of 1.35 is smaller than the estimated value of 2 that was used to determine the performance of the thruster in Chapter 6 and results in a larger achievable thrust level of up to 1.24 mN. For conservatism it is decided to use an inlet over outlet pressure ratio of 1.65, resulting in an achievable thrust of 1 mN. This decision is based on the fact that the performance of the pressure regulator is assumed to be identical to compressed air when using water as a working medium. The required heating power to achieve the thrust level of 1 mN is 2.33 W (from Figure 6.2b), whereas the total input power, assuming a thruster efficiency of 50 %, is approximately 4.7 W.

9.4 Requirement Compliance

Table 9.18 provides a summary of the requirements, indication weather each one is met, and if not, suggest a potential mitigation strategy. The most crucial requirements that are not (fully) met are requirement *PROP-PIPE-05*, *PROP-PIPE-06*, and *PROP-PIPE-13*. The first two are important, as they impact the overall design of the propulsion systems. The smallest system exceeds the allocated mass budget, whereas all three systems exceed their respective height constraint. *PROP-PIPE-13* is crucial, as galvanic corrosion can cause premature functioning of the propulsion system. The suggested mitigation strategies must be followed to limit the effects of the non-compliance with the previously mentioned requirements.

Table 9.18: Requirement verification table.

Requirement ID	**Requirement**	**Compliant**	**Explanation**	**Mitigation Strategy**
PROP-PIPE-01	The piping shall allow for propellant to flow from the tank towards the thruster.	Yes	There is an undisturbed flow path from the tank to the thruster.	Not required.
PROP-PIPE-02	The configuration of the piping shall be identical across the three system sizes.	Yes	The piping configuration is applicable to all three system.	Not required.
PROP-PIPE-03	The piping shall ensure that no impurities enter the thruster.	Yes	There is a propellant filter in the flow path.	Not required.

Continued on next page

Requirement ID	Requirement	Compliant	Explanation	Mitigation Strategy
PROP-PIPE-04	The piping shall not exceed the 92 x 92 mm (XY) boundaries.	Yes	The piping tray is 92 x 92 mm.	Not required.
PROP-PIPE-05	The tankage height (Z) shall not exceed 50 mm / 100 mm / 150 mm.	No	Part of the piping assembly exceeds the specified Z-boundaries.	Partial mitigation: make use of a TunaCan add-on.
PROP-PIPE-06	The total mass of the tankage shall not exceed 347 g / 695 g / 1043 g.	Partial	The tankage mass of the 200 Ns is above the allocated mass budget.	More cut-outs in piping tray and use (part of) the design margin.
PROP-PIPE-07	The piping shall survive a maximum expected operating pressure of 10 bar.	Yes	Pressure relief valve will dump propellant when the pressure exceeds 10 bar.	Not required.
PROP-PIPE-08	The lines and fittings shall have a burst safety factor >= 4.	Yes	All lines and fittings working pressure are above 4 times the MEOP.	Not required.
PROP-PIPE-09	All pressure components, other than lines and fittings, shall have a burst safety factor >= 2.5.	Partial	The pressure and temperature transducer and solenoid valve do not meet this requirement.	Both are flight-proven components with a maximum operating pressure above 20 bar (2 times the system MEOP), so no mitigation required.
PROP-PIPE-10	The pressure and temperature of the propellant shall be electronically monitored.	Yes	There is a pressure and temperature transducer present.	Not required.
PROP-PIPE-11	The feed system shall leak before burst.	Yes	There is a pressure relief valve present.	Not required.
PROP-PIPE-12	The piping shall allow for filling and draining of both pressurant and propellant.	Yes	There is a fill/drain valve present.	Not required.
PROP-PIPE-13	The piping material shall be compatible with gaseous nitrogen, water, and Ti-6Al-4V.	Partial	Possibility of galvanic corrosion due to the presence of 316L stainless steel and grade 5 titanium.	Use of a propellant filter and demineralized water as propellant.
PROP-PIPE-14	The piping shall be mechanically integrated within the propulsion system according to the CS14 interface standard.	Yes	The piping tray mounting holes are in-line with the CS14 PCB.	Not required.

9.5 Conclusion

This chapter outlined the design of the piping, including the required components, their respective location, the resulting pressure drops within the system, and the effect on performance of the propulsion system in terms of required heating power and thrust.

The piping consists of a piping tray, a fill/drain valve, a pressure relief valve, a pressure relief valve holder, a pressure and temperature transducer, a propellant filter, a pressure regulator, a thruster valve, 1/16 inch OD tubing, and connectors. All components, except the piping tray, conceptual thruster design, pressure relief valve holder, and some elbow connectors are COTS components. The use of COTS was decided on as it increases the reliability of the system and reduces cost. The piping weighs a total of 283 g and requires a maximum power of approximately 3.2 W. A detailed breakdown of the individual component masses and power consumption was provided in Table 9.9.

The total pressure drop over the piping was calculated using the Darcy-Weisbach relation, the discharge coefficients, and the Lohm rates, combined with several extrapolations of component performance and assumptions on the functioning of the pressure regulator with water as a working medium. It was determined that the pressure drop over the pressure regulator is the largest (0.57 bar), whereas the pressure drop over all the other components is negligible (115 Pa). For conservatism, a total pressure drop of 0.86 bar over the pressure regulator is used, resulting in a chamber pressure of 1.33 bar and an achievable thrust of 1 mN. The performance of the propulsion system is identical for all three propulsion systems, as the piping is identical. The performance is summarized in Table 9.19.

Table 9.19: Thruster performance.

Parameter	**Value**
Chamber pressure [bar]	1.33
Mass flow rate [mg/s]	0.79
Thrust [mN]	1
Specific impulse [s]	130
Required heating power [W]	2.33

The tankage mass breakdown for all three systems was outlined in Table 9.10. The mass budget of the 200 Ns system was exceeded by 77 grams. Part of the excess mass can be deducted from the 58 gram design margin, resulting in a total mass budget overrun of 19 grams. One option, to ensure that the mass budget is not exceeded, is to create more cut-out in the piping tray. However, this can lead to thermal problems when the system is in space. It is decided that the 19-gram mass overrun is accepted, and possibly negated by other budget entries being below their maximum values. The latter is discussed when the system is fully assembled.

Finally, the piping assembly exceeded the allocated height budgets for all three systems. The use of a TunaCan add-on was proposed to mitigate part of these overruns, whereas the remaining budget overrun for the 200 Ns was accepted, as reducing the propellant tank height could yield a total deliverable impulse below the required 200 Ns.

9.6 Recommendations

Two recommendations are proposed for the piping design. A first recommendation is to perform a thorough trade-off for each piping component. While several options were considered for each component, only the selected ones are discussed in this chapter. This yielded a possible piping design. However, performing detailed trade-offs can result in a more compact and lightweight design, potentially reducing or even eliminating the aforementioned budget overruns.

The second recommendation is to test the thruster to determine its losses. A safety factor of 25 % was applied to the required propellant volume, partly to account for these unknown losses. Understanding the thruster's losses could enable the use of a smaller propellant tank, helping to further reduce the tankage mass and volume budget overruns.

Finite Element Analyses on Tank Design 10

This chapter outlines the finite element analysis (FEA) that is performed on the three propellant tanks. An introduction is provided in Section 10.1, followed by the modelling of the tank in Section 10.2. Next, a mesh convergence study is performed in Section 10.3. This study is followed by an internal pressure analysis in Section 10.4, and a structural redesign of the tanks in Section 10.5. A launch load analysis, buckling analysis, and natural frequency analysis is conducted in respectively Section 10.6, Section 10.7, and Section 10.8. The chapter is concluded in Section 10.9, whereas several recommendations are provided in Section 10.10.

10.1 Introduction

The propellant tank shell was designed in Chapter 8 using analytical relationships that were provided by the ASME Boiler and Pressure Vessel Code. However, these relationships do not account for the effects of the wall-mounted PMD and integrated mechanical interfaces that connect the tank to the propulsion system. A finite element analysis (FEA) is required not only to verify the design in terms of its structural integrity, but also to determine the displacement of the tank components. The latter was not investigated in the analytical tank design, as they were deemed negligible due to the relatively low tank pressures. In retrospect, these deflections should have been incorporated into the analytical tank design, as they can significantly impact the assembly of the propulsion systems in terms of component spacing.

The Linear Structural Validation (LSV) Toolkit from the 3DExperience software, under the student licence provided by Delft University of Technology, is used for the analyses. This toolkit allows for calculating the stresses and displacements of the tank that occur during propellant loading and launch conditions through the structural analysis. Furthermore, the critical buckling loads and natural frequency modes of the propellant tank can be calculated.

The displacements, as calculated by the LSV toolkit, indicate how much each point is moved from its original location in millimetres. Furthermore, the stresses resulting from these deformations are calculated as so-called Von Mises Stress (σ_{VM}) [125]:

$$\sigma_{VM} = \sqrt{\frac{1}{2}\left[\left(\sigma_x - \sigma_y\right)^2 + \left(\sigma_y - \sigma_z\right)^2 + \left(\sigma_z - \sigma_x\right)^2\right] + 3\left(\tau_{xy}^2 + \tau_{yz}^2 + \tau_{zx}^2\right)} \tag{10.1}$$

where σ_i indicate the stress the i-direction and τ_{jk} the shear stress in the jk-plane, as visualised in Figure 10.1.

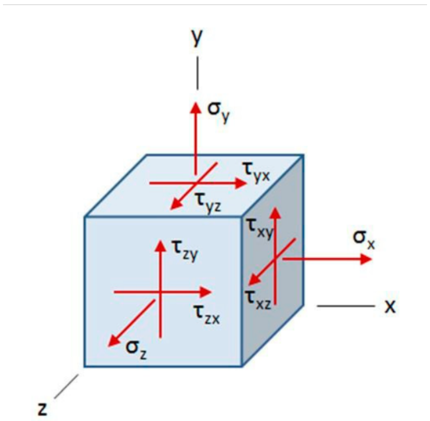

Figure 10.1: Visual representation of the six stress components in the Von Mises stress equation [125].

The goal of the analyses performed in this chapter is to verify the tank designs, and to investigate the need for any local structural reinforcements and possible component spacing. The final tank design, including the mechanical interfaces with the rest of the propulsion system, must adhere to the requirements that were outlined in Chapter 8, of which the ones applicable to the structural performance are repeated below:

- *PROP-TANK-06*: "The propellant tanks shall survive a maximum expected operationg pressure of 10 bar."
- *PROP-TANK-07*: "The propellant tank shall have a design factor of safety of 1.25 for yield."
- *PROP-TANK-08*: "The propellant tank shall have a design factor of safety of 1.4 for ultimate load."
- *PROP-TANK-17*: "The propellant tank shall survive an axial acceleration of 8.5g."
- *PROP-TANK-18*: "The propellant tank shall survive a lateral acceleration of 3g."
- *PROP-TANK-19*: "The minimum resonant frequency of the mechanical interface between the propellant tank and the main structure of the propulsion system shall be larger than 35 Hz."

Finally, the Von Mises stress within the tank shell, as calculated by the LSV toolkit, cannot exceed the design stress of 678.6 MPa that resulted from:

$$\sigma_m = min\left(\frac{\sigma_y}{FoS_y} \quad ; \quad \frac{\sigma_u}{FoS_u}\right) \tag{10.2}$$

where the tensile yield and ultimate strength of Ti-6Al-4V are 880 MPa and 950 MPa respectively (see Table 8.4).

10.2 Modelling the Propellant Tanks

A first step in analysing the tank design is to model the assembly. The propellant tanks are split into three parts: the bottom endcap with a 1.6 mm diameter tank outlet hole, the cylindrical shell with integrated vanes, and the top endcap. Furthermore, the mechanical interfaces are integrated in the top and bottom endcap design, as shown in Figure 10.2.

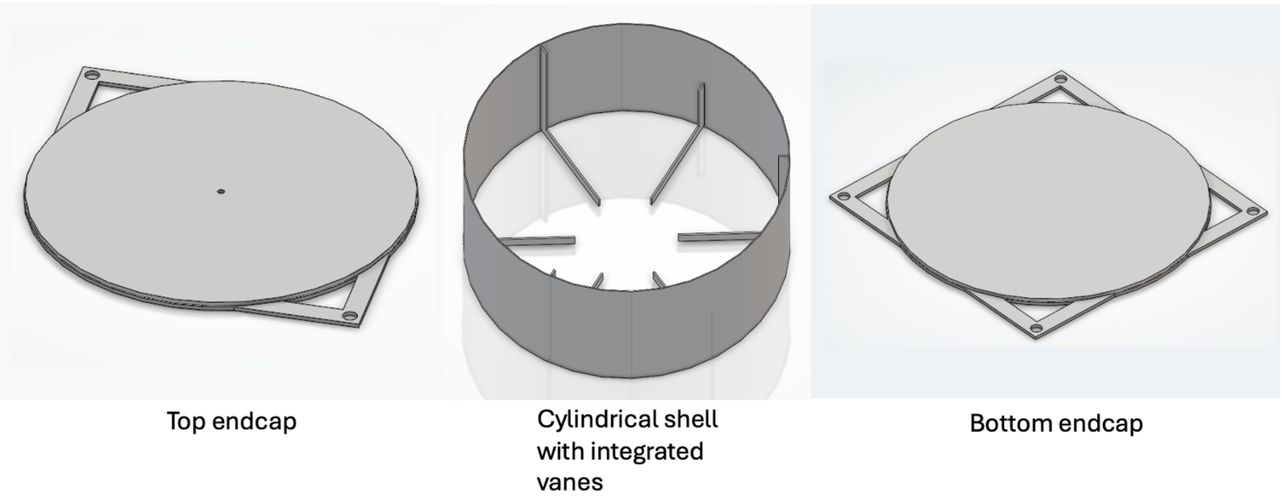

Figure 10.2: Visualisation of the three components that are used to model the 200 Ns propellant tank.

The sponge is excluded from the analyses as the integration of the sponge with the tank structure was left for future work and can therefore not be modelled accurately. Moreover, excluding the sponge from the analysis will result in conservative deformations and stress levels, as it will carry some load in the real design.

Three bonded contact connections are used to connect the tank components. This type of connection represents a weld and ensures that the components remain firmly attached throughout the different analyses [126]. These connections are applied between the tank bottom endcap and the cylindrical shell wall, the bottom of the vanes and the bottom endcap, and between the cylindrical shell wall and the top endcap. There is no bonded contact connection between the top of the tall vanes and the top endcap, as it is physically impossible to weld these during the tank assembly.

Finally, a clamp boundary condition is applied to the six mechanical interfaces which connect the tank with the rest of the propulsion system. This boundary condition prevents the attachment points from moving and deforming throughout the different analyses [126].

10.3 Mesh Convergence Study

The accuracy of finite element analysis solutions improves with smaller mesh sizes, but only up to a certain limit. Beyond this point, the solution stabilizes and no longer changes with further reductions in mesh size, indicating convergence.

Identifying the mesh size at which convergence occurs is essential to ensure both the computational efficiency and reliability of the results.

To determine the converged mesh size, a mesh convergence study is conducted on the smallest (200 Ns) and largest (600 Ns) propellant tanks. The study examines how stress and displacement results vary with a mesh refinement under an internal pressure of 10 bar. This load case is chosen, as it is assumed to be the highest load that the system will endure throughout its lifetime (requirement *PROP-TANK-06*). Furthermore, the tetrahedron mesh size is decreased from 10 mm per element to 1 mm. The mesh could not be decreased beyond this point, as the student licence is limited to a million mesh elements per analysis.

Measurements of displacement and stress are taken at three locations: the centre of the outer skin of the top endcap, the centre of the cylindrical tank wall, and the exterior of the tank outlet. These locations are chosen to ensure that a converged solution is found for all three components.

The results of the mesh convergence study are visualised in Figure 10.3 and Figure 10.4. The deflection and Von Mises stress at the centre of the cylindrical tank wall are plotted separately from the top and bottom endcaps due to their large difference in absolute values. Convergence of this cylindrical tank wall would be difficult to identify when combining these results with the rest of the system.

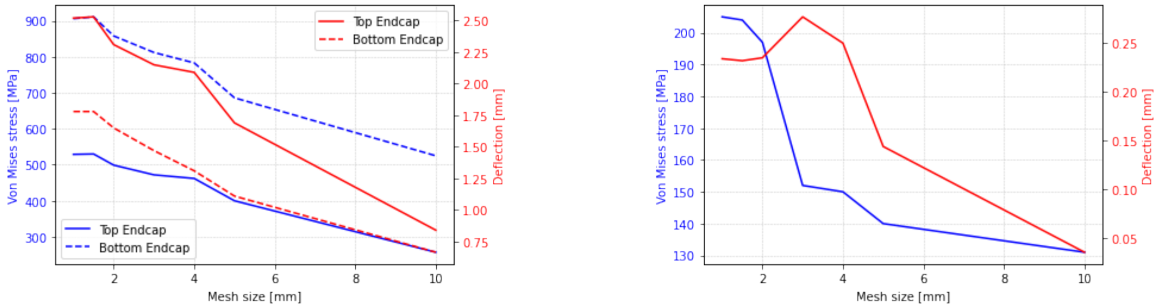

(a) Stress and deflection of the top and bottom endcap.

(b) Stress and deflection of the cylindrical shell.

Figure 10.3: Mesh convergence study results for the 200 Ns propellant tank.

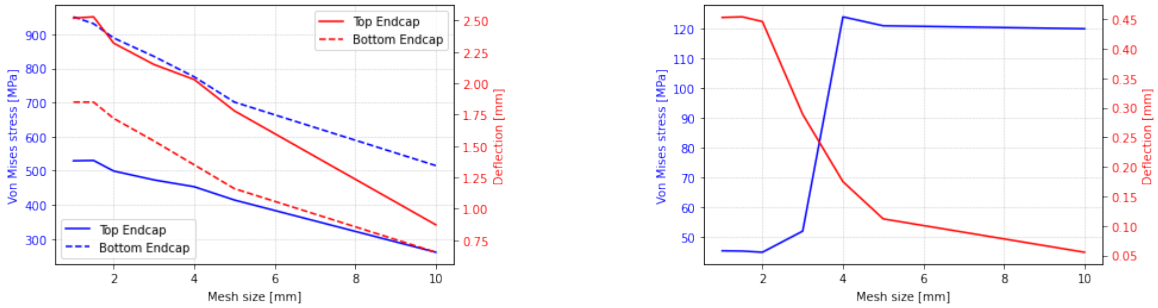

(a) Stress and deflection of the top and bottom endcap.

(b) Stress and deflection of the cylindrical shell.

Figure 10.4: Mesh convergence study results for the 600 Ns propellant tank.

It can be seen that a converged solution, in terms of the deflection and stresses, is achieved for all three components at a mesh size of 1.5 mm. Reducing the mesh size below this value does not significantly impact the results of the analyses. However, it must be noted that these apparent convergences are a result of manually measuring the stresses and displacements within the components and are prone to errors, as measuring at the exact same location each time is proven difficult. The sudden convergence at a mesh size of 1.5 mm, after a continuous increase (or decrease) of the results, is seen as suspicious, and should be verified by further decreasing the mesh sizes. However, this is not possible as the student license is limited to one million nodes, constraining the minimum possible mesh size to 1 mm. This mesh size is therefore used throughout this chapter, as it provides the best indication of a converged solution for the 200 Ns and 600 Ns system. Furthermore, it is assumed that a 1 mm mesh size will also yield a converged solution for the 400 Ns system, as both the smallest and largest systems indicated convergence.

10.4 Internal Pressure Analysis

This section outlines the structural response of the smallest tank, in terms of stress and displacement, to an internal pressure of 10 bar (equivalent to the maximum expected operating pressure as specified by requirement *PROP-TANK-06*). Visualizations of the results for the 400 Ns and 600 Ns systems are provided in Appendix A and are excluded from this section due to their similarity in stress levels, stress locations, and tank component displacements.

Figure 10.5 shows the stress levels within the 200 Ns propellant tank that result from an internal pressure of 10 bar, where the stress levels that exceed the design stress of 678.6 MPa are shown in dark grey. Several observations can be made from this figure. First, it shows that the design stress is exceeded in multiple locations, including at the interfaces between the cylindrical shell and endcaps. The latter is an unexpected result, as the tank was designed according to the ASME Boiling and Pressure Vessel Code. This rise in stress is a result of the endcaps preventing the cylindrical skin from deforming, which results in a significant bending moment that was not anticipated by the ASME code. Furthermore, it can be seen that the current vane design and integration yields large stress concentrations due to the presence of many 90-degree angles. Finally, the design stress is exceeded at the tank outlet, which is anticipated as stress concentrates around such cutouts.

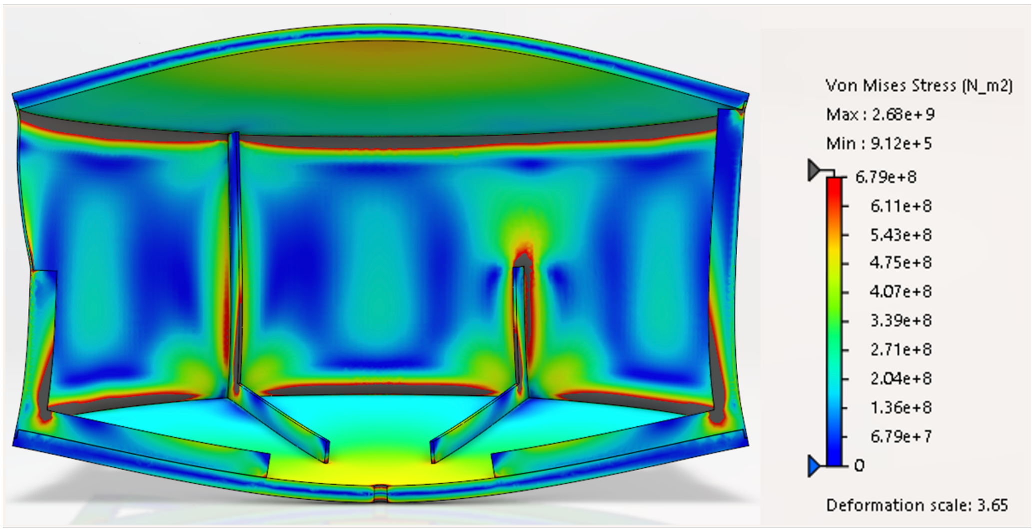

Figure 10.5: Stress within the 200 Ns tank structure as a result of a 10 bar internal pressure.

Figure 10.6 visualises the stress in the mechanical interfaces that are attached to the top and bottom endcap. Only half of both endcaps are shown, as the problem is symmetric. It is evident that the stress is concentrating around the sharp (approximately 45-degree) corners where the mechanical interface attaches to cylindrical tank.

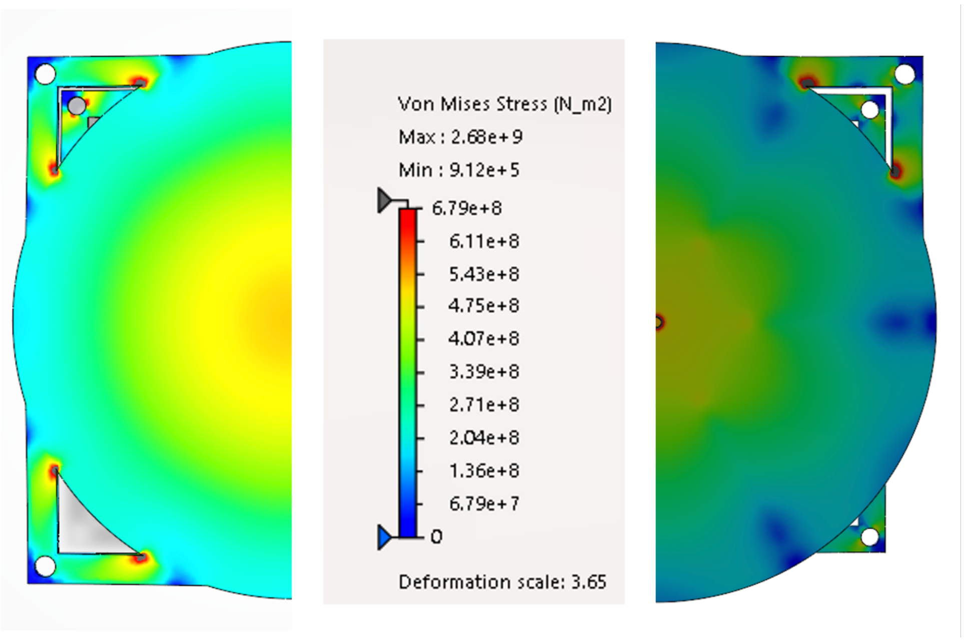

Figure 10.6: Stress within the 200 Ns top and bottom endcaps as a result of a 10 bar internal pressure.

Finally, Figure 10.7 shows the displacement of the tank walls. The top endcap has the largest displacement as there is no internal structure that prevents it from deforming. The bottom endcap does have an internal structure which results in a significantly smaller displacement.

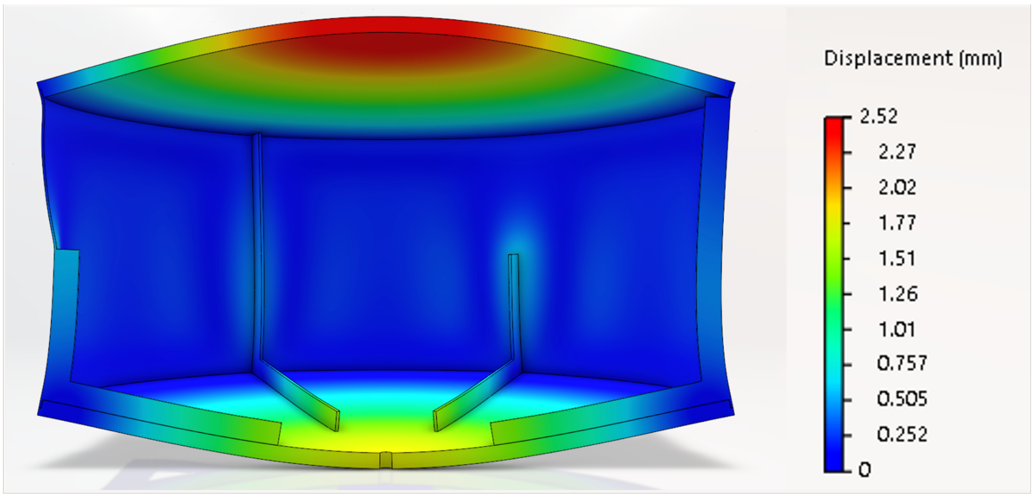

Figure 10.7: Displacement of the 200 Ns tank structure as a result of a 10 bar internal pressure.

A summary of the top and bottom endcap displacements is provided in Table 10.1, where the similarities between the three tanks in terms of displacement (and therefore stress as both properties are linked) becomes evident. The relatively large deflections are undesired as they increase the overall system height without adding any additional value to the system. Reinforcements are required to not only decrease the stress within the tank structure, but also to limit the deflection of both the top and bottom endcaps.

Table 10.1: Displacement (in mm) of the top and bottom endcaps in the Z-direction.

System	**200 Ns**	**400 Ns**	**600 Ns**
Top endcap	2.52	2.52	2.52
Bottom endcap	1.78	1.83	1.85

10.5 Tank Redesign for Internal Pressure Load

A redesign of the tank is required, as the stresses exceed to maximum allowed stress of 678.6 MPa as was shown in the previous section. Furthermore, the displacements of both the top and bottom endcap, as was shown in Table 10.1 are relatively large and will increase the system height. An iterative approach is used by applying local reinforcements and edge fillets at locations where the design stress is exceeded. The decision to apply local reinforcements, rather than simply increasing the wall thickness everywhere, is beneficial in terms of mass and usable propellant. The intermediate results of this iterative approach are excluded from this thesis due to the many iterations that were performed.

As mentioned in the previous section (and can be verified by comparing Figure 10.5 with the figures in Appendix A), the locations at which the design stress is exceeded, and the stress levels themselves are comparable across the three systems. This allows for applying the same modifications to the three tank designs. The following design alterations yields a design that can survive the internal pressure load of 10 bar:

1. A 0.8 mm thick and 10 mm tall reinforcement ring at the top and bottom of the cylindrical tank shell. This increases the local skin thickness to 1.1 mm.
2. A 10 mm edge fillet at the 90-degree bend in the vanes.
3. A 2 mm edge fillet on all three corners of the mechanical interface.
4. A 0.5 mm edge fillet on both sides of the tank outlet.
5. A 0.3 x 3 mm edge fillet on the end of each vane (at the side that is attached to the cylindrical tank wall).

The last design alteration is applied for conservatism, as without this edge fillet the stress would exceed the ultimate strength of the material for a very small part of the tank wall. This small area could be a result of a finite element analysis artifact due to the sharp angle at the interface. However, this cannot be proven as the mesh cannot be further refined without losing accuracy in the top and bottom endcap stress levels due to the limitation regarding the number of mesh elements of the student license. All design modifications are shown in Figure 10.8.

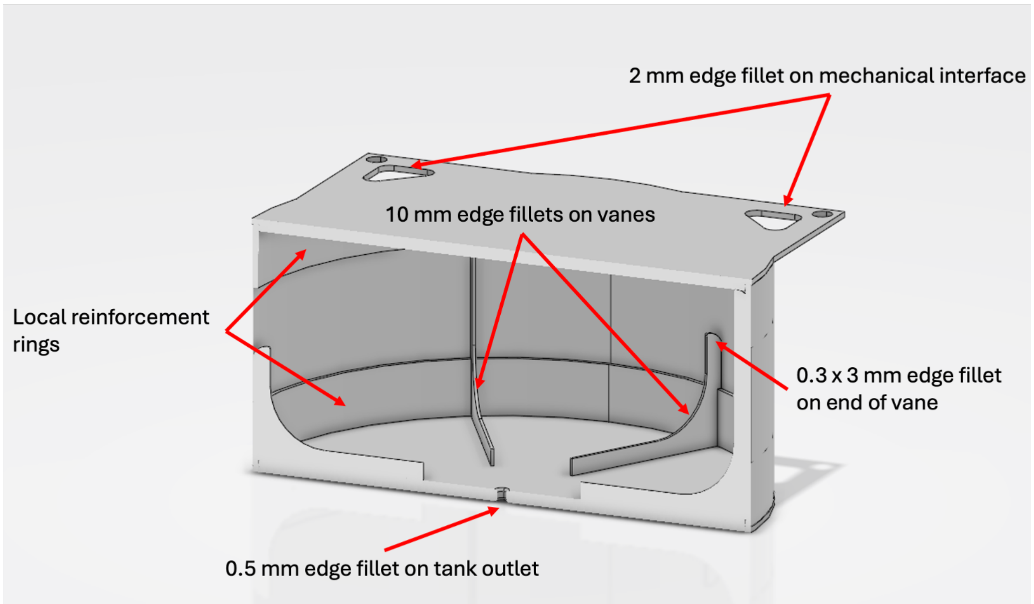

Figure 10.8: Visualization of the five tank modifications.

Figure 10.9 visualises the stress within the 200 Ns tank structure when all modifications, except the last one, are applied. A clear concentration of stress can be seen at the point where the top of the vanes attach to the tank walls. Now, Figure 10.10 shows the accuracy of this simulation which is calculated as the ratio of errors in element energy density to the total element energy density [126]. A clear overlap between the location of the stress concentration and the 0% simulation accuracy can be seen here. Further mesh refinement to examine this behaviour is not possible due to the software's inability to apply local mesh improvements, as the vane and cylindrical shell are modelled as a single component, and the limitation of one million mesh elements which does not allow for a global mesh refinement. A 0.3 x 3 mm edge fillet is therefore applied to the top of all vanes where they interface with the tank wall.

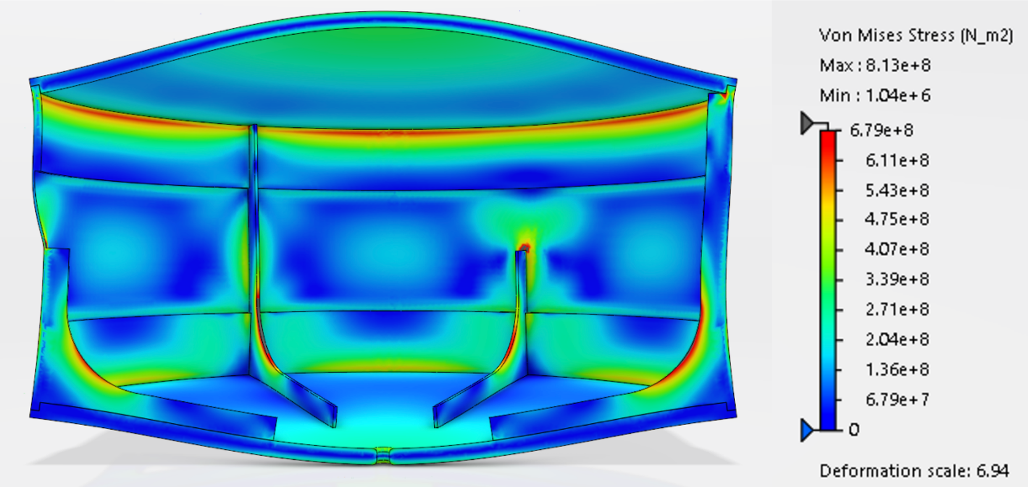

Figure 10.9: Stress within the redesigned 200 Ns tank structure, excluding the edge fillets on the end of each vane, as a result of a 10 bar internal pressure.

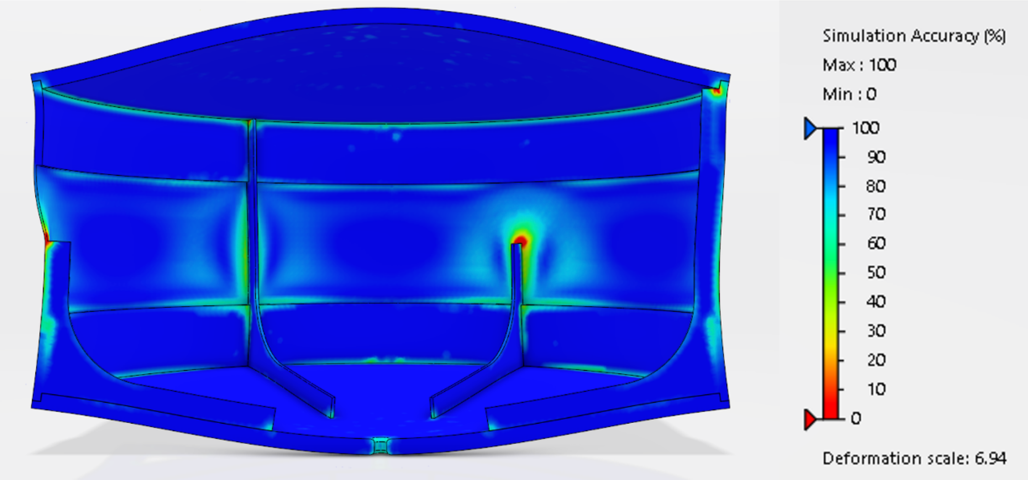

Figure 10.10: Simulation accuracy of the 200 Ns internal pressure analysis.

Figure 10.11 shows the stress within the 200 Ns tank structure where all five design modifications are applied. The results of the 400 Ns and 600 Ns systems are visualised in Appendix A, as the stresses, locations of these stresses, and the deformations for these systems are comparable. It can be seen that the stress is below the design stress of 678.6 MPa at most locations. However, there are some local stress concentrations at the edge fillet of the vane and, again, at the point where the top of the vanes connect to the tank wall. These local stress concentrations are not seen as problematic, as they are all below the tensile yield strength of Ti-6Al-4V (equal to 880 MPa).

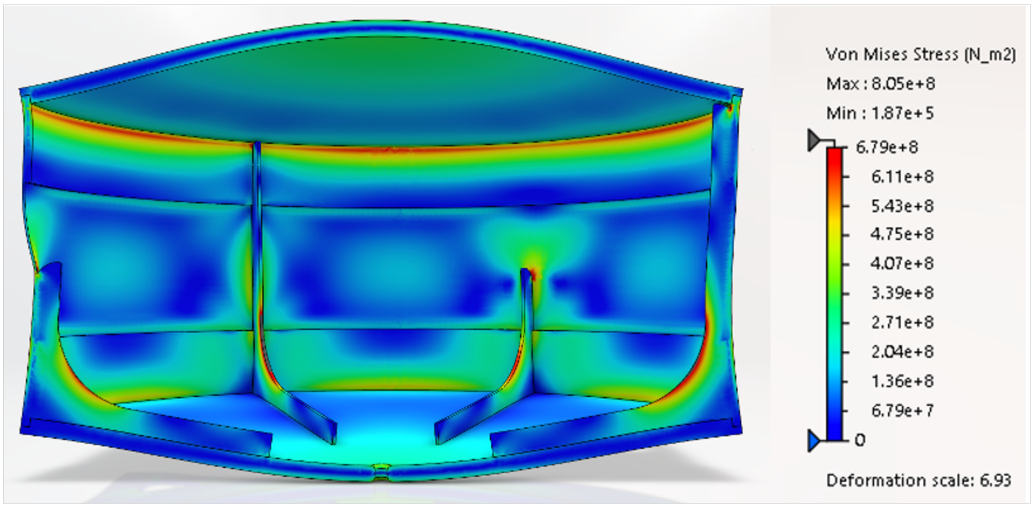

Figure 10.11: Stress within the redesigned 200 Ns tank structure as a result of a 10 bar internal pressure.

Figure 10.12 shows the stress in both the top and bottom endcap. The 2 mm edge fillets, applied at the corners of all mechanical interfaces, result in significantly decreased stress levels. All stress concentrations that were found in the original interface design disappeared, and are now well below the design stress.

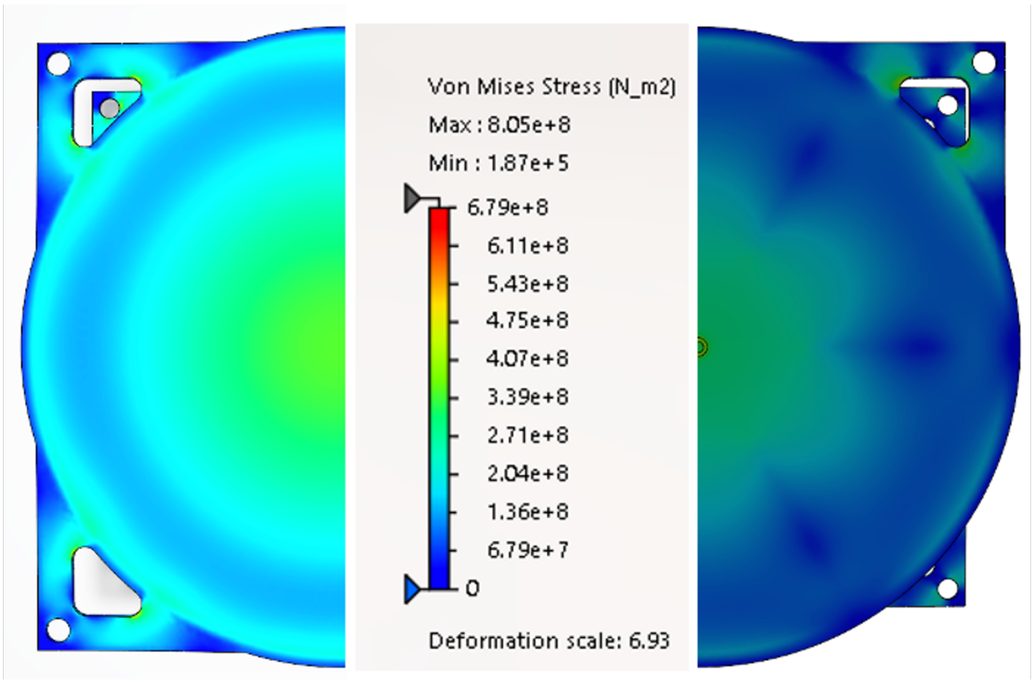

Figure 10.12: Stress within the redesigned 200 Ns top and bottom endcaps as a result of a 10 bar internal pressure.

Finally, Figure 10.13 shows the displacement of the tank structure when all design modifications are applied. A significant decrease in both the top and bottom endcap, as a result of these design alterations, is observed. A summary of the maximum displacements of the top and bottom endcaps for all systems is provided in Table 10.2.

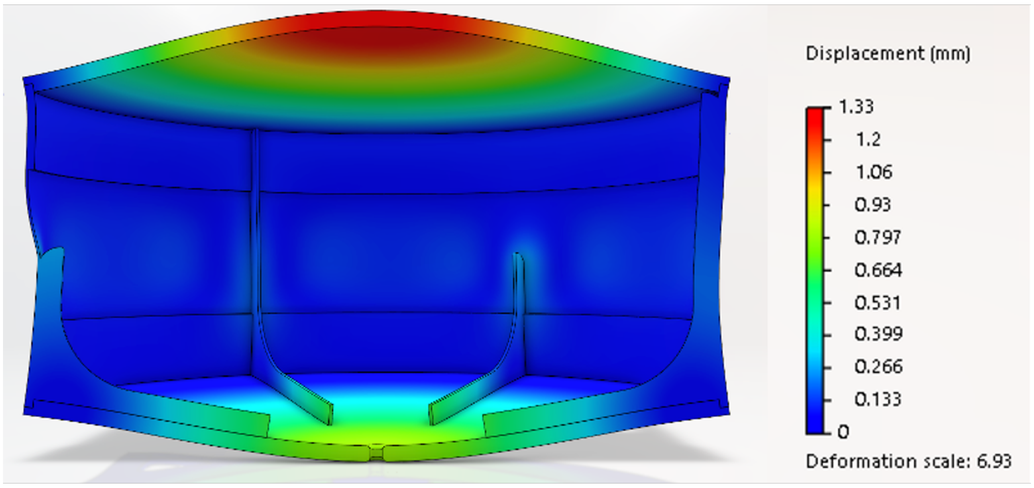

Figure 10.13: Displacement of the redesigned 200 Ns tank structure as a result of a 10 bar internal pressure.

Table 10.2: Displacement (in mm) of the top and bottom endcaps in the Z-direction.

System	**200 Ns**	**400 Ns**	**600 Ns**
Top endcap	1.33	1.33	1.33
Bottom endcap	0.806	0.854	0.873

10.6 Launch Load Analysis

This section describes the launch load analysis that is performed for the three reinforced propellant tanks, where the worst-case acceleration of 8.5g (as described in requirement *PROP-TANK-17*) is applied to the structure of the tanks while the mechanical interfaces remain clamped. Moreover, the mass of the propellant is modelled as non-structural mass that is attached only to the cylindrical shell. The propellant mass is not attached to the top and bottom endcap, as this will yield a lower stress within, and displacement of, the integrated mechanical interfaces. The latter is crucial, as there must be sufficient spacing between the propulsion system components to prevent damage during launch. Applying the propellant mass only to the cylindrical shell will result in a theoretically lower deflection of both endcaps, as the hydrostatic pressure on these two surfaces is now neglected. However, the hydrostatic pressures are insignificant compared to the applied internal pressure of 10 bar, as shown in Table 10.3, and can therefore be neglected.

Table 10.3: Maximum hydrostatic pressure on both top and bottom endcap during an axial acceleration of 8.5g.

System	**200 Ns**	**400 Ns**	**600 Ns**
Propellant density [kg/m^3]	998		
Fill ratio [-]	0.75		
Internal tank height [mm]	40.1	80.2	120.1
Hydrostatic pressure [Pa]	2503	5006	7496

Figure 10.14 shows a split view of the stress within both the top (left side) and bottom (right side) endcap of the 200 Ns propellant tank as a result of the 8.5g acceleration that is applied. The stress within both endcaps during an acceleration applied in the negative X-direction is omitted due to the symmetry of the tank in that plane. It can be concluded that the mechanical interfaces survive the maximum expected acceleration level of 8.5g, as the stress within the interfaces is below the design stress of 678.6 MPa for all cases. The same conclusion can be drawn for the 400 Ns and 600 Ns propellant tanks, as shown in Appendix A.

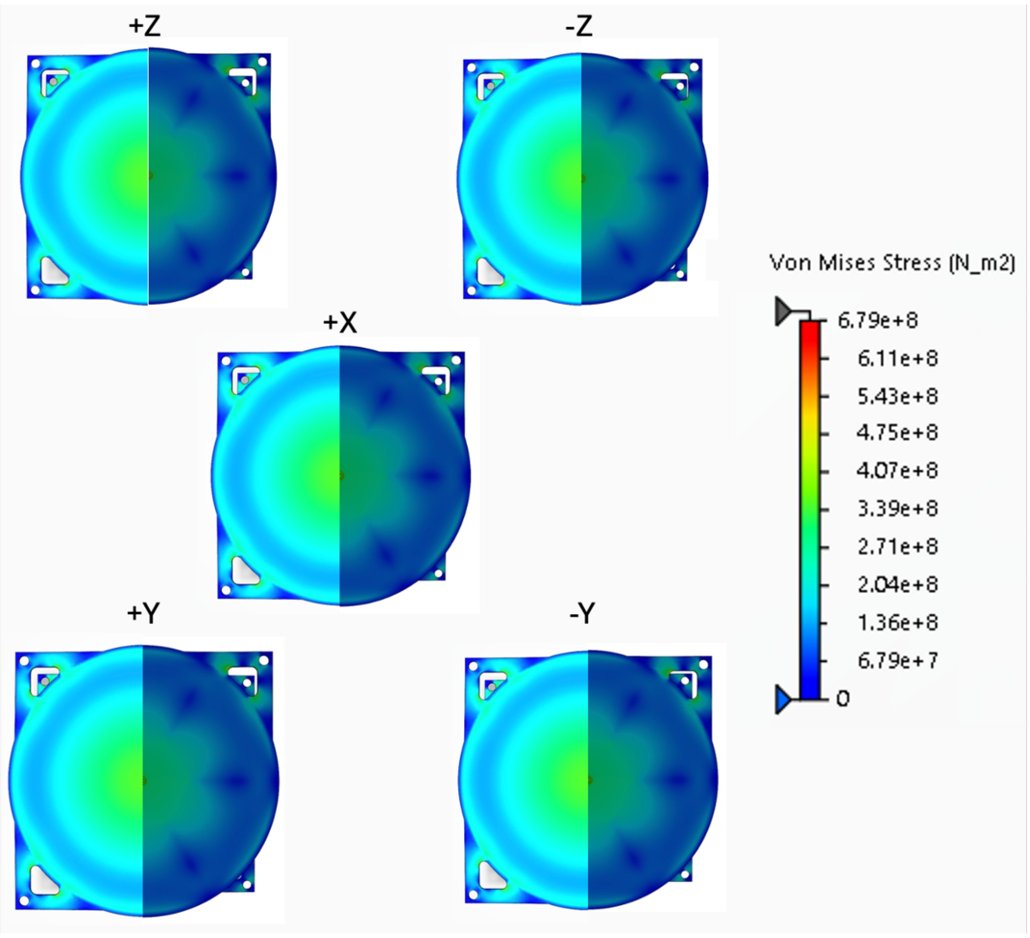

Figure 10.14: Von Mises stress distribution in the top (left) and bottom (right) endcaps of the 200 Ns system under 8.5g acceleration.

Table 10.4 summarizes the maximum displacement of both the top and bottom endcap for the three systems. A slight increase in deflection, compared to the results found in Section 10.5, is observed for the top endcap during an acceleration in the negative Z-direction whereas the deflection of the bottom endcap increases for an acceleration in the positive Z-direction. Moreover, the deflection of both the top and bottom endcaps do not change for an acceleration in the X- and Y-direction. The maximum displacements of both top and bottom endcaps are indicated in **bold face**.

Table 10.4: Deflections (in mm) of top and bottom endcap under an 8.5g acceleration.

System	**200 Ns**		**400 Ns**		**600 Ns**	
Endcap	Top	Bottom	Top	Bottom	Top	Bottom
+Z	1.32	**0.819**	1.31	**0.874**	1.3	**0.899**
-Z	**1.34**	0.794	**1.35**	0.835	**1.36**	0.847
+X, +Y, -Y	1.33	0.806	1.33	0.854	1.33	0.873

A vertical spacing of 1.4 mm at the top endcap, and 0.9 mm at the bottom endcap is required to ensure that the propellant tanks can deform safely without causing damage to itself and the surrounding components.

10.7 Buckling Analysis

This section outlines the buckling analysis conducted on the three reinforced propellant tanks, necessitated by the initial vacuum required at the start of the filling procedure (as detailed in Chapter 9). No buckling is expected during the operational lifetime of the tank after filling, as the end-of-life tank pressure is approximately 2.19 bar. An external pressure of 1 atm (or 101325 Pa) is applied to the tank walls to evaluate the critical buckling load. The results of these analyses are summarized in Table 10.5, where it can be seen that the critical buckling load decreases significantly for the larger systems. This behaviour is expected, as larger aspect ratio structures (= height / width) buckle more easily. The critical buckling load of all systems is above 1 atm and will therefore not fail due to buckling. A visualization of the buckling modes for the three systems is provided in Appendix A.

Table 10.5: Critical buckling load of the three propellant tank structures.

System	**200 Ns**	**400 Ns**	**600 Ns**
Critical buckling load [atm]	12.0	3.6	2.2

10.8 Natural Frequency Analysis

This section outlines the last step in the finite element analysis of the propellant tanks, namely the natural frequency analysis. The first natural frequency of each tank must be above 35 Hz to prevent resonance between the tank and the launcher as described by *PROP-TANK-19*. It must be noted that the propellant is neglected in this analysis and that vibration testing is required to determine the effects of the propellant, such as sloshing and dampening, on the natural frequencies. Figure 10.15 visualizes the first vibration mode of each system size, whereas the first three natural frequencies of each system are summarized in Table 10.6. The colours in Figure 10.15 represents a measure of the distance that each point moved from its original location shown in the middle column as the blue tank structures. The tank structures on the left and right side of this origin indicate their extreme positions throughout the vibrational modes. The first three vibration modes of each system are shown in Appendix A.

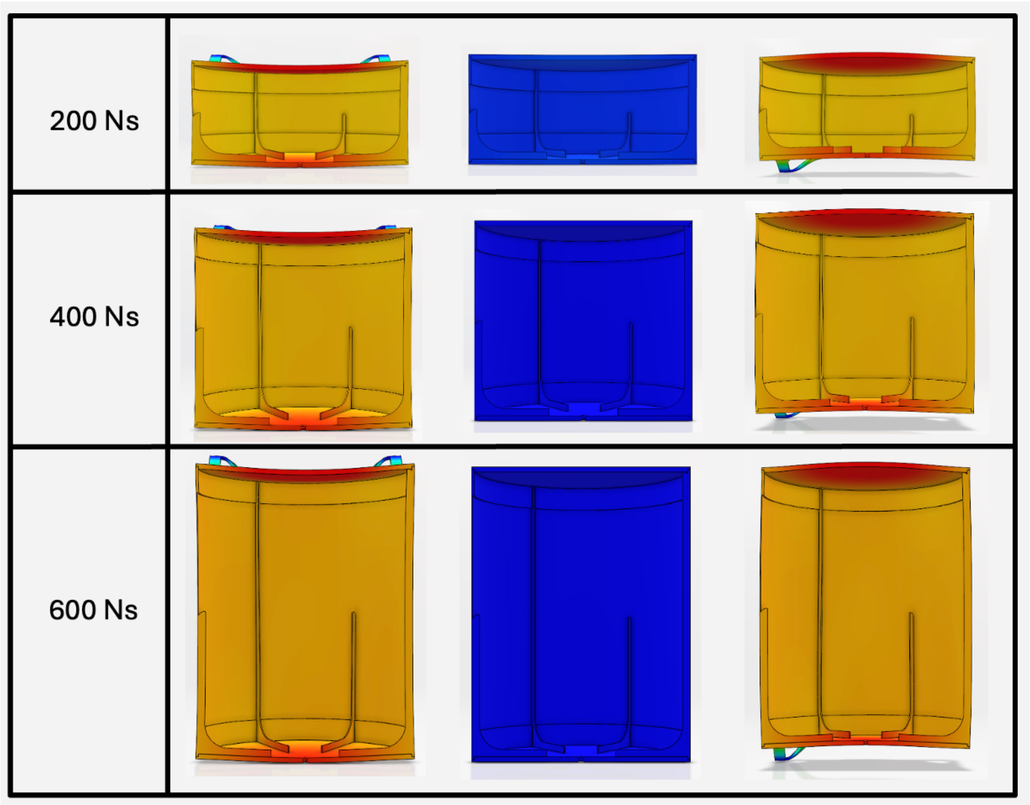

Figure 10.15: Visualization of the first vibration mode of each system.

Table 10.6: First three vibration modes (in Hz) for each propulsion system.

System	**200 Ns**	**400 Ns**	**600 Ns**
Mode 1	613.6	587.5	564.4
Mode 2	1954.0	1916.8	1690.6
Mode 3	2756.3	2615.1	1691.2

It is observed that all base frequencies are well above 35 Hz, suggesting that there is no resonance between the tank and the launcher. Additionally, all fundamental vibration modes oscillate within the same plane (in the +-Z-direction). This is expected, as the analytical design of the mechanical interface showed a large discrepancy between the axial and lateral natural frequencies, of which the axial natural frequency (in the +- Z-direction) was the lowest. However, there is a large discrepancy between these results and the estimated natural frequencies that were calculated in Section 8.6, where the latter resulted in significantly lower axial natural frequencies. This increase in natural frequency hints towards an increased stiffness of the system and can partly be attributed to the mechanical interfaces that attach the tank to the propulsion system at multiple points. The preliminary calculations did not take these multiple attachment points into account and modelled each interface as a cantilever beam. This significantly reduces the natural frequency of each interface, as the stiffness is underestimated. Furthermore, the inclusion of 2 mm edge fillet on each corner of the mechanical interfaces in the reinforced design increases the moment of inertia, thereby enhancing stiffness and resulting in a higher natural frequency. Finally, the integration of stiffening elements within the tank structure, such as vanes and localized reinforcements, further enhances the overall stiffness of the structure, resulting in an increased natural frequency.

10.9 Conclusions

This chapter outlined the finite element analysis that was performed on all three propellant tanks. This analysis was required, as the preliminary tank shell design was solely based on analytical relationships from the ASME Boiler and Pressure Vessel Code that did not include the effects of the PMD and mechanical interface between the tank and the rest of the propulsion system.

Several analyses were performed on the three tank designs, namely an internal pressure analysis, a launch load analysis, a buckling analysis, and a natural frequency analysis. The propellant tank design required several modifications to achieve stress levels below the design stress off 678.6 MPa at the maximum expected internal pressure of 10 bar due to unforeseen bending of the skin and stress concentrations at the vane corners and tank outlet. The following reinforcements were applied to the three tank designs:

1. A 0.8 mm thick and 10 mm tall reinforcement ring at the top and bottom of the cylindrical tank shell. This increases the local skin thickness to 1.1 mm.
2. A 10 mm edge fillet at the 90-degree bend in the vanes.
3. A 2 mm edge fillet on all three corners of the mechanical interface.
4. A 0.5 mm edge fillet on both sides of the tank outlet.
5. A 0.3 x 3 mm edge fillet on the end of each vane (at the side that is attached to the cylindrical tank wall).

This updated design yielded stresses below the design stress with some small local stress concentrations above the design stress and below the yield stress. Moreover, the top and bottom endcap displacements were reduced to a maximum deflection of 1.36 mm for the top endcap and 0.899 mm for the bottom endcap. These deflections were found for an internal pressure of 10 bar and axial acceleration of 8.5g (the maximum acceleration as described by requirement *PROP-TANK-17*). A 1.4 mm gap is required between the top endcap and the rest of the propulsion system, whereas a 0.9 mm gap is required between the bottom endcap and piping components to avoid damage of both the tank design and rest of the propulsion system.

Furthermore, the critical buckling load of all three reinforced propellant tanks were above 1 atm (or 101325 Pa) and allow for vacuum filling of the tank. Buckling of the tank during its operation lifetime was not considered, as the end-of-life pressure is approximately 2.19 bar. Finally, all fundamental frequencies of the empty reinforced propellant tanks were well above the minimum required frequency (as described by requirement *PROP-TANK-19* to avoid resonance with the launcher) of 35 Hz.

10.10 Recommendations

Several recommendations are proposed for further research. First, it is recommended to adopt an industry-standard FEA software such as Abaqus. While the 3DExperience software was convenient due to its seamless CAD model integration, mastering Abaqus would provide more advanced analysis capabilities.

A second recommendation is to perform the analyses on the complete tank assembly by modelling all components, including the sponge, vane, top endcap, bottom endcap, and cylindrical shell as separate elements to enhance the accuracy of the analyses.

Third, integrating the liquid propellant into the tank model is essential to enhance the accuracy of the launch load analysis and natural frequency analysis.

Fourth, a mesh convergence study should be performed for each type of analysis, and for all tank sizes. A uniform mesh size of 1 mm was used throughout this chapter, as it showed convergence for the internal pressure analysis. Conducting a mesh convergence study for each type of analysis would validate the accuracy of the results.

Fifth, a vibrational analysis of the fully assembled propulsion systems, including propellant, should be carried out in addition to the tank designs. This was not included in the current work due to time constraints but is critical for understand the dynamic behaviour of the propulsion systems.

Finally, a finite element analysis of the fully assembled propulsion systems is required to confirm its structural rigidity. This step, though outside the scope of this thesis, would provide a clearer overview of the system's performance under operational conditions.

Thermal Analysis

11

This chapter outlines the thermal analysis that is performed on the design of the three propulsion systems. The goal of the analysis is to calculate not only the temperatures within the system, but to also analyse the need for special coatings, propellant heaters and a possible limitation on the burn duration of the thruster. First, the propulsion system is reduced to a simplified thermal network in Section 11.1, where all the incoming and outgoing heat sources are outlined, combined with the methodology to solve for each node temperature. Second, the orbital cases considered are discussed in Section 11.2, followed by the calculation of the view and Gebhart factors in Section 11.3. Next, the thermal analysis is performed on the two extreme orbital cases, being the cold and hot case, in Section 11.4. Finally, all findings are summarized in Section 11.5, whereas several recommendations are outlined in Section 11.6.

11.1 Thermal Network Representation

Figure 11.1 shows the simplified thermal network that represents the three propulsion systems. Four assumptions are made to create this network: first, it is assumed that the propulsion system consists only of a thruster (node 1), a circular, flat piping tray (node 2) with the same radius as the tank bottom endcap (node 3), propellant (node 4), and the remainder of the tank shell (node 5). The TunaCan add-on is excluded from this analysis for temporal reasons: it was designed after the thermal analysis. All other components are excluded from the model to simplify the analysis.

Second, it is assumed that there is no conduction between the nodes. This assumption is only valid when there are thermal insulators between the adjacent node interfaces. The exclusion of conduction will result in larger temperature differences between the different nodes, whereas in reality the temperatures will be distributed more evenly across the different components. The more extreme nodal temperatures that result from this assumption makes the analysis conservative.

Third, it is assumed that the propellant is not touching the tank walls and can only gain and lose thermal energy through radiation. The propellant is represented as a solid cylinder that is equidistant from the cylindrical tank wall and flat endcaps. This assumption allows for neglecting convection. In reality, propellant is clinging to the tank walls and endcaps as a result of the vanes and sponge guiding propellant towards the tank outlet, allowing for heat exchange through convection and conduction. Excluding these forms of heat exchange will result in larger temperature differentials which makes the analysis more conservative.

Finally, it is assumed that the remainder of cylindrical part of the propellant tank (node 5) is located within the spacecraft, with a temperature matching the spacecraft's interior temperature (T_{sc}), which ranges from 5 to 25 °C. This simplification is made, as it is difficult to model the CubeSat bus structure in which the propulsion system is integrated. Moreover, the bottom endcap and piping tray are located within the spacecraft, whereas the thruster and outside of the piping tray interact the space environment.

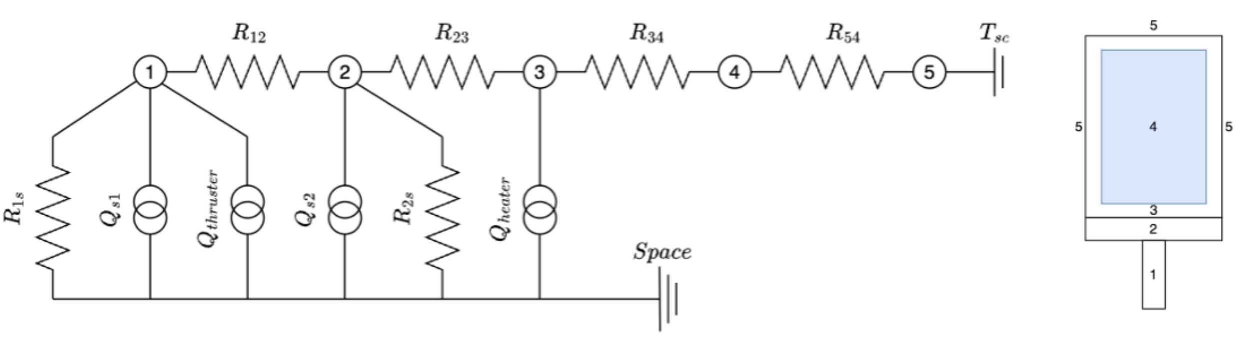

Figure 11.1: Thermal network representation of the three propulsion systems.

11.1.1 Thermal Network Elements

Neglecting both convection and conduction results in a thermal network that consists only of radiative links between the nodes, as shown in Figure 11.1. These radiative links are defined as:

$$R_{ij} = \epsilon_i A_i B_{ij} \tag{11.1}$$

where R_{ij} is the radiative link between node i and node j, ϵ_i is the emissivity of node i, A_i is the area of node i, and B_{ij} is the Gebhart factor from node i to node j. Furthermore, node 1, 2, and 3 have input powers from the environment (Q_{s1} and Q_{s2}), thruster ($Q_{thruster}$), and heater (Q_{heater}). The environmental thermal loads into node i consist of a direct solar load (Q_{sun-i}), a planetary infrared load (Q_{IR-i}), and an albedo load ($Q_{albedo-i}$). These loads are defined as [127]:

$$Q_{sun-i} = \alpha_i A_i S_c \tag{11.2}$$

$$Q_{IR-i} = \epsilon_i A_i \sigma T_{earth}^4 \left(\frac{R_e}{R_e + h_{orbit}}\right)^2 \tag{11.3}$$

$$Q_{albedo-i} = a\alpha_i A_i S_c \left(\frac{R_e}{R_e + h_{orbit}}\right)^2 \tag{11.4}$$

where α_i is the absorptivity of node i, ϵ_i is the emissivity of node i, A_i is the projected area of node i that receives the thermal load, S_c is the solar flux constant (equal to 1361 W/m^2), σ is the Stefan-Boltzmann constant, T_{earth} is the Earth's effective temperature (the surface temperature adjusted to account for the greenhouse effect), R_e is the radius Earth, h_{orbit} is the orbital altitude, and a is the albedo coefficient (equal to 0.3 for Earth).

The tank heater is attached to the bottom endcap (node 3) in this thermal analysis. The reason for placing the heater here, and not to the cylindrical tank wall, is due to the boundary temperature assumption that is placed on the cylindrical tank wall. Attaching the heater to the cylindrical shell will not increase the heat that is radiating from the wall towards the propellant due to this boundary temperature assumption.

11.1.2 Thermal Network Reductions

The thermal network is to be reduced to a single node to calculate the temperature of that specific node. Four network reductions are therefore required to solve for the thruster temperature (node 1), piping tray (node 2), tank bottom endcap (node 3), and the propellant temperature (node 4). No network reduction for node 5 is required, as this node is always equal to the spacecraft temperature. The network is reduced using the method that was taught in the "Spacecraft Thermal Design" course [128].

Reducing to node 1: thruster temperature

First, node 5 is converted to a power source (Q_{54}) and a radiative coupling (R_{54}) for all four nodal reductions:

$$Q_{54} = R_{54} \sigma T_{sc}^4 \tag{11.5}$$

Next, node 4 is removed:

$$Q_3 = Q_{heater} + \frac{R_{34} Q_{54}}{R_{34} + R_{54}} \tag{11.6}$$

$$R_3 = \frac{1}{\frac{1}{R_{34}} + \frac{1}{R_{54}}} \tag{11.7}$$

Removing node 3:

$$Q_2 = Q_{s2} + \frac{R_{23} Q_3}{R_{23} + R_3} \tag{11.8}$$

$$R_2 = R_{2s} + \frac{1}{\frac{1}{R_{23}} + \frac{1}{R_3}} \tag{11.9}$$

Finally, removing node 2 yield the total power that flows into node 1 and the total heat that radiates from node 1:

$$Q_1 = Q_{s1} + Q_{thruster} + \frac{R_{12} Q_2}{R_{12} + R_2} \tag{11.10}$$

$$R_1 = R_{1s} + \frac{1}{\frac{1}{R_{12}} + \frac{1}{R_2}} \tag{11.11}$$

Reducing to node 2: piping tray temperature

First, node 4 is removed:

$$Q_3 = Q_{heater} + \frac{R_{34}Q_{54}}{R_{34}+R_{54}} \tag{11.12}$$

$$R_3 = \frac{1}{\frac{1}{R_{34}}+\frac{1}{R_{54}}} \tag{11.13}$$

Second, node 1 and 3 are removed to obtain the total power that flows into node 2 and the total heat that radiates from node 2:

$$Q_2 = Q_{s2} + \frac{R_{23}Q_3}{R_{23}+R_3} + \frac{R_{12}\left(Q_{s1}+Q_{thruster}\right)}{R_{12}+R_{1s}} \tag{11.14}$$

$$R_2 = R_{2s} + \frac{1}{\frac{1}{R_{23}}+\frac{1}{R_3}} + \frac{1}{\frac{1}{R_{12}}+\frac{1}{R_{1s}}} \tag{11.15}$$

Reducing to node 3: bottom endcap temperature
First, node 1 is removed:

$$Q_2 = Q_{2s} + \frac{R_{12}\left(Q_{s1}+Q_{thruster}\right)}{R_{12}+R_{1s}} \tag{11.16}$$

$$R_2 = R_{2s} + \frac{1}{\frac{1}{R_{12}}+\frac{1}{R_{1s}}} \tag{11.17}$$

Second, node 2 and 4 are removed to obtain the total power that flows into node 3 and the total heat that radiates from node 3:

$$Q_3 = Q_{heater} + \frac{R_{23}Q_2}{R_{23}+R_2} + \frac{R_{34}Q_{54}}{R_{34}+R_{54}} \tag{11.18}$$

$$R_3 = \frac{1}{\frac{1}{R_{23}}+\frac{1}{R_2}} + \frac{1}{\frac{1}{R_{34}}+\frac{1}{R_{54}}} \tag{11.19}$$

Reducing to node 4: propellant temperature

First, node 1 is removed:

$$Q_2 = Q_{2s} + \frac{R_{12}\left(Q_{s1}+Q_{thruster}\right)}{R_{12}+R_{1s}} \tag{11.20}$$

$$R_2 = R_{2s} + \frac{1}{\frac{1}{R_{12}}+\frac{1}{R_{1s}}} \tag{11.21}$$

Next, node 2 is removed:

$$Q_3 = Q_{heater} + \frac{R_{23}Q_2}{R_{23}+R_2} \tag{11.22}$$

$$R_3 = \frac{1}{\frac{1}{R_2}+\frac{1}{R_{23}}} \tag{11.23}$$

Finally, node 3 is removed:

$$Q_4 = Q_{54} + \frac{R_{34}Q_3}{R_{34}+R_3} \tag{11.24}$$

$$R_4 = R_{54} + \frac{1}{\frac{1}{R_{34}}+\frac{1}{R_3}} \tag{11.25}$$

11.1.3 First-order Approximation Method

The temperature of the nodes can now be calculated throughout the orbit using the first-order approximation method [128]:

$$T_{i_{t+\Delta t}} = T_{i_t} + \frac{Q_i - R_i\sigma T_{i_t}^4}{m_i c_{p_i}}\Delta t \tag{11.26}$$

where T_i is the temperature of node i, Q_i is the power that goes into node i, R_i is the radiative link between node i and space, m_i is the mass of node i, c_{p_i} is the specific heat capacity of node i, and Δt is the time step.

11.2 Thermal Environments

Two orbits are considered in this analysis: an orbit where the propulsion system gets no direct solar load throughout the orbit, and an orbit where the propulsion system gets the maximum direct solar load. These two orbital cases are visualized in Figure 11.2, and analysed for the three systems at an orbital altitude of 300 km and 1000 km. The lower bound orbital altitude is a result from the system requirement analysis that was performed in Subsection 4.2.7, where it was concluded that it is unfeasible to meaningfully use the propulsion system to maintain orbits below this altitude.

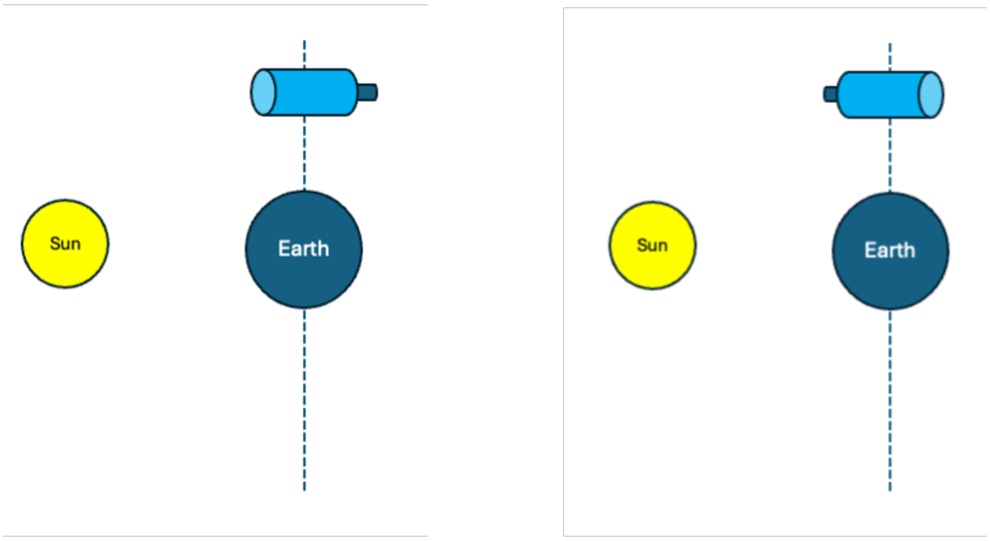

(a) Case 1

(b) Case 2

Figure 11.2: Visualisation of the two orbits considered in the thermal analysis.

The reason for choosing these two orbits is that they reflect the worst-case scenarios in terms of incoming thermal loads. The first case, where the propulsion system does not acquire any direct solar load throughout the entire orbit, will result in the coldest possible system. The second case, where the propulsion system does obtain the direct solar load throughout the entire orbit, will result in the hottest system possible. The propulsion system will obtain an infrared and albedo load in both cases.

11.2.1 Projected Areas and Thermal Loads

As was shown in Section 11.1, the area of the nodes that receive the thermal loads must be calculated for each orbit. The equations used for determining these areas are summarized in Table 11.1 and are independent on the orbital altitude. Table 11.2 summarizes the thermal loads (using Equation 11.2 - Equation 11.4) where it is shown that the thermal loads do depend on the orbital altitude. Furthermore, these incoming thermal loads are independent on the system size (200 Ns, 400 Ns, and 600 Ns system), as the piping tray and thruster are identical across all three platforms.

Table 11.1: Projected area equations that see the incoming thermal load.

Cold Case		
Area	Thruster	Tray
Sun	0	0
Earth	$\pi r_{thruster} h_{thruster} + \pi r^2_{thruster}$	$l^2_{tray} - 2 r_{thruster} h_{thruster}$
Hot Case		
Area	Thruster	Tray
Sun	$\pi r^2_{thruster}$	$l^2_{tray} - \pi r^2_{thruster}$
Earth	$\pi r_{thruster} h_{thruster} + \pi r^2_{thruster}$	$l^2_{tray} - 2 r_{thruster} h_{thruster}$

Table 11.2: Incoming thermal load for both orbit cases.

Orbital case	**Case 1**		**Case 2**	
Orbital altitude	300 km	1000 km	300 km	1000 km
Direct solar radiation [W]	0.00	0.00	5.41	5.41
Infrared radiation [W]	0.265	0.217	0.265	0.217
Albedo [W]	1.67	1.37	1.67	1.37
Total incident power [W]	1.93	1.58	7.35	7.00

The two extreme thermal scenarios can be identified by examining Table 11.2, where the coldest case occurs when the incident power is at its lowest (case 1 at 1000 km altitude), and the hottest case when the incident power is at its highest (case 2 at 300 km altitude). Furthermore, the coldest case in terms of the temperature of each node will be at the lowest spacecraft temperature (of 5 °C) whereas the hottest case will be at the highest spacecraft temperature (of 25 °C). The effect of the system size on the nodal temperature is yet unknown, and requires performing the thermal analysis. The true worst cases (coldest and hottest case) in terms of node temperature will be determined in this analysis, and are to be used for determining the extreme node temperatures, and the possible need for a heater and surface coating on the outside of the piping tray.

11.3 Propulsion System View Factors and Gebhart Factors

Equation 11.1 contains the Gebhart factor B_{ij}. This factor represents the fraction of radiation emitted by area i which is absorbed by area j, and includes reflections between the two surfaces. A Gebhart factor is a function of view factors, emissivities, and other Gebhart factors [128]:

$$B_{ij} = F_{ij}\epsilon_j + \sum_{n=1}^{k}(1-\epsilon_k)F_{ik}B_{kj} \tag{11.27}$$

where n indicate the number of surfaces that are part of an enclosure. Furthermore, the sum of Gebhart factors from a surface must be equal to one [128]:

$$\sum B_{ij} = 1 \tag{11.28}$$

and there is a reciprocal relationship between the factors B_{ij} and B_{ji} [128]:

$$\epsilon_i A_i B_{ij} = \epsilon_j A_j B_{ji} \tag{11.29}$$

As previously mentioned, view factors are required to calculate Gebhart factors. A view factor represents the same principle as a Gebhart factor with the only difference being that there are no reflections between the considered surfaces. In other words: the surfaces act as perfect black bodies. Like Gebhart factors, the sum of view factors from a surface must be equal to one [129]:

$$\sum F_{ij} = 1 \tag{11.30}$$

whereas the following reciprocal relationship between the factors F_{ij} and F_{ji} holds [129]:

$$A_i F_{ij} = A_j F_{ji} \tag{11.31}$$

It is important to note that the view and Gebhart factors for the propulsion system are, unlike the projected areas for the environmental thermal loads, independent on the type of orbit.

11.3.1 View Factors

The propulsion system can be split in three parts: the thruster, tray and space, the tray and tank bottom endcap, and the tank bottom endcap, propellant and remained of the tank shell. Splitting the system into these three parts simplifies the calculations, as the view and Gebhart factors for the thruster, tray and space, and the tray and tank bottom endcap are independent of the propulsion system size. Only the view and Gebhart factors of the tank bottom endcap, propellant and remainder of the tank shell part change for each system size (200 Ns, 400 Ns, and 600 Ns system).

Thruster-tray-space system

The first few view factors of the thruster-tray-space system can be determined without any calculations. First, the thruster (node 1) and tray (node 2) and cannot see themselves, hence their view factors are equal to zero. Second, the view factors F_{s1} and F_{s2} are equal to 0 as space (s) is infinitely large compared to the thruster and tray, resulting in F_{ss} = 1 (as a result of Equation 11.30).

Calculating the view factors F_{12} and F_{21} is more difficult, and require the use of an existing expression [130]:

$$F_{12} = \frac{B_c}{8R_cH_c} + \frac{1}{2\pi}\left\{\cos^{-1}\left(\frac{A_c}{B_c}\right) - \frac{1}{2H_c}\left[\frac{(A_c+2)^2}{R_c^2} - 4\right]^{-\frac{1}{2}} \times \cos^{-1}\left(\frac{A_cR_c}{B_c}\right) - \frac{A_c}{2R_cH_c}\sin^{-1}R_c\right\} \tag{11.32}$$

where

$$R_c = \frac{r_1}{r_2}; \qquad H_c = \frac{h_{thruster}}{r_2}; \qquad A_c = H_c^2 + R_c^2 - 1; \qquad B_c = H_c^2 - R_c^2 + 1$$

where r_1 is the radius of the thruster (equal to 5 mm), r_2 is the radius of the piping tray (equal to 46 mm), and $h_{thruster}$ is the length of the thruster that is sticking out of the tray (equal to 20 mm). The resulting view factors are summarized in Table 11.3.

Table 11.3: View factors of the thruster-tray-space system.

F	**1**	**2**	**s**	$\sum$
1	0	0.358	0.642	1
2	0.034	0	0.966	1
s	0	0	1	1

Tray-tank bottom endcap system

The view factors of the tray-tank bottom end cap can be determined without any calculations, as the tray and endcap cannot see themselves, whereas the tray sees the complete endcap and the endcap sees the full tray. Table 11.4 outlines these four view factors.

Table 11.4: View factors of the tray-bottom endcap system.

F	**2**	**3**	$\sum$
2	0	1	1
3	1	0	1

Tank bottom endcap-propellant-tank shell system

The view factors of this system do change for each system size. First, the propellant surface and bottom end-cap cannot see themselves: F_{33} = 0 and F_{44} = 0. Second, the bottom endcap sees both the propellant and remainder of the tank shell, the propellant sees both the bottom endcap and the remainder of the tank shell, and the tank shell sees the bottom endcap and the propellant.

The view factor F_{34} is calculated using:

$$F_{34} = \frac{\pi r_p^2 + 2\pi r_p h_p}{A_4} \tag{11.33}$$

where r_p and h_p are the radius and height of cylindrical propellant surface, and A_4 is the propellant surface area. This relationship is valid as the bottom end cap sees the circular bottom and the side of the cylindrical propellant surface. These propellant dimensions are calculating using the previously stated assumption that the propellant is floating equidistant from the cylindrical shell and endcaps, and the fill ratio of the tank itself. First, the distance between the propellant and tank walls (d_p) is calculated using:

$$V_{prop} = F_i V_{tank} = \pi r_p^2 h_p = \pi (r_{tank} - d_p)^2 (h_{tank} - 2d_p) \tag{11.34}$$

where V_p is the propellant volume, V_{tank} is the tank volume, F_i is the fill ratio (equal to 75 %), r_{tank} is the radius of the tank, and h_{tank} is the height of the tank. The radius and height of the propellant are then calculated using:

$$r_p = r_{tank} - d_p \tag{11.35}$$

$$h_p = h_{tank} - 2d_p \tag{11.36}$$

The view factor F_{35} is calculated by realising that the sum of all view factors originating from node 3 must be equal to one. Furthermore, the view factors F_{43} and F_{53} can be calculated using the reciprocal relationship (Equation 11.31). F_{45} is then calculated using the summation relationship for all view factors that originate from node 4 and allows for calculation F_{54} using the reciprocal relationship. Finally, F_{55} is determined using the summation relationship for node 5. The outcome of these calculations are summarized for all three systems in Table 11.5.

Table 11.5: View factors of the bottom endcap-propellant-tank shell system.

200 Ns system				
F	**3**	**4**	**5**	$\sum$
3	0	0.731	0.269	1
4	0.238	0	0.762	1
5	0.092	0.800	0.108	1
400 Ns system				
F	**3**	**4**	**5**	$\sum$
3	0	0.822	0.178	1
4	0.183	0	0.817	1
5	0.038	0.784	0.178	1
600 Ns system				
F	**3**	**4**	**5**	$\sum$
3	0	0.868	0.132	1
4	0.146	0	0.854	1
5	0.021	0.791	0.188	1

11.3.2 Gebhart Factors

Calculating all Gebhart factors using Equation 11.27 is a tedious process and not required due to the summation and reciprocity relationships. Moreover, only the Gebhart factors that are represented in Figure 11.1 are required and include: B_{12}, B_{21}, B_{1s}, B_{2s}, B_{23}, B_{32}, B_{34}, B_{43}, B_{45}, and B_{54}.

An example of how to calculate the Gebhart factors for a system consisting of two nodes (node i and node j) is shown below. This method is then applied to the three separate systems (thruster-tray-space, tray-endcap, endcap-propellant-wall). The Gebhart factors are calculated for the i-j system, assuming that the view factors F_{ii}, F_{ij}, F_{ji}, and F_{jj} are known.

First, B_{ii} is written out in full:

$$B_{ii} = \frac{F_{ii}\epsilon_i + (1-\epsilon_j)F_{ij}B_{ji}}{1-(1-\epsilon_i)F_{ii}} \tag{11.37}$$

This Gebhart factor is a function of B_{ji}:

$$B_{ji} = \frac{F_{ji}\epsilon_i + (1-\epsilon_i)F_{ji}B_{ii}}{1-1-\epsilon_j)F_{jj}} \tag{11.38}$$

which in turn is a function of B_{ii} again. The relationship between these two factors can be written as a matrix equation:

$$[A] \cdot \bar{B} = [C] \tag{11.39}$$

$$\begin{bmatrix} 1 & \frac{(\epsilon_j - 1)F_{ij}}{1-(1-\epsilon_i)F_{ii}} \\ \frac{(\epsilon_i - 1)F_{ji}}{1-(1-\epsilon_j)F_{jj}} & 1 \end{bmatrix} \cdot \begin{bmatrix} B_{ii} \\ B_{ji} \end{bmatrix} = \begin{bmatrix} \frac{F_{ii}\epsilon_i}{1-(1-\epsilon_i)F_{ii}} \\ \frac{F_{ji}\epsilon_i}{1-(1-\epsilon_j)F_{jj}} \end{bmatrix} \tag{11.40}$$

and solved, given that the A-matrix is invertible. The Gebhart factor B_{ij} is calculated using the reciprocity relationship and B_{jj} is calculated using the summation relationship that states that the sum of Gebhart factors from a surface is equal to 1. The Gebhart factors for the thruster-tray-space, tray-endcap, and endcap-propellant-wall systems are summarized in Table 11.6, Table 11.7, and Table 11.8 respectively.

Table 11.6: Gebhart factors of the thruster-tray-space system.

B	**1**	**2**	**s**	$\sum$
1	0.001	0.051	0.948	1
2	0.005	0.001	0.994	1

Table 11.7: Gebhart factors of the tray-bottom endcap system.

B	**2**	**3**	$\sum$
2	0.246	0.754	1
3	0.352	0.648	1

Table 11.8: Gebhart factors of the bottom endcap-propellant-tank shell system.

200 Ns system				
B	**3**	**4**	**5**	$\sum$
3	0.009	0.893	0.098	1
4	0.091	0.637	0.272	1
5	0.034	0.915	0.051	1
400 Ns system				
B	**3**	**4**	**5**	$\sum$
3	0.004	0.924	0.072	1
4	0.064	0.639	0.296	1
5	0.015	0.911	0.074	1
600 Ns system				
B	**3**	**4**	**5**	$\sum$
3	0.003	0.940	0.057	1
4	0.049	0.642	0.308	1
5	0.009	0.914	0.077	1

11.4 Thermal Analysis

The thermal analysis can be performed for the four nodes now that the thermal load, Gebhart factors, and radiative links between the components are determined. Table 11.9 outlines the input that are used in the analysis, where it is assumed that the mass of the piping tray (node 2) is equal to the total mass of the piping (calculated in Chapter 9).

Table 11.9: Inputs used for the thermal analysis.

Absorptivities and Emissivities [131][132][133]	
$\alpha_{titanium}$ [-]	0.5
$\epsilon_{titanium}$ [-]	0.3
$\alpha_{316L_{stainless}}$ [-]	0.47
$\epsilon_{316L_{stainles}}$ [-]	0.14
ϵ_{water} [-]	0.96
Thermal Environment [127][128]	
T_{earth} [K]	255
T_{sc} [K]	273-298
Albedo coefficient [-]	0.33
Solar constant [W/m^2]	1361
Specific Heat Capacities [65][134][135]	
Titanium [J/kg·K]	526.3
316L Stainless steel [J/kg·K]	500
Water [J/kg·K]	4187
Node Masses	
Thruster [kg]	0.04
Piping tray [kg]	0.283
Tank bottom [kg]	0.062

11.4.1 Extreme Thermal Case Search

As previously described, the cold case occurs when the thruster is not facing the Sun at an orbital altitude of 1000 km, with a bus temperature of 5 °C. The hot case occurs when the thruster is facing the Sun throughout the orbit at an orbital altitude of 300 km and a bus temperature of 25 °C. The only remaining unknown is the effect of the system size on the temperature of the nodes.

Figure 11.3 shows the cold case for the smallest (200 Ns) and largest (600 Ns) system. The minimum and maximum propellant temperature are equal to respectively 10 °C and 50 °C as per requirement *PROP-TANK-05*, whereas the minimum and maximum tray temperature is set to 0 °C and 100 °C to prevent freezing and boiling of the propellant in the piping. Furthermore, the "Propellant average" is set to the average temperature of the propellant itself and the tank bottom:

$$T_{avg_{3-4}} = \frac{1}{2}\left(T_3 + T_4\right) \tag{11.41}$$

where T_3 is the temperature of the tank bottom endcap and T_4 is the temperature of the propellant. This average temperature is more realistic than the separate temperatures, as they are both in contact during the mission. However, all temperatures, including the propellant and tank bottom temperature, must be within their respective bounds.

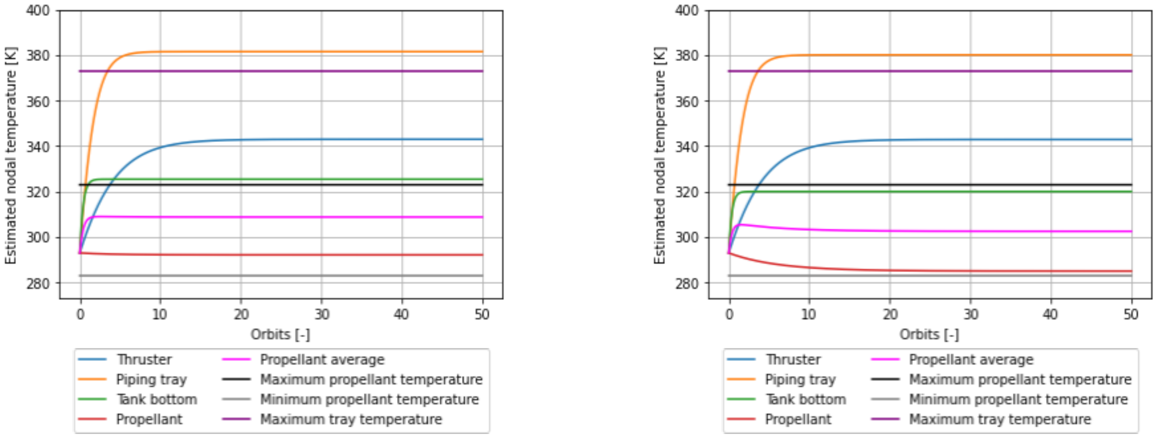

(a) Smallest (200 Ns) propulsion system.

(b) Largest (600 Ns) propulsion system.

Figure 11.3: Estimated node temperatures for the extreme cold case.

It can be seen that the largest (600 Ns) propulsion system yields the lowest node temperatures and is therefore chosen as the cold case in this thermal analysis. Figure 11.4 shows the estimate node temperature for both the smallest and largest systems for the hot case, where it is clear that the smallest system has the highest node temperatures.

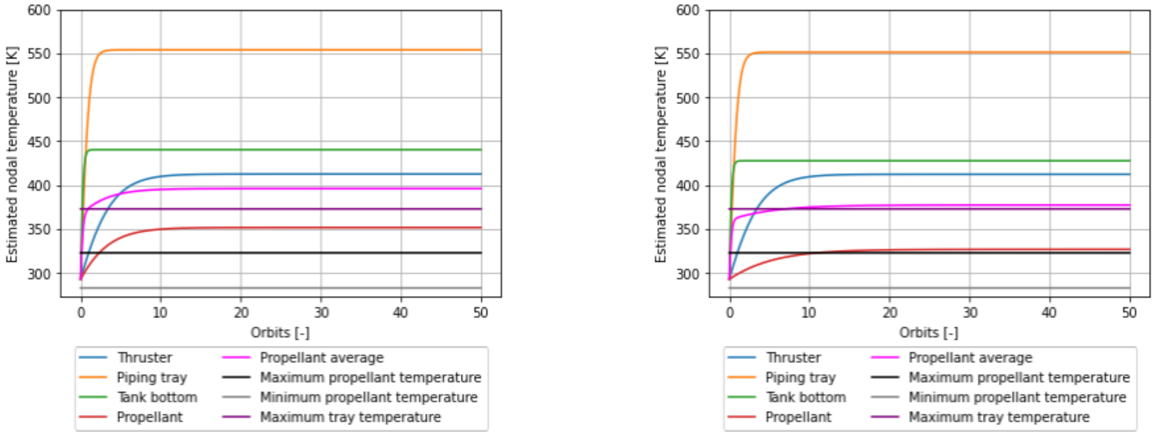

(a) Smallest (200 Ns) propulsion system.

(b) Largest (600 Ns) propulsion system.

Figure 11.4: Estimated node temperatures for the extreme hot case.

The steady-state node temperatures, including the previously stated limit temperatures, for both the extreme cold and hot case are summarized in Table 11.10. It is evident that the temperature of the piping tray exceeds the maximum allowable temperature for the cold case, whereas the piping tray, tank bottom end-cap, and propellant average temperatures are above their respective limit for the extreme hot case. Furthermore, it must be noted that the maximum allowable temperature of the thruster (equal to 650 °C: the temperature below which the thermal stability of 316L stainless steel is proven [136]) is excluded from the graphs to provide a more detailed visual of the node temperature distributions.

Table 11.10: Steady-state node temperatures (in K).

Case	**Cold**	**Hot**	**Lower Limit**	**Upper Limit**
Thruster	343	413	273	923
Piping tray	380	554	273	373
Tank bottom endcap	320	440	283	323
Propellant	285	352	283	323
Propellant average	303	396	283	323

11.4.2 Application of a Thermal Coating

As was stated above, temperature limits are exceeded for both the extreme cold and hot case. A white coating is to be applied to the outside of the piping tray to lower the node temperatures to below their respective maximum values. The coating specifications are outlined in Table 11.11, whereas the steady state temperatures, including the upper and lower bounds, are summarized in Table 11.12.

Table 11.11: Thermal coating specifications [132].

Name	Zerlauts Z-93 White Paint
Absorptivity	0.17
Emissivity	0.92

Table 11.12: Steady-state node temperatures (in K) when a coating is applied to the outside of the piping tray.

Case	**Cold**	**Hot**	**Lower Limit**	**Upper Limit**
Thruster	350	413	273	923
Piping tray	272	331	273	373
Tank bottom endcap	276	311	283	323
Propellant	278	301	283	323
Propellant average	277	306	283	323

The node temperatures for the hot case are all within the stated temperature limits, whereas all temperatures, except the thruster temperature, are below the minimum required temperature for the cold case. One method of increasing these temperatures for the cold case is to add a heater to the bottom endcap of the propellant tank. The updated steady-state node temperature when adding a 0.5 W and 1 W heater to the bottom endcap are summarized in Table 11.13.

Table 11.13: Steady-state node temperatures (in K) when a heater is attached to the bottom endcap of the propellant tank.

Heating Power	**0.5 W**	**1.0 W**
Thruster	350	351
Piping tray	277	281
Tank bottom endcap	314	342
Propellant	284	290
Propellant average	299	316

It is concluded that attaching a 0.5 W heater to the tank bottom endcap is sufficient to raise the node temperatures above the minimum, and below the maximum required values.

11.4.3 Determining the Maximum Burn Duration

The maximum burn duration of the thruster is constrained by either the nodal temperatures or the stability and controllability of the thruster in terms of mass flow rate, chamber pressure, and input power [20]. An input power of 4.7 W is applied to the thruster during a manoeuvre, derived from the required heating power of 2.33 W to produce 1 mN of thrust (from Table 9.19) and assuming a thruster efficiency of 50%). Half of the input power (2.33 W) is then lost through thermal losses and radiates to the piping tray and space during a burn manoeuvre. The effect of this heat dissipation on the nodal temperatures is visualized for the extreme hot case in Figure 11.5. It is clear that none of the node temperatures is limiting the burn duration, as all steady state temperatures stay within their respective bounds. This observation suggests that the maximum burn duration for the extreme cold case is also not limited by the node temperatures.

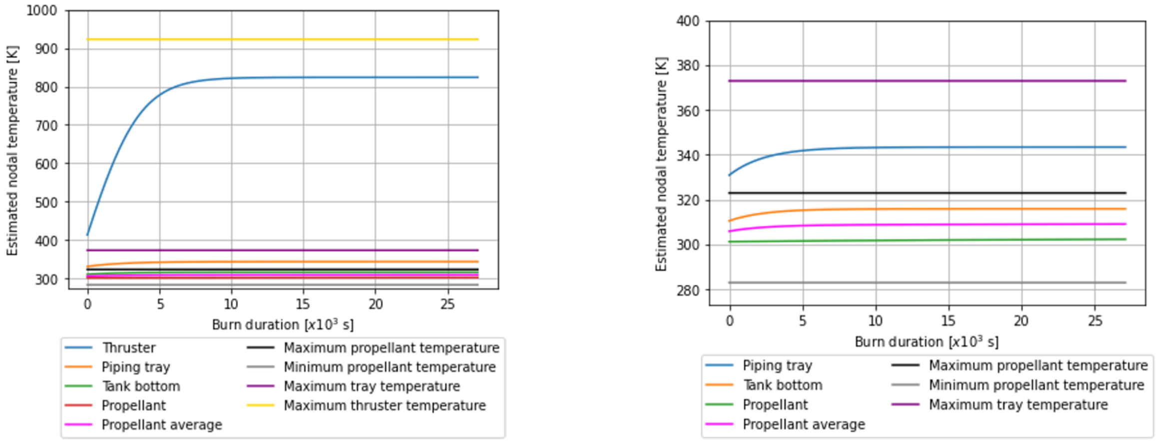

(a) Normal view (including thruster).

(b) Detailed view (excluding thruster).

Figure 11.5: Node temperatures when the thruster is activated for the hot case.

However, the maximum allowable burn duration is set at 3000 seconds, based on tests conducted on the VLM thruster that was outlined in Chapter 4. These tests demonstrated the thruster's stability and controllability in terms of chamber pressure, mass flow rate, and input power within this time frame [20]. Testing of the redesigned thruster is required to verify this burn duration. Figure 11.6 shows the node temperatures for the two extreme cases when a 3000-second manoeuvre is performed whereafter all nodal temperatures return to their steady state values. It must be noted that the heater is turned off during the manoeuvre for the extreme cold case.

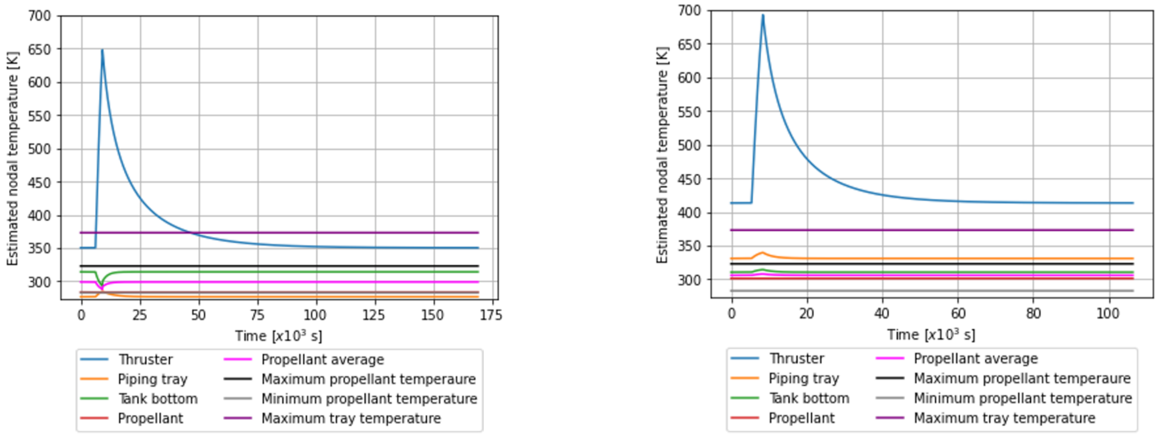

(a) Cold case.

(b) Hot case.

Figure 11.6: Node temperatures during a burn manoeuvre of 3000 seconds.

The first observation is that, for the cold case, the temperatures of the tank's bottom endcap and the propellant decrease during the manoeuvre. This occurs because the heater is turned off during the burn. A second observation is the difference in cooling periods between the two orbital cases: the cold case requires a 44-hour cooling period, while the hot case requires 27 hours to return to the steady-state temperatures. However, it must be noted that the nodal temperatures already approach their steady-state values at half these durations. The discrepancy between the cooling periods of the extreme hot and cold case is due to the tank heater that is activated during the cooling period of the extreme cold case. This is done to prevent the propellant temperature from dropping below the minimum required value of 283 K. The nodal temperatures at steady-state, and after a 3000-second manoeuvre, are summarized in Table 11.14.

Table 11.14: Node temperatures (in K) for steady-state and burn manoeuvres.

Case	**Cold case**		**Hot case**	
Instance	Steady State	Manoeuvre	Steady State	Manoeuvre
Thruster	350	648	413	693
Piping tray	277	285	331	340
Tank bottom endcap	314	300	311	314
Propellant	284	284	301	302
Propellant average	299	292	306	308

11.5 Conclusions

This chapter outlined the thermal analysis which was performed on the three propulsion systems to get an understanding of the component temperatures in extreme orbit cases and to investigate the need for thermal coatings and heaters. The systems were reduced to thermal networks consisting of 5 nodes: the thruster, piping tray, tank bottom endcap, propellant, and the remainder of the tank shell. It was concluded that the 600 Ns propulsion system, at an orbital altitude of 1000 km, resulted in the worst cold case, whereas the 200 Ns propulsion system, at an orbital altitude of 300 km, resulted in the worst hot case in terms of node temperatures throughout the orbit. A Zerlauts Z-93 white paint coating was required to reduce the node temperatures for both the cold and hot case. The resulting temperatures were within bounds for the hot case after applying the coating to the outside of the piping tray. However, the cold case temperatures dropped below their minimum allowed values, therefore requiring a heater that supplies a continuous power of 0.5 W into the tank bottom endcap. Furthermore, it was calculated that the maximum burn duration was not limited by the upper bound temperatures of the different nodes. A maximum burn duration of 3000 seconds was decided on as a result of tests that were performed on the technology demonstrator thruster design (as outlined in Chapter 4). A cooling period of 44 and 27 hours is required after such a manoeuvre for respectively the extreme cold and extreme hot case. The system performance is summarized in Table 11.15, whereas the estimated worst-case component temperature ranges are detailed in Table 11.16.

Requirement *PROP-INT-2* can be updated accordingly now the minimum and maximum allowed nodal temperatures are know: "The propulsion system shall stay in a temperature range between **0** °C and **650** °C."

Table 11.15: Propulsion system performance summary.

Parameter	Value
Thrust [mN]	1
Maximum burn duration [s]	3000
Thruster input power [W]	4.7
Heater power [W]	0.5

Table 11.16: Estimated component temperature ranges (in K).

Component	Temperature Range
Thruster	350 - 693
Piping tray	277 - 340
Tank bottom	300 - 314
Propellant	292 - 308

11.6 Recommendations

This thermal analysis was performed to get an understanding of the component temperatures and the need for a heater and coatings. The results found in this chapter are not exact, as they are based on a variety of assumptions and simplifications. Several recommendations can be made for future research that will improve the results found in this section.

A first improvement that can be made is to include the entire propulsion system without any simplifications. This includes all piping components, the use of a real spacecraft rather than replacing it with a boundary temperature, the addition of the TunaCan add-on, and not neglecting important thermal exchange mechanisms as conduction through the mechanical interfaces and convection between the tank and propellant. An example of a detailed thermal network representation of the propulsion system can be found in Appendix B.

A second improvement in a continuation on the first one, namely to design the thruster in detail. It was shown that the conceptual thruster design, as outlined in Chapter 9, could burn indefinitely when looking at the estimated node temperatures. However, the burn duration was limited to 3000 seconds in this chapter, as tests on the technology demonstrator thruster verified both stability and controllability within this time frame. The burn duration must be verified through tests on the redesigned thruster. This is left for future work, as the detailed design of the thruster is outside the scope of this thesis.

A third improvement is to investigate more orbit cases, including ones that have eclipses. The changing thermal load that the propulsion system receives results in thermal cycling that can damage components, including coatings, over time. Furthermore, it is advised to consider not only more thermal coatings, but also the stability of the applied coating as changes in absorptivity and emissivity can greatly impact the propulsion system temperatures.

Finally, it is advised to make use of thermal modelling software such as ESATAN and COMSOL. The use of software will yield, when applied correctly, more accurate results.

Propulsion System Assembly 12

This chapter outlines the final propulsion system configurations. First, the system design, including all components, spacers, and fasteners are discussed in Section 12.1. This is followed by the mass, volume, and power breakdowns in Section 12.2. Next, the final system performance is outlined in Section 12.3, whereas the compliance with the requirements that were outlined at the start of this thesis is investigated in Section 12.4. The chapter is concluded in Section 12.5 with a short discussion on possible mitigation strategies for the mass and volume budget overruns.

12.1 System Design

This section describes the entire layout of the three propulsion systems, including all components, and how they are attached.

12.1.1 Additional Components

Several components are still required to complete the propulsion systems, namely a printed circuit board (PCB), the TunaCan add-on, propellant tank heaters, and mounting hardware. Technical drawings of all non-COTS components can be found in Appendix C.

Printed Circuit Board

The printed circuit board is the brain of the propulsion system, as it not only controls the thruster and tank heaters, but also communicates the system health to the spacecraft within it is integrated. As discussed in Chapter 7, a 92 x 92 mm^2 PCB is used to ensure compliance with the CS14 standard. The computer aided design (CAD) model of this PCB is visualized in Figure 12.1, whereas the specifications of the PCB are summarized in Table 12.1.

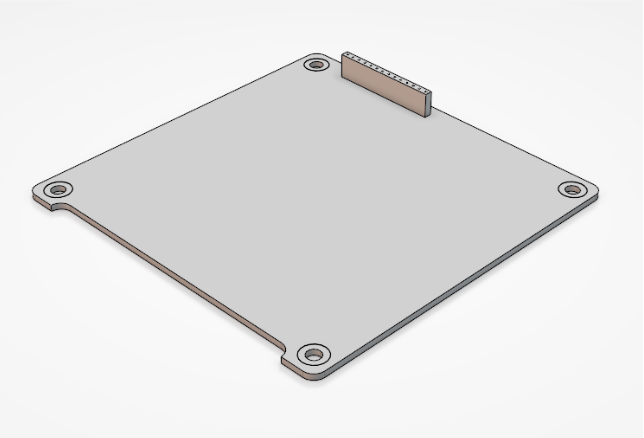

Figure 12.1: CAD model of the PCB.

Table 12.1: Printed circuit board specifications [23][137].

Parameter	Value
Material	FR-4
Dimensions (LxWxH)	92 x 92 x 1.6 mm^3
Mass	24.9 g

TunaCan Add-on

The TunaCan add-on is required to house the extruded pressure regulator and thruster, as discussed in Chapter 9. The diameter and height of this structure are limited to 64 and 36 mm respectively [138]. Only 15.7 mm of the maximum allowed height is used, as this precisely encapsulates both the pressure regulator and thruster, where the nozzle exit is level with the TunaCan's surface. The CAD model of the TunaCan add-on is visualized in Figure 12.2, whereas the specifications are summarized in Table 12.2.

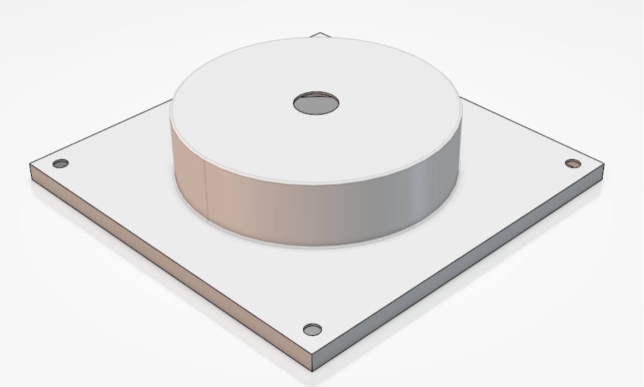

Figure 12.2: CAD model of the TunaCan.

Table 12.2: TunaCan specifications.

Parameter	**Value**
Material	316L Stainless steel
Dimensions (LxWxH)	92 x 92 x 20 mm^3
Mass	51.5 g

Propellant Heaters

The need for propellant heaters is discussed in Chapter 11, where it was estimated that a single 0.5 W heater, applied to the tank bottom endcap, is sufficient to maintain a propellant temperature between 10 and 50 °C. However, due to the many assumptions made in the thermal analysis and the additional TunaCan add-on, it is decided to use three custom, polyimide 0.5 W tank heaters that are mounted to the cylindrical tank shell. These heaters are centered on the long wall-mounted vanes, as propellant is attached to the entire wall along these structures, and allow for heat to spread throughout the propellant. Custom polyimide Zoppas Industries heaters are used, as they have a high operating temperature, are thin, lightweight, easy to install, and have low outgassing in vacuum [139]. A breakdown of the heater structure is shown in Figure 12.3, whereas the specifications of the custom heaters are summarized in Table 12.3.

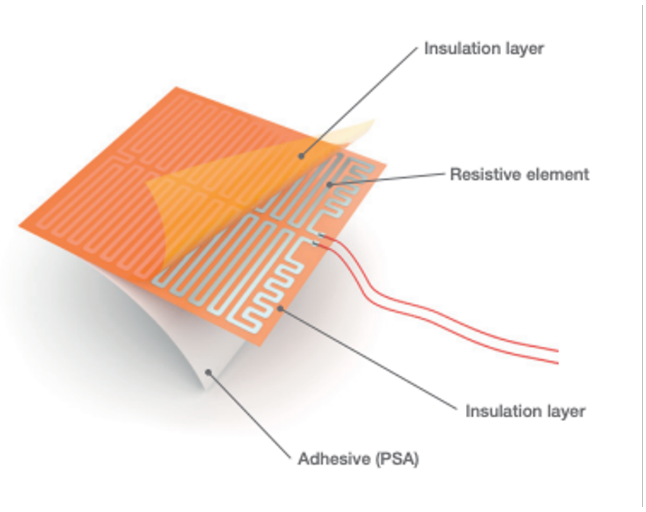

Figure 12.3: Zoppas Industries polyimide heater [139].

Table 12.3: Tank heater specifications [139] [140].

Parameter	Value
Manufacturer	Zoppas Industries
Material	Polyimide
Dimensions (LxWxt)	50 x 25 x 0.2 mm^3
Mass	0.72 g
Resistance	172 Ohm
Power	0.5 W
Operating temperature range	-65 to + 150 °C

Mounting Hardware

The mounting hardware are the last components required for the propulsion systems. This includes spacers, (lock) nuts, and connecting rods. The spacers are required to ensure that the propellant tank endcaps can deflect under internal pressure (as discussed in Chapter 10 and for mounting the TunaCan add-on to the piping tray. The latter is required, as both the propellant filter and pressure and temperature transducer protrude from the piping tray. The nuts are used to fasten the piping tray and tank to the connecting rods, whereas the lock nuts are used to bolt the PCB and TunaCan add-on to the connecting rods. It is assumed that the nuts have an inner diameter (ID) of 3.5 mm, and a flat hexagon side length of 3 mm. Moreover, all fasteners, spacers, and rods are constructed out of grade 5 titanium, where the spacers have an ID of 3.5 mm, and the rods an outer diameter (OD) of 3.5 mm and a thread pitch of 0.5 mm. These dimensions are chosen to ensure compatibility with the PCB and tank design. The CAD model of the spacers, (lock) nuts, and connecting rod are visualized in Figure 12.4, whereas the specifications are summarized in Table 12.4.

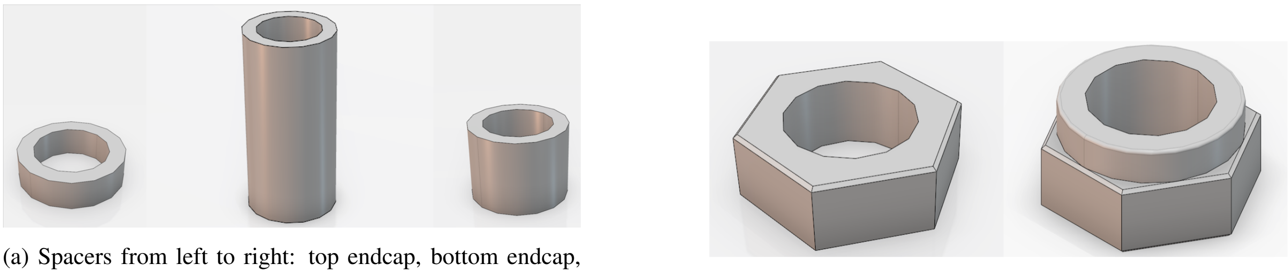

(a) Spacers from left to right: top endcap, bottom endcap, and TunaCad add-on.

(b) Fasteners from left to right: nut and lock nut

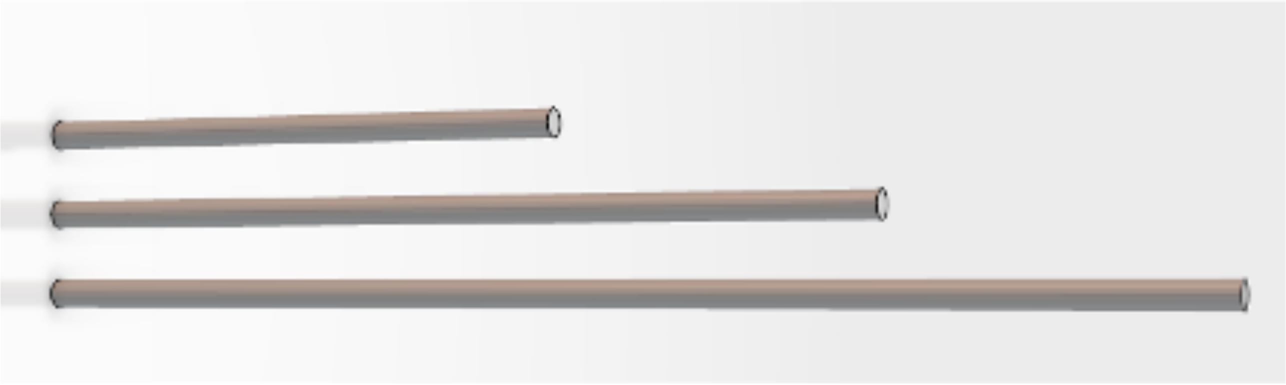

(c) Connecting rods from top to bottom: 200 Ns, 400 Ns, and 600 Ns

Figure 12.4: Cad model of mounting hardware.

Table 12.4: Mounting hardware specifications.

Parameter	Value
Nut	
Material	Ti-6Al-4V
Dimensions (ID x H)	3.5 x 2 mm^2
Mass	0.12 g
Lock Nut	
Material	Ti-6Al-4V

Continued on next page

Parameter	**Value**
Dimensions (ID x H)	3.5 x 3 mm^2
Mass	0.17 g
Top Endcap Spacer	
Material	Ti-6Al-4V
Dimensions (ODxIDxH)	5 x 3.5 x 1.4 mm^3
Mass	0.062 g
Bottom Endcap Spacer	
Material	Ti-6Al-4V
Dimensions (ODxIDxH)	5 x 3.5 x 10.43 mm^3
Mass	0.23 g
TunaCan Spacer	
Material	Ti-6Al-4V
Dimensions (ODxIDxH)	5 x 3.5 x 3.78 mm^3
Mass	0.17 g
Connecting Rods (200 Ns / 400 Ns / 600 Ns)	
Material	Ti-6Al-4V
Dimensions (ODxH)	3.5 x 64.6 mm^2 / 3.5 x 104.7 mm^2 / 3.5 x 144.6 mm^2
Mass	2.5 g / 4.0 g / 5.6 g

12.1.2 Assembling the System

Figure 12.5 shows an exploded view of the 200 Ns propulsion system, where the connecting rods are excluded for clarity. The assembly of the 400 Ns and 600 Ns are identical to the 200 Ns, and are therefore not shown. The propulsion systems are fastened from the TunaCan add-on to the PCB as follows: The TunaCan add-on is fastened to the piping tray with 4 lock nuts and spacers between the TunaCan and the piping tray due to the aforementioned protrusion of the propellant filter and pressure and temperature transducer. The piping tray is fastened to the TunaCan using 2 nuts, whereas two spacers are placed between the piping tray and propellant tank. These spacers are required to ensure that the bottom endcap of the tank can deflect under the maximum expected operating pressure of 10 bar under launch load conditions (see Section 10.6). The bottom and top of the tank are fastened using a total of 6 lock nuts. Furthermore, there are 4 spacers between the top endcap and the PCB to allow for a 1.4 mm deflection of the top endcap (as was calculated for a 10-bar internal pressure during launch in Section 10.6). Finally, the PCB is fastened using 4 lock nuts.

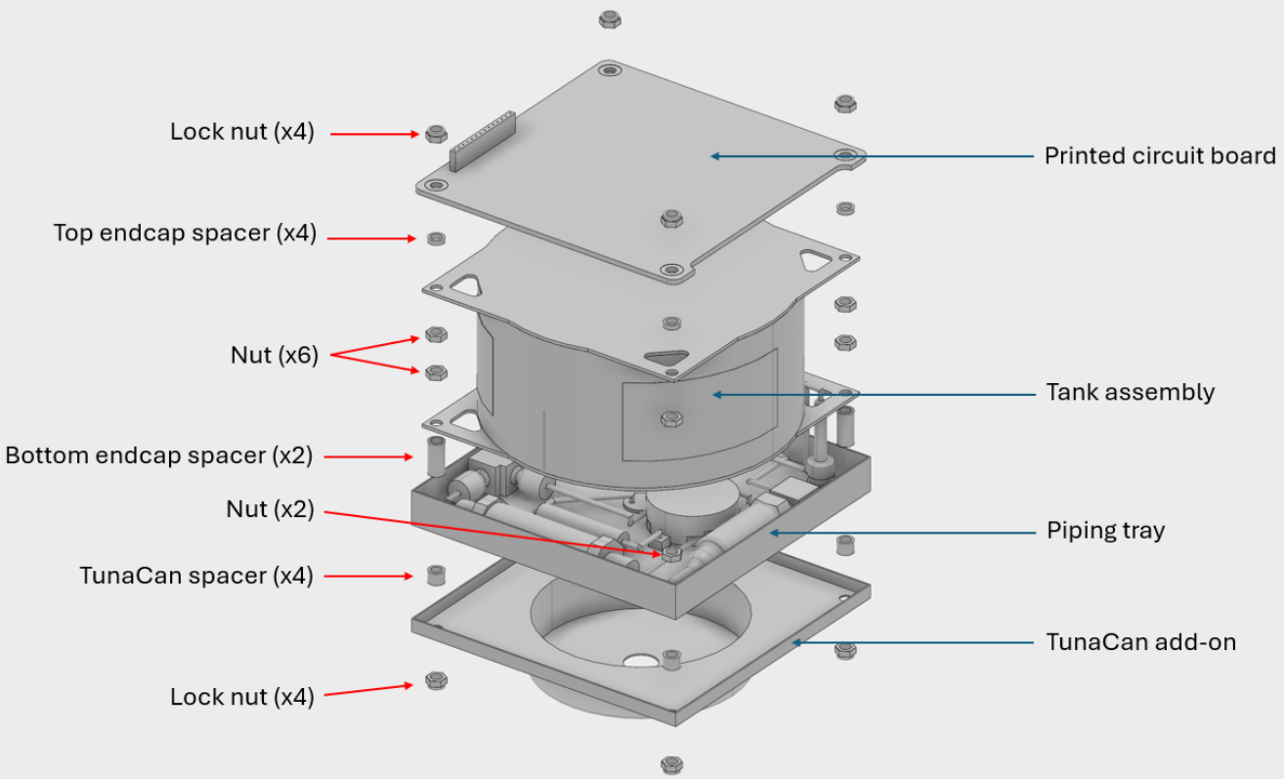

Figure 12.5: Exploded view of the 200 Ns propulsion system.

The use of lock nuts to fasten the propulsion system at both extremities ensures that the system remains assembled throughout the mission. The fact that these nuts lock the system does not mean that it cannot be disassembled. Similar all-metal, titanium lock nuts are rated for 15 torque cycles [141].

12.1.3 Assembled Propulsion Systems

Figure 12.6 shows an isometric view of the three propulsion systems, where a decal is applied to the PCB, the connection rod threads are visible, and the heaters are dyed orange.

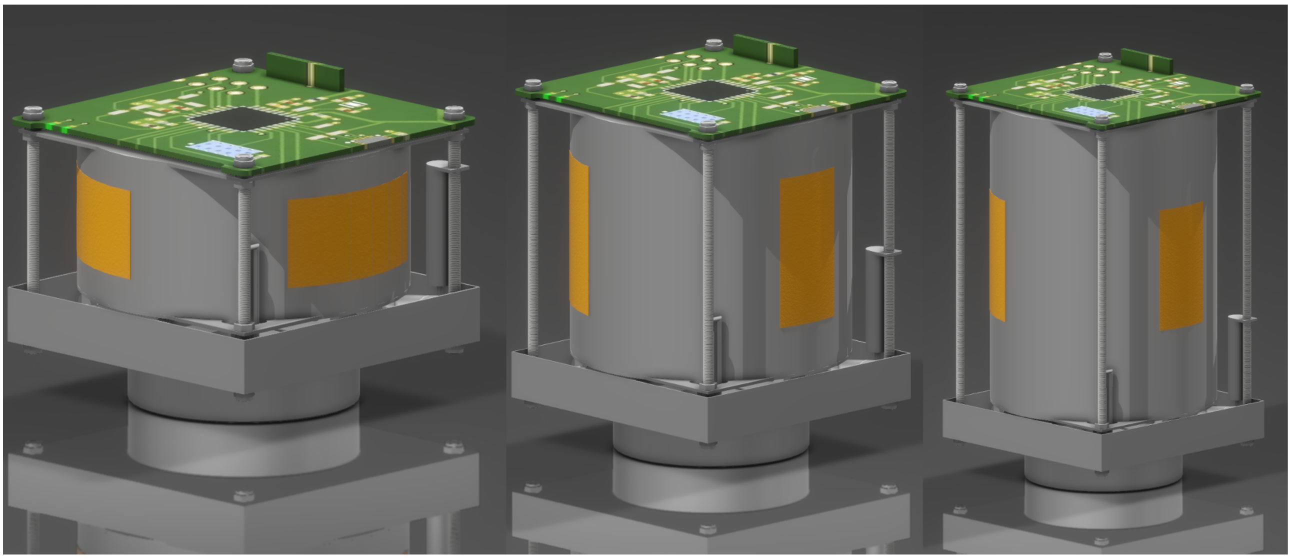

Figure 12.6: Visual of the three propulsion systems from left to right: 200 Ns, 400 Ns, and 600 Ns.

12.2 Budgets

This section outlines the mass, volume, and power breakdowns of the three propulsion systems.

12.2.1 Mass Breakdown

Table 12.5 shows the mass budgets that were generated at the start of the design phase (Chapter 7). These budgets were based on percentages of the system dry mass [56].

Table 12.5: Mass budgets for the 200 Ns, 400 Ns, and 600 Ns propulsion systems (masses are in grams).

System	**200 Ns**	**400 Ns**	**600 Ns**
Wet mass	700	1350	2000
Propellant mass	197	393	589
Dry mass	503	957	1411
Structures and mounts	39	74	109
Controls and wiring	19	37	54
Thruster	40	40	40
Tankage	347	696	1045
Design margin	58	110	163

Table 12.6 shows the mass breakdown of the tankage, which includes the tank shell, PMD, and piping (including the tray). It must be noted that all masses in this section, except the piping components of which the mass was specified in their respective datasheets, are calculated from the component volume that is provided by the 3DExperience software. It can be observed that the tankage mass for the 200 Ns is significantly over its allocated mass budget. This overrun can party be negated by using the 58 g design margin. Moreover, the usable tank volume is decreased slightly by the presence of the PMD and tank reinforcements, which will result in a smaller propellant and pressurant mass.

Table 12.6: Tankage mass breakdown (masses are in grams).

System	**200 Ns**	**400 Ns**	**600 Ns**
Tank Shell			
Top endcap	64.2		
Bottom endcap	62.2		
Cylindrical shell	16.2	31.5	46.8
Reinforcement rings	22.4		
Total shell mass	165	180	196
Propellant Management Device			
Sponge	1.28		
Vanes	2.59	3.79	4.70
Total PMD mass	3.87	5.07	5.98
Piping			
Piping tray	65.9		
Tubing	3.3		
Propellant filter	55.0		
Solenoid valve	4.8		
Pressure regulator	66.0		
Pressure regulator connector	4.0		
Pressure and temperature transducer	10.0		
Transducer connector	5.0		
Fill/drain valve	5.0		
Cross connector	32.0		
Tee connector	21.0		
Pressure relief valve	4.5		
Pressure relief valve holder	5.0		
Total piping mass	282		
Tankage Masses			
Total mass	451	467	484
Allocated budget	347	696	1045
Residual Budget	-104	229	561

Table 12.7 shows the mass breakdown of the controls and wiring, which includes the PCB and tank heaters. The mass of the wiring is not included, as the detailed electric design is left for future work. The 200 Ns is slightly over its allocated controls and wiring mass budget.

Table 12.7: Controls and wiring mass breakdown (masses are in grams).

System	**200 Ns**	**400 Ns**	**600 Ns**
PCB	24.9		
Polyimide tank heaters	2.15		
Total mass	27.0		
Allocated budget	19	37	54
Residual budget	*-8.03*	9.97	27.0

Table 12.8 shows the mass breakdown of the structures and mounts, which includes the TunaCan add-on. The 200 Ns propulsion system exceeds this structures and mounts mass budget by 27.2 grams, whereas the 400 Ns system is just within its allocated mass budget.

Table 12.8: Structures and mounts mass breakdown (masses are in grams).

System	**200 Ns**	**400 Ns**	**600 Ns**
Spacers	1.84		
Fasteners	2.29		
Rods	10.6	16.8	23.0
TunaCan add-on	51.5		
Total mass	66.2	72.4	78.6
Allocated budget	39	74	109
Residual budget	*-27.2*	1.6	30.4

Table 12.9 shows the mass breakdown of each propulsion system, where the thruster mass is still assumed to be 40 grams. Moreover, the propellant and pressurant mass is recalculated by taking into account the fill ratio of 0.75, and the volume that the PMD design and tank reinforcements occupy. The latter is outlined in the usable volume breakdown of the propellant tank.

Table 12.9: Mass breakdown of the 200 Ns, 400 Ns, and 600 Ns propulsion systems (masses are in grams).

System	**200 Ns**	**400 Ns**	**600 Ns**
Thruster	40.0	40.0	40.0
Tankage	451	467	484
Structures and mounts	66.2	72.4	78.6
Controls and wiring	27.0	27.0	27.0
Dry mass	584	607	629
Propellant mass	193	391	587
Wet mass	777	998	1217
Allocated budget	700	1350	2000
Residual budget	*-77*	352	783

The 200 Ns system is over its allocated mass budget by 77 grams, whereas the other systems are well within their allocated mass budget. There are several strategies to reduce the system mass, including the removal of the TunaCan structure. However, it is not likely that any of these strategies will decrease the mass by 77 grams, as will be discussed in Section 12.5.

12.2.2 Volume Breakdown

There was no volume budget generated at the start of the design, as there were no existing relationships found in literature for the volume breakdown of electrothermal propulsion systems. Moreover, the lack of detailed volume breakdowns for existing systems made generating such a budget difficult and high speculative at best. However, the combination of requirement *PROP-SYST-2* and *PROP-INT-1* limits the design space to a width and length (the X- and Y-direction in Figure 7.1) to 92 x 92 mm, whereas the height is restricted to 50 mm, 100 mm, and 150 mm for the 200 Ns, 400 Ns, and 600 Ns system respectively.

Table 12.10 shows the volume breakdown of the three propellant tanks. This is provided, as it allows for determining the usable tank volumes, given the modified PMD and tank shell design. The updated propellant and pressurant mass (or fluid mass) can be calculated using this usable tank volume and the fill ratio of 0.75:

$$M_{fluid} = (1 - F_i)\rho_{pres}V_{tank} + F_i\rho_{prop}V_{tank} \tag{12.1}$$

where M_{fluid} is the combined mass of the propellant and pressurant, F_i is the fill ratio, V_{tank} is the usable tank volume, ρ_{pres} is the density of the pressurant (nitrogen), and ρ_{prop} is the density of the propellant (water) at the BOL pressure of 8.75 bar.

Table 12.10: Usable propellant tank volume of the 200 Ns, 400 Ns, and 600 Ns systems.

System	**200 Ns**	**400 Ns**	**600 Ns**
Tank Shell Volume			
Shell thickness [mm]	0.3		
Head thickness [mm]	2.1		
Tank outer radius [mm]	46		
Outer tank height [mm]	44.3	84.4	124.3
Internal volume [L]	0.263	0.526	0.788
PMD Volume			
Sponge [mL]	0.29		
Vanes [mL]	0.58	0.86	1.06
Reinforcement Volume			
Reinforcement rings [mL]	5.06		
Usable Tank Volume			
Total volume [L]	0.257	0.520	0.782
Fill ratio [-]	0.75		
Pressurant volume [L]	0.064	0.130	0.195
Propellant volume [L]	0.193	0.390	0.586

Table 12.11 shows the volume breakdown of the three propulsion systems, where the volume is provided in U's (1 U is a 10 x 10 x 10 cm^3 cube). The height of each system is measured from the top of the PCB to the bottom of the non-cylindrical part of the TunaCan add-on. The height of the cylindrical TunaCan add-on is neglected, as the launch canister includes spacing to accommodate this protrusion. Both the 200 Ns and 400 Ns exceed their respective design envelope of 0.5 U and 1.0 U. This overrun was already anticipated after the tank design, as requirement *PROP-TANK-03* allowed for using the entire height budget of 50 mm, 100 mm, and 150 mm. In hindsight, it would have been better to limit the tankage height budget to values below the maximum allowed height to prevent this volume overrun. However, limiting the height would have resulted in a lower total deliverable impulse of the two smallest system, as there would not have been sufficient volume for the propellant to deliver the specified total impulses.

Table 12.11: Volume breakdown of the 200 Ns, 400 Ns, and 600 Ns propulsion systems.

System	**200 Ns**	**400 Ns**	**600 Ns**
Length x width [mm^2]	92 x 92		
Height [mm]	63	103.1	143
Volume [U]	0.63	1.031	1.43
Allocated budget [U]	0.5	1	1.5
Residual budget	*-0.13*	*-0.031*	0.07

12.2.3 Power Breakdown

Like the volume budget, there was no power budget generated at the start of the design phase. The power that each system can use is limited by requirement *PROP-SYST-4* to 25 W. Table 12.12 shows the breakdown of the power usage across the different components for both thrusting and non-thrusting conditions. It is assumed that the efficiency of the thruster, in terms of power, is 50%. It seems like the three systems use the same amount of power. This is true for the thruster and tankage, as the piping is identical across the three systems. However, the required propellant heater power will differ between the three systems, as the tank shell area and propellant and pressurant mass vary. This effect was not investigated in the thermal analysis, as only the worst hot and cold case were analysed. The latter required a 0.5 W heater to keep the nodal temperatures of the 600 Ns system within their respective bounds. Lower heater power is therefore excepted for the 200 Ns and 400 Ns systems.

Table 12.12: Breakdown of the power usage across the different components.

Component	**Value (idle / thrusting)**
Thruster	0 W / 4.7 W
Solenoid valve	0 W / 3 W
Pressure and temperature transducer	0.16 W / 0.16 W
Tank heater (x3)	< 1.5 W / 0 W
Total	< 1.65 W / < 7.86 W
Allocated budget	25 W
Residual budget	> 23.3 W / > 17.1 W

12.3 System Performance

This section outlines the system performance in terms of thrust, specific impulse, power usage, maximum burn duration, minimum impulse bit, total impulse, and lifetime. The performance of each system is summarized in Table 12.13. It must be noted that the minimum impulse bit (MIB) is assumed to be equal to 1 mNs (hence a 1 second burn). The feasibility of this MIB must be verified through testing of the thruster that is to be designed. Moreover, the total impulse of the three systems is calculated by assuming that the thruster performance is equal to its ideal performance (i.e. no losses) and that the expulsion efficiency remained the same for the modified vane design. Finally, the maximum number of cycles for each system is calculated by dividing the total impulse by the MIB. The actual cycle life must be equal to that of the 600 Ns system, as the piping is identical across the three systems. The only actuator that is required for thrusting (the solenoid valve) is rated for more than 100 million cycles.

Requirement *PROP-SYST-5* can now be updated accordingly: "The propulsion system shall function for **at least 700,000 cycles**." The transition from expressing lifetime in months to thrust cycles is made because assigning a specific time-based lifetime to any system is challenging, as it depends on the mission type.

Table 12.13: Propulsion system performance.

System	200 Ns	400 Ns	600 Ns
Thrust [mN]	1		
Specific impulse [s]	130.2		
Power (idle/thrusting) [W]	< 1.65 / < 7.86		
Maximum burn duration [s]	3000		
Minimum impulse bit [mNs]	1		
Total impulse [Ns]	226	465	700
Lifetime [$\cdot 10^3$ cycles]	700		

12.4 Requirement Compliance

This section compares the requirements that were generated at the start of this thesis (from now on called base requirements) with the final system designs.

12.4.1 List of Updated Requirements

The list of updated, base requirements, their associate compliance, and motivation, are outlined in Table 12.14. The term "updated" refers to the replacement of TBDs in the initial requirements with updated values throughout this thesis.

Table 12.14: Requirement verification table.

Requirement ID	(Updated) Requirement	Compliant	Motivation
System Requirements			
PROP-SYST-1	The propulsion system shall be compatible with multiple propellant tank sizes	Yes	The only difference between the three systems is the tank size and length of the connecting rods.
PROP-SYST-2	The total size of the propulsion system shall be within 0.5 U / 1.0 U / 1.5 U.	Partial	The 200 Ns and 400 Ns systems exceed the volume budget.
PROP-SYST-3	The total wet mass of the propulsion system at launch shall not exceed 0.7 kg / 1.35 kg / 2.0 kg.	Partial	The 200 Ns system exceeds the wet mass requirement by 77 grams.
PROP-SYST-4	The power consumption of the propulsion system shall not exceed 25 W.	Yes	The idle / thrust power is < 1.65 W / < 7.86 W.
PROP-SYST-5	The propulsion system shall function for > 700k cycles	Yes	The solenoid valve allows for > 10^8 cycles.
Performance Requirements			
PROP-PERF-1	The propulsion system shall deliver a total impulse of 200 Ns / 400 Ns / 600 Ns.	Yes	A total impulse of respectively 226 Ns / 465 Ns / 700 Ns is achieved when assuming ideal thruster performance.
PROP-PERF-2	The propulsion system shall deliver a maximum thrust of 5.7 mN	Yes	A 1 mN thrust level is achieved.
PROP-PERF-3	The propulsion system shall deliver a minimum thrust of 0.5 mN	Yes	A 1 mN thrust level is achieved.
PROP-PERF-4	The propulsion system shall operate on a supply voltage of <TBD>V.	N/A	The detailed electric system design is left for future work.
Functional Requirements			
PROP-FUNC-1	The propulsion system shall use water as propellant.	Yes	Self explanetory.

Continued on next page

Requirement ID	**(Updated) Requirement**	**Compliant**	**Motivation**
PROP-FUNC-2	The propulsion system shall have at least an idle and thrust mode.	Yes	The solenoid valve allows for both idling and thrusting.
	Interface Requirements		
PROP-INT-1	The mechanical interface between the propulsion system and the satellite shall be compliant with the CubeSat CS14 standard.	Yes	All interfaces are in-line with the CS14 PCB mounting holes.
PROP-INT-2	The propulsion system shall stay in a temperature range between 0 °C and 650 °C	Yes	The thermal analysis showed that the temperatures are maintained within this range. A more detailed thermal analysis and testing is required to verify the results.
PROP-INT-3	The electrical interface between the propulsion system and the satellite shall be compliant with the CubeSat CS14 standard.	Partial	The PCB is in accordance with this standard, whereas the detailed electric system design is left for future work.
PROP-INT-4	The propulsion system shall allow for filling and draining of the propellant at any time when the satellite is accessible to human operators	Yes	There is a fill/drain valve that is accessible when the TunaCan add-on is removed.
	Reliability, Availability, Maintainability, and Safety (RAMS) Requirements		
PROP-RAMS-1	The pressure within the propulsion system shall not exceed 10 bar.	Yes	A pressure relief valve will dump propellant when the pressure within the system exceeds 10 bar.
PROP-RAMS-2	The materials used in the propulsion system shall be compatible with the chosen propellant.	Yes	Grade 5 titanium and (316L) stainless steel are compatible with water and gaseous nitrogen.
PROP-RAMS-3	The materials used in the propulsion system shall not be flammable, toxic, or hazardous to the satellite and operators.	Partial	Inhaling nitrogen in large quantities can be hazardous.

12.4.2 Requirement Tree

Figure 12.7 shows a requirement tree that links all the generated component requirements to the base requirements. There are several base requirements that do not have an associated component requirement: *PROP-SYST-4*, *PROP-PERF-2*, *PROP-PERF-3*, *PROP-PERF-4*, *PROP-FUNC-1*, and *PROP-FUNC-2*.

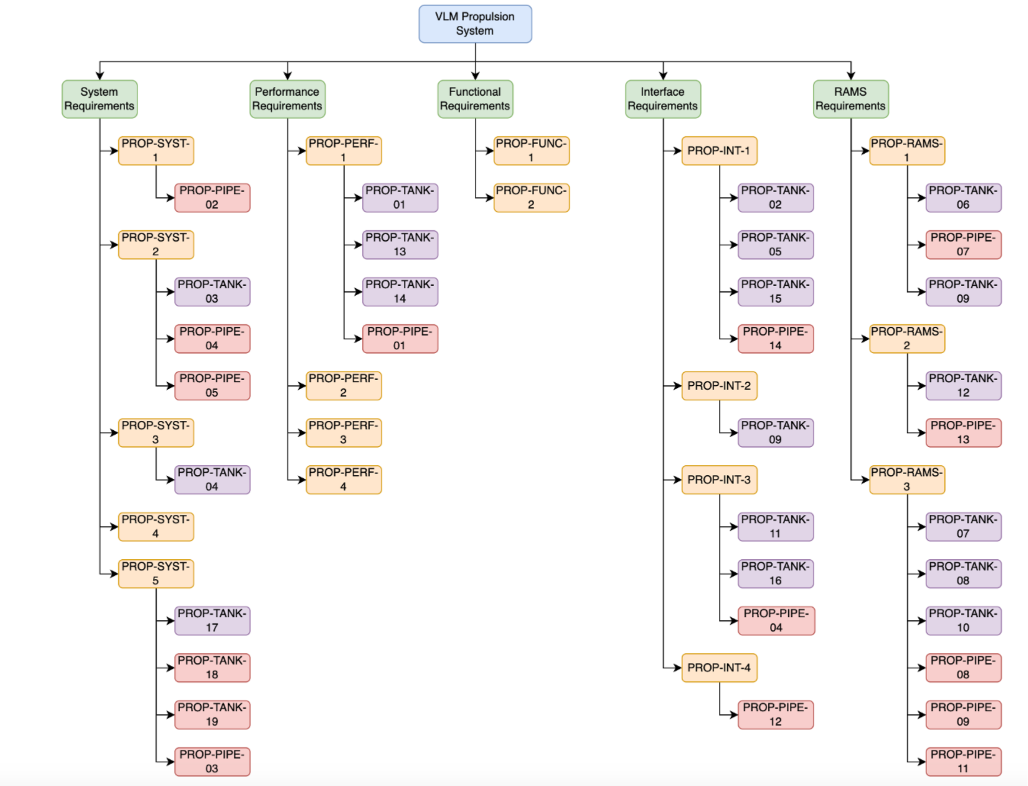

Figure 12.7: Requirement tree.

Requirement *PROP-SYST-4* is not linked to any component requirement, as there was no power budget generated at the start of the design phase. Moreover, the requirements *PROP-PERF-2*, *PROP-PERF-3*, and *PROP-FUNC-2* are not linked to any of the component requirements, as they are based on design choices. Furthermore, *PROP-PERF-4* is not linked to any of the component requirements, as the detailed electrical design of the propulsion system is left for future work. Finally, *PROP-FUNC-1* is not linked to any of the component requirements, as it resulted from a separate trade-off that was performed before the start of the system design.

12.5 System Optimizations

The 200 Ns system exceeds both the wet mass and system volume requirement, whereas the 400 Ns system exceeds the system volume requirement. The system heights (thus its associated volume) and wet mas can be reduced by increasing the fill ratio. The initial fill ratio was limited to a value of 0.75 by the positive expulsion devices, whereas the current PMD design (a sponge and vanes) would allow for a larger fill ratio.

However, the EOL tank pressure decreases when increasing the fill ratio. This decrease in EOL tank pressure results in a lower achievable thrust, as shown for the 200 Ns system in Figure 12.8. It is clear that the maximum fill ratio is limited by the minimum required thrust level of 0.5 mN (at a fill ratio of 0.877).

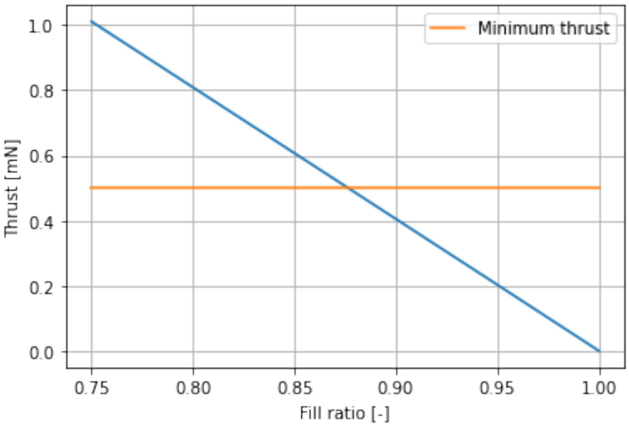

Figure 12.8: Thrust as a function of the fill ratio.

This decrease in performance can be negated by increasing the BOL tank pressure. However, the maximum pressure within the system is limited to 10 bar (requirement *PROP-RAMS-1*). Moreover, increasing the tank pressure beyond the 10 bar would require a more reinforced tank, resulting in less usable volume for the propellant, a lower achievable total impulse, and the need for an even higher fill ratio to ensure that the minimum required total impulse is achieved. This vicious circle is shown in Figure 12.9. It is therefore decided to accept the additional mass for the smallest 200 Ns system, and the excess height of both the 200 Ns and 400 Ns system.

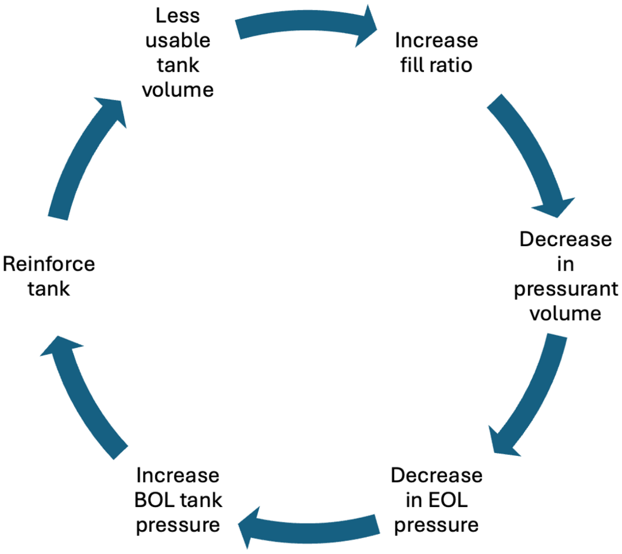

Figure 12.9: Viscous circle that shows the effects of increasing the fill ratio while maintaining a thrust level of 1 mN and a total impulse level of 200 Ns, 400 Ns, and 600 Ns.

Another possibility is to accept the loss in performance in terms of the achievable thrust level. Figure 12.10a shows the system height and achievable thrust level as a function of the fill ratio for both the 200 Ns and 400 Ns systems, whereas Figure 12.10b shows the wet mass and achievable thrust level of the 200 Ns system as a function of the fill ratio.

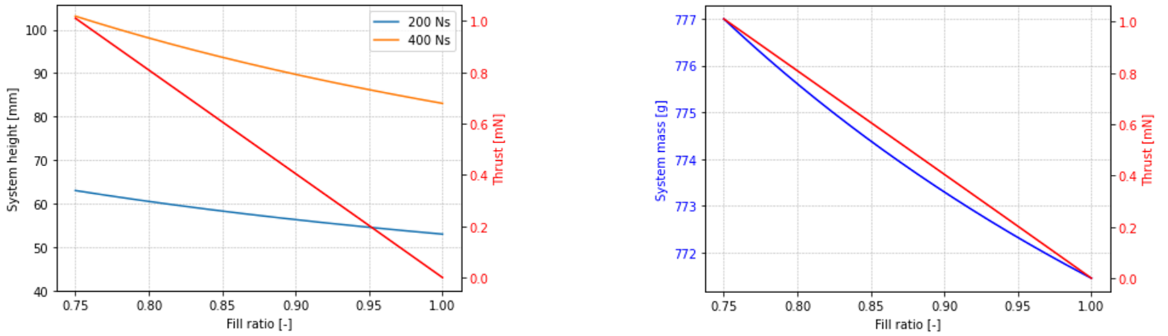

(a) System height and thrust as a function of the fill ratio for both the 200 Ns and 400 Ns systems.

(b) System mass and thrust as a function of the fill ratio for the 200 Ns system.

Figure 12.10: System height, mass, and achievable thrust as function of the tank fill ratio.

It is clear that the 200 Ns system will never comply with either the volume (maximum allowed system height equal to 50 mm) or wet mass budget (equal to 700 g). The 400 Ns system already complied with the wet mass budget (equal to 1350 g) and is also able to meet the system height budget when decreasing the maximum achievable thrust level to 0.89 mN: a performance decrease of 11 %. However, the previously described viscous circle when attempting to maintain the system performance in terms of the thrust level, the inability to meet either the wet mass or volume budget for the 200 Ns system when decreasing the thrust level, and the loss in system performance for the 400 Ns to comply with the volume requirement led to accepting the additional mass for the smallest 200 Ns system, and the excess height of both the 200 Ns and 400 Ns systems in this thesis. Potential customers can be made aware of the possibilities regarding the trade-off between the achievable thrust level, system mass, and system height.

Conclusion 13

The absence of a TU Delft-designed VLM propulsion system was the basis of my thesis that aimed to achieve the following research objective:

"Designing a modular micro-resistojet propulsion system that is capable of delivering three distinct total impulse levels, based on a pre-existing VLM thruster developed by the TU Delft, with a focus on integration into a CubeSat configuration."

The following research questions and sub-questions were proposed to achieve this objective, and are each answered in their separate section:

Section 13.1: ***What are suitable requirements for a VLM propulsion system?***

- What missions can be flown with a VLM propulsion system, and how do these missions dictate the requirements?
- What are the constraints acting on the propulsion system?

Section 13.2: ***What is the best propellant to meet the propulsion system requirements?***

- How does the requirement of total impulse influence the choice of propellant?
- How does the choice of propellant influence the required input power and thrust level?
- How does the choice of propellant influence the propellant mass of the system?
- How does the choice of propellant influence the required system volume?
- How does the choice of propellant influence the material selection of the feed system?
- How does the choice of propellant influence the required temperature levels within the propulsion system?

Section 13.3: ***What propulsion system architecture would most effectively meet the system requirements?***

- What components must be present in the propulsion system?
- How does the use of a modular system influence the design of the propulsion system?
- What trade-offs are performed for each of the propulsion system components?
- How does each component of the propulsion system contribute to meeting the overall system requirements?
- How does the selected propulsion system architecture integrate with the rest of the spacecraft?
- How does the propulsion system architecture comply with relevant regulatory and safety standards?

13.1 What are suitable requirements for a VLM propulsion system?

A wide variety of missions can be flown with a VLM propulsion system, given the fact that sufficient power is available for the thruster. CubeSats are a more suitable vehicle to integrate such a system in compared to PocketQubes as a result of this power requirement and were chosen as the vehicle of choice for the design of the system. An orbital lifetime analysis, performed on a 3U CubeSat with a ballistic coefficient of 164, was used to investigate suitable scenarios in which a VLM propulsion system could meaningfully prolong the lifetime of CubeSats orbiting Earth. These mission scenarios dictated the system requirements in terms of thrust level (to minimize gravity losses) and total impulse (to maintain an orbital altitude above 300 km for a prolonged duration). A minimum thrust of 0.5 mN, and total impulse levels of 200 Ns, 400 Ns and 600 Ns were settled on.

The CubeSat format, combined with the thrust level and total impulse levels, constrains the design in terms of power, mass, volume, safety, handling, thrust and temperature levels, and interfaces. These constraints were generated using the relationships for VLM propulsion systems that were found in the literature study between thrust and power, total impulse and system volume, and wet mass and system volume. The constraints were subsequently documented in a list of requirements in Section 4.2, and contained some TBD's that were to be filled in throughout the design of the systems.

13.2 What is the best propellant to meet the propulsion system requirements?

A trade-off between five propellants, ammonia, butane, R134a, R236fa, and water was performed to determine which is best suited for a VLM propulsion system, given the list of the system requirements that was generated. Four trade-off criteria were introduced, namely system density, performance, flammability, and health risk. The performance criterion included the achievable thrust levels, specific impulse, volumetric impulse, and the required heating power, and were calculated for chamber temperatures ranging between 300K and 550 K, and chamber pressures between 2 and 5 bar.

The type of propellant significantly impacted the deliverable total impulse, system volume, and propellant mass. The relationship between these parameters and the propellant was mainly found when looking at the achievable impulse per volume of propellant, where water achieved the largest value. Water was followed by ammonia, R134a, R236fa, and butane. Combining the fact that water had the largest achievable impulse per volume, and the high density at storage conditions, resulted in water requiring little propellant mass and system volume, which made it an efficient propellant to use in terms of mass and volume.

However, water required a significantly larger heating power to achieve these high impulse levels. This trend continued when looking at the achievable thrust levels as a function of the required heating power. Water required a significantly large heating power to achieve thrust levels comparable to that of the other four propellants. Nevertheless, these heating powers were all well within the limit of 25 W (as per requirement *PROP-SYST-4*) assuming a thruster efficiency of 50%.

Another interesting observation that was made is that an increase in chamber temperature does not significantly influence the achieved thrust levels, whereas in increase in chamber pressure does meaningfully impact the thrust levels. A sidenote to this observation is that, obviously, the combination of chamber temperature and pressure must always be above the boiling point for the thruster to function properly. Water required the largest chamber temperature at both chamber pressures (2 and 5 bar) to vaporize the propellant. That said, water remained liquid for the entire tank pressure range (between 2 and 10 bar) at a tank temperature of 293 K, whereas the other propellants became gaseous below some pressure. The latter was seen as undesirable, as gaseous propellant requires a larger tank volume.

Water eventually won the trade-off for the above-mentioned reasons. Moreover, the choice of propellant did not affect the material selection in a significant way, as all considered propellants were used in existing systems. It did, however, impact the safety of the human operators, as water is non-flammable, non-toxic, and stable.

13.3 What propulsion system architecture would most effectively meet the system requirements?

The design of the propulsion system began after water was chosen as the propellant. A propulsion system consists of various elements, including the type of feed system, propellant tank, and piping. The design process detailed in this thesis began with a trade-off analysis for the feed system.

Four types of feed systems were compared: blow-down, pressure regulated, hybrid (a combination of blow-down tank with a regulated mass flow rate), and pump-fed systems based on their performance, required fluid (both pressurant and propellant) mass, required fluid volume, and reliability. The pump-fed system was neglected before the trade-off was initiated due to its high complexity. Both helium and nitrogen were investigated as possible pressurants for this trade-off. Three assumptions were made: first, it was assumed that the propellant was just at its boiling point in the chamber. Second, it was assumed that the pressure drop between the tank and thrust chamber was negligibly small, and third, it was assumed that the expansion of the pressurant was isothermal at a constant tank temperature of approximately 293 K. The pressure regulated system achieved the largest thrust of up to 2.9 mN, whereas the blow-down system yielded the worst performance in terms of thrust. The hybrid feed system won the trade-off despite its worse performance in terms of thrust compared to the pressure regulated system. The difference in achievable thrust was deemed small (2.9 mN vs 2.36 mN for respectively the pressure regulated and hybrid system), while the pressure regulated system required an additional tank to store its pressurant. This would have resulted in a larger structural mass and volume, whereas both feed systems were already volume limited in terms of their performance. The reliability between the two systems was deemed comparable, as only one additional component is required for the pressure regulated system. Finally, nitrogen was chosen as pressurant, as helium is more prone to leakage whilst only requiring an insignificantly reduced fluid mass over the use of nitrogen.

A detailed mass budget and design envelope was generated after the type of feed system, the combination of a blow-down and pressure regulated system, was chosen. A safety factor of 1.25 was applied to the required total impulse levels of 200 Ns, 400 Ns, and 600 Ns systems respectively. This safety factor was applied to compensate for an expulsion efficiency smaller than 100%, and to compensate for any inefficiencies of the thruster. The ideal performance of the VLM thruster prototype was used in this thesis as the detailed design of the thruster was deemed outside the scope of this thesis. A power and volume budget were excluded due to the difficulty in finding a detailed breakdown of both parameters for existing systems. The creation of these budgets would have been inaccurate, and speculative at best.

The mass budget and design envelope was followed by the propellant tank design, where not only the tank shell was design, but also the mechanical interfaces and propellant management devices (PMDs). A list of requirements was generated, followed by a trade-off for the tank shape and material. These two trade-offs were combined, as they impacted each other significantly in terms of the required shell mass, tank height, and the manufacturability. The tank shapes included in the trade-off were a spherical tank, a cylindrical tank with flat and hemispherical endcaps, and a rectangular tank. Aluminium 6061-T6, 304L stainless steel, grade 5 titanium, and Inconel-718 were included as possible tank shell materials. Composites were neglected due to their need for a liner material and the manufacturing complexity. The spherical tank shape was eliminated before the start of the trade-off, as the required tank radii exceeded the design envelope. The cylindrical tank with hemispherical endcaps was eliminated at the start of the trade-off due to inefficient use of the available system volume. The cylindrical tank with flat endcaps, made from grade 5 titanium, won the trade-off as it used the resulted in the smallest shell mass and height. Furthermore, it required a constant wall thickness of 0.3 mm and endcap thickness of 2.1 mm for all three tank designs. The rectangular tank design demanded significantly greater mass and height, along with varying wall thicknesses for each tank wall and system size, which added to the complexity of manufacturing. However, all viable tank designs, including the chosen cylindrical tank with flat endcaps, utilized a significant portion of the mass budget and design envelope in terms of height. The relatively heavy shell mass and height resulted in budget and design envelope runs later in the system design process.

The tank shape and shell material trade-off was followed by the mechanical interface design. This interface was designed as a simple L-shaped beam that aligned with the attachment holes of the PCB, which allowed for easy integration within the propulsion system. The interface was sized for launch loads and natural frequency through simplified expressions and several assumptions. Six L-shaped interfaces, four located at the top endcap, and two at the bottom endcap of the propellant tank, are used with a width and thickness of 5 mm and 1 mm respectively.

A propellant management device trade-off was performed next, which included both positive expulsion devices such as bladders, diaphragms, and pistons, and surface tension devices including vanes, galleries, sponges, traps, and troughs. A combination of a radial sponge and vanes (surface tension devices) won the trade-off, a both the solubility of the pressurant into the propellant and propellant sloshing were not considered an issue. Positive expulsion devices would have won the trade-off when a significant portion of the pressurant would have dissolved into the propellant, or when the slosh dampening capabilities of such devices were required. The radial sponge consists of 70 sponge panels, whereas 3 short and 3 long vanes are used. The combination of short (reaching to half the tank height) and long vanes (reaching the top of the tank) was required to increase the expulsion efficiency of the surface tension device configuration. The long vanes were still required to ensure that all propellant is moved towards the sponge.

The PMD trade-off was followed by the design of the piping. The design of the piping is identical across the three propulsion systems, and results in the same performance in terms of thrust and specific impulse. Several components were required to achieve the required performance whilst adhering to all system requirements. A commercial-off-the-shelf (COTS) fill/drain valve, pressure relief valve, pressure and temperature transducer, propellant filter, pressure regulator, solenoid valve, union cross and tee connectors, and 1/16 inch OD tubing were chosen that ensured system performance within the specified requirements. Furthermore, custom elbow connectors, a pressure relief valve holder, piping tray, and a conceptual thruster housing were designed. The piping allowed for a constant thrust of 1 mN at a thruster input power of 4.7 W (assuming a 50% thruster efficiency), a valve actuation power of 3 W, and a pressure and temperature transducer power of 0.16 W. The total piping, excluding thruster, weighs 282 grams. This mass, combined with the mass of the tank shell, mechanical interface, and PMD exceeded the tankage mass budget of the 200 Ns system by 104 grams. Part of this budget overrun was compensated by the design margin of 58 grams. Furthermore, the height of the smaller 200 Ns and 400 Ns exceeded the design envelope and resulted in the systems being larger than a 1.0 U and 1.5 U system respectively. It was decided to accept this additional height, and to add a TunaCan structure to the propulsion systems that encloses the protruding propellant filter, pressure and temperature transducer, pressure regulator, and thruster.

A finite element analysis was then performed on the three tank designs, and included an internal pressure analysis, launch load analysis, buckling analysis, and natural frequency analysis. The internal pressure analysis showed that the tank failed below the maximum expected operating pressure (MEOP) of 10 bar due to unforeseen bending of the interface between the endcaps and cylindrical shell. A redesign of the tank was required to ensure that all tank designs survived this load. The tank modifications, which included reinforcement rings and edge fillets, survived the internal pressure, launch load, and buckling analysis. Furthermore, the natural frequencies of the empty tank were well above the minimum required launcher resonance frequency of 35 Hz. However, it was found that spacers between the top and bottom endcap were required to allow for these endcaps to displace under the internal pressure and launch loads. Four 1.4 mm tall spacers were placed between the top endcap and the PCB, whereas 10.4 mm spacers were placed between the bottom endcap and the piping tray. The latter is significantly taller than the top endcap, as it must reach the piping tray to which the piping components attach. The bottom endcap itself only deflected 0.9 mm under the worst load case (8.5 g axial acceleration at an internal pressure of 10 bar).

The finite element analysis on the propellant tank was followed by a thermal analysis of the entire propulsion systems, where each system was simplified to a thermal network consisting of 5 nodes: the thruster, piping tray, tank bottom endcap, propellant, and the remaining tank shell wall. Conduction and convection were neglected in this analysis to simplify the calculations. The goal of the thermal analysis was not to determine the exact temperature of each component, but to get an idea of the temperature ranges and need for possible coatings and tank heaters. A thermal analysis, performed on a worst cold and hot case, lead to the need for a white coating on the exterior of the piping tray, and the need for a 0.5 W tank heater. Moreover, the maximum burn duration was limited to 3000 seconds by the proven stability and controllability of the technology demonstrator thruster in terms of chamber pressure, mass flow rate, and input power. This burn duration required a cooling down period of 44 hours for the cold case, and 27 hours for the hot case to return to the steady-state node temperatures.

The thesis was concluded by assembly of the three propulsion systems. The systems were assembled by fastening the PCB, tank shell, piping tray, and TunaCan add-on to the connection rods using both nuts and lock nuts. The lock nuts were placed at both extremes of the connection rods to ensure that the system would not disassemble itself during the mission duration. The three fully assembled systems weighted in at 777 grams for the 200 Ns system, 998 grams for the 400 Ns, and 1217 grams for the 600 Ns system. Moreover, the systems heights were 63 mm, 103 mm, and 143 mm for the 200 Ns, 400 Ns and 600 Ns system respectively. The 200 Ns system mass was 77 grams heavier than initially budgeted, whereas both the 200 Ns and 400 Ns exceeded their volume requirements of 0.5 U and 1.0 U. These budget overruns were accepted, as the 200 Ns system was not able to meet either the mass or volume budget for any fill ratio, whereas decreasing both the system mass and volume would yield either a lower performance in terms of thrust or deliverable total impulse. A requirement tree was created that visualized how all generated requirements linked back to the requirements that were proposed at the start of this thesis. All requirements, except the aforementioned mass and volume requirements and the electrical interface requirement were met. The latter was not met, as the electrical design was left for future work.

The modularity of the propulsion systems was mainly found in the tank design, as all other components, with the obvious exception of the connecting rods, were identical across the three systems. This simplified the design that allowed for delivering three distinct total impulse levels, whilst maintaining the same performance in terms of thrust and specific impulse, significantly.

To conclude, the propulsion system architecture that would most effectively meet the system requirements consists, according to the outcome of all performed trade-offs, analyses, and considerations throughout this thesis, of:

- A printed circuit board.
- A cylindrical tank with flat endcaps.
- A PMD assembly consisting of a radial sponge and six vanes.
- A piping assembly that consists of a piping tray, propellant filter, thruster valve, pressure regulator, pressure relief valve, pressure and temperature transducer, fill/drain valve, and a thruster.
- A TunaCan add-on with a Zerlauts Z-93 coating on the surface that is in contact with the space environment.
- Three 0.5 W tank heaters that are attached to the cylindrical part of the propellant tank.
- Various mounting hardware, such as connecting rods, spacers, and fasteners.

The systems are designed in accordance with the CS14 CubeSat standard in terms of outer dimensions and locations of the mechanical interfaces. This allows for easy integration in any CubeSat that adhere to this standard.

Recommendations 14

This chapter presents recommendations for further research into the design of a VLM propulsion system. Some of these recommendations are repeated from the respective chapters, while others reflect general insights and realizations gained throughout the thesis and after completing the design process.

Thruster design
All propulsion systems dimensions and performance in this thesis are based on the thruster chip performance, which was calculated using ideal rocket theory. A detailed design, manufacturing, and testing of the VLM thruster (thruster chip and housing) is required to validate the system designs that are proposed in this chapter. The unknown thruster efficiency was partly compensated for by applying a 25% margin on the required total impulse for each system, which increases the required tank volume, associated tank height, and total wet mass. Knowing the true performance of the thruster could result in smaller propulsion systems, and more accurate performance figures in general. Moreover, the thermal analysis on the entire system can be improved significantly when knowing the thruster's efficiency and components of which it is constructed, as the most limiting component operating temperature can restrict the maximum burn duration.

Volume and power budgets
There were no volume and power budgets generated at the start of the design phase of this thesis, as it was difficult to find detailed power and volume breakdowns of electrothermal propulsion systems. The importance of generating such budgets, especially the volume budget as this was exceeded by both the 200 Ns and 400 Ns systems, can be seen in the propellant tank design chapter, where the height requirement (*PROP-TANK-03*) was taken to be equal to the maximum available height for each system due to the lack of a tank volume budget. This led to tank heights that were close to the available height. Generating these budgets at the start of the design phase could have yielded smaller systems. However, the tank heights are linked to the required total impulse, and therefore the required propellant mass. The latter was determined, again, using ideal rocket theory. Moreover, the required tank height is linked to the design envelope in terms of width and height, which is limited by the CS14 PCB design to 92 x 92 mm^2: significantly smaller than the initially anticipated 100 x 100 mm^2 area. Research into the feasibility of achieving the required total impulse levels of 200 Ns and 400 Ns within their allocated volume budget is required.

Not generating a power budget did not negatively impact the design of the systems, as all systems remained well below the maximum power level of 25 W. However, it is always good practise to generate such a budget at the start of the system design.

Tank design
Several tank shapes were considered in the design of the propellant tank, including a cylindrical tank with hemispherical and elliptical endcaps. These designs were eliminated before the start of the trade-off partly due to the additional required tank height required for the endcaps. However, it was not considered that these hemispherical and elliptical shapes would require a smaller wall thickness and would deflect less than the other shapes (rectangular and cylindrical tank with flat endcaps). The cylindrical tank with flat endcaps eventually won the trade-off, as it required the smallest shell mass and tank height. However, a finite element analysis showed the significant deflection and unforeseen bending stress within the skin. This required tank reinforcements and spacers between the tank and adjacent systems. Including the deflection of the tank shall, rather than just the shell mass and height, could yield a different outcome in terms of the optimal tank shape.

Propellant management device design
Several recommendations regarding the design of the PMD can be made. First, a more thorough slosh analysis is required, as a preliminary slosh analysis determined that propellant sloshing was not problematic, which contributed to the decision to eliminate the positive expulsion devices.

Second, the assembly of the PMD, and integration with the tank structure, must be investigated in more detail, as this was left for future work. The method of assembly and integration affects the (flow) performance of the PMD in a yet unknown way.

A third and final recommendation is linked to the previous one, as the effects of the tank reinforcements on the performance of the PMD, and the performance of the assembled PMD in general, must be verified through testing to ensure that propellant is led from the propellant pool towards the sponge under zero-g conditions. Moreover, the expulsion efficiency must be determined accurately, as this effects the achievable total impulse levels significantly. A drop-tower test is proposed, as this is more cost-effective than sending the PMD design into space.

Piping design

A shortage on time, combined with the wide variety of possible components, led to configuring a piping assembly without performing a proper trade-off for each component. It is recommended to perform a thorough trade-off for each component, as this can yield a more compact and lightweight design.

Finite element analyses

Several recommendations are proposed for further research regarding the structural analysis of the systems. First, it is recommended to use a software that is more suitable for performing such analyses, rather than the Linear Structural Validation library from the 3DExperience software. The use of such software was left for future work due to time constraints.

A second recommendation is to perform the structural analysis on the loaded tank, where all components, including the sponge and propellant, are modelled as separate elements. This will increase the accuracy of the analyses.

Third, it is recommended to perform a mesh convergence study for all performed analysis, rather than using the converged mesh dimensions that were found for the internal pressure analysis. The latter was done due to time constraints, and the physical limitation of a million mesh elements per simulation.

Fourth, it is recommended to perform the finite element analyses, including a vibrational analysis, on the three propulsion system assemblies. This will provide an insight in the dynamic behaviour of the systems, and will validate the structural integrity of the systems throughout their operational lifetime.

Thermal analysis

Several recommendations are proposed for the thermal analysis that was performed on the three propulsion systems in this thesis. The thermal analysis was performed not to precisely calculate component temperatures, but to get an insight into the temperature ranges and the need for thermal coatings and/or heaters. However, it is required to accurately determine the component temperatures for a range of missions to ensure proper functioning of the systems. Therefore, a first recommendation to perform a thermal analysis on the entire, non-simplified, propulsion systems using a thermal modelling software such as ESATAN or COMSOL. This will not only provide more accurate temperature levels, but also the temperature distributions within the components themselves.

A second recommendation is a continuation of the first one, namely to use a detailed, space-grade thruster design in the thermal analysis (the thruster design that was discussed at the start of this chapter). Both the temperature below which the thermal stability of 316L stainless steel is proven (equal to 650 °C) and the duration during which the stability and controllability of the technology demonstrator thruster was shown (equal to 3000 s) were used to determine that maximum burn duration of the thruster. However, the thruster consists of more parts than just the housing material, including the thruster chip, electronics, and seals. The most limiting maximum operating temperature of these materials is to be used to calculate the maximum burn duration of the thruster in terms of temperatures. Moreover, the interval in which the stability and controllability of the technology demonstrator was shown likely differs from that of the redesigned thruster. Testing of the redesigned thruster is required to verify this maximum burn duration in terms of the stability and controllability.

A third recommendation is the investigate not only more thermal coatings, but also the thermal stability of these coatings. The emissivity and absorptivity of coatings tend to change over time due to thermal cycling and the radiation environment of space.

A final recommendation is to investigate more missions, including ones with eclipses. Eclipses will introduce more frequent thermal cycling of the components, of which the effects must be investigated to ensure the structural integrity of the applied coatings, components and system assemblies throughout the entire mission duration.

Electrical system design

The electrical design of the propulsion systems was left for future work. This includes the PCB design, routing of the wiring, thrust programmes, and system health monitoring. These electrical system considerations must be designed in accordance with the CS14 electrical interface standard to ensure compatibility with all CubeSats that adhere to this standard (as outlined in requirement PROP-INT-3). The requirement on the supply voltage (requirement PROP-PERF-4) can be updated once the electrical system is fully designed.

References

[1] National Geographic Education. “USSR Launches Sputnik.” (2023), [Online]. Available: https://education.nationalgeographic.org/resource/ussr-launches-sputnik/.

[2] NanoAvionics. “How Many Satellites Are in Space?” (2023), [Online]. Available: https://nanoavionics.com/blog/how-many-satellites-are-in-space/.

[3] A. F. El-Sayed, “Rocket Propulsion,” in *Fundamentals of Aircraft and Rocket Propulsion*. London: Springer London, 2016, pp. 907–991, ISBN: 978-1-4471-6796-9. DOI: 10.1007/978-1-4471-6796-9_11. [Online]. Available: https://doi.org/10.1007/978-1-4471-6796-9_11.

[4] D. O’Reilly, G. Herdrich, and D. Kavanagh, *Electric Propulsion Methods for Small Satellites: A Review*, 2021.

[5] K. Lemmer, “Propulsion for cubesats,” *Acta Astronautica*, vol. 134, pp. 231–243, 2017.

[6] A. Cervone, D. C. Guerrieri, M. d. A. C. e Silva, and F. Leverone, “5.1 historical background and principle of operation,” *Space Micropropulsion for Nanosatellites: Progress, Challenges and Future*, p. 125, 2022.

[7] D. C. Guerrieri, M. d. A. C. e Silva, A. Cervone, and E. Gill, “Optimum Design of Low-Pressure Micro-Resistojet Applied to Nano-and Pico-Satellites,” in *ESA Space Propulsion 2018 Conference*, 2018, SP2018_00108.

[8] N. Hejmanowski, C. Woodruff, R. Burton, and D. Carroll, “CubeSat High Impulse Propulsion System (CHIPS),” Jun. 2015.

[9] CU Aerospace. “CHIPS - Data Sheet.” Accessed on February 27, 2024. (2024), [Online]. Available: https://cuaerospace.com/Portals/0/SiteContent/assets/PDF/CHIPS-Data-Sheet-230724-180.pdf.

[10] J. Asakawa *et al.*, “AQT-D: Demonstration of the Water Resistojet Propulsion System by the ISS-Deployed CubeSat,” 2019.

[11] J. Asakawa, K. Nishii, H. Koizumi, N. Takeda, R. Funase, and K. Komurasaki, “Engineering Model Development of the Water Resisojet Propulsion System: AQUARIUS for the SLS EM-1 CubeSat: EQUULEUS,” in *35th International Electric Propulsion Conference, Atlanta, USA, IEPC-2017-401*, 2017.

[12] Y. Nakagawa *et al.*, *On-orbit Demonstration of the Water Resistojet Propulsion System on Commercial 6U-Sat SPHERE-1 EYE*, Small Satellite Conference 2023, Presentation given at the Small Satellite Conference 2023, 2023.

[13] Y. Nakagawa *et al.*, “On-Orbit Demonstration of the Water Resistojet Propulsion System on Commercial 6U-Sat SPHERE-1 EYE,” 2023.

[14] Pale Blue Co. “Pale Blue Co. - Products.” Accessed on February 27, 2024. (2024), [Online]. Available: https://pale-blue.co.jp/product/.

[15] G. D. Krebs. “RAMPART.” (2024), [Online]. Available: https://space.skyrocket.de/doc_sdat/rampart.htm.

[16] G. Moore *et al.*, “3D Printing and MEMS Propulsion for the RAMPART 2U CUBESAT,” 2010.

[17] K. Palmer, Z. Li, and S. Wu, “In-Orbit Demonstration of a MEMS-based Micropropulsion system for Cubesats,” 2016.

[18] M. Robin, T. Brogan, and E. Cardiff, “An ammonia microresistojet (MRJ) for micro satellites,” in *44th AIAA/ASME/SAE/ASEE Joint Propulsion Conference & Exhibit*, 2008, p. 5288.

[19] Busek Co. Inc. “Micro Resistojet - Datasheet.” (2021), [Online]. Available: https://satcatalog.s3.amazonaws.com/components/979/SatCatalog_-_Busek_-_Micro_Resistojet_-_Datasheet.pdf?lastmod=20210710023805.

[20] V. Pallichadath *et al.*, “In-orbit micro-propulsion demonstrator for PICO-satellite applications,” *Acta Astronautica*, vol. 165, pp. 414–423, 2019, ISSN: 0094-5765. DOI: https://doi.org/10.1016/j.actaastro.2019.09.004. [Online]. Available: https://www.sciencedirect.com/science/article/pii/S0094576519312536.

[21] M. A. Silva, D. C. Guerrieri, H. van Zeijl, A. Cervone, and E. Gill, “Vaporizing liquid microthrusters with integrated heaters and temperature measurement,” *Sensors and Actuators A: Physical*, vol. 265, pp. 261–274, 2017.

[22] D. C. Guerrieri, M. A. Silva, H. Van Zeijl, A. Cervone, and E. Gill, “Fabrication and characterization of low pressure micro-resistojets with integrated heater and temperature measurement,” *Journal of Micromechanics and Microengineering*, vol. 27, no. 12, p. 125 005, 2017.

[23] J. Bouwmeester, *PQ9 and CS14 Electrical and Mechanical Subsystem Interface Standard for PocketQubes and CubeSats*, version V1, 2018. DOI: 10.34894/6MVBCZ. [Online]. Available: https://doi.org/10.34894/6MVBCZ.

[24] Z. Bobbitt. “Calculating P-Value for Correlation in Excel.” (2020), [Online]. Available: https://www.statology.org/p-value-correlation-excel/.

[25] Aurora Propulsion Technologies. “ARO - Aurora Resistojet One.” (2020), [Online]. Available: https://aurorapt.fi/downloads/ARO.pdf.

[26] E. O. Portal. “AQT-D (AQua Thruster-Demonstrator).” (2019), [Online]. Available: https://www.eoportal.org/satellite-missions/aqt-d#spacecraft.

[27] A. Cervone, B. Zandbergen, D. C. Guerrieri, M. De Athayde Costa e Silva, I. Krusharev, and H. Van Zeijl, “Green micro-resistojet research at Delft University of Technology: new options for Cubesat propulsion,” *CEAS Space Journal*, vol. 9, pp. 111–125, 2017.

[28] Satellite Catalog. “PBR-10 - Satellite Catalog.” (2024), [Online]. Available: https://www.satcatalog.com/component/pbr-10/.

[29] Satellite Catalog. “PBR-20 - Satellite Catalog.” (2024), [Online]. Available: https://www.satcatalog.com/component/pbr-20/.

[30] Pale Blue. “PBR-20 - Datasheet.” (2024), [Online]. Available: https://satcatalog.s3.us-west-1.amazonaws.com/components/1219/SatCatalog_-_Pale_Blue_-_PBR-20_-_Datasheet.pdf?lastmod=20240130084451.

[31] SteamJet Space Systems. “The Steam Thruster.” (2024), [Online]. Available: https://steamjet.space/#products.

[32] SteamJet Space Systems. “Steam TunaCan Thruster.” (2024), [Online]. Available: https://satsearch.co/products/steamjet-space-steam-tunacan-thruster.

[33] G. Quinsac and C. R. Koppel, “Electric Thruster Selection Criteria: a System Point of View,” in *SP2020+ 1_395, 7th Space Propulsion Conference*, vol. 1, 2020.

[34] ThrustMe. “Superheated Water Vapor Propulsion & Reaction Control System - Datasheet.” (2024), [Online]. Available: https://www.thrustme.fr/base/stock/ProductBannerFiles/16_20230727-thrustme-rcs.pdf.

[35] Bradford Space. “Comet - Water-based Propulsion for Small Satellites.” (2019), [Online]. Available: https://satcatalog.s3.amazonaws.com/components/897/SatCatalog_-_Bradford_Space_-_Comet-1000_-_Datasheet.pdf?lastmod=20210710014123.

[36] Bradford Space. “Comet-1000 - Satellite Catalog.” (2024), [Online]. Available: https://www.satcatalog.com/component/comet-1000/.

[37] S. Silvestrini, M. A. Silva, and A. Cervone, “Closed-Loop Thrust Control for Micropropulsion Systems,” in *68th International Astronautical Congress: Unlocking Imagination, Fostering Innovation and Strengthening Security, IAC 2017: Unlocking Imagination, Fostering Innovation and Strengthening Security*, IAF, 2017.

[38] M. A. Silva, D. C. Guerrieri, and A. Cervone. “Water as propellant for small spacecraft: first results of TU Delft’s thrusters.” (2017), [Online]. Available: https://spaceinstitute.tudelft.nl/water-as-propellant-for-small-spacecraft-first-results-of-tu-delfts-thrusters/.

[39] “12U/16U CubeSat Bus,” ISISPACE Group. (2024), [Online]. Available: https://www.isispace.nl/product/12u-16u-cubesat-bus/.

[40] A. Cervone, *Micro-Propulsion*. Delft University of Technology, Jun. 2022.

[41] J. R. Wertz, D. F. Everett, and J. J. Puschell, *Space mission engineering : the new SMAD* (Space technology library ; v. 28). Hawthorne, CA: Microcosm Press, 2011, ISBN: 9781881883159.

[42] D. C. Guerrieri, M. A. C. Silva, A. Cervone, and E. Gill, “Selection and Characterization of Green Propellants for Micro-Resistojets,” *Journal of Heat Transfer*, vol. 139, no. 10, p. 102 001, May 2017, ISSN: 0022-1481. DOI: 10.1115/1.4036619. [Online]. Available: https://doi.org/10.1115/1.4036619.

[43] A. Kramer, “Orbit control of a very small satellite using electric propulsion,” Ph.D. dissertation, Julius-Maximilians-Universitat Wurzburg Graduate School of Science and Technology, 2021.

[44] K. V. Mani, F. Topputo, A. Cervone, *et al.*, “Dual chemical-electric propulsion systems design for interplanetary cubesats,” in *Proceedings of the ESA Space Propulsion Conference, Seville, Spain*, 2018, pp. 14–18.

[45] P. Linstrom and W. Mallard, *NIST Chemistry Webbook*, NIST Standard Reference Database No. 69, Accessed: April 25, 2024, Gaithersburg, MD, 2023. [Online]. Available: http://webbook.nist.gov.

[46] J. Hart. “Hazardous materials identification.” (Nov. 2021), [Online]. Available: https://www.nfpa.org/news-blogs-and-articles/blogs/2021/11/05/hazardous-materials-identification.

[47] Airgas Inc. “Material Safety Data Sheet - Ammonia.” (Jan. 2019), [Online]. Available: https://www.airgas.com/msds/001003.pdf.

[48] Airgas Inc. “Material Safety Data Sheet - Butane.” (Jan. 2020), [Online]. Available: https://www.airgas.com/msds/001007.pdf.

[49] Airgas Inc. “Material Safety Data Sheet - R134a.” (Feb. 2021), [Online]. Available: https://www.airgas.com/msds/001055.pdf.

[50] Airgas Inc. “Material Safety Data Sheet - R236fa.” (Apr. 2017), [Online]. Available: https://www.airgas.com/msds/001163.pdf.

[51] B. Zandbergen, *Thermal Rocket Propulsion*. Delft University of Technology, Sep. 2022.

[52] A. E. S. Nosseir, A. Cervone, and A. Pasini, “Modular Impulsive Green Monopropellant Propulsion System (MIMPS-G): For CubeSats in LEO and to the Moon,” *Aerospace*, vol. 8, no. 6, 2021, ISSN: 2226-4310. DOI: 10.3390/aerospace8060169. [Online]. Available: https://www.mdpi.com/2226-4310/8/6/169.

[53] B. Zandbergen, *Spacecraft (Bus) Design and Sizing*. Delft University of Technology, 2020.

[54] I. Krusharev, R. Poyck, Q. Bellini, B. Zandbergen, and A. Cervone, “Cubesat Micro-Propulsion Systems for Extending the Capabilities of Academic Projects,” Jan. 2014.

[55] Parker. “Selecting and Applying Accumulators.” (2013), [Online]. Available: http://www.hydraulicindustrial.com/parker/catalogs/parkercatalog_acc-Accumulators-SelectionGuide.pdf.

[56] M. Micci and A. Ketsdever, *Micropropulsion for Small Spacecraft*. American Institute of Aeronautics and Astronautics, 2000, ISBN: 1-56347-448-4.

[57] Space X. “Falcon User’s Guide.” (Sep. 2021), [Online]. Available: https://www.spacex.com/media/falcon-users-guide-2021-09.pdf.

[58] O. A. Alduchov and R. E. Eskridge, “Improved Magnus form approximation of saturation vapor pressure,” *Journal of Applied Meteorology (1988-2005)*, pp. 601–609, 1996.

[59] Aerospace Specification Metals Inc. “Aluminium 6061-T6.” (2024), [Online]. Available: https://asm.matweb.com/search/SpecificMaterial.asp?bassnum=MA6061t6.

[60] Navstar Steel Corporation. “6061 T6 Aluminium Plate.” (2024), [Online]. Available: https://www.navstarsteel.com/6061-t6-aluminium-plate.html.

[61] Chalco Aluminum. “6061 Aluminum Tube.” (2024), [Online]. Available: https://www.chalcoaluminum.com/product/aluminum-tube/6061-aluminum-tube/.

[62] Aerospace Specification Metals Inc. “AISI Type 304L Stainless Steel.” Accessed: 2024-07-01. (2024), [Online]. Available: https://asm.matweb.com/search/SpecificMaterial.asp?bassnum=MQ304L.

[63] Octal Metals. “04/304L Stainless Steel Plate, Sheet & Coil.” Accessed: 2024-07-01. (2024), [Online]. Available: https://www.octalmetals.com/304-stainless-steel-plate-sheet/#:~:text=Thickness%20Range%3A%200.02mm%20%2D%204mm%2C%204.5mm%20%2D%20100mm..

[64] Roopam Steel. “ASTM A249 TP 304L STAINLESS STEEL SEAMLESS BOILER TUBE.” Accessed: 2024-07-01. (2024), [Online]. Available: https://www.roopamsteel.com/astm-a269-stainless-steel-304l-tube.html.

[65] Aerospace Specification Metals Inc. “Titanium Ti-6Al-4V (Grade 5), Annealed.” Accessed: 2024-07-01. (2024), [Online]. Available: https://asm.matweb.com/search/SpecificMaterial.asp?bassnum=MTP641.

[66] Pearl Overseas. “Grade 5 Titanium Sheet.” Accessed: 2024-07-01. (2024), [Online]. Available: https://www.pearloverseas.co.in/grade5-titanium-sheet-plate.html.

[67] Continental Steel Co. “Titanium alloy pipe.” Accessed: 2024-07-01. (2024), [Online]. Available: https://www.continental-steel.com/alloy-seamless-pipe/Titanium-alloy-pipe.html.

[68] Aerospace Specification Metals Inc. “Special Metals INCONEL® Alloy 718.” Accessed: 2024-07-01. (2024), [Online]. Available: https://asm.matweb.com/search/SpecificMaterial.asp?bassnum=NINC34.

[69] Hitesh Steel. “Inconel 718 Plate.” Accessed: 2024-07-01. (2024), [Online]. Available: https://www.hiteshsteel.com/inconel-alloy-718-plate-sheet-strip-coil.html#thickness.

[70] Fastwell Engineering Pvt Ltd. “Alloy 718 Seamless Tubing Suppliers.” Accessed: 2024-07-01. (2024), [Online]. Available: https://www.fastwell.in/inconel-718-tube.html.

[71] R. Porter and H. Stanford, “Propellant expulsion in unmanned spacecraft,” *SAE Transactions*, pp. 93–126, 1965.

[72] PMD Technology. “PMD Technology.” Accessed: 2024-07-05. (2011), [Online]. Available: http://www.pmdtechnology.com/Index.html.

[73] J. Faupel, “Pressure vessels of noncircular cross section (commentary on New Rules for ASME Code),” *Journal of Pressure Vessel Technology*, pp. 255–267, 1979. DOI: https://doi.org/10.1115/1.3454631.

[74] I. G. Moneva, *Design and Structural Analysis of the Propellant Tank for a Water Resistojet*, http://resolver.tudelft.nl/uuid:d61333e4-8450-4b52-b15c-bd38b3ad1673, Jul. 2025.

[75] *Boiler and Pressure Vessel Code: An International Code - Section VIII: Rules for Construction of Pressure Vessels*, ASME, Jul. 2023. [Online]. Available: https://infosolda.com.br/wp-content/uploads/2024/02/ASME-Sec-VIII-Div1-2023.pdf.

[76] S. Mattson, "20 - Welding of aluminium," in *Welding Processes Handbook (Second Edition)*, ser. Woodhead Publishing Series in Welding and Other Joining Technologies, K. Weman, Ed., Second Edition, Woodhead Publishing, 2012, pp. 207–220, ISBN: 978-0-85709-510-7. DOI: https://doi.org/10.1533/9780857095183.207. [Online]. Available: https://www.sciencedirect.com/science/article/pii/B9780857095107500203.

[77] S. Ahmed and P. Saha, "Selection of optimal process parameters and assessment of its effect in micro-friction stir welding of AA6061-T6 sheets," *The International Journal of Advanced Manufacturing Technology*, vol. 106, no. 7-8, pp. 3045–3061, Jan. 2020. DOI: 10.1007/s00170-019-04840-6.

[78] M. C. Santos, A. R. Machado, W. F. Sales, M. A. S. Barrozo, and E. O. Ezugwu, "Machining of aluminum alloys: A review," *The International Journal of Advanced Manufacturing Technology*, vol. 86, no. 9-12, pp. 3067–3080, 2016. DOI: 10.1007/s00170-016-8431-9.

[79] G.-L. Chern and Y.-C. Chang, "Using two-dimensional vibration cutting for micro-milling," *International Journal of Machine Tools and Manufacture*, vol. 46, no. 6, pp. 659–666, 2006, ISSN: 0890-6955. DOI: https://doi.org/10.1016/j.ijmachtools.2005.07.006. [Online]. Available: https://www.sciencedirect.com/science/article/pii/S0890695505001604.

[80] A. Mehta *et al.*, "Additive manufacturing and mechanical properties of the dense and crack free Zr-modified aluminum alloy 6061 fabricated by the laser-powder bed fusion," *Additive Manufacturing*, vol. 41, p. 101 966, 2021, ISSN: 2214-8604. DOI: https://doi.org/10.1016/j.addma.2021.101966. [Online]. Available: https://www.sciencedirect.com/science/article/pii/S2214860421001317.

[81] B. Chaudhary, N. K. Jain, J. Murugesan, and V. Patel, "Friction stir powder additive manufacturing of Al 6061 alloy: Enhancing microstructure and mechanical properties by reducing thermal gradient," *Journal of Materials Research and Technology*, vol. 26, pp. 1168–1184, 2023, ISSN: 2238-7854. DOI: https://doi.org/10.1016/j.jmrt.2023.07.270. [Online]. Available: https://www.sciencedirect.com/science/article/pii/S2238785423017994.

[82] Y. M. Ahmed, K. S. M. Sahari, and M. Ishak, "Welding of titanium (Ti-6Al-4V) alloys: a review," in *Proceedings National Graduate Conference, Universiti Tenaga Nasional, Putrajaya Campus*, 2012, pp. 8–10.

[83] I. A. Daniyan, A. Adeodu, K. Mpofu, B. Ramatsetse, and R. Muvunzi, "Enhancing the machinability of titanium alloy (TI6Al4V): A comprehensive review of literature," *Advances in Manufacturing Technologies*, pp. 4–21, 2022.

[84] A. Attanasio, M. Gelfi, A. Pola, E. Ceretti, and C. Giardini, "Influence of material microstructures in micromilling of Ti6Al4V alloy," *Materials*, vol. 6, no. 9, pp. 4268–4283, 2013.

[85] Z. Wu, S. P. Narra, and A. Rollett, "Exploring the fabrication limits of thin-wall structures in a laser powder bed fusion process," *The International Journal of Advanced Manufacturing Technology*, vol. 110, no. 1, pp. 191–207, 2020.

[86] F. de Oliveira Campos, A. C. Araujo, A. L. Jardini Munhoz, and S. G. Kapoor, "The influence of additive manufacturing on the micromilling machinability of Ti6Al4V: A comparison of SLM and commercial workpieces," *Journal of Manufacturing Processes*, vol. 60, pp. 299–307, 2020, ISSN: 1526-6125. DOI: https://doi.org/10.1016/j.jmapro.2020.10.006. [Online]. Available: https://www.sciencedirect.com/science/article/pii/S1526612520306745.

[87] J. T. Tharappel and J. Babu, "Welding processes for Inconel 718-A brief review," in *IOP Conference Series: Materials Science and Engineering*, IOP Publishing, vol. 330, 2018, p. 012 082.

[88] K. Mahesh, J. T. Philip, S. Joshi, and B. Kuriachen, "Machinability of Inconel 718: A critical review on the impact of cutting temperatures," *Materials and Manufacturing Processes*, vol. 36, no. 7, pp. 753–791, 2021.

[89] V. Tepponen, S. Westman, P. Nyamekye, and I. Poutiainen, "Optimized Inconel 718 pressure vessel manufactured with laser powder bed fusion," in *IOP Conference Series: Materials Science and Engineering*, IOP Publishing, vol. 1296, 2023, p. 012 019.

[90] J. W. Hartwig, "Propellant management devices for low-gravity fluid management: past, present, and future applications," *Journal of Spacecraft and Rockets*, vol. 54, no. 4, pp. 808–824, 2017.

[91] S. De Brock, R. Grove, R. Sloma, D. Balzer, Y. BRILL, and G. Yankura, "A survey of current developments in surface tension devices for propellant acquisition," *Journal of Spacecraft and Rockets*, vol. 8, no. 2, pp. 83–98, 1971.

[92] J. R. Roberts, E. R. Basurto, and P.-Y. Chen, *Slosh design handbook I*. National Aeronautics and Space Administration, 1966, vol. 1.

[93] L. Wang, X. Zhang, Y. Yun, J. Liu, W. Li, and B. Huang, “Numerical simulation of the reorientation process under different conditions in a vane-type surface tension propellant tank,” *Microgravity Science and Technology*, vol. 34, no. 3, p. 37, 2022.

[94] M. Debreceni, D. Jaekle, and T. Kuo, “Development of a titanium propellant tank,” in *39th AIAA/ASME/SAE/ASEE Joint Propulsion Conference and Exhibit*, 2003, p. 4604.

[95] *CubeSat Design Specification*, Rev 14.1, California Polytechnic State University, Feb. 2022.

[96] C. A. Carter and E. G. Lightsey, “CubeSat Slosh Dynamics and Its Effect on Precision Attitude Control for the VISORS Distributed Spacecraft Telescope Mission,” *Atlanta: Georgia Tech*, 2020.

[97] Y. X. Ni, B. Feng, J. Wang, X. Lu, S. Qu, and J. Weng, “Decyl bis phosphonate–protein surface modification of Ti–6Al–4V via a layer-by-layer technique,” *Journal of materials science*, vol. 44, pp. 4031–4039, 2009.

[98] F. T. Dodge *et al.*, *The new" dynamic behavior of liquids in moving containers"*. Southwest Research Inst. San Antonio, TX, 2000.

[99] R. H. Lee, A. Bauer, M. D. Killingsworth, T. Lilly, J. Duncan, and A. Ketsdever, “Free-molecule-microresistojet performance using water propellant for nanosatellite applications,” *Journal of Spacecraft and Rockets*, vol. 45, no. 2, pp. 264–269, 2008.

[100] R. Sun, W. Hu, and Z. Duan, “Prediction of nitrogen solubility in pure water and aqueous NaCl solutions up to high temperature, pressure, and ionic strength,” *Journal of solution chemistry*, vol. 30, pp. 561–573, 2001.

[101] G. M. Huggins *et al.*, “Development of a CubeSat-scale green monopropellant propulsion system for NASA’s lunar flashlight mission,” in *AIAA Scitech 2021 Forum*, 2021, p. 1976.

[102] V. G. Levich, *Physicochemical Hydrodynamics*. Prentice Hall, 1962.

[103] D. E. Jaekle, “Propellant Management Device Conceptual Design and Analysis: Sponges,” in *AIAA 29th Joint Propulsion Conference and Exhibit*, Jun. 1993.

[104] M. Lazzarin, F. Barato, N. Bellomo, F. Moretto, D. Paulon, and D. Rondini. “SPONGE - Student Experiment Documentation.” Accessed: 2024-09-20. (Sep. 2010), [Online]. Available: https://rexusbexus.net/wp-content/uploads/2015/07/RX09_SPONGE_SED-v5_0-2010Sep07.pdf.

[105] “The engineering toolbox.” (2001), [Online]. Available: https://www.engineeringtoolbox.com/.

[106] A. Steckel, “Integrated Propellant Storage and Feed System: FY18 Engineering Research Technical Investment Program,” Massachusetts Institute of Technology, Technical Report, 2019.

[107] J. W. Hartwig, *Liquid acquisition devices for advanced in-space cryogenic propulsion systems*. Case Western Reserve University, 2014.

[108] A. De Quero, P. Pontelandolfo, and R. Putzu, “Microgravity PMD investigations by miniaturization of the test sample,” in *51st AIAA/SAE/ASEE Joint Propulsion Conference*, 2015, p. 4149.

[109] J. W. Hartwig, *Liquid acquisition devices for advanced in-space cryogenic propulsion systems*. Case Western Reserve University, 2014.

[110] D. JAEKLE JR, “Propellant management device conceptual design and analysis-Vanes,” in *27th Joint Propulsion Conference*, 1991, p. 2172.

[111] *Air Force Space Command Manual 91-710*, Volume 3, California Polytechnic State University, Jul. 2004.

[112] K. ACAMPORA and H. Wichmann, “Component development for micro propulsion systems,” in *28th Joint Propulsion Conference and Exhibit*, 1992, p. 3255.

[113] The Lee Company. “Pressure Relief Valves.” (2025), [Online]. Available: https://www.theleeco.com/industries/space/products/pressure-relief-valves/.

[114] The Lee Company, *Technical Hydraulic Handbook*, Apr. 2024. [Online]. Available: https://www.theleeco.com/uploads/2024/04/THH-12th-Edition-2020_4.24.pdf#page=332.

[115] EFE, *Datasheet - Sub-Miniature Pressure and Temperature Transducer - PCM127*. [Online]. Available: https://www.efe-sensor.com/product/pcm120/.

[116] Swagelok, *Filters*, 2022. [Online]. Available: https://www.swagelok.com/downloads/webcatalogs/en/ms-01-92.pdf.

[117] Beswick Engineering, *Miniature Fluid Power Products*, May 2021. [Online]. Available: https://www.beswick.com/wp-content/uploads/2021/05/Beswick-Catalog-119-Interactive-Version_High-Res.pdf.

[118] Swagelok, *Gaugeable Tube Fittings and Adapter Fittings*, May 2023. [Online]. Available: https://www.swagelok.com/downloads/webcatalogs/en/ms-01-107.pdf.

[119] Swagelok, *Tubing Data*, Oct. 2023. [Online]. Available: https://www.swagelok.com/downloads/webcatalogs/en/ms-01-107.pdf.

[120] Structural Engineering Resources. “Galvanic Corrosion.” (Jul. 2024), [Online]. Available: https://structx.com/Material_Properties_001.html.

[121] Industrial Specialties Manufacturing. “316L Stainless Steel Chemical Compatibility Chart.” (Oct. 2023), [Online]. Available: https://marketing.industrialspec.com/acton/attachment/30397/f-003a/1/-/-/-/-/316l-stainless-steel-chemical-compatibility-from-ism.pdf.

[122] H. Wilson. “Equivalent Lengths of Pipe Fittings and Valves.” (2024), [Online]. Available: https://www.katmarsoftware.com/articles/pipe-fitting-equivalent-length.htm.

[123] The Lee Company, *IMH Handbook of Hydraulics and Pneumatics*, Jul. 2020. [Online]. Available: https://www.ddp.nl/wp-content/uploads/2020/07/Industrial-Microhydraulics-8th-Edition-2020.pdf.

[124] Beswick Engineering, *Combined Data PRD3*, May 2019. [Online]. Available: https://www.beswick.com/wp-content/uploads/2019/05/PRD3_Flow_Curve.pdf.

[125] R. Patel *et al.*, “A Transdisciplinary Approach for Analyzing Stress Flow Patterns in Biostructures,” *Mathematical and Computational Applications*, vol. 24, no. 2, p. 47, 2019.

[126] Dassault Systemes. “3DEXPERIENCE User Assistance.” (2024), [Online]. Available: https://www.3ds.com/support/documentation/user-guides.

[127] D. Anantha Raman, *Thermal environment and design considerations of the Foresail-2 satellite mission*, 2023.

[128] I. U. Balbin and N. van der Pas, “Spacecraft Thermal Analysis,” University Lecture, Slides, May 2023.

[129] ECSS, *Thermal design handbook - Part 1: View factors*. ESA Requirements and Standards Division, Dec. 2011.

[130] J. Howell, *A Catalog of Radiation Configuration Factors*, https://www.thermalradiation.net/tablecon.html, 1982.

[131] ECSS, *Thermal design handbook - Part 5: Structural Materials: Metallic and Composite*. ESA Requirements and Standards Division, Dec. 2011.

[132] J. H. Henninger, “Solar absorptance and thermal emittance of some common spacecraft thermal-control coatings,” NASA, Tech. Rep., 1984.

[133] The Engineering ToolBox, *Radiation - Surface Emissivity Coefficients*, https://www.engineeringtoolbox.com/radiation-heat-emissivity-d_432.html, 2003.

[134] Aerospace Specification Metals Inc. “AISI Type 316L Stainless Steel, annealed bar.” Accessed: 2024-11-01. (2024), [Online]. Available: https://asm.matweb.com/search/SpecificMaterial.asp?bassnum=mq316q.

[135] The Engineering ToolBox, *Water - Specific Heat vs. Temperature*, https://www.engineeringtoolbox.com/specific-heat-capacity-water-d_660.html, 2004.

[136] S. Wang, J. Li, Y. Cao, B. Gao, Q. Mao, and Y. Li, “Thermal stability and tensile property of 316L stainless steel with heterogeneous lamella structure,” *Vacuum*, vol. 152, pp. 261–264, 2018, ISSN: 0042-207X. DOI: https://doi.org/10.1016/j.vacuum.2018.03.040. [Online]. Available: https://www.sciencedirect.com/science/article/pii/S0042207X18301398.

[137] EDCOR. “Printed Circuit Boards (PCB).” (2024), [Online]. Available: https://edcorusa.com/pages/printed-circuit-boards-pcb?srsltid=AfmBOorYKQ8YJN6XVIdM0e_9vOFpfxE1fz_HTZKGyIUy-UofgrGf71xU.

[138] ISISpace Group. “ISIS Advised Envelope - 3-Unit CubeSat Dimensions.” Drawing. (Sep. 2014), [Online]. Available: https://www.isispace.nl/wp-content/uploads/2015/12/ISIS.STS_.0.1.003-RevB-Sheet1-1-3U-CubeSat-Dimensions-A0.pdf.

[139] Zoppas Industries. “Flexible Heater for Space Market (Satellite - Vehicle - Launcher and Ground Segment).” (2024), [Online]. Available: https://satsearch.co/products/zoppas-industries-space-flexible-heater-polymide-fep.

[140] Massachusetts Institute of Technology (MIT). “Material Property Database - Polyimide.” (2024), [Online]. Available: https://www-mit-edu.tudelft.idm.oclc.org/~6.777/matprops/polyimide.htm.

[141] Extreme Bolt. “Lock Nuts.” (2024), [Online]. Available: https://www.extreme-bolt.com/lock-nuts.html.

Finite Element Analysis Figures A

A.1 Internal Pressure Analysis

A.1.1 400 Ns System

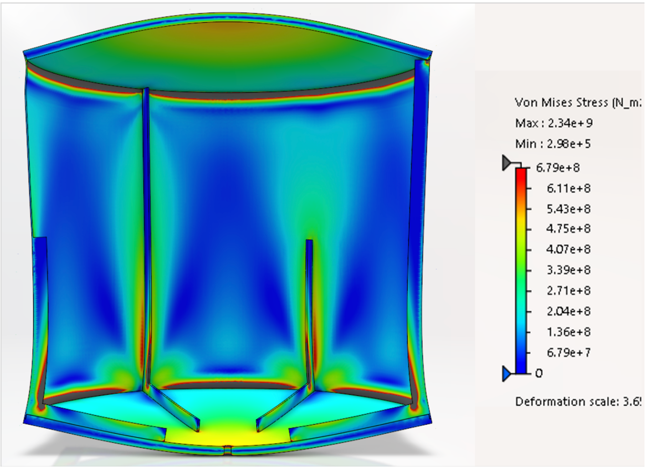

Figure A.1: Stress within the 400 Ns tank structure as a result of a 10 bar internal pressure.

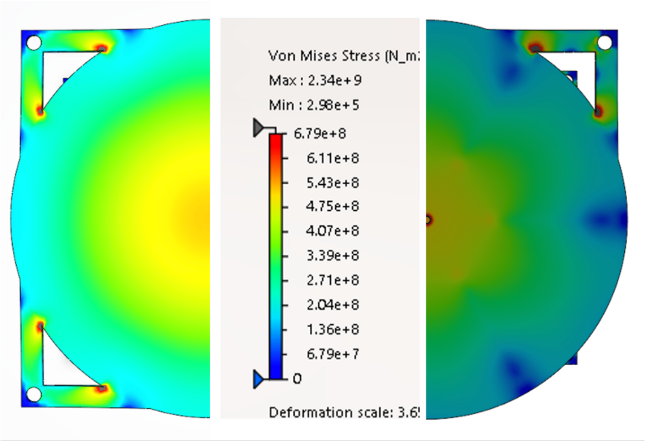

Figure A.2: Stress within the 400 Ns tank top and bottom endcaps as a result of a 10 bar internal pressure.

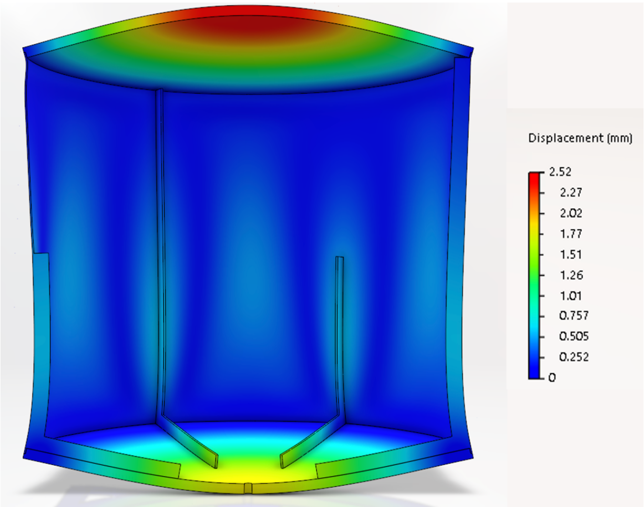

Figure A.3: Displacement of the 400 Ns tank structure as a result of a 10 bar internal pressure.

A.1.2 600 Ns System

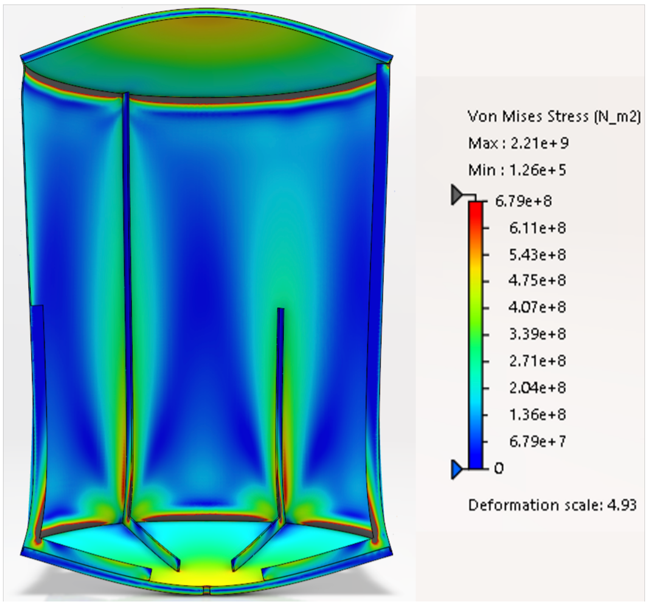

Figure A.4: Stress within the 600 Ns tank structure as a result of a 10 bar internal pressure.

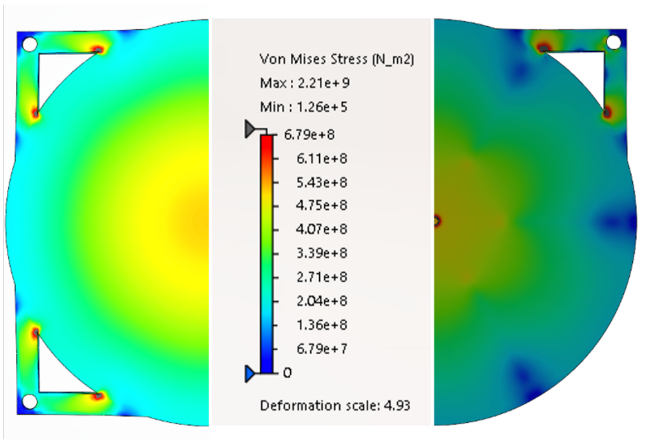

Figure A.5: Stress within the 600 Ns top and bottom endcaps as a result of a 10 bar internal pressure.

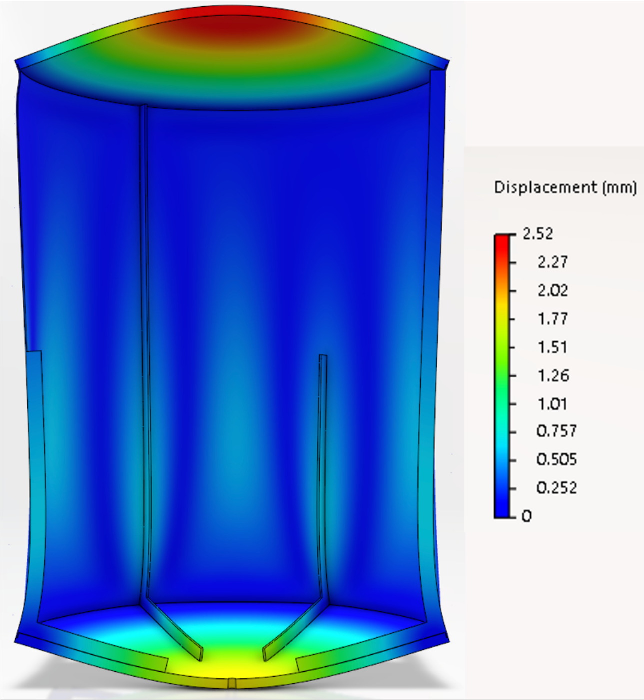

Figure A.6: Displacement of the 600 Ns tank structure as a result of a 10 bar internal pressure.

A.2 Tank Redesign for Internal Pressure Load

A.2.1 400 Ns System

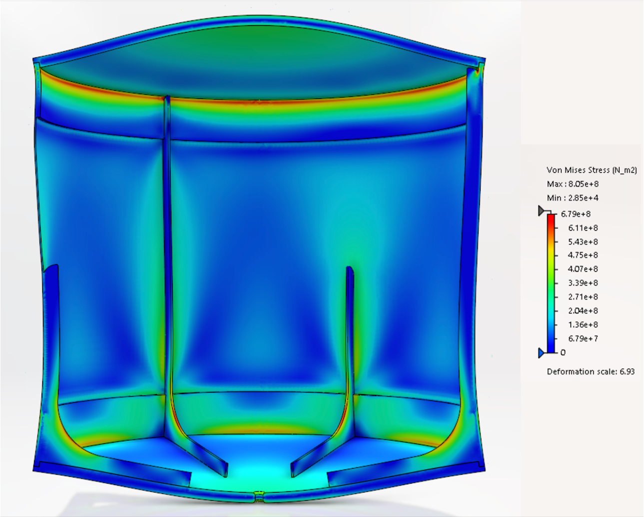

Figure A.7: Stress within the redesigned 400 Ns tank structure as a result of a 10 bar internal pressure.

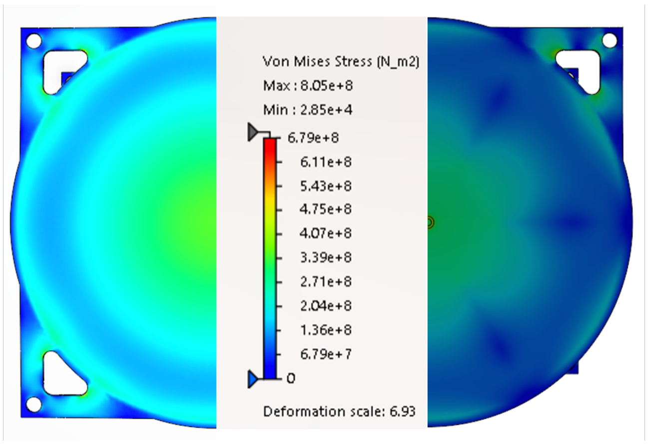

Figure A.8: Stress within the redesigned 400 Ns top and bottom endcaps as a result of a 10 bar internal pressure.

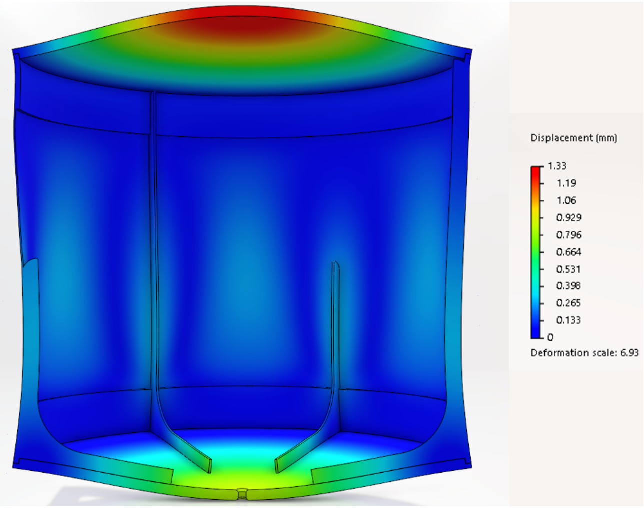

Figure A.9: Displacement of the redesigned 400 Ns tank structure as a result of a 10 bar internal pressure.

A.2.2 600 Ns System

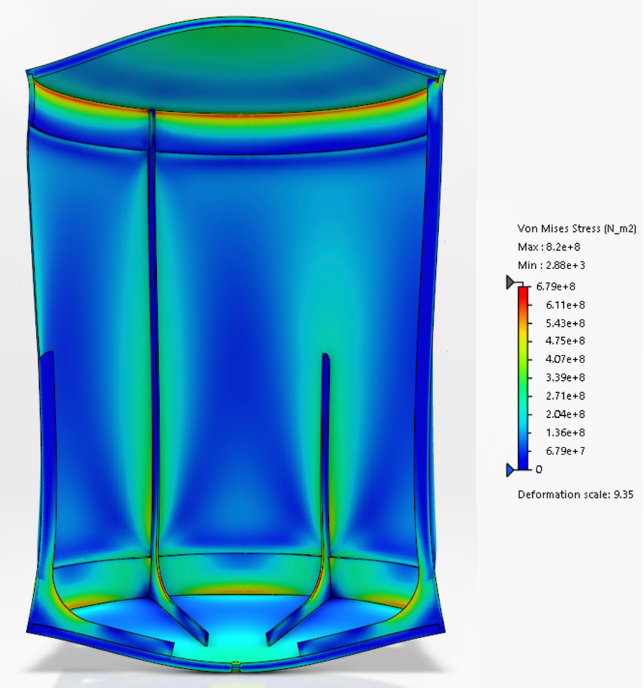

Figure A.10: Stress within the redesigned 600 Ns tank structure as a result of a 10 bar internal pressure.

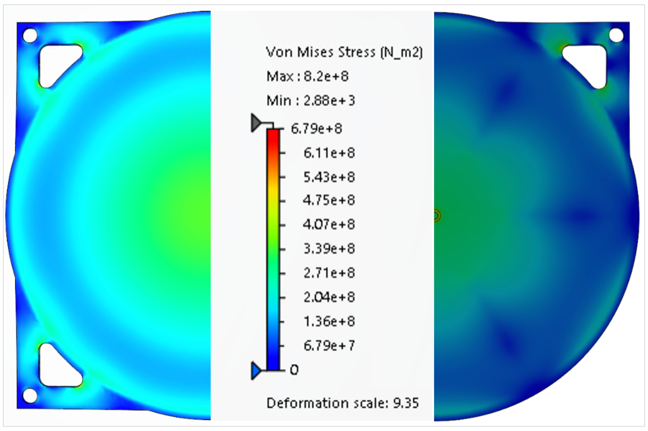

Figure A.11: Stress within the redesigned 600 Ns top and bottom endcaps as a result of a 10 bar internal pressure.

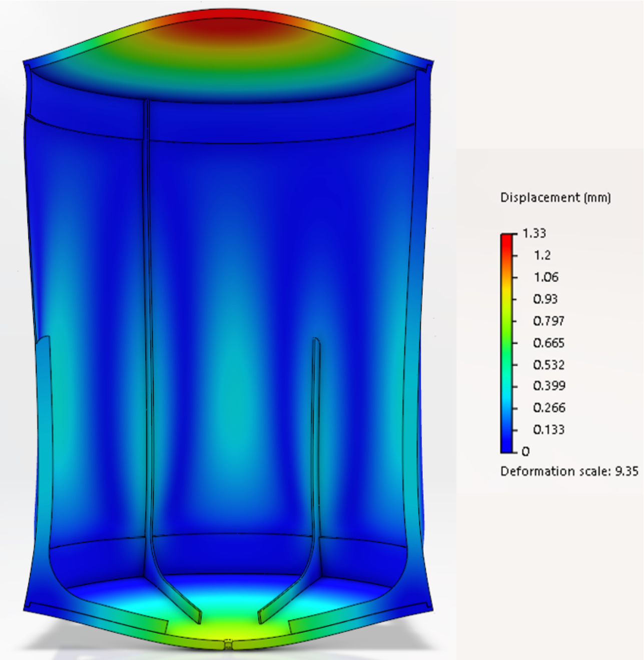

Figure A.12: Displacement of the redesigned 600 Ns tank structure as a result of a 10 bar internal pressure.

A.3 Launch Load Analysis

A.3.1 400 Ns System

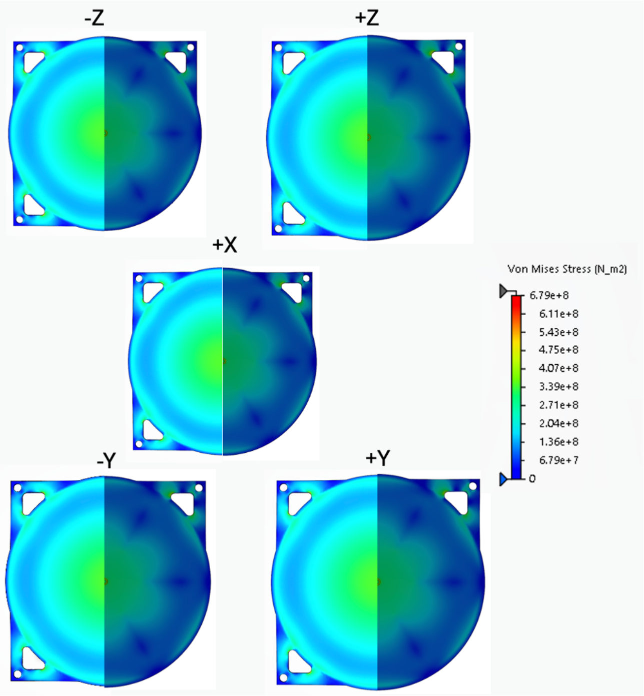

Figure A.13: Von Mises stress distribution in the top (left) and bottom (right) endcaps of the 400 Ns system under 8.5g acceleration.

A.3.2 600 Ns System

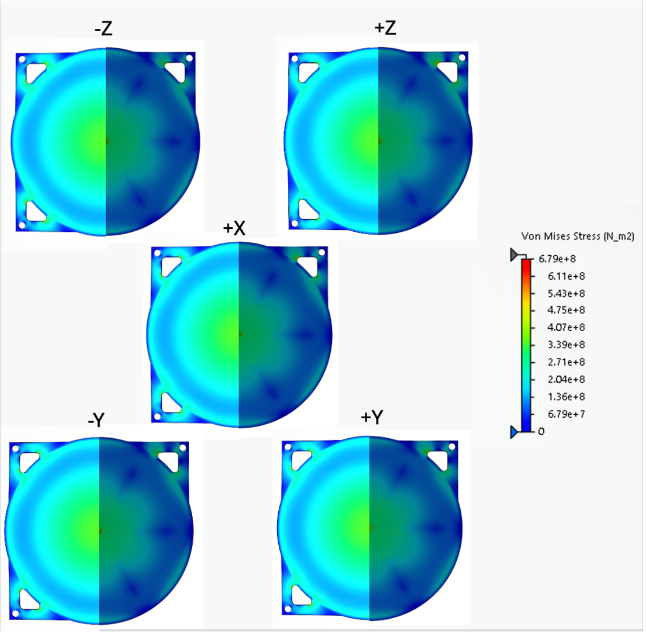

Figure A.14: Von Mises stress distribution in the top (left) and bottom (right) endcaps of the 600 Ns system under 8.5g acceleration.

A.4 Buckling Analysis

A.4.1 200 Ns System

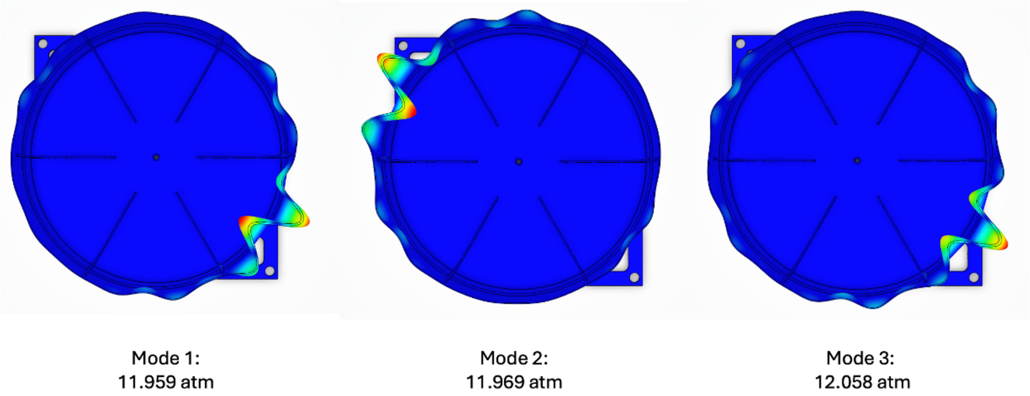

Figure A.15: First three buckling modes and its associated critical buckling load (in atm) of the redesigned 200 Ns tank structure.

A.4.2 400 Ns System

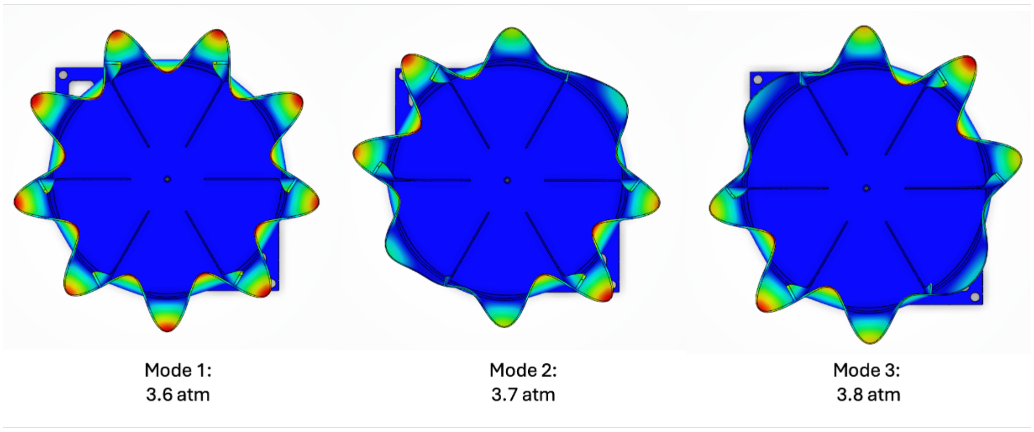

Figure A.16: First three buckling modes and its associated critical buckling load (in atm) of the redesigned 400 Ns tank structure.

A.4.3 600 Ns System

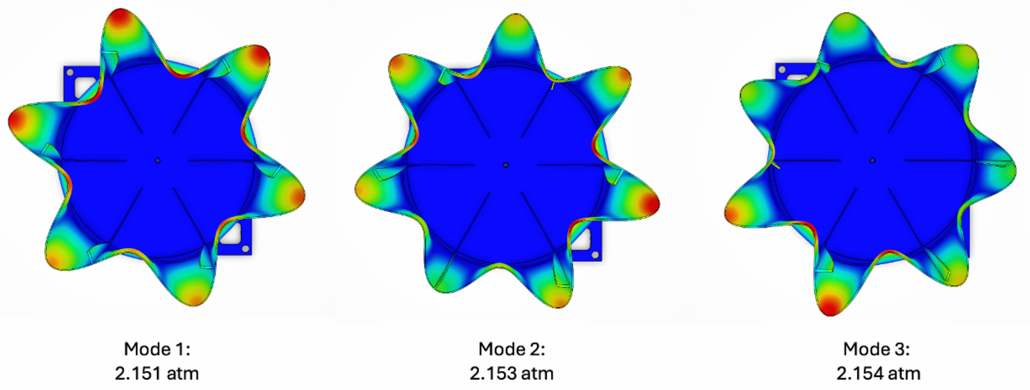

Figure A.17: First three buckling modes and its associated critical buckling load (in atm) of the redesigned 600 Ns tank structure.

A.5 Natural Frequency Analysis

A.5.1 200 Ns System

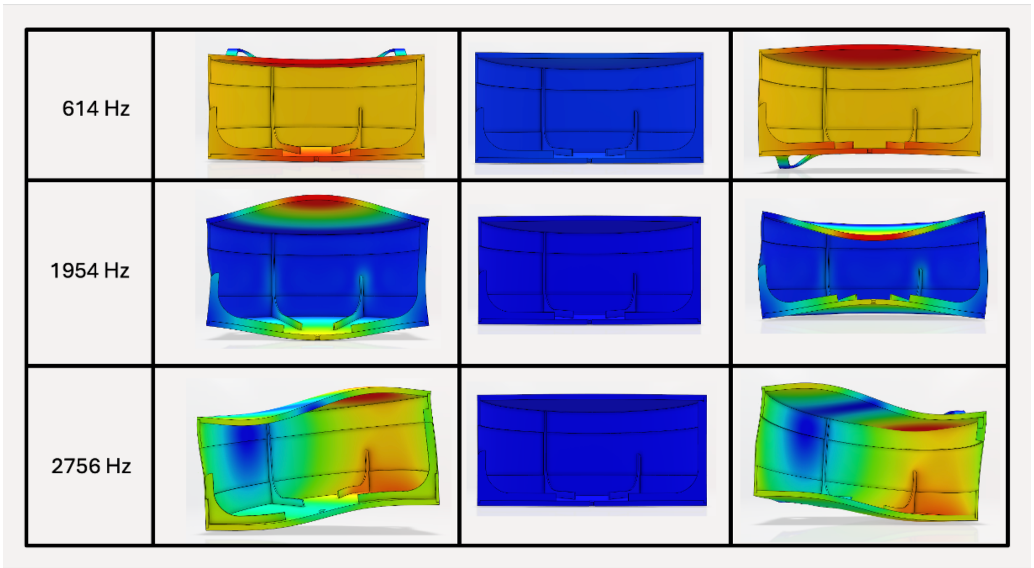

Figure A.18: First three vibrational modes of the redesigned 200 Ns tank structure.

A.5.2 400 Ns System

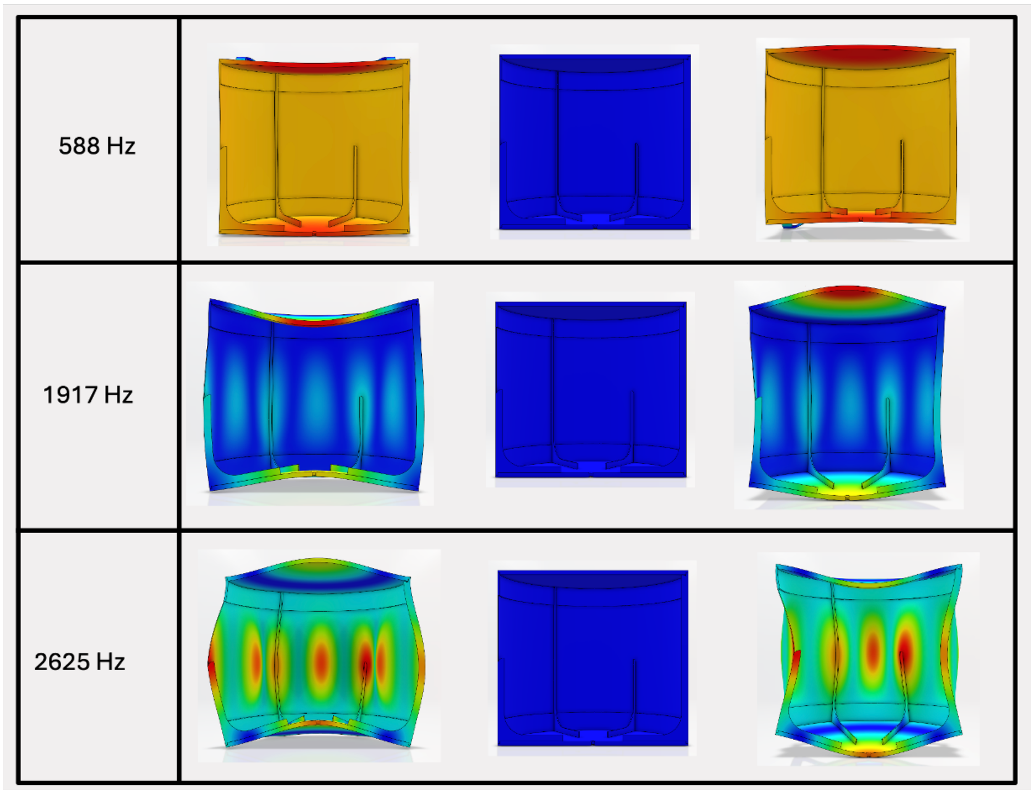

Figure A.19: First three vibrational modes of the redesigned 400 Ns tank structure.

A.5.3 600 Ns System

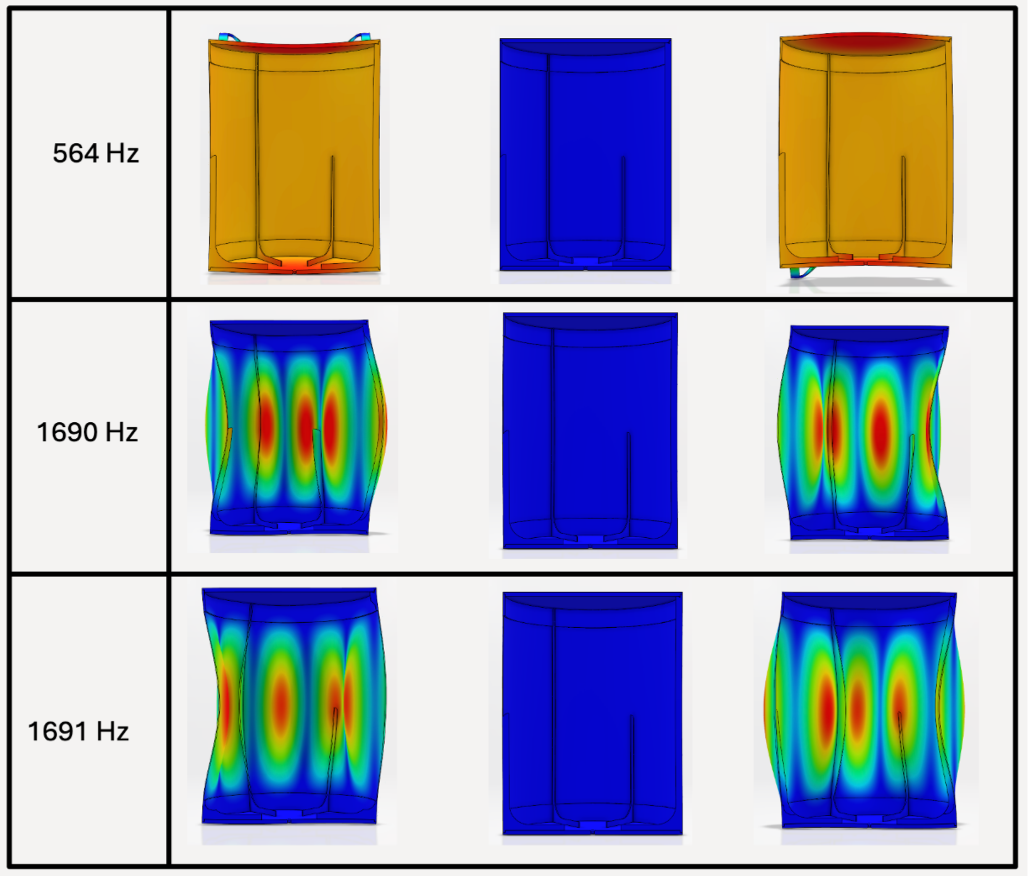

Figure A.20: First three vibrational modes of the redesigned 600 Ns tank structure.

B

Detailed Thermal Network

Figure B.2 shows a more detailed thermal network representation of the propulsion systems, where the additional nodes represent the TunaCan add-on (node 0), the spacecraft bus (node 6), and the connection rods (node 7). The individual piping components are excluded from this network and represented still as a single node (node 2) that combines the piping components and the piping tray itself. In reality, each piping component will have a conductive and radiative link with the piping tray, and a radiative link to the tank's bottom endcap (node 3). Moreover, the internal volume of the piping will have a radiative, conductive and convective links with the propellant that flows through them. Showing all these individual thermal links within one large network will clutter the page, and result in a less clear overview of the thermal exchanges. The legend, where the description of each node and thermal link is given, is shown in Figure B.1.

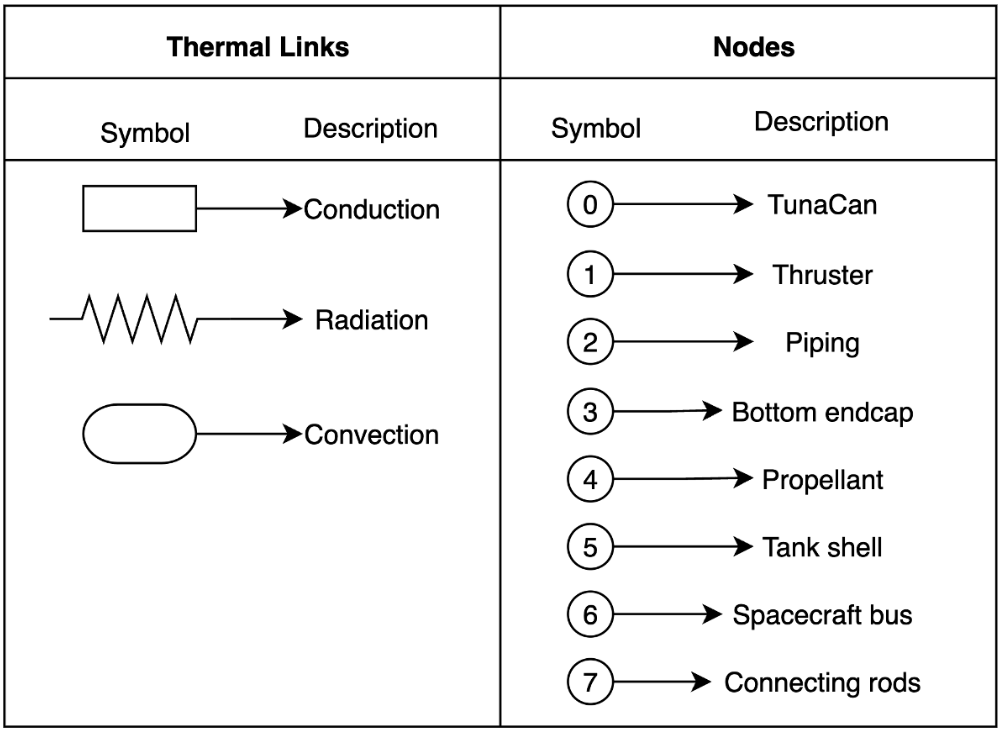

Figure B.1: Legend for Figure B.2.

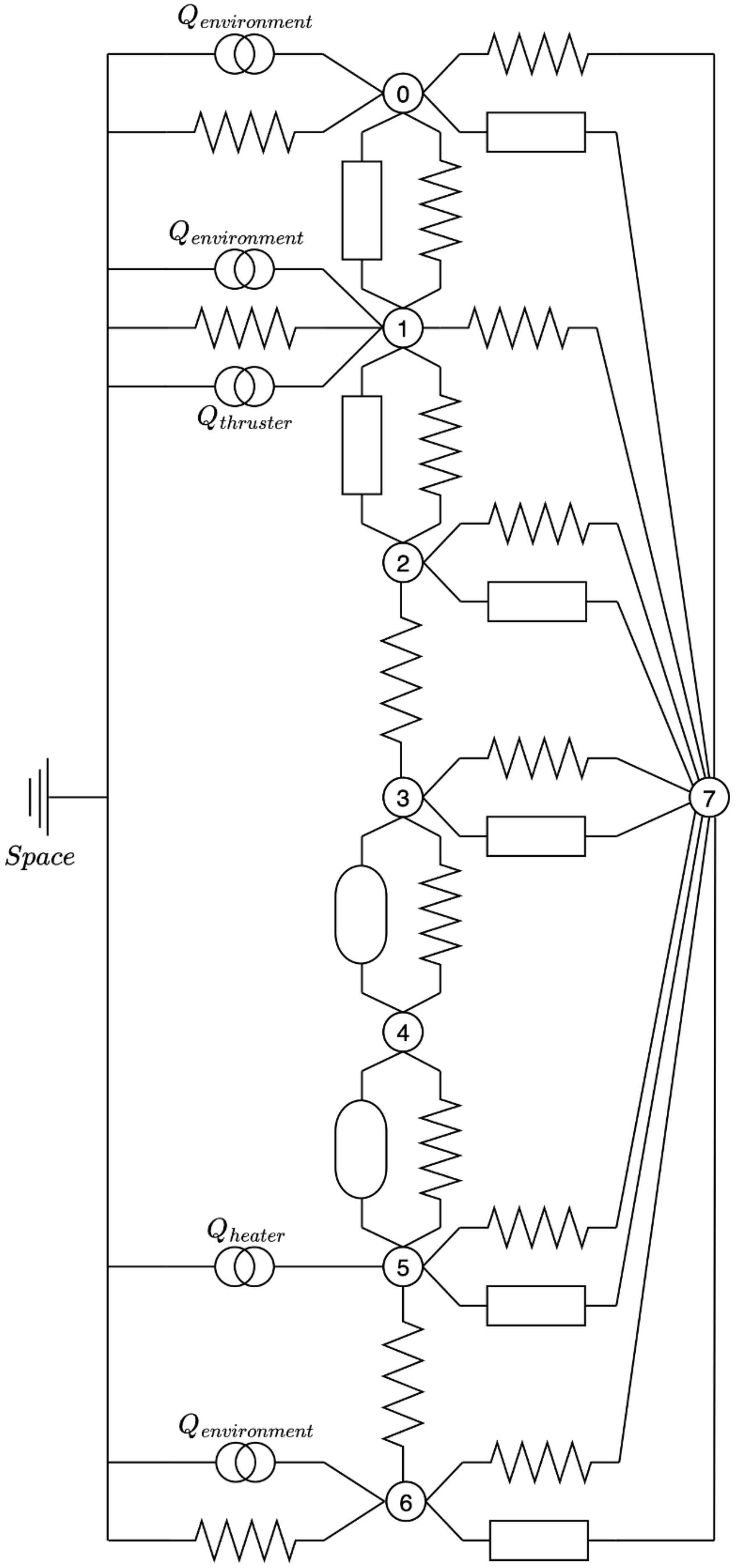

Figure B.2: Detailed thermal network representation of the propulsion system.

C

Engineering Drawings

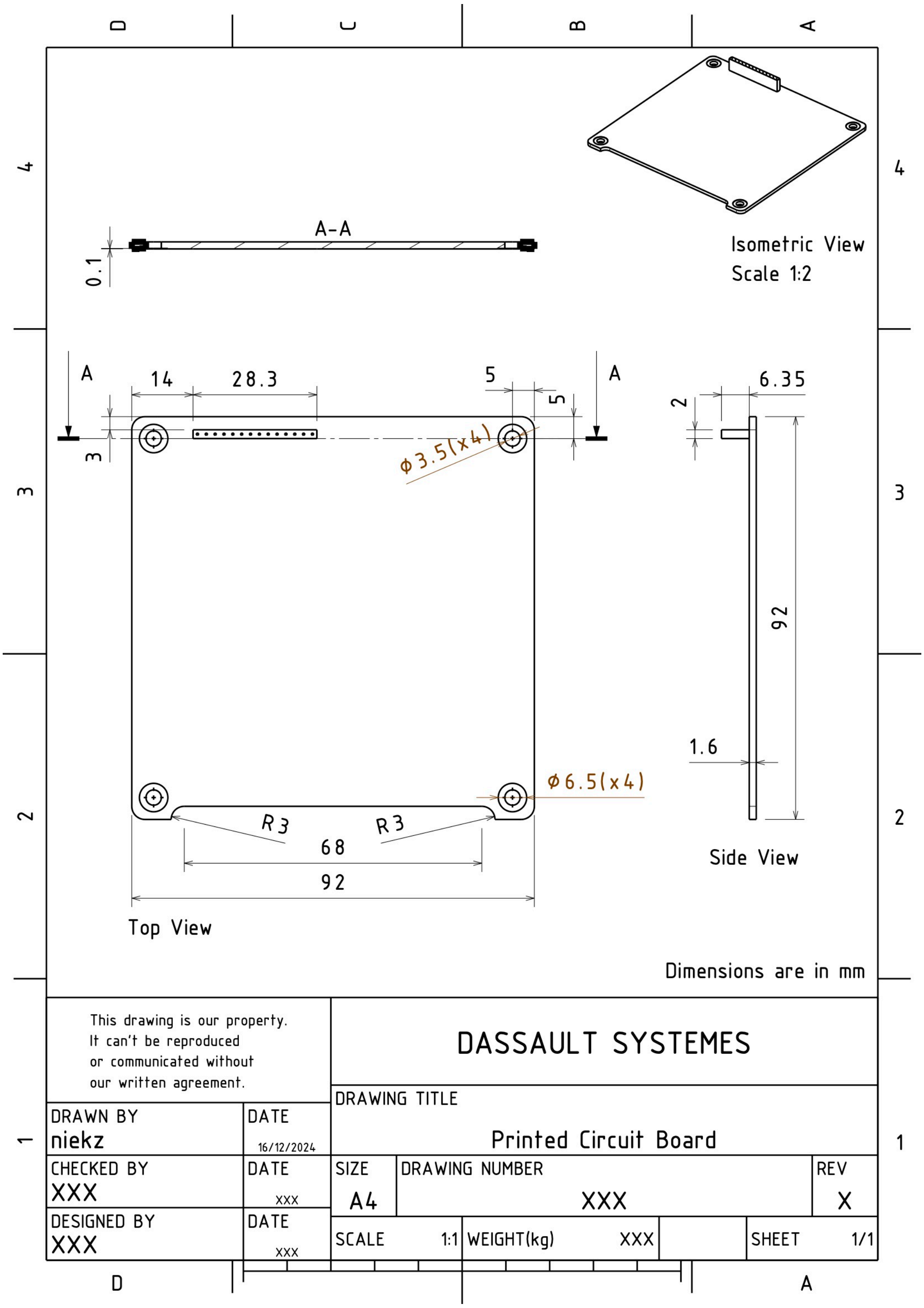

Figure C.1: Engineering drawing of the printed circuit board.

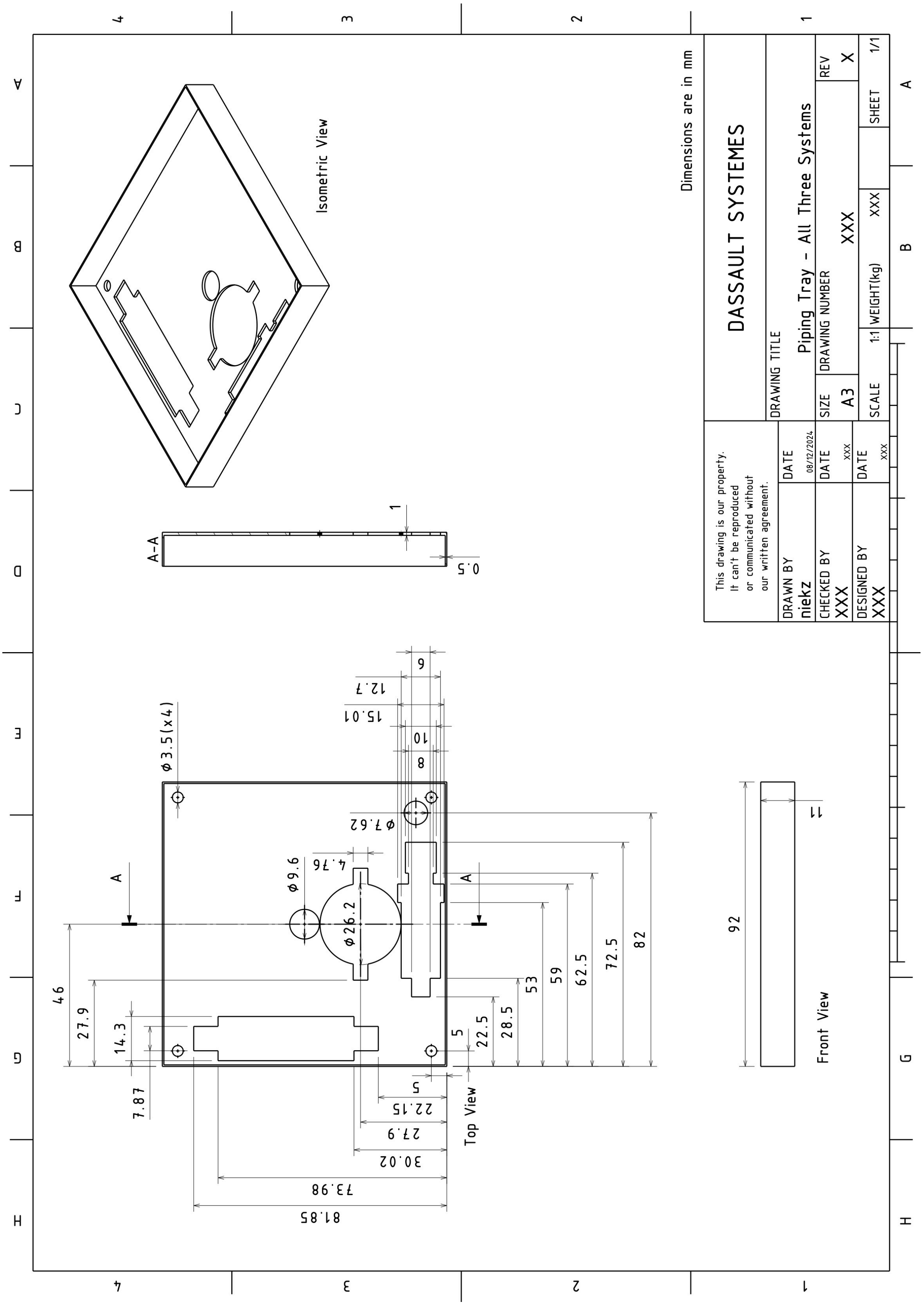

Figure C.2: Engineering drawing of the piping tray.

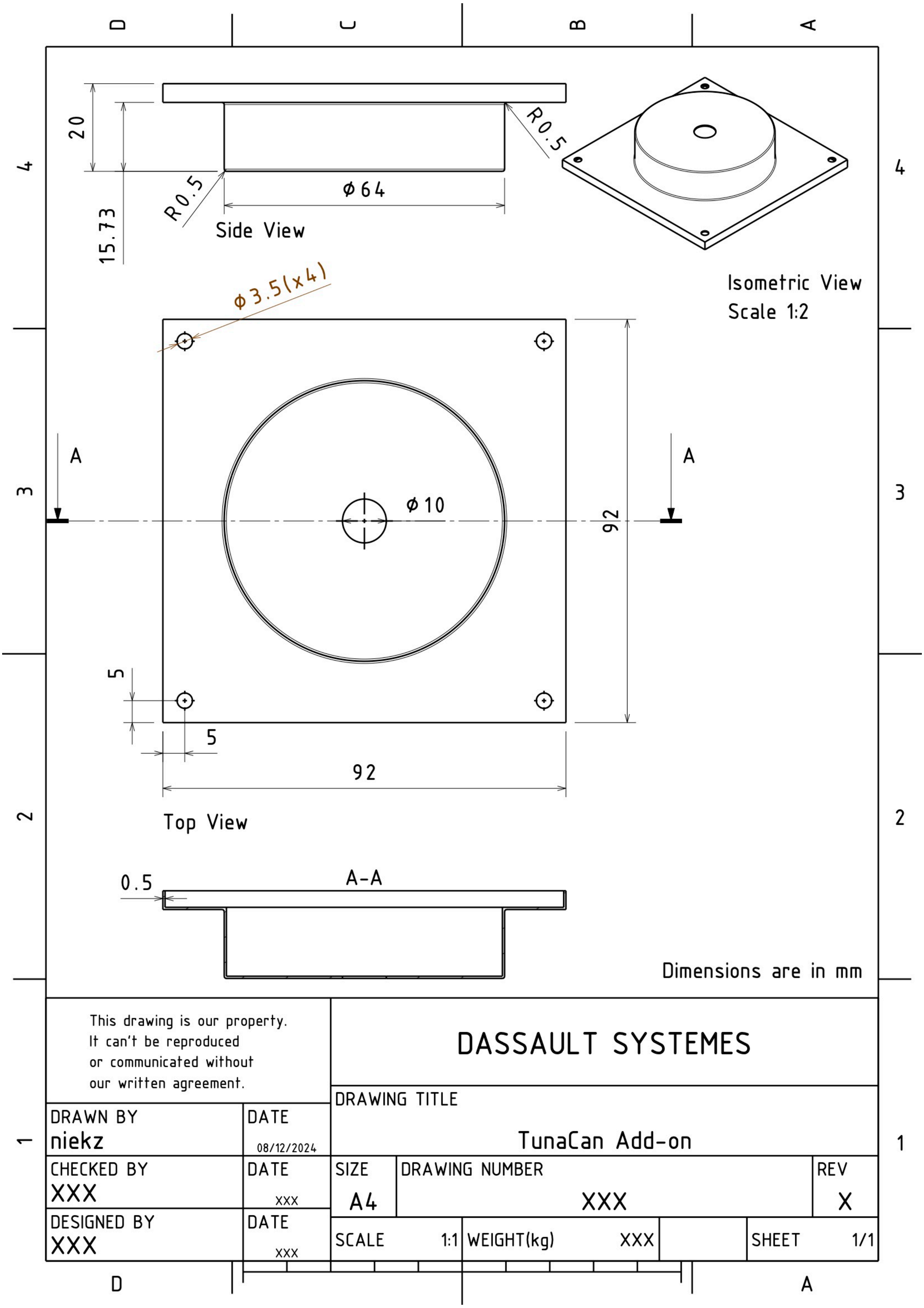

This drawing is our property.
It can't be reproduced
or communicated without
our written agreement.

DASSAULT SYSTEMES

DRAWING TITLE
TunaCan Add-on

DRAWN BY niekz
DATE 08/12/2024
CHECKED BY XXX
DATE xxx
DESIGNED BY XXX
DATE xxx

SIZE A4
DRAWING NUMBER XXX
REV X
SCALE 1:1
WEIGHT(kg) XXX
SHEET 1/1

Figure C.3: Engineering drawing of TunaCan add-on.

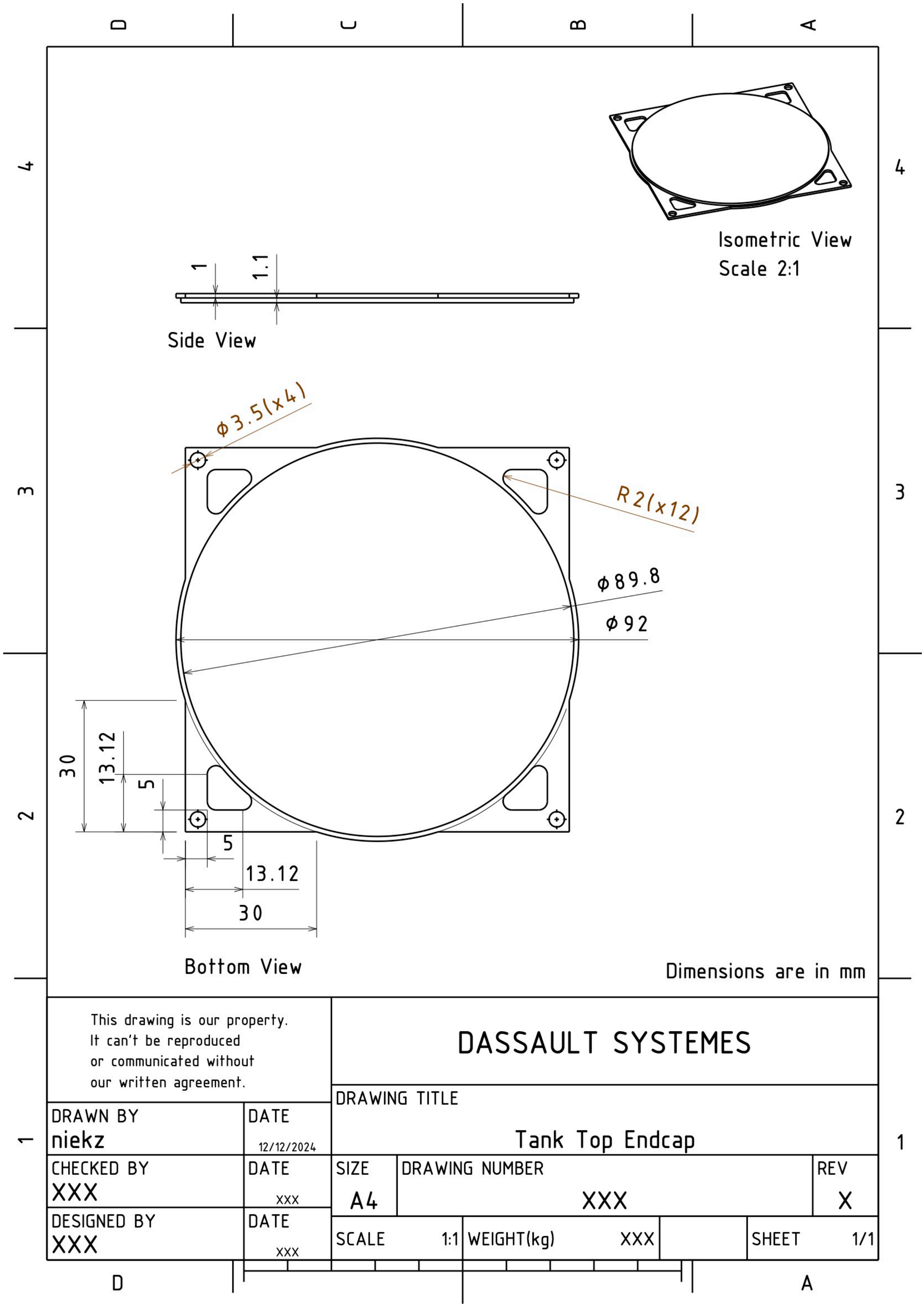

Figure C.4: Engineering drawing of top endcap.

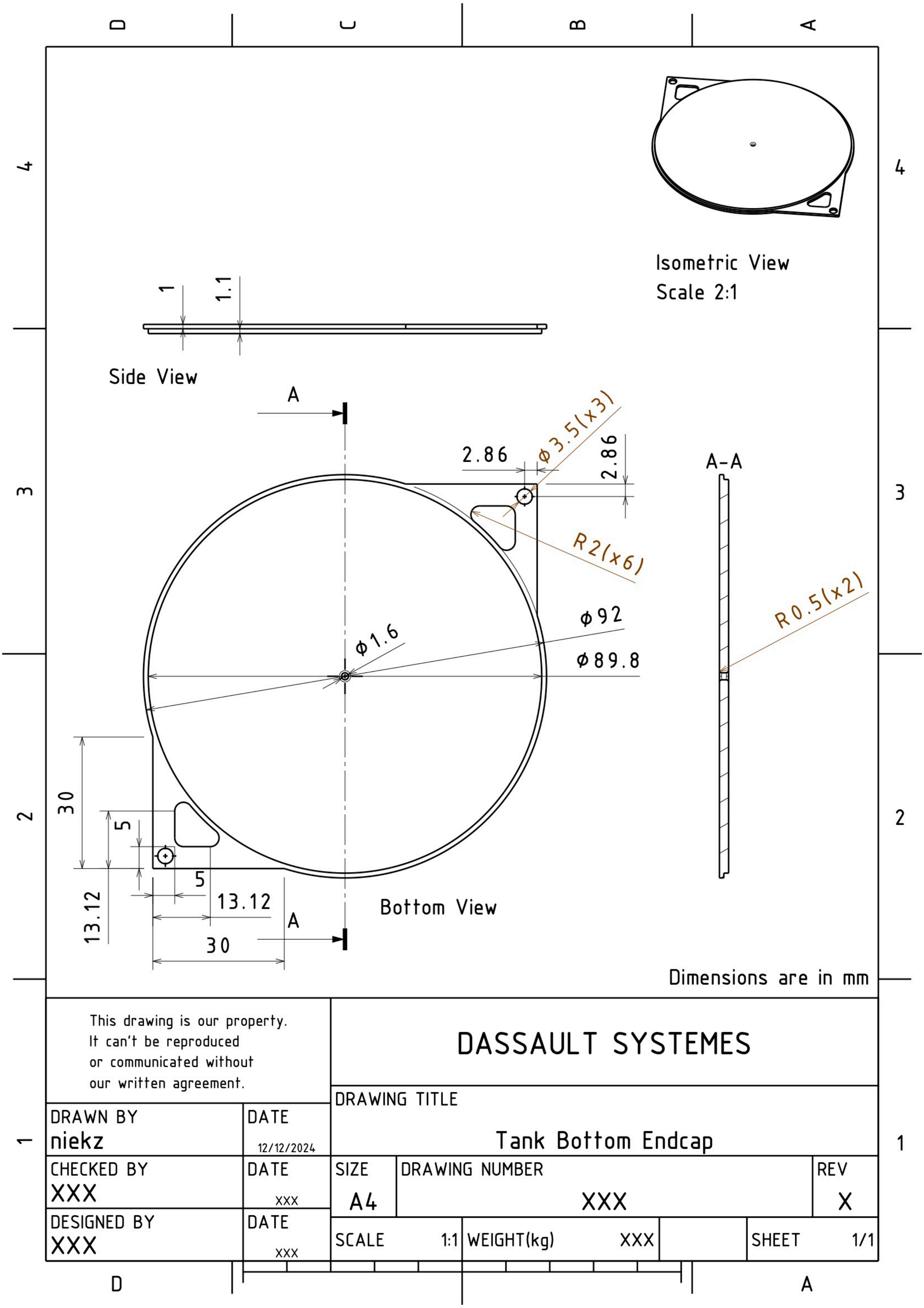

Figure C.5: Engineering drawing of bottom endcap.

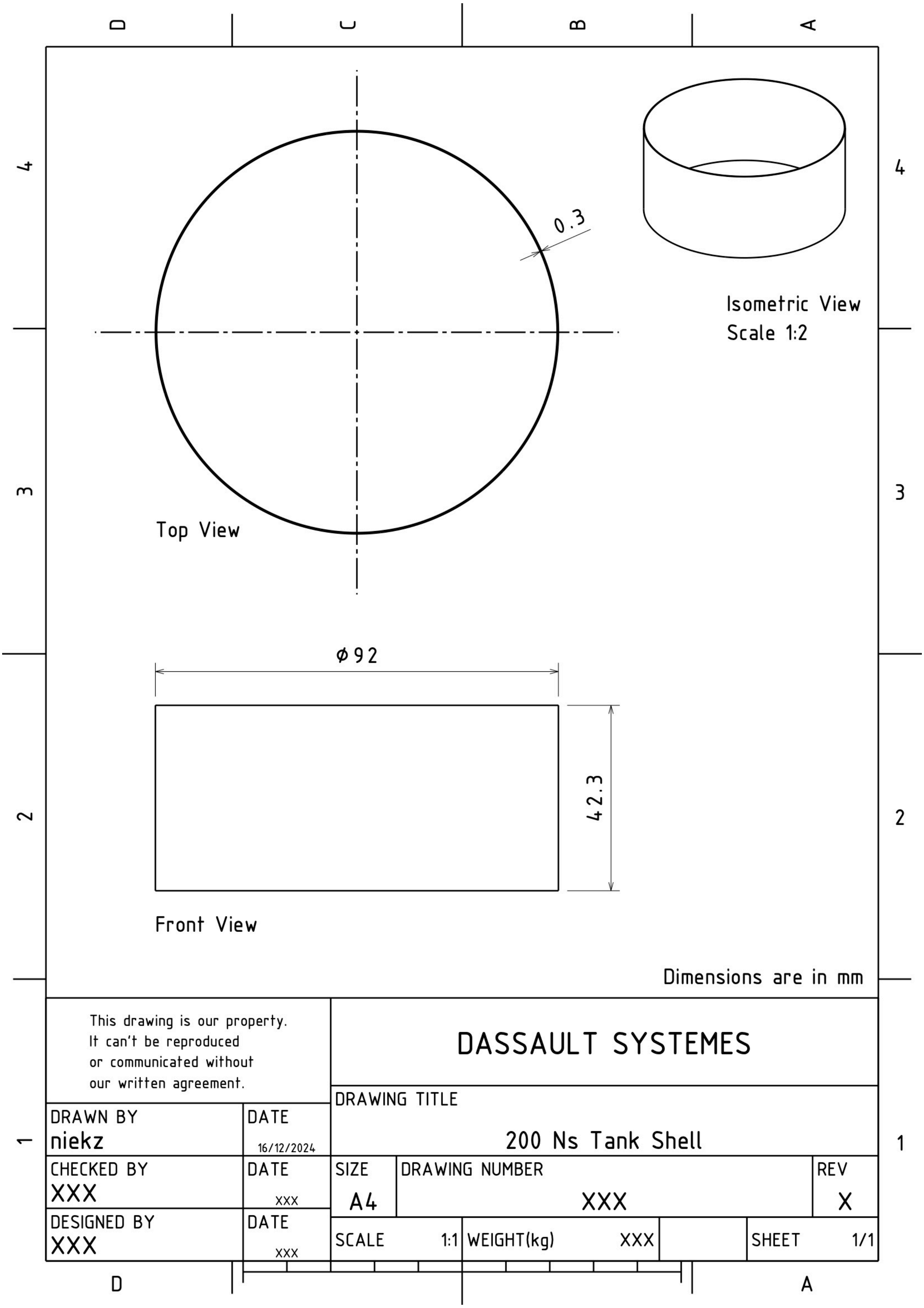

Figure C.6: Engineering drawing of the 200 Ns tank shell.

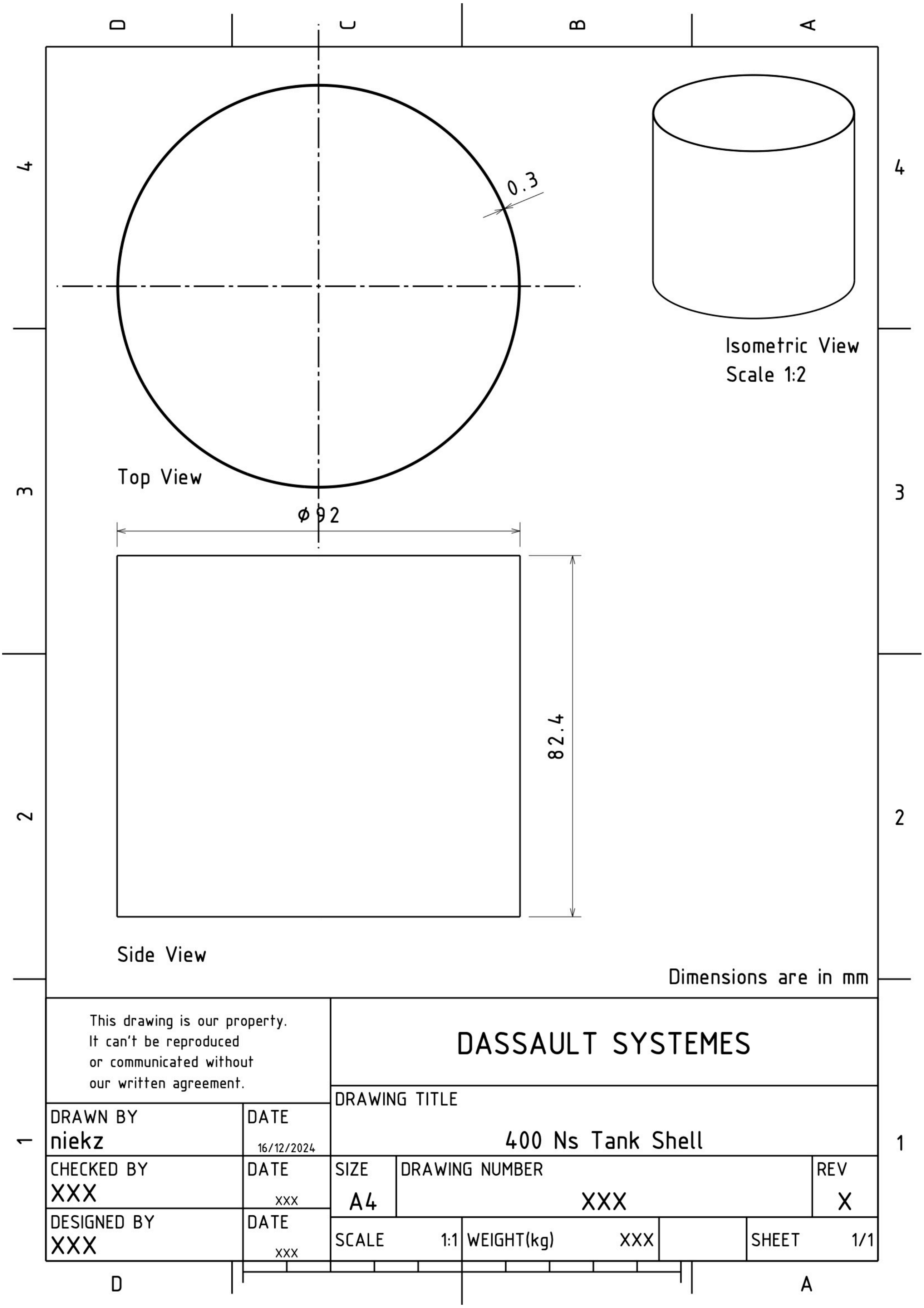

Figure C.7: Engineering drawing of 400 Ns tank shell.

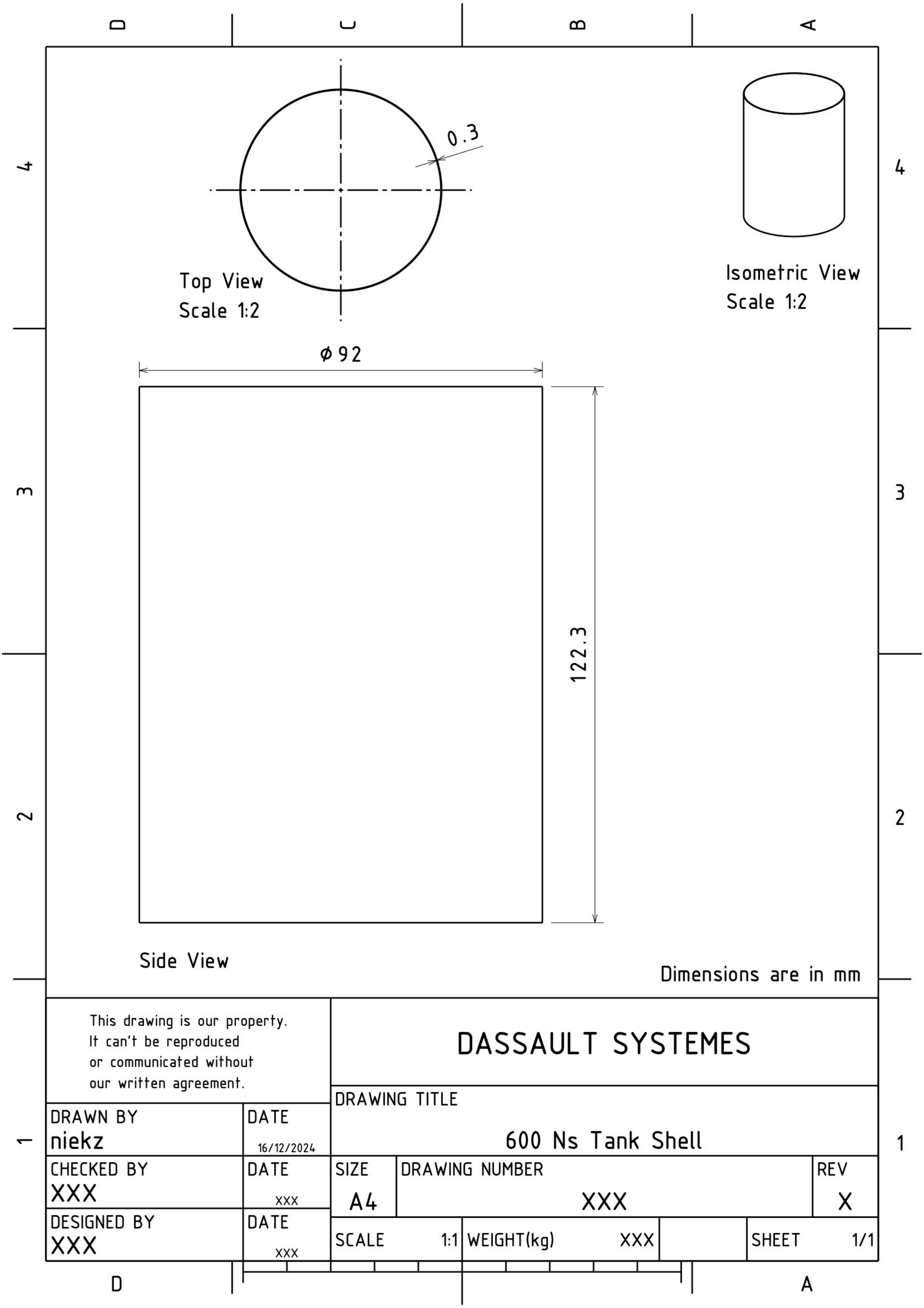

Figure C.8: Engineering drawing of the 600 Ns tank shell.

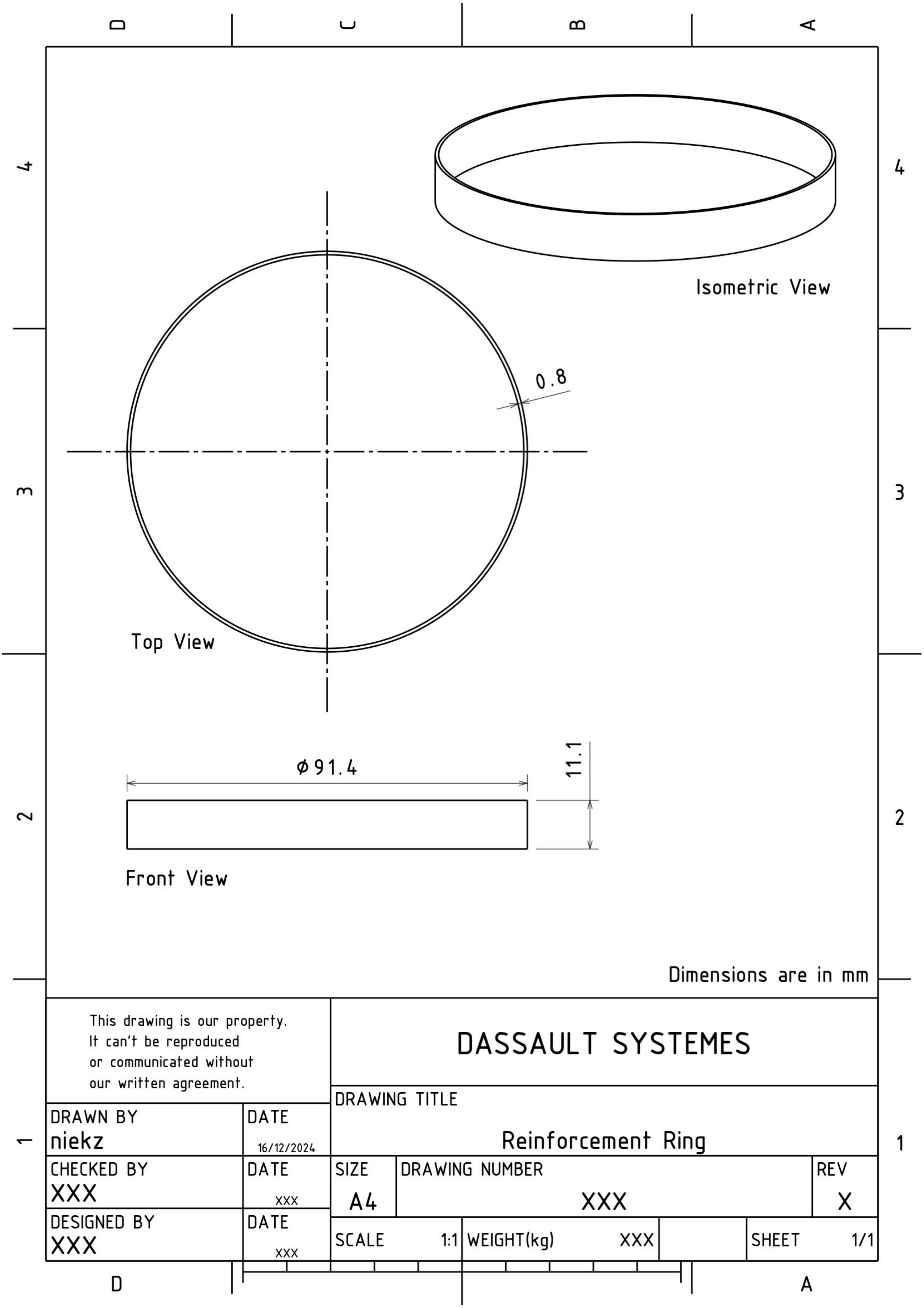

Figure C.9: Engineering drawing of the reinforcement ring.

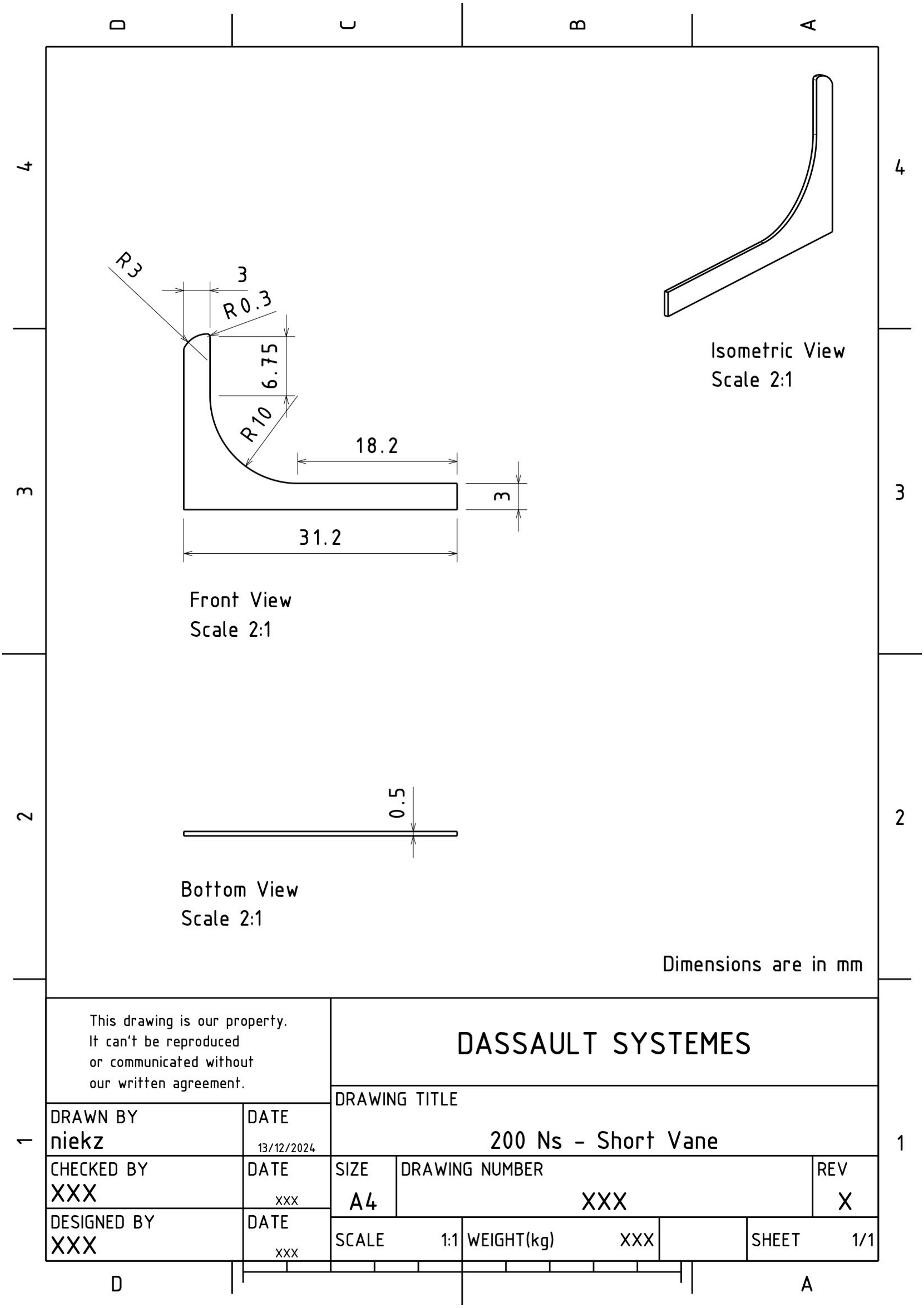

Figure C.10: Engineering drawing of the 200 Ns short vane.

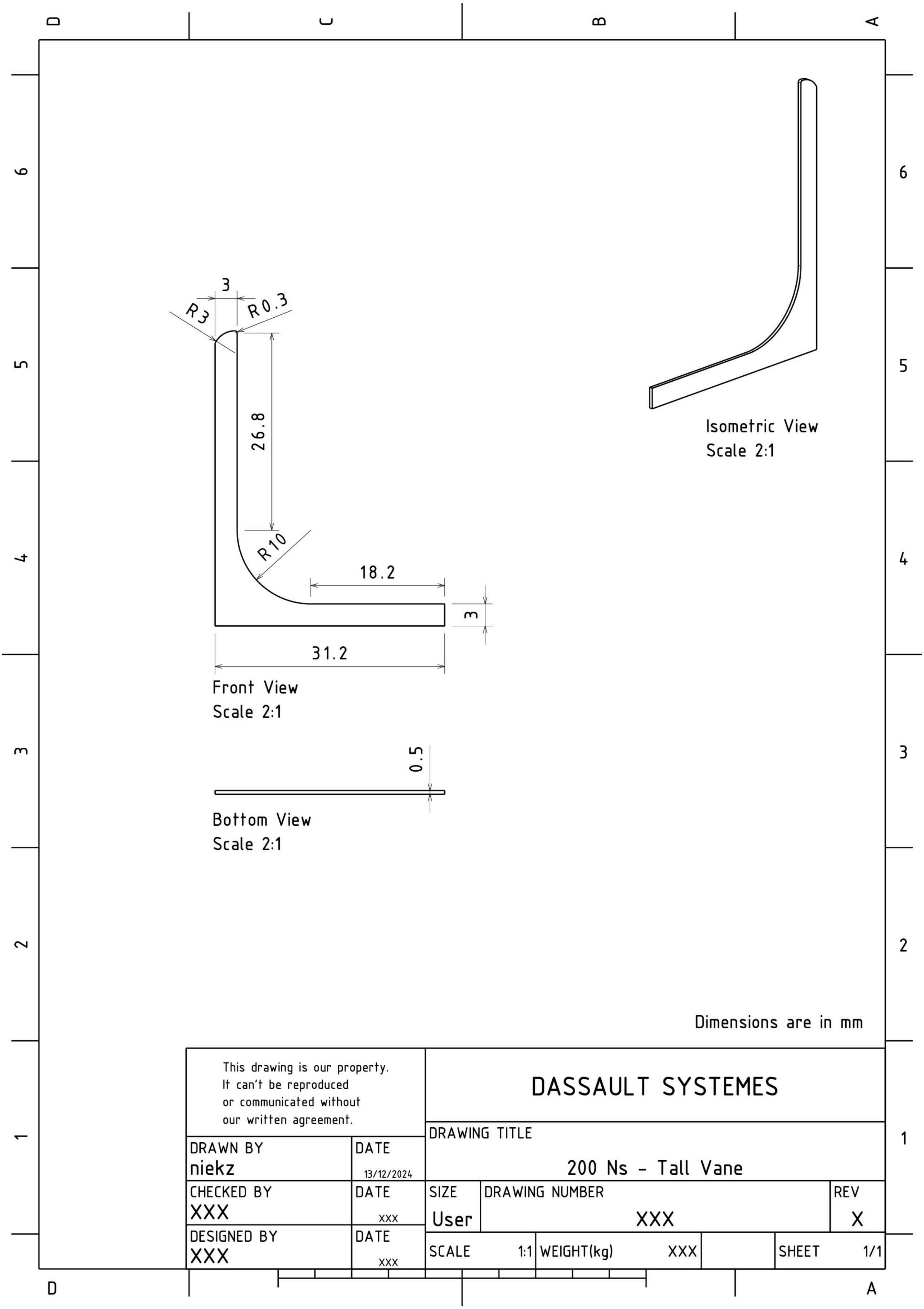

Figure C.11: Engineering drawing of the 200 Ns tall vane.

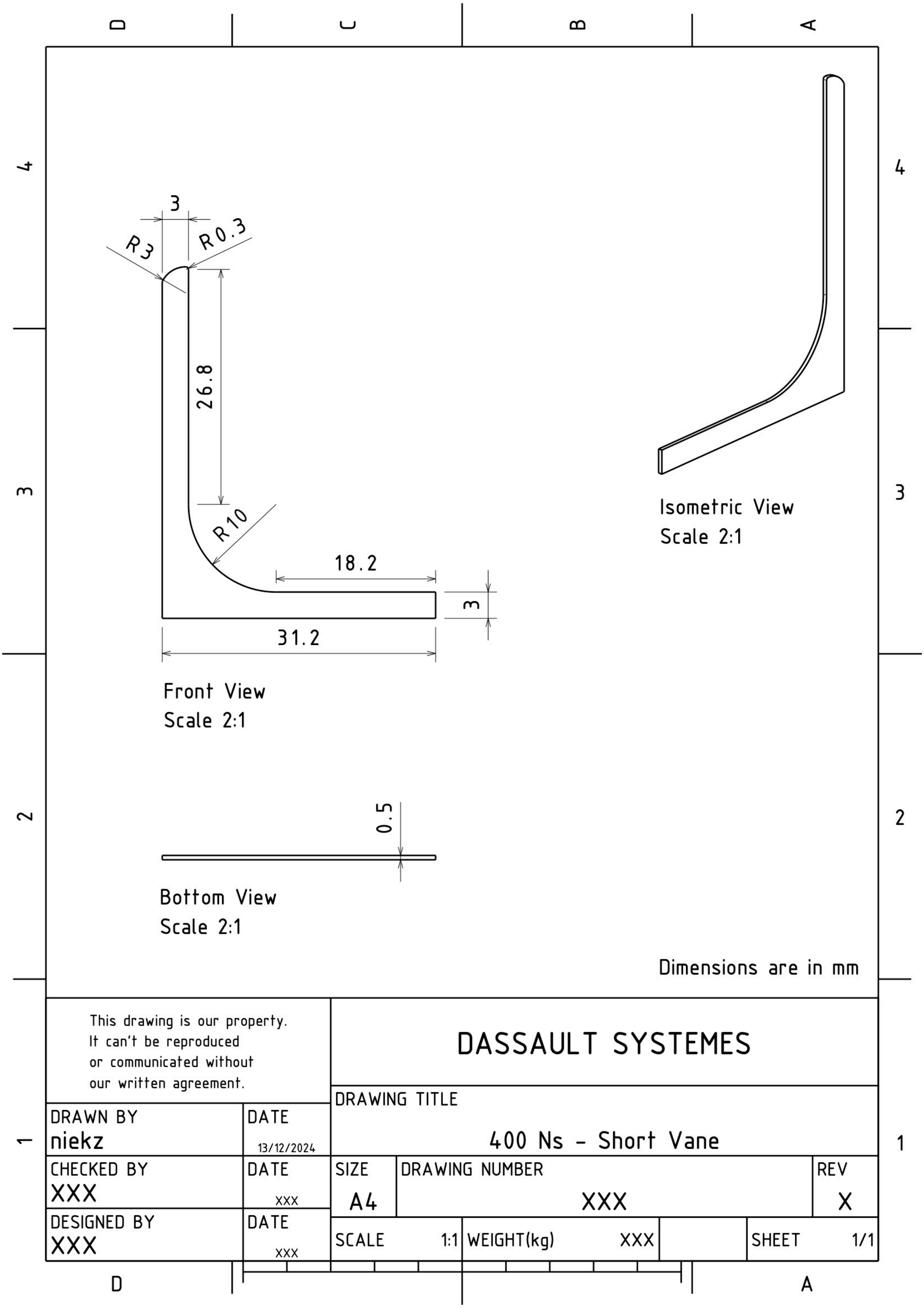

Figure C.12: Engineering drawing of the 400 Ns short vane.

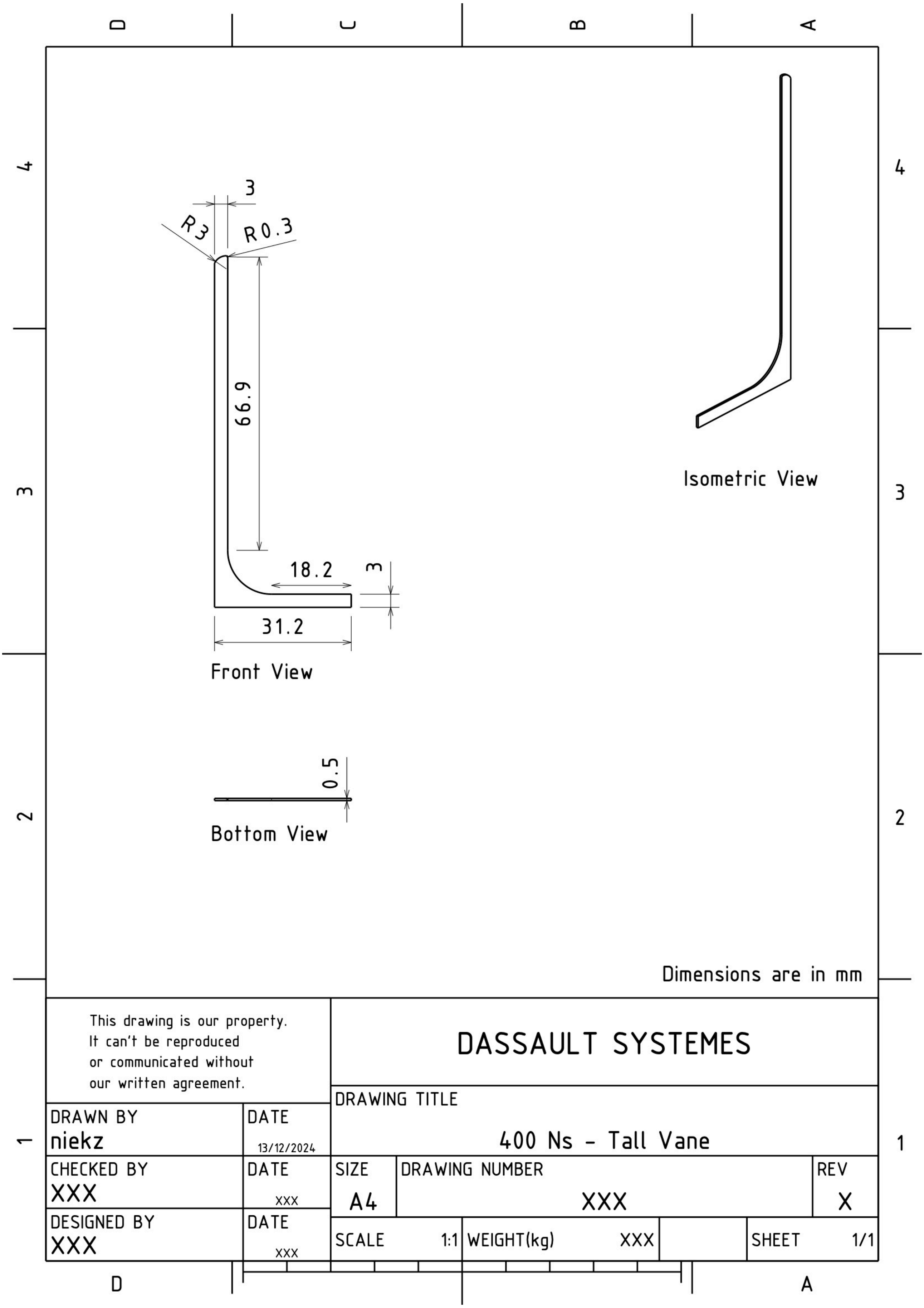

This drawing is our property.
It can't be reproduced
or communicated without
our written agreement.

DASSAULT SYSTEMES

DRAWN BY niekz	DATE 13/12/2024
CHECKED BY XXX	DATE XXX
DESIGNED BY XXX	DATE XXX

DRAWING TITLE 400 Ns - Tall Vane

SIZE A4	DRAWING NUMBER XXX	REV X

SCALE 1:1
WEIGHT(kg) XXX
SHEET 1/1

Figure C.13: Engineering drawing of the 400 Ns tall vane.

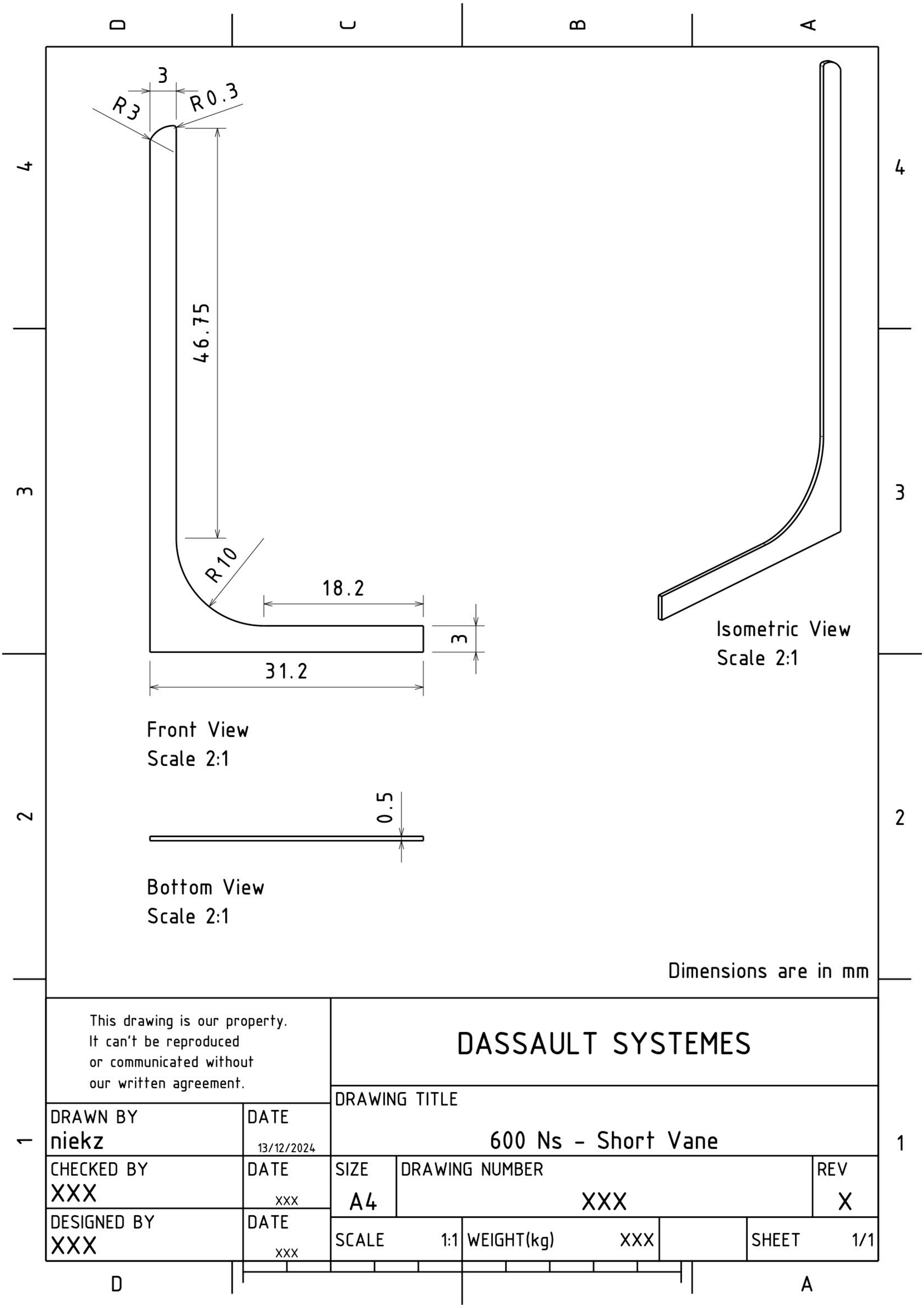

Figure C.14: Engineering drawing of the 600 Ns short vane.

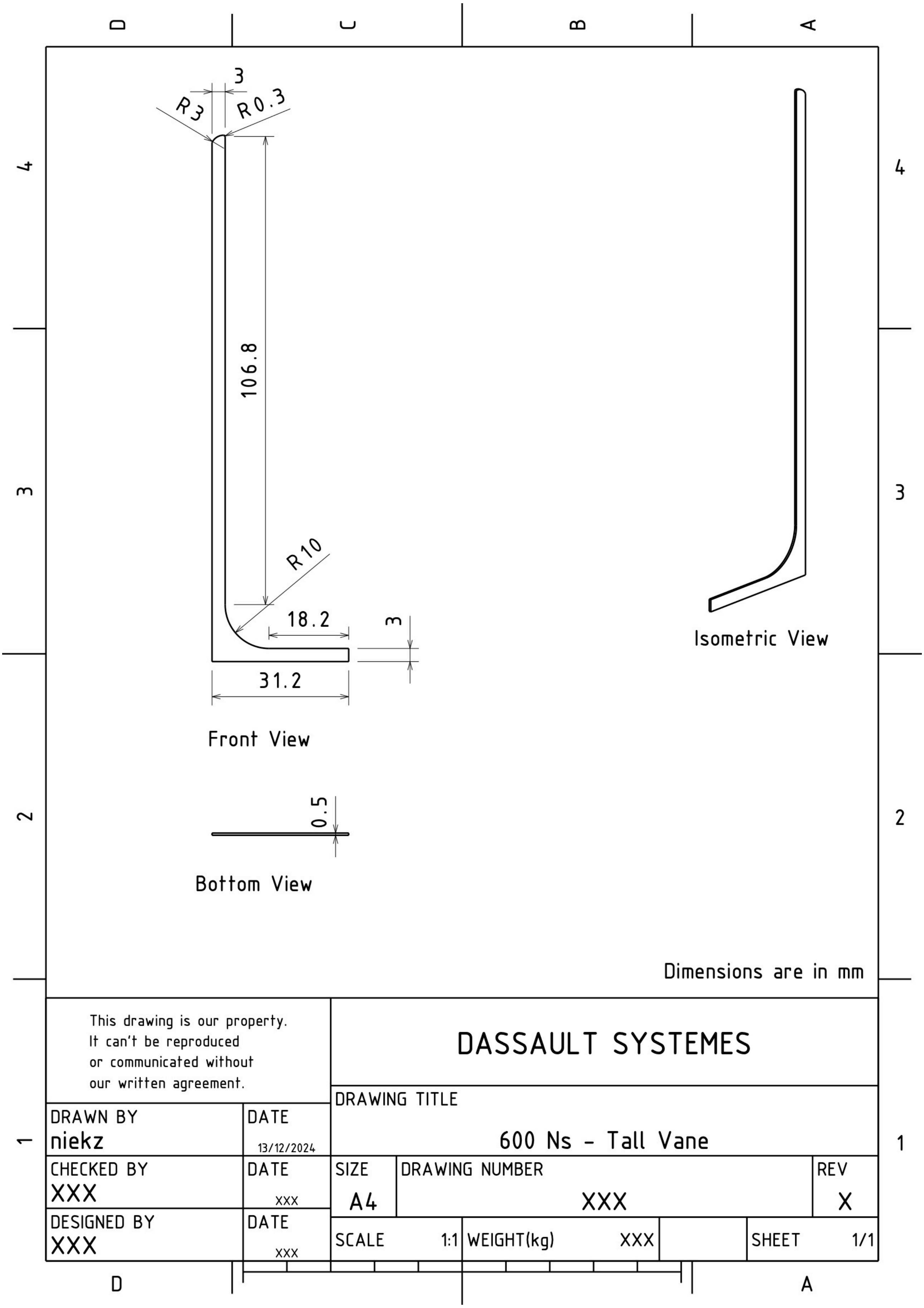

Figure C.15: Engineering drawing of the 600 Ns tall vane.

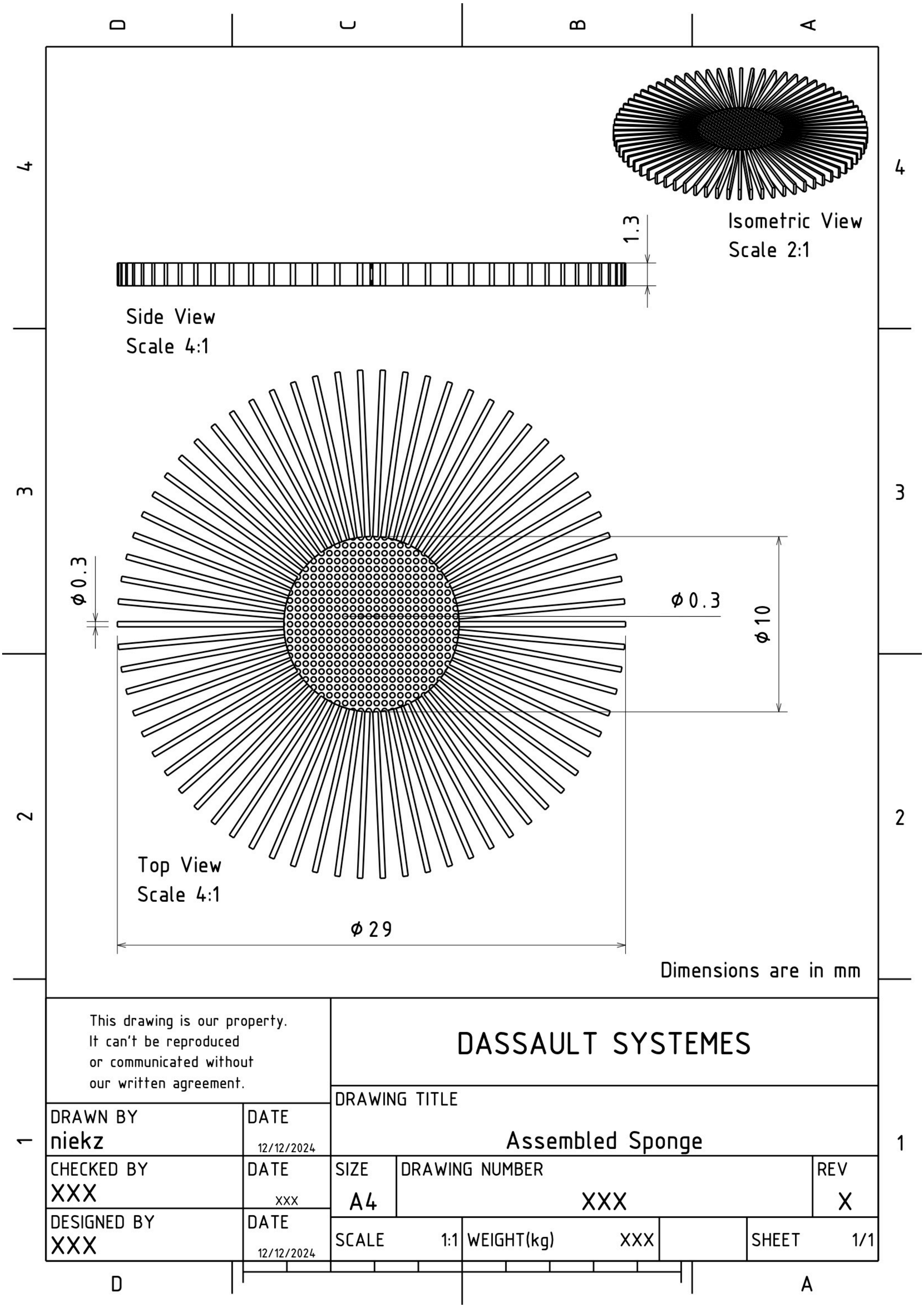

Figure C.16: Engineering drawing of the sponge PMD.

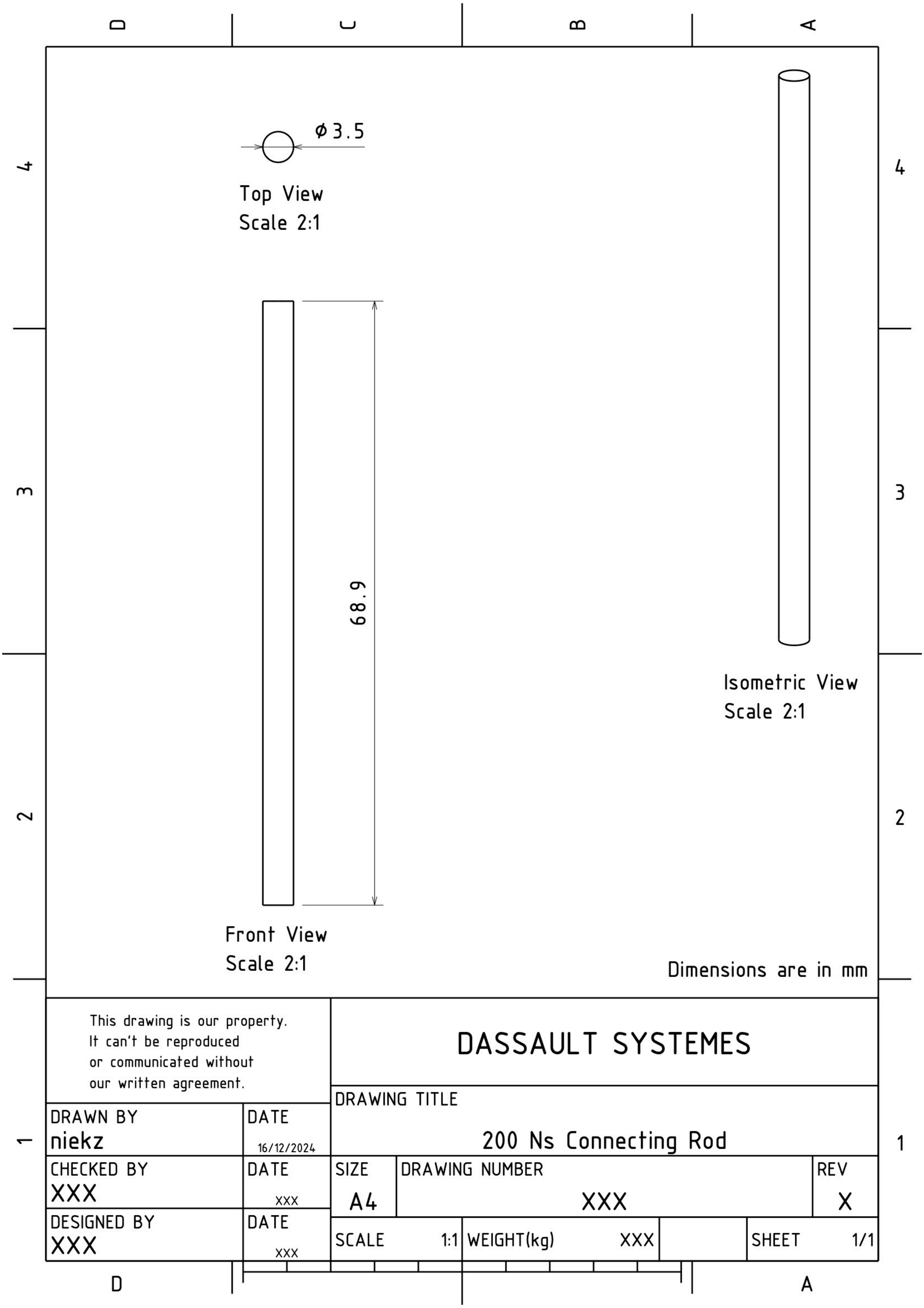

Figure C.17: Engineering drawing of the 200 Ns connecting rod.

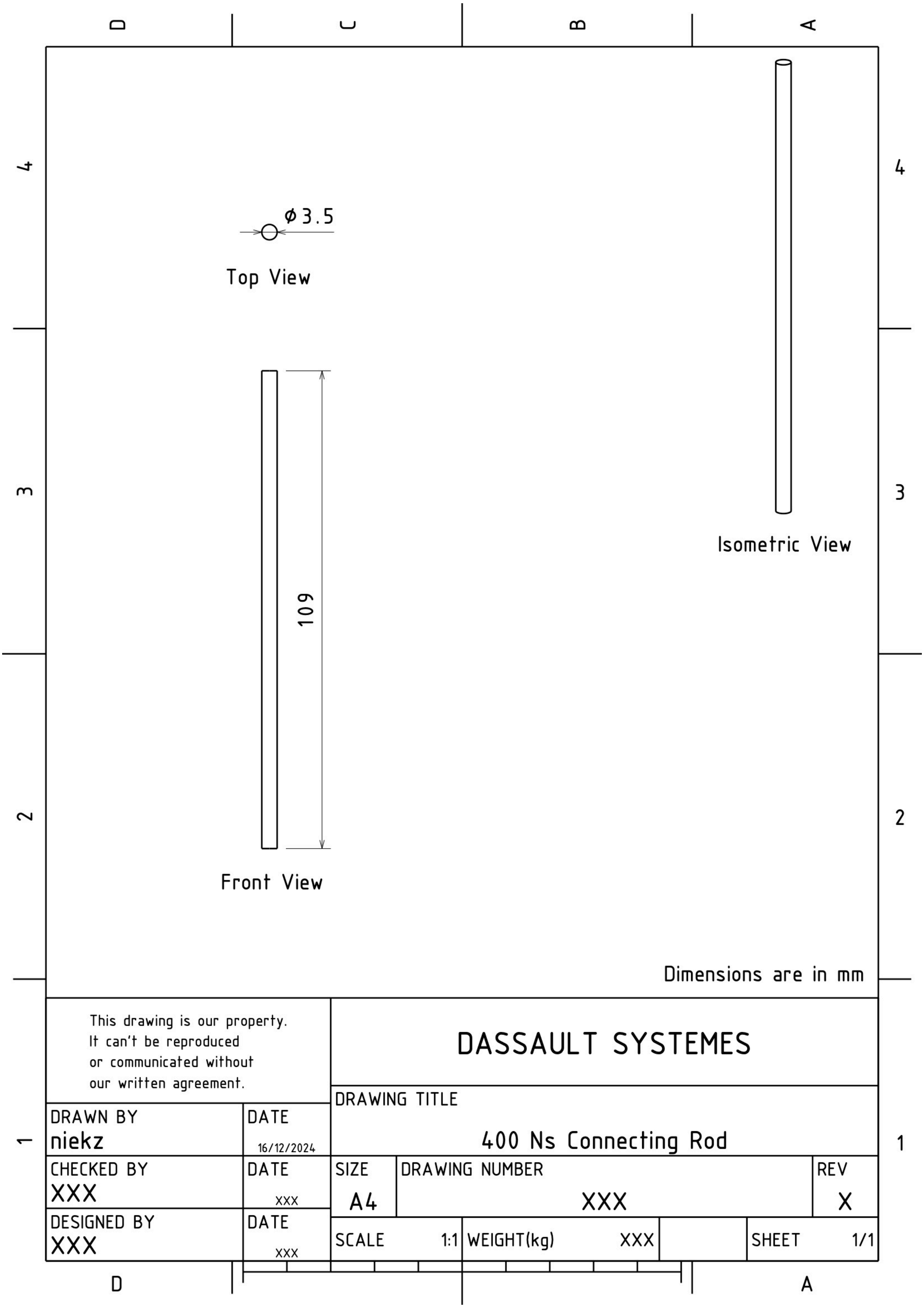

Figure C.18: Engineering drawing of the 400 Ns connecting rod.

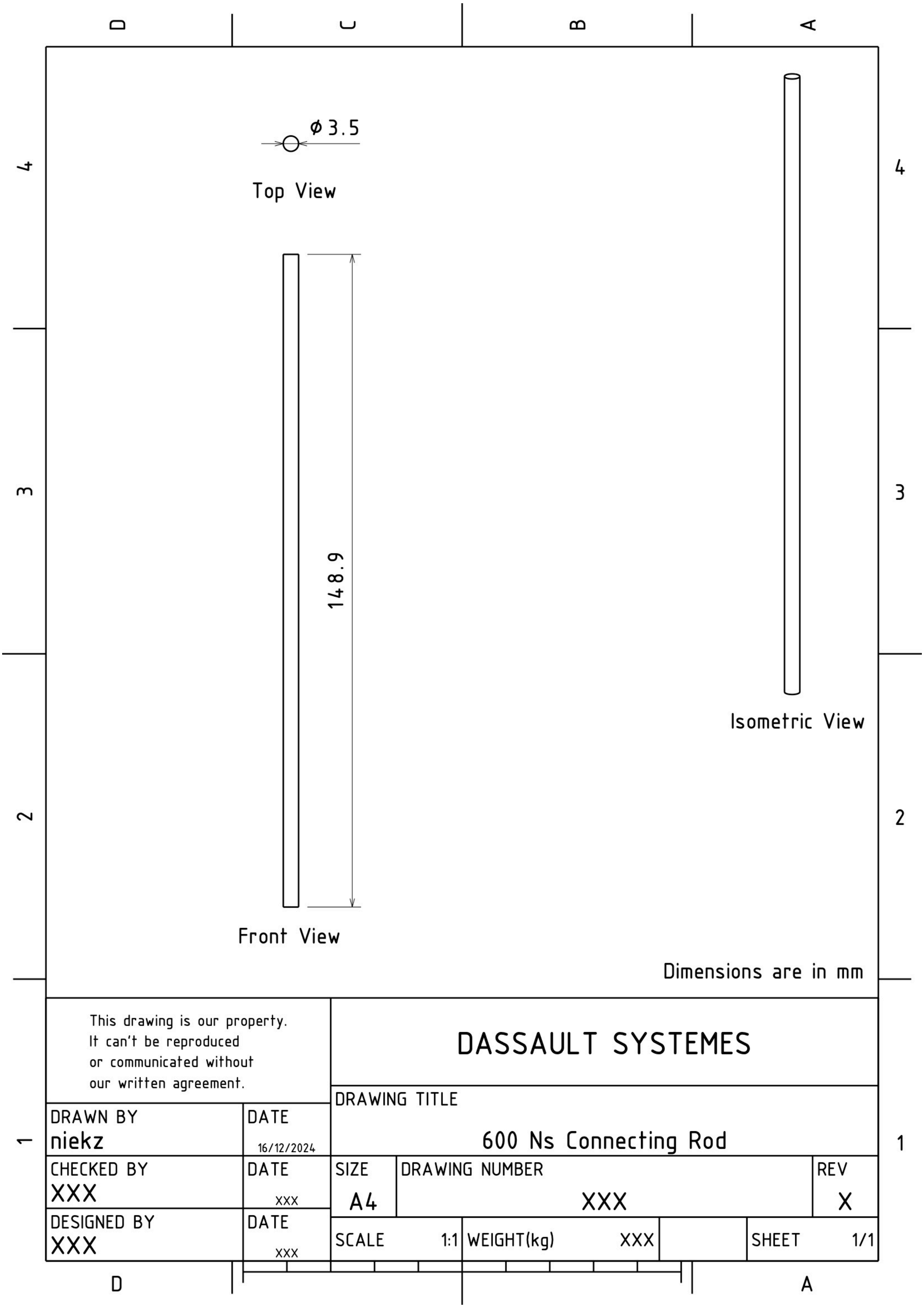

Figure C.19: Engineering drawing of the 600 Ns connecting rod.

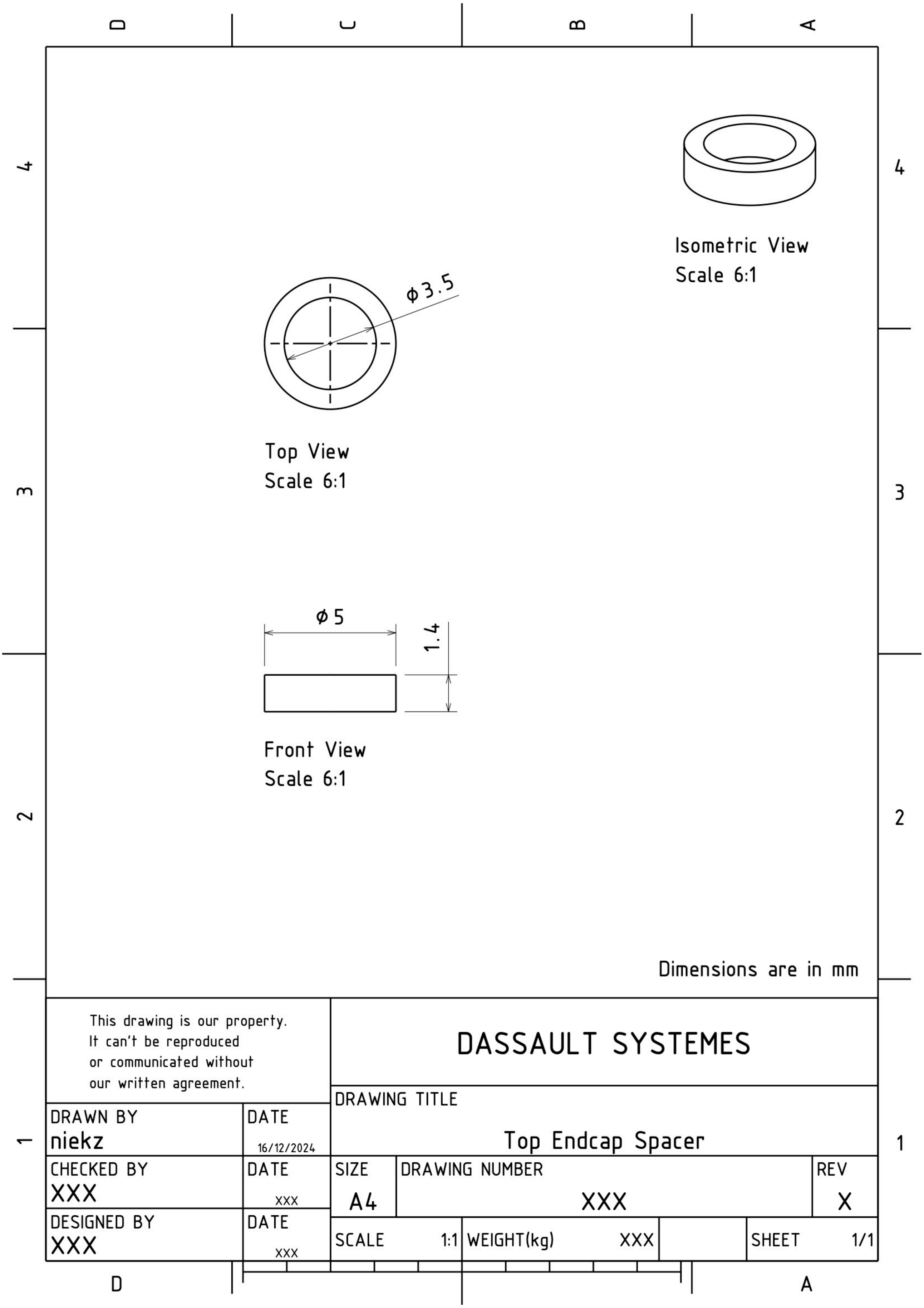

This drawing is our property.
It can't be reproduced
or communicated without
our written agreement.

DASSAULT SYSTEMES

DRAWN BY niekz	DATE 16/12/2024	DRAWING TITLE Top Endcap Spacer				
CHECKED BY XXX	DATE XXX	SIZE A4	DRAWING NUMBER XXX			REV X
DESIGNED BY XXX	DATE XXX	SCALE 1:1	WEIGHT(kg) XXX		SHEET 1/1	

Figure C.20: Engineering drawing of the top endcap spacer.

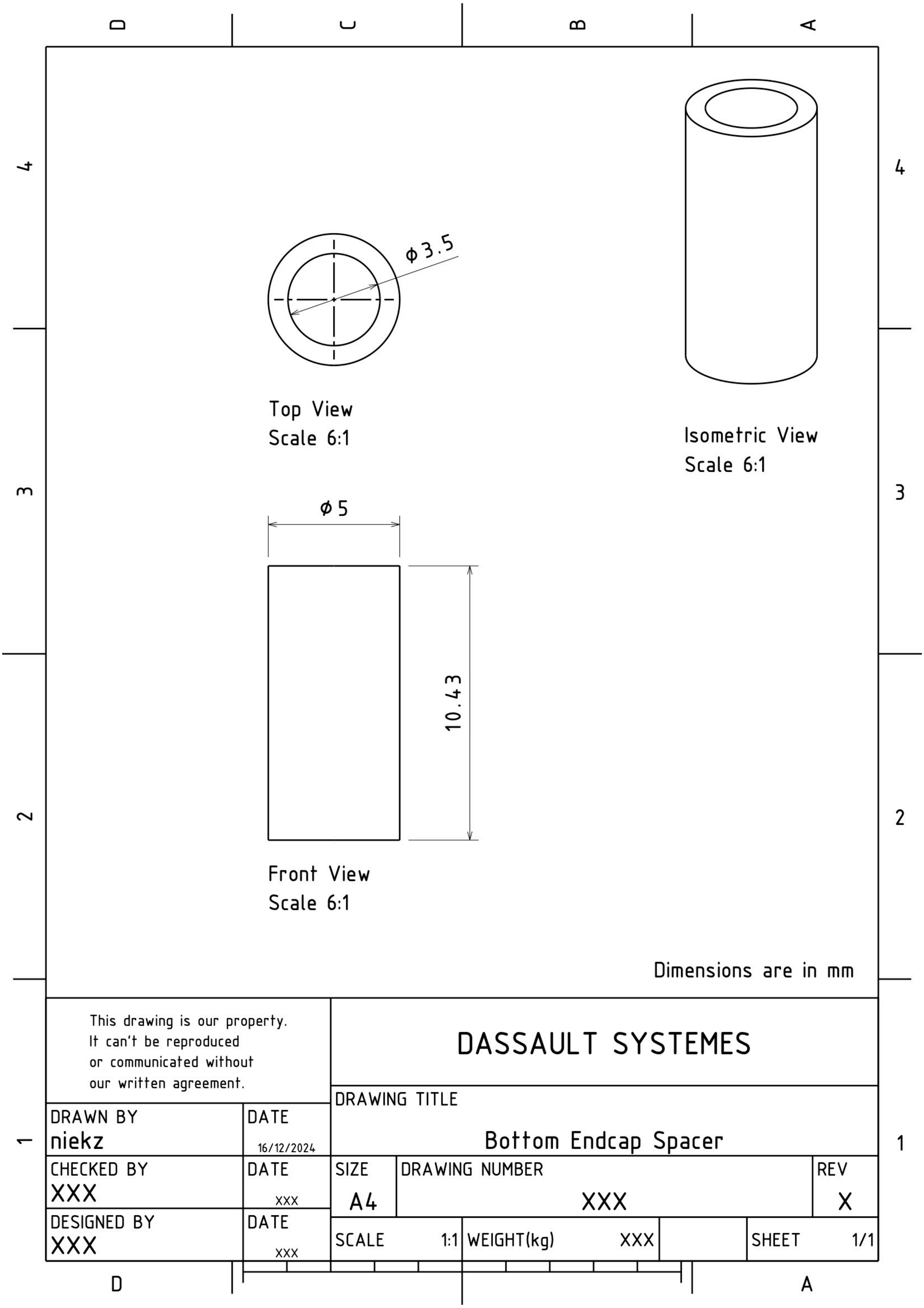

Figure C.21: Engineering drawing of the bottom endcap spacer.

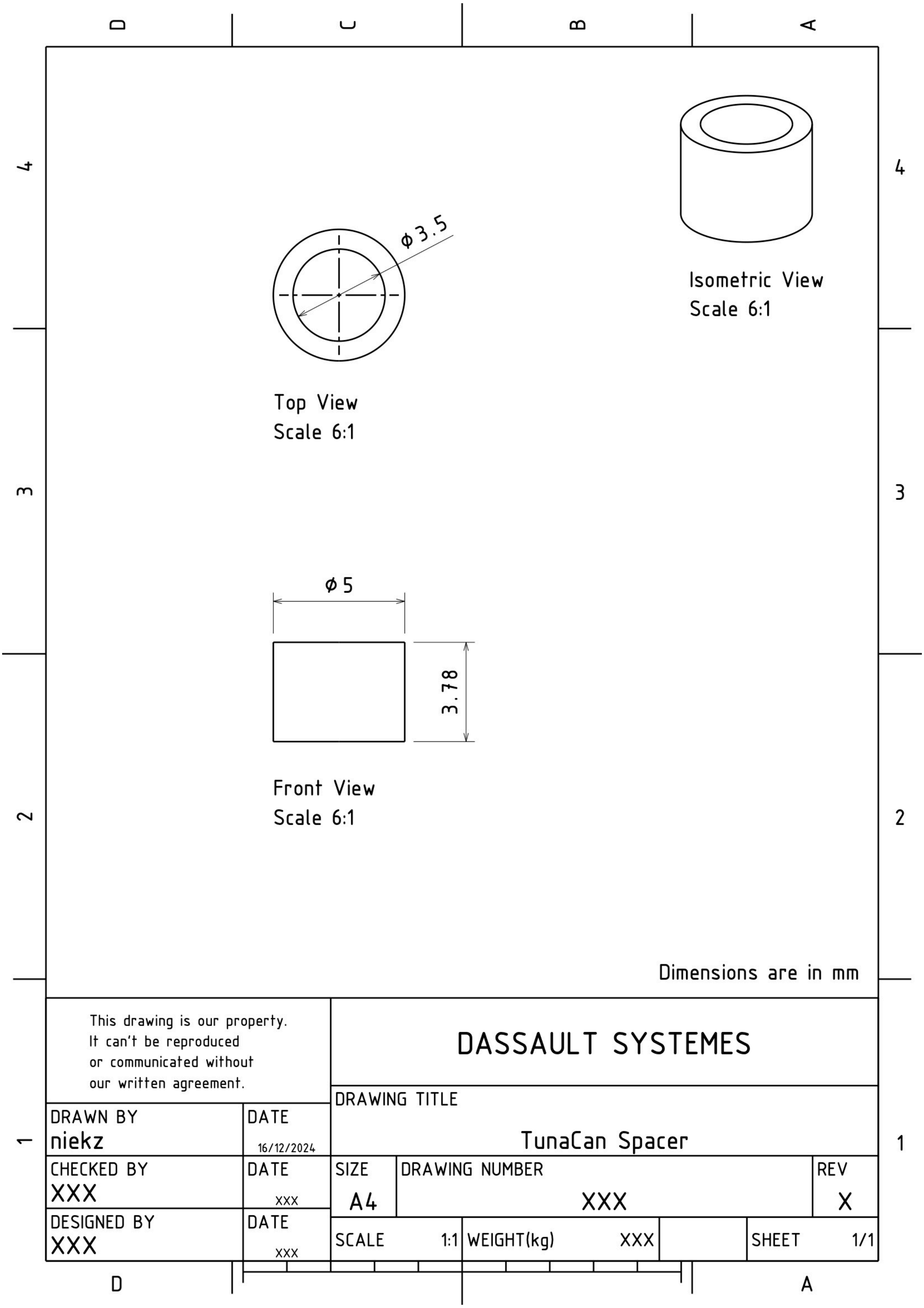

This drawing is our property.
It can't be reproduced
or communicated without
our written agreement.

DASSAULT SYSTEMES

DRAWING TITLE
TunaCan Spacer

DRAWN BY niekz
DATE 16/12/2024
CHECKED BY XXX
DATE xxx
DESIGNED BY XXX
DATE xxx
SIZE A4
DRAWING NUMBER XXX
REV X
SCALE 1:1
WEIGHT(kg) XXX
SHEET 1/1

Figure C.22: Engineering drawing of the TunaCan spacer.

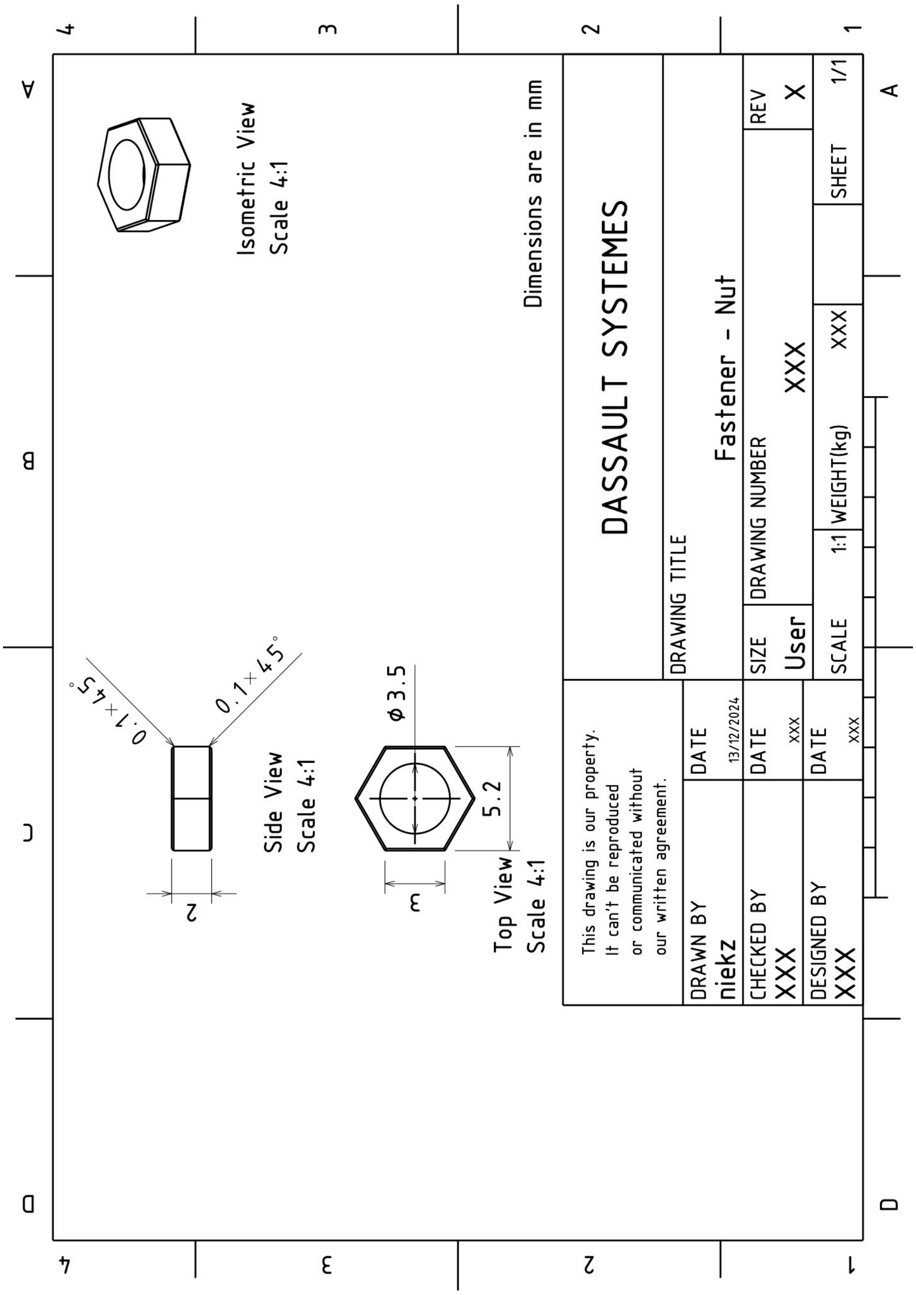

Figure C.23: Engineering drawing of the nut.

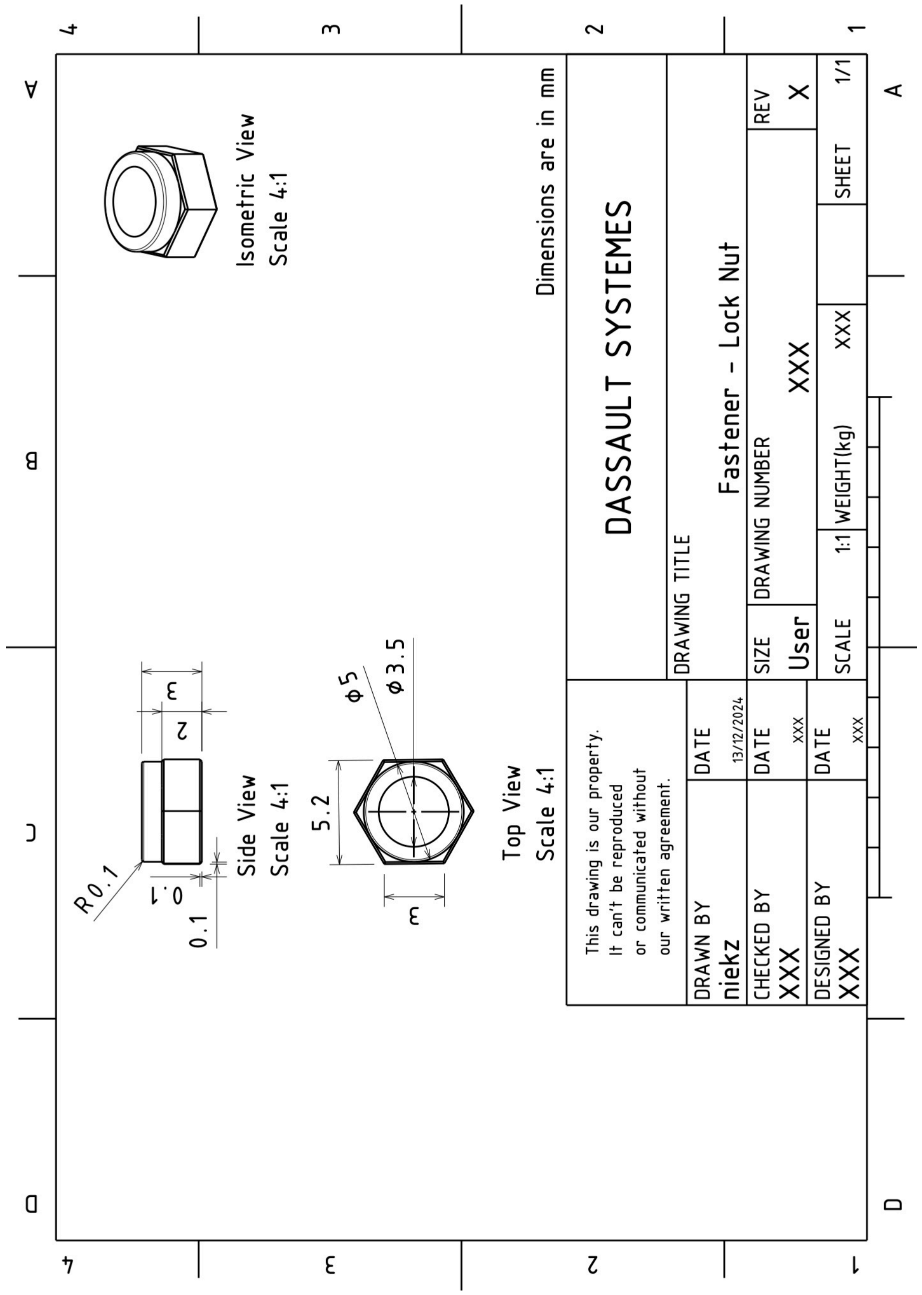

Figure C.24: Engineering drawing of the lock nut.

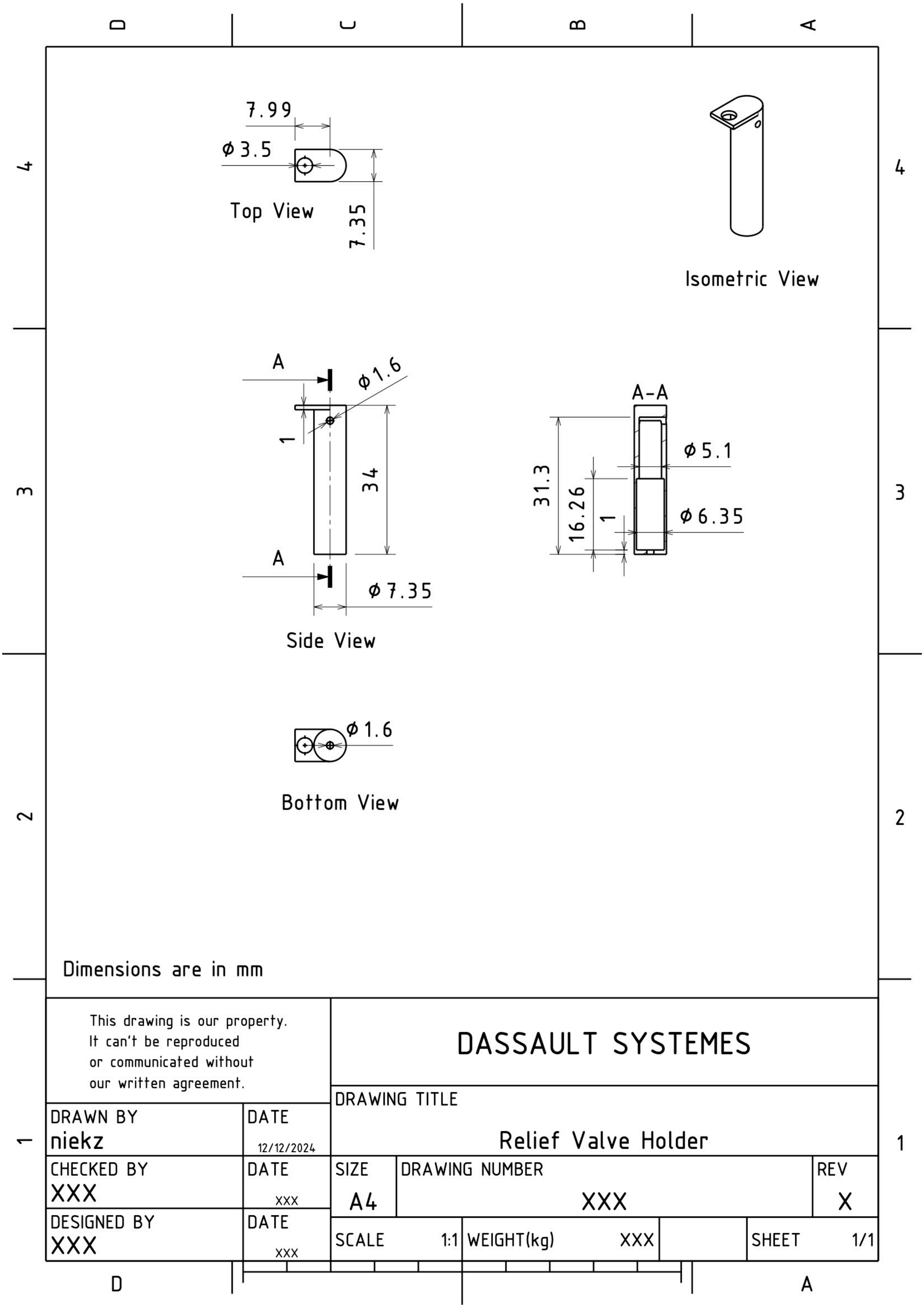

This drawing is our property.
It can't be reproduced
or communicated without
our written agreement.

DASSAULT SYSTEMES

DRAWN BY niekz	DATE 12/12/2024	DRAWING TITLE Relief Valve Holder	
CHECKED BY XXX	DATE XXX	SIZE A4	DRAWING NUMBER XXX — REV X
DESIGNED BY XXX	DATE XXX	SCALE 1:1	WEIGHT(kg) XXX — SHEET 1/1

Figure C.25: Engineering drawing of the pressure relief valve holder.

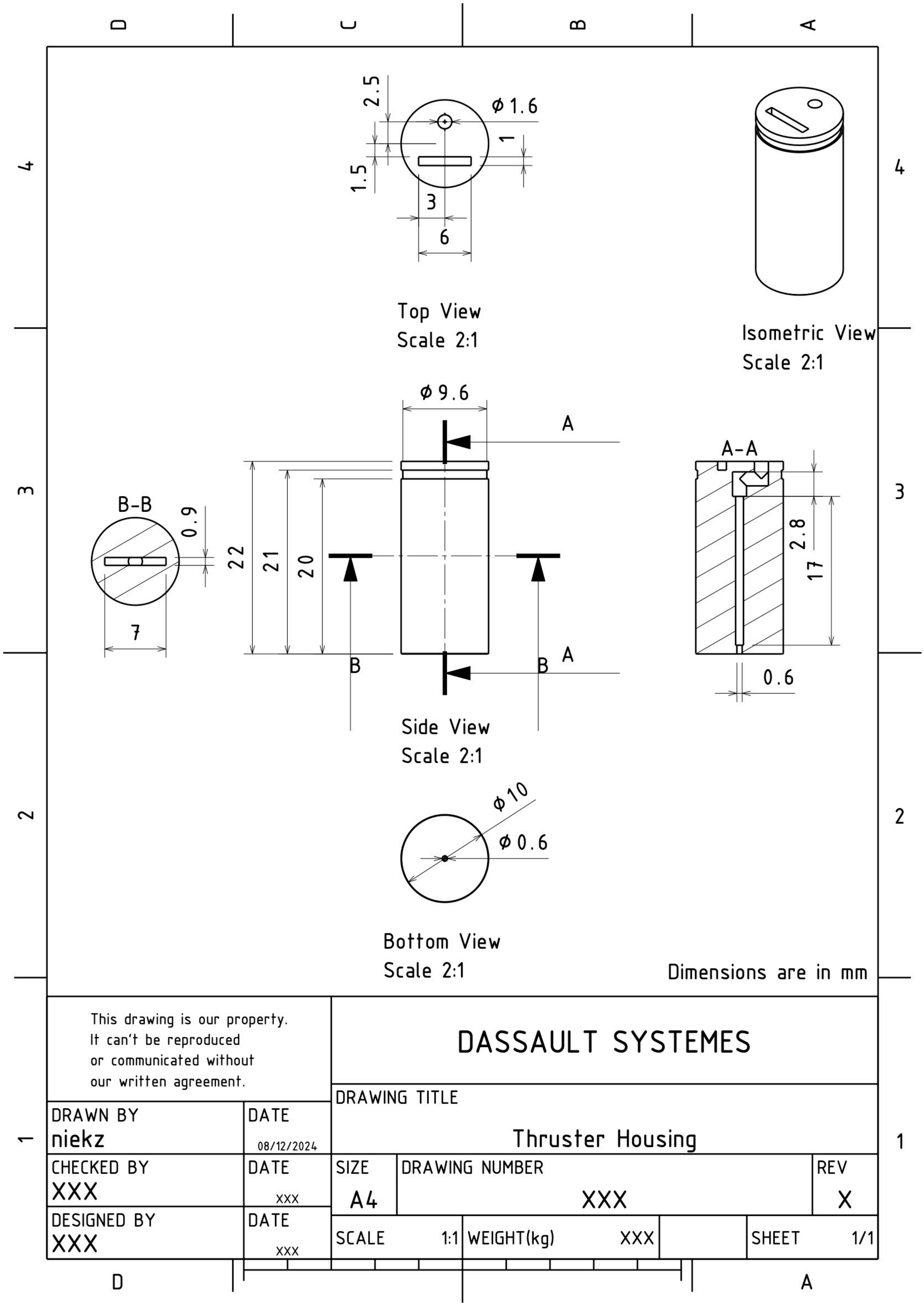

This drawing is our property.
It can't be reproduced
or communicated without
our written agreement.

DASSAULT SYSTEMES

DRAWING TITLE: Thruster Housing

DRAWN BY: niekz
DATE: 08/12/2024
CHECKED BY: XXX
DATE: XXX
DESIGNED BY: XXX
DATE: XXX
SIZE: A4
DRAWING NUMBER: XXX
REV: X
SCALE: 1:1
WEIGHT(kg): XXX
SHEET: 1/1

Figure C.26: Engineering drawing of the conceptual thruster housing.

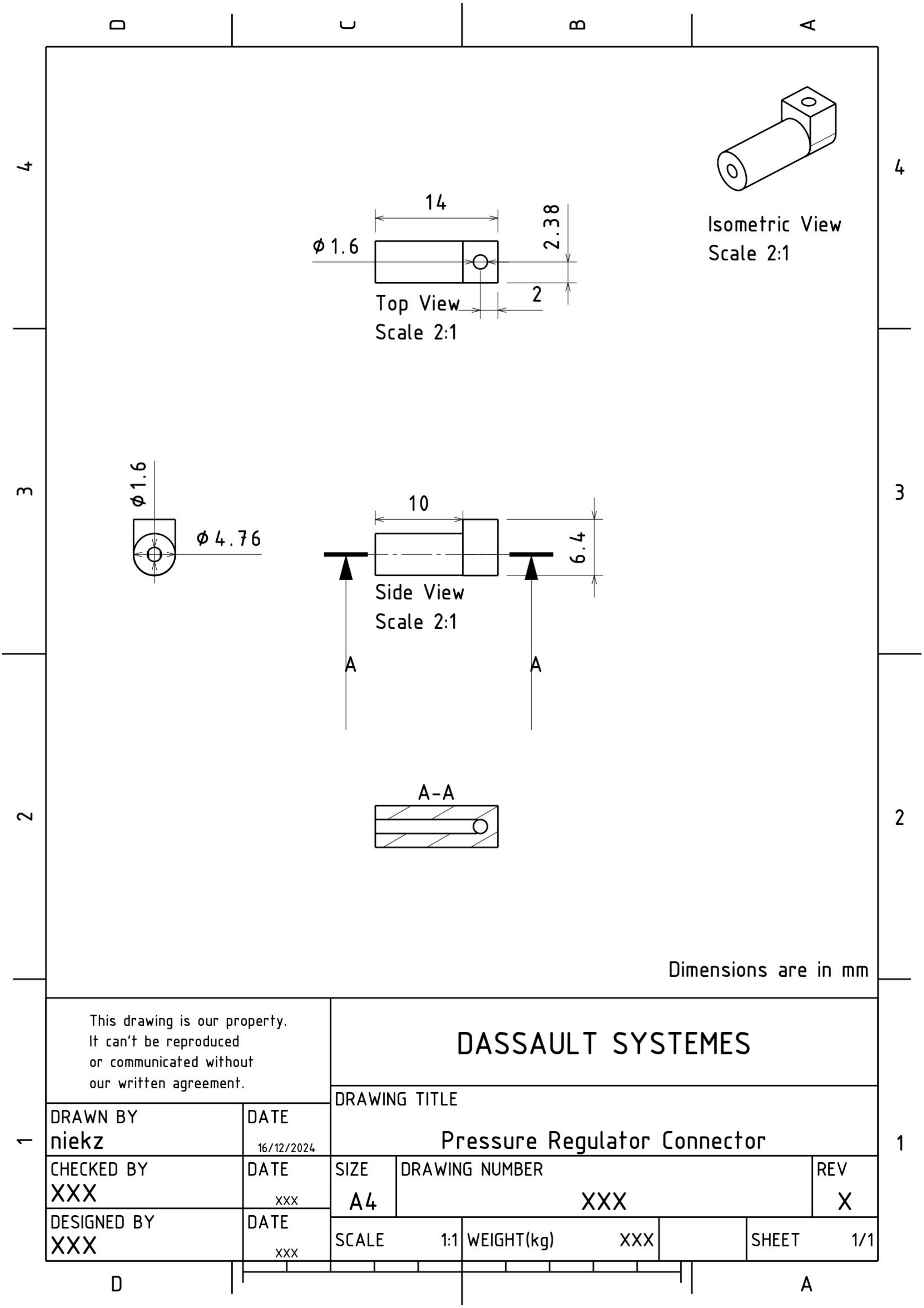

Figure C.27: Engineering drawing of the pressure regulator connector.

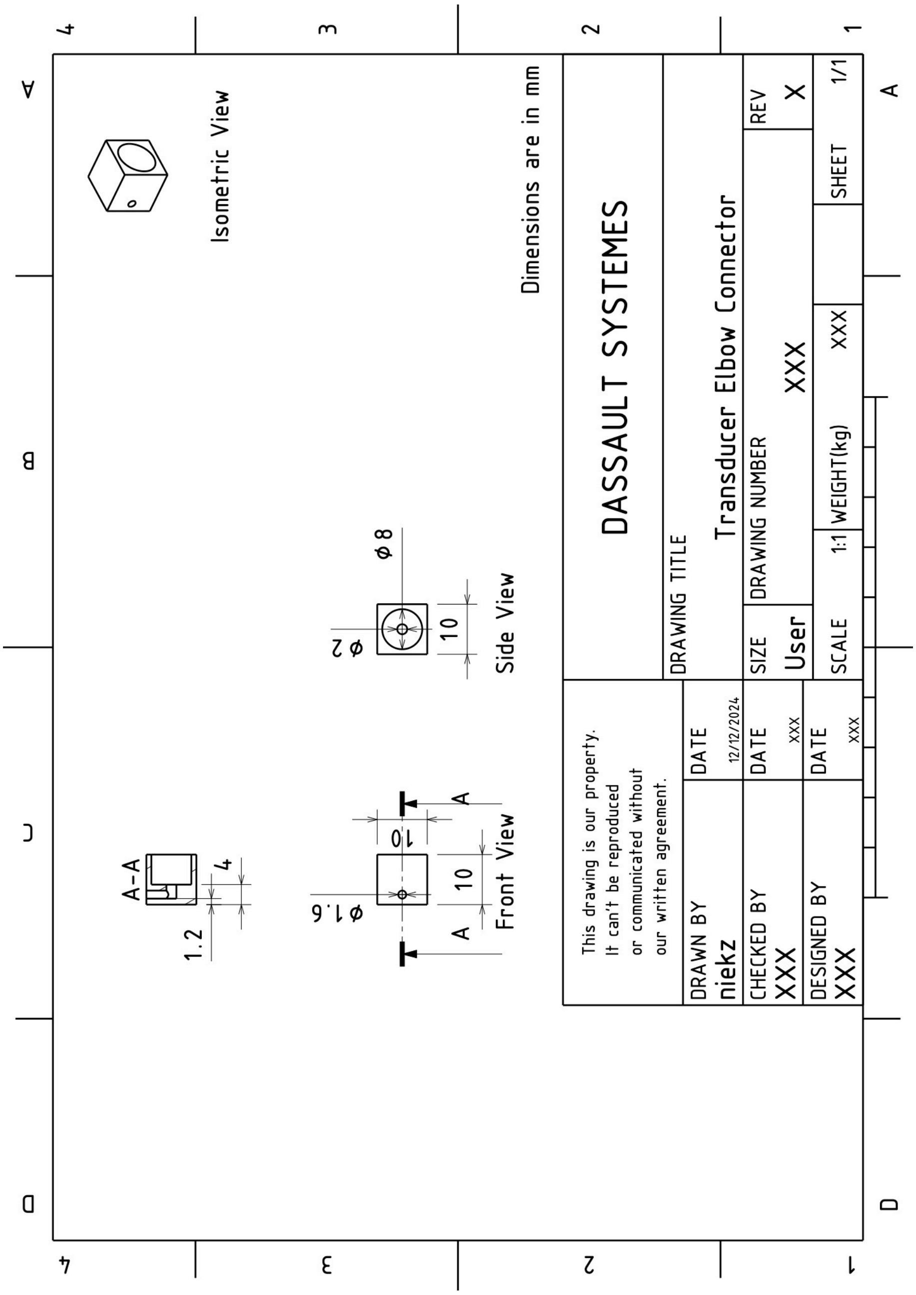

Figure C.28: Engineering drawing of the pressure and temperature transducer connector.